

PATHWAYS FOR LOW EMISSIONS UTILIZING SPRAY TARGETED REACTIVITY  
STRATIFICATION (STARS) IN HIGH EFFICIENCY NATURAL GAS  
DUAL FUEL COMBUSTION

by

KENDYL RYAN PARTRIDGE

SUNDAR RAJAN KRISHNAN, COMMITTEE CHAIR  
KALYAN KUMAR SRINIVASAN, COMMITTEE CO-CHAIR  
AJAY AGRAWAL  
JOSHUA BITTLE  
JAMES SHOGREN-HARRIS

A DISSERTATION

Submitted in partial fulfillment of the requirements  
for the degree of Doctor of Philosophy  
in the Department of Mechanical Engineering  
in the Graduate School of  
The University of Alabama

TUSCALOOSA, ALABAMA

2022

Copyright Kendyl Ryan Partridge 2022  
ALL RIGHTS RESERVED

## ABSTRACT

Internal combustion engines are a key aspect of society, and their continued use poses challenges from an environmental standpoint since they emit pollutant and greenhouse gas emissions. This dissertation focuses on experimental analysis of dual-fuel low temperature combustion (LTC), which can be used as a strategy to reduce engine-out emissions and increase engine efficiencies. Dual fuel LTC uses two different fuels, a high reactivity fuel (HRF) and a low reactivity fuel (LRF). The HRF has a higher cetane number than the LRF, which allows for easier auto-ignition in compression ignition engines. Dual fuel engines also utilize high air to fuel ratios to achieve LTC. This, combined with early injection timings of the HRF, helps to reduce oxides of nitrogen ( $\text{NO}_x$ ) emissions. At low load conditions, this is a problem since higher cycle-to-cycle variations can increase pollutants such as unburned hydrocarbons (UHC) and carbon monoxide (CO). To combat this, a firm understanding of dual fuel LTC is required, as well as a strategy for reducing the cycle-to-cycle variations. The first part of this work further identifies a combustion heat release ‘transformation region’ across different HRF injection timings wherein in-cylinder conditions arise that are conducive for ultra-low  $\text{NO}_x$  emissions. This phenomenon occurs for different IC engine platforms and different fueling combinations. An experimental analysis, 0D chemical kinetic analysis, and 3D computation fluid dynamic (CFD) analysis were combined to elucidate the underlying causes for this phenomenon. The local stratification level of the fuel/air mixture was identified as the likely cause of combustion heat release transformation with changing HRF injection timing. The second part of

the present work builds upon the findings of the first part by utilizing local stratification to mitigate cycle-to-cycle variations that are present at low loads. A framework of experiments was formulated for both a low engine load of 5 bar gross indicated mean effective pressure (IMEP<sub>g</sub>) and a high load of 15 bar IMEP<sub>g</sub>, wherein an injection strategy concept termed Spray TArgeted Reactivity Stratification (STARS) was utilized using both diesel and Polyoxymethelene-dimethyl-ether (POMDME) as HRFs. A steep decrease in UHC and CO emissions (> 80% reductions) as well as improved engine operation stability were demonstrated using both HRFs with dual fuel LTC at 5 bar IMEP<sub>g</sub>. Further, potential for emissions mitigation and efficiency improvement are discussed, as well as differences in the experimental results shown between the differing HRFs.

## DEDICATION

This dissertation is dedicated to my loving mother and father. Without their continued guidance and love I would never have been able to be able to write this dissertation, let alone become the person I am today.

## LIST OF ABBREVIATIONS AND SYMBOLS

AHRR	Apparent Heat Release Rate
BMEP	Brake Mean Effective Pressure
BTDC	Before Top Dead Center
CA 5-90	Combustion Duration
CA5	5% of Cumulative Heat Release (Start of Combustion)
CA50	50% of Cumulative Heat Release (Combustion Phasing)
CA90	90% of Cumulative Heat Release (End of Combustion)
CAD	Crank Angle Degree
CO	Carbon Monoxide
CO <sub>2</sub>	Carbon Dioxide
COV <sub>IMEP</sub>	Coefficient of Variation of Indicated Mean Effective Pressure
DFLTC	Dual Fuel Low Temperature Combustion
EOI	End of Injection
EVC	Exhaust Valve Closure
EVO	Exhaust Valve Opening
GCI	Gasoline Compression Ignition
GHG	Greenhouse Gas
H <sub>2</sub> O	Water
HCCI	Homogenous Charge Compression Ignition

HRF	High Reactivity Fuel
HTHR	High Temperature Heat Release
IFCE	Indicated Fuel Conversion Efficiency
IMEP	Indicated Mean Effective Pressure
IMEP <sub>g</sub>	Gross Indicated Mean Effective Pressure
ISCO	Indicated Specific Carbon Monoxide
ISHC	Indicated Specific Unburned Hydrocarbons
ISNO <sub>x</sub>	Indicated Specific Oxides of Nitrogen
IVC	Intake Valve Closure
IVO	Intake Valve Opening
LHV	Lower Heating Value
LRF	Low Reactivity Fuel
LTHR	Low Temperature Heat Release
MPRR	Maximum Pressure Rise Rate
N-C <sub>12</sub> OQOOH	Ketohydroperoxide Radical
NG	Natural Gas
NO <sub>x</sub>	Oxides of Nitrogen
OH	Hydroxyl Radical
OME	Oxymethylene Dimethyl Ether
P	Cylinder Pressure
P <sub>Boost</sub>	Absolute Intake Boost Pressure
P <sub>Crit</sub>	Critical Pressure
PES	Percent Energy Substitution

POMDME	Polyoxymethylene Dimethyl Ether
RCCI	Reactivity Controlled Compression Ignition
$R_{Univ}$	Universal Gas Constant
SCRE	Single Cylinder Research Engine
SOI	Start of Injection
SOI1	First Introduced Injection
SOI2	Second Introduced Injection
STARS	Spray Targeted Reactivity Stratification
T	In-Cylinder Temperature
$T_{Crit}$	Critical Temperature
TDC	Top Dead Center
UHC	Unburned Hydrocarbons
$\gamma$	Ratio of Specific Heats
$\eta_{Comb}$	Combustion Efficiency
$\phi$	Equivalence Ratio
$\phi_{React}$	Reaction Ratio

## ACKNOWLEDGMENTS

I would firstly like to acknowledge my committee chair and co-chair, Dr. Sundar Rajan Krishnan, and Dr. Kalyan Kumar Srinivasan. Without their constant support, and incredible amount of patience, none of the work presented in this dissertation could have been achieved. They also helped me tremendously outside of the classroom and lab environment, by introducing me to ideas and concepts that I would have otherwise never been exposed to. For this, I will be forever grateful. I would also like to acknowledge the remaining committee members of Dr. Ajay Agrawal, Dr. Joshua Bittle, and Dr. James Shogren-Harris. Their excellent questions and comments helped to create a work that I am very proud of, and one that I hope they are also proud to have been associated with.

Secondly, I want to thank all my colleagues with whom I have worked with and become friends with during my graduate school career. Kyle and Shameem helped introduce me to the life of working in the lab and gave me good footing to build upon. Hamid was one of the hardest working individuals I have ever met and taught me so much about how to navigate life and work. Prabhat was one of the best roommates I could have had, has given me invaluable advice and guidance throughout rough times in my life, not to mention he is a good chef as well. Deiva helped to re-energize me when things were looking bleak and always had a different perspective to offer, which always helped to propel myself and the lab forward. Abhinandhan was invaluable in lending a hand with anything I needed and was always eager to learn anything new, and I look forward to seeing his progress in the lab after I leave. Austin and Phillip were always kind and

helpful in all things and were always game to talk about philosophy. All these people helped shape me as a person and helped shape my graduate school career, and I will forever be thankful for their help and support.

Lastly, I would like to acknowledge and thank my close friends and family. Without my mother and father, Lisa and Kenneth, I wouldn't be here today. They gave me all the opportunities in life that I could have ever asked for, and I could not have asked for a better upbringing than the one they gave me. I also want to thank some of my closest friends: Jordan, Joel, Zach, and Rob. They were always there to pick me up when I was down. They introduced me to some of my now favorite activities like camping, hiking, and golf. They have given me some of the best laughs that I have ever had, and I will forever cherish them.

## CONTENTS

ABSTRACT .....	ii
DEDICATION .....	iv
LIST OF ABBREVIATIONS AND SYMBOLS .....	v
ACKNOWLEDGMENTS .....	viii
LIST OF TABLES .....	xiv
LIST OF FIGURES .....	xvi
I. INTRODUCTION .....	1
1.1 BACKGROUND AND RATIONALE FOR DUAL FUEL COMBUSTION .....	1
1.2 OVERVIEW OF SPRAY TARGETED REACTIVITY STRATIFICATION .....	5
1.3 POLYOXYMETHYLENE DIMETHYL ETHER AS A FUEL IN IC ENGINES .....	7
1.4 ORGANIZATION OF THE DISSERTATION.....	8
II. AN EXPERIMENTAL AND COMPUTATIONAL ANALYSIS OF COMBUSTION HEAT RELEASE TRANSFORMATION IN DUAL FUEL COMBUSTION.....	10
2.1 ABSTRACT.....	10
2.2 INTRODUCTION .....	11
2.3 EXPERIMENTAL SETUP.....	14
2.4 EXPERIMENTAL PROCEDURE .....	17
2.5 EXPERIMENTAL RESULTS.....	19
2.6 0-D CHEMICAL KINETIC STUDY .....	26

2.7	3D COMPUTATIONAL FLUID DYNAMIC SIMULATIONS .....	35
2.8	SUMMARY AND CONCLUSIONS .....	48
III. EXPERIMENTAL ANALYSIS OF COMBUSTION HEAT RELEASE TRANSFORMATION FOR DIESEL-NATURAL GAS AND POMDME-NATURAL GAS DUAL FUEL COMBUSTION ON A HIGH COMPRESSION RATIO SINGLE- CYLINDER ENGINE .....		
		51
3.1	ABSTRACT.....	51
3.2	INTRODUCTION .....	52
3.3	EXPERIMENTAL SETUP.....	54
3.4	DIESEL-NATURAL GAS RESULTS.....	59
3.5	POMDME-NATURAL GAS RESULTS .....	65
3.6	SUMMARY AND CONCLUSIONS .....	71
IV. COMBUSTION ANALYSIS FOR DUAL FUEL STRATEGIES APPLIED TO REDUCE ENGINE OUT HC, CO, AND NO <sub>x</sub> EMISSIONS USING DIESEL- NATURAL GAS AND POMDME-NATURAL GAS.....		
		73
4.1	ABSTRACT.....	73
4.2	INTRODUCTION .....	74
4.3	EXPERIMENTAL SETUP.....	79
4.4	EXPERIMENTAL PROCEDURE.....	83
4.5	SUMMARY AND CONCLUSIONS .....	87
4.5.1	STEP 1: SOI SWEEP.....	87
4.5.2	STEP 2(a): SPLIT INJECTION (STARS) SWEEP .....	90
4.5.3	STEP 2(b): PES SWEEP .....	98
4.5.4	INJECTION SPLIT RATIO SWEEP.....	102
4.5.5	RAIL PRESSURE SWEEP .....	105

4.5.6	ABSOLUTE BOOST PRESSURE SWEEP.....	108
4.6	CONCLUSIONS.....	112
V. A COMPARATIVE ANALYSIS OF HIGH LOAD NATURAL GAS DUAL FUEL COMBUSTION IGNITED BY DIESEL AND POMDME.....		
		114
5.1	ABSTRACT.....	114
5.2	INTRODUCTION .....	115
5.3	EXPERIMENTAL SETUP.....	117
5.4	EXPERIMENTAL PROCEDURE .....	117
5.5	EXPERIMENTAL RESULTS – DIESEL/NATURAL GAS.....	119
5.5.1	STEP 1: PES & SOI SWEEP.....	119
5.5.2	STEP 2: SECOND INJECTION (STARS) SWEEP .....	126
5.5.3	STEP 3: INJECTION SPLIT RATIO SWEEP.....	130
5.5.4	STEP 4: RAIL PRESSURE SWEEP .....	138
5.5.5	STEP 5: COUPLED SOI SWEEP .....	141
5.5.6	STEP 6: BOOST PRESSURE SWEEP .....	145
5.6	EXPERIMENTAL RESULTS – POMDME/NATURAL GAS.....	147
5.6.1	STEP 1: PES & SOI SWEEP.....	147
5.6.2	STEP 2: SECOND INJECTION (STARS) SWEEP .....	152
5.6.3	STEP 3: INJECTION SPLIT RATIO SWEEP.....	154
5.6.4	STEP 4: COUPLED SOI SWEEP .....	156
5.6.5	STEP 5: RAIL PRESSURE SWEEP .....	159
5.6.6	STEP 6: ABSOLUTE BOOST PRESSURE SWEEP .....	163
5.7	CONCLUSIONS.....	167

VI. SUMMARY OF CONCLUSIONS AND RECOMMENDATIONS FOR FUTURE WORK .....	169
REFERENCES .....	174
APPENDIX.....	186

## LIST OF TABLES

Table 2.1. General Engine Specifications.....	15
Table 2.2. Details of experimental sensors and their accuracies. ....	16
Table 2.3. Engine Operating Conditions.....	17
Table 2.4. Start of LTHR and HTHR, end of injection (EOI), and injection duration. ....	23
Table 2.5. Pressure and temperature at the onset of LTHR and HTHR for each SOI. ....	24
Table 2.6. Pressure and temperature at CAD = 338.6. ....	26
Table 2.7. Parameters for Chemkin sweeps.....	27
Table 3.1. Single cylinder research engine specifications. ....	54
Table 3.2. Engine operating conditions for both diesel and POMDME.....	57
Table 3.3. Details of sensors used on CR = 18.5 engine platform.....	58
Table 3.4. Start of LTHR and start of HTHR for diesel/natural gas combustion on the 18.5:1 compression ratio SCRE.....	63
Table 3.5. Pressure and temperature @ start of LTHR and HTHR for diesel/natural gas combustion on the 18.5:1 CR engine platform. ....	63
Table 3.6. POMDME and diesel fuel properties.....	66
Table 3.7. Onset of LTHR and onset of HTHR locations for POMDME/natural gas on the 18.5:1 CR engine platform.....	69
Table 3.8. Pressure and temperature at the onset of LTHR and HTHR for POMDME/natural gas on the 18.5:1 CR engine platform.....	69
Table 4.1. General engine specifications. ....	80
Table 4.2. Details of experimental sensors and their accuracies. ....	82
Table 4.3. Fuel properties. ....	83

Table 5.4. Injection Timings, Injection Duration, Flowrates, and IMEP for June 13, 2022 and June 18, 2022 data.....	134
Table A.1. HCCI IC engine model parameters.....	186
Table A.2. Operating parameters for each case .....	187

## LIST OF FIGURES

Figure 1.1. Passenger-miles projections for OECD and non-OECD countries through the year 2050. [2].....	2
Figure 1.2. Visualization of low temperature combustion regimes within the $\phi$ -T space. [5].....	3
Figure 1.3. Dual fuel LTC concept using propane as the LRF and diesel as the HRF. [7] .....	5
Figure 1.4. STARS combustion concept.....	6
Figure 2.1. Single Cylinder Research Engine Experimental Setup. ....	15
Figure 2.2. AHRR for SOIs of 320, 322, 325, 328, and 330 CAD at 5 bar IMEPg, 80% PES.....	19
Figure 2.3. CA5, CA50, and CA5-90 values at 5 bar IMEPg, 80% PES. ....	20
Figure 2.4. Indicated Specific NO <sub>x</sub> Emissions at 5 bar IMEPg, 80% PES. ....	21
Figure 2.5. Indicated specific NO <sub>x</sub> vs. indicated fuel conversion efficiency.....	21
Figure 2.6. Enhanced view of AHRR showing the start of LTHR and HTHR with start of LTHR locations designated with a dot-dashed line and start of HTHR designated with a dashed line, both colored with respect to the corresponding SOI.....	22
Figure 2.7. Volumetric heat production for an initial pressure of 30 bar to 50 bar. ....	28
Figure 2.8. Ketohydroperoxide evolution for different initial pressures from 30 bar to 50 bar. ....	29
Figure 2.9. Volumetric heat production for an initial temperature of 830 to 930 K.....	30
Figure 2.10. Ketohydroperoxide mole fraction for an initial temperature of 830 to 930 K. ....	31
Figure 2.11. (a) Volumetric heat production and (b) natural log of volumetric heat production at different equivalence ratios.....	33

Figure 2.12. Natural log of volumetric heat production rate over the early reaction period (0 to 1 ms) at different equivalence ratios .....	34
Figure 2.13. Local reaction ratio vs. local temperature colored by ketohydroperoxide mass fractions for SOIs = 320, 325, and 330; CAD = 337-339.....	38
Figure 2.14. Local reaction ratio vs. local temperature, with colored by ketohydroperoxide mass fractions for SOIs = 320, 325, and 330; CAD = 340-342.....	39
Figure 2.15. Local reaction ratio vs. local temperature colored by ketohydroperoxide mass fractions for SOIs = 320 and 330 and a range of 0 - 0.005 mass fraction. ....	41
Figure 2.16. Reaction ratio histogram for each SOI at the respective start of LTHR locations. ....	42
Figure 2.17. Local reaction ratio vs. local temperature colored by CO <sub>2</sub> mass fractions for SOIs = 320, 325, and 330; CAD = 343-345. ....	43
Figure 2.18. Local reaction ratio vs. local temperature colored by CO <sub>2</sub> mass fractions for SOIs = 320, 325, and 330; CAD = 346-348. ....	44
Figure 2.19. Mass fraction of CO and OH at CAD = 344 for SOIs of 320 and 330 CAD. ....	46
Figure 3.1. Detailed engine layout.....	56
Figure 3.2. AHRR for SOIs of 320, 322, 324, 326, 328, and 330 CAD for CR = 18.5 engine at 5 bar IMEP <sub>g</sub> , 80% PES. ....	60
Figure 3.3. Indicated specific NO <sub>x</sub> values vs. IFCE for diesel/natural gas on the CR = 18.5 engine.....	61
Figure 3.4. LTHR portion of the AHRR curve for diesel/natural gas on the CR = 18.5:1 engine with dashed vertical lines representing the onset of HTHR and dot-dashed vertical lines representing the onset of LTHR, both colored with respect to the corresponding SOI. ....	62
Figure 3.5. AHRR vs. Temperature for diesel-natural gas combustion on the 18.5 CR engine platform. ....	64
Figure 3.6. AHRR profiles for POMDME/natural gas operation on the 18.5 CR engine platform.....	67
Figure 3.7. LTHR portion of the AHRR profiles for POMDME/natural gas on the 18.5:1 CR engine platform.....	68

Figure 3.8. Temperature at the onset of HTHR for both diesel and POMDME on an 18:1 CR engine platform.....	70
Figure 4.1. Detailed experimental setup.....	81
Figure 4.2. Detailed experimental procedure.....	84
Figure 4.3. Cylinder pressure (top), AHRR (middle), and emissions values (bottom) for diesel-NG (left) and POMDME-NG (right). ....	89
Figure 4.4. MPRR and $COV_{IMEP}$ values for diesel/natural gas (left) and POMDME/natural gas (right). ....	90
Figure 4.5. MPRR and $COV_{IMEP}$ for the SOI2 sweep for diesel/NG (left) and POMDME/NG (right).....	91
Figure 4.6. Cylinder pressure (top), AHRR (middle), and emissions (bottom) results for SOI2 sweep at each SOI2 timing for both diesel-NG (left) and POMDME-NG (right). ....	92
Figure 4.7. CA5, CA50, and C90 for diesel/NG (left) and POMDME natural gas (right) at each SOI2 injection timing. ....	93
Figure 4.8. LTHR portion of the AHRR curve for diesel/NG (left) and POMDME/natural gas (right).....	94
Figure 4.9. HRF flow rates for each SOI2.....	95
Figure 4.10. LTHR vs. in-cylinder temperature for diesel/NG (left) and POMDME/natural gas (right). ....	95
Figure 4.11. Residence time above 10% peak temperature and 20% peak temperature in CAD for diesel-NG (left) and POMDME-NG (right) with the residence times for the ‘best’ operating point from SOI1 being shown as horizontal lines. ....	98
Figure 4.12. Cylinder Pressure (top), AHRR (middle), and emissions (bottom) results from a PES sweep for both diesel/NG (left) and POMDME/NG (right).....	99
Figure 4.13. CA5, CA50, and CA90 results from a PES sweep for both diesel/NG (left) and POMDME/NG (right). ....	100
Figure 4.14. IFCE and combustion efficiency for results from a PES sweep for diesel/NG (left) and POMDME/NG (right) operation. ....	101

Figure 4.15. Residence time results from a PES sweep for diesel/NG (left) and POMDME/NG (right) operation.....	102
Figure 4.16. AHRR and emissions results at different injection ratios for diesel/NG (left) and POMDME/NG (right) operation. ....	103
Figure 4.17. Residence time results for injection split ratio sweep of POMDME/NG. ....	105
Figure 4.18. AHRR (top) and emissions (bottom) results for a rail pressure sweep using diesel/NG (left) and POMDME/NG (right) fueling combinations. ....	106
Figure 4.19. Residence time results for a rail pressure sweep using diesel/NG (left) and POMDME/NG (right) fueling combinations. ....	108
Figure 4.20. Cylinder pressure (top), AHRR (middle), and emissions (bottom) for a boost pressure sweep using diesel/NG (left) and POMDME/NG (right).....	109
Figure 4.21. Calculated real gas temperature(top) and residence time (bottom) for a boost pressure sweep using diesel/NG (left) and POMDME/NG (right).....	110
Figure 4.22. Exhaust temperatures for each boost pressure point for both diesel/NG and POMDME/NG. ....	111
Figure 5.1. Detailed experimental procedure for diesel/NG operation.....	118
Figure 5.2. Detailed experimental procedure for POMDME/NG operation. ....	118
Figure 5.3. ISHC, ISCO, and ISNO <sub>x</sub> values for an SOI sweep using diesel/NG operation at 15 bar IMEPg.....	120
Figure 5.4. Cylinder pressure profiles for SOI sweep at 15 bar IMEPg, 95% PES, with diesel/NG combustion.....	122
Figure 5.5. AHRR profiles for SOI sweep at 15 bar IMEPg, 95% PES, with diesel/NG combustion.....	122
Figure 5.6. CA5, CA50, and CA90 for the SOI sweep of 15 bar IMEPg, 95% PES using diesel/NG. ....	124
Figure 5.7. IFCE and Combustion Efficiency for an SOI sweep at 15 bar IMEPg and 95% PES using diesel/natural gas .....	125
Figure 5.8. Cylinder pressure curves for an SOI2 sweep at 15 bar IMEPg, SOI1 = 280 CAD, .....	127

Figure 5.9. AHRR profiles for an SOI2 sweep at 15 bar IMEPg, SOI1 = 280 CAD, PES = 95% with diesel/NG.....	128
Figure 5.10. CA5, CA50, CA90, IFCE, combustion efficiency, MPRR, COV <sub>IMEP</sub> , and emissions for an SOI2 sweep at 15 bar IMEPg, SOI1 = 280 CAD, PES = 95% with diesel/NG. ....	129
Figure 5.11. MPRR for each cycle for an injection split ratio of 0.48 at 15 bar IMEPg, SOI1 = 280 CAD, SOI2 = 295 CAD, and a PES = 95%. ....	131
Figure 5.12. AHRR profiles for diesel only operating points.....	132
Figure 5.13. AHRR comparison between the data from June 13, 2022 and June 18, 2022 at similar injection split ratios, SOI1 = 280 CAD, SOI2 = 295 CAD, PES = 95%, and at 15 bar IMEPg.....	133
Figure 5.14. Cylinder pressure and AHRR profiles for an injection split ratio sweep at 15 bar IMEPg, SOI1 = 280 CAD, SOI2 = 295 CAD, PES = 95% with diesel/NG.....	136
Figure 5.15. CA5, CA50, CA90, IFCE, combustion efficiency, MPRR, COV <sub>IMEP</sub> , and emissions for an injection split ratio sweep at 15 bar IMEPg, SOI1 = 280 CAD, SOI2 = 295 CAD, and a PES = 95% with diesel/NG.....	137
Figure 5.16. Cylinder pressure and AHRR profiles for a rail pressure sweep at 15 bar IMEPg, SOI1 = 280 CAD, SOI2 = 295 CAD, Split ratio = 0.59, and PES = 95% with diesel/NG. ....	139
Figure 5.17. CA5, CA50, CA90, IFCE, combustion efficiency, MPRR, COV <sub>IMEP</sub> , and emissions for a rail pressure sweep at 15 bar IMEPg, SOI1 = 280 CAD, SOI2 = 295 CAD, Split Ratio = 0.59, and a PES = 95% with diesel/NG. ....	140
Figure 5.18. Cylinder pressures for a coupled SOI sweep at 15 bar IMEPg, Split ratio = 0.59, P <sub>Rail</sub> = 500 bar and PES = 95% with diesel/NG.....	141
Figure 5.19. AHRR profiles for a coupled SOI sweep at 15 bar IMEPg, split ratio = 0.59, P <sub>Rail</sub> = 500 bar and PES = 95% with diesel/NG.....	142
Figure 5.20. CA5, CA50, CA90, IFCE, combustion efficiency, MPRR, COV <sub>IMEP</sub> , and emissions for a coupled SOI sweep at 15 bar IMEPg, split ratio = 0.59, P <sub>Rail</sub> = 500 bar, and a PES = 95% with diesel/NG. ....	143
Figure 5.21. Cylinder pressure and AHRR profiles for a boost pressure sweep at 15 bar IMEPg, SOI1 = 295 CAD, SOI2 = 310 CAD, split ratio = 0.59, P <sub>Rail</sub> = 500 bar and PES = 95% with diesel/NG.....	145

Figure 5.22. CA5, CA50, CA90, IFCE, combustion efficiency, MPRR, COV <sub>IMEP</sub> , and emissions for a coupled SOI sweep at 15 bar IMEP <sub>g</sub> , split ratio = 0.59, P <sub>Rail</sub> = 500 bar, and a .....	146
Figure 5.23. ISHC, ISCO, and ISNO <sub>x</sub> values for an SOI and PES sweep using diesel/POMDME operation at 15 bar IMEP <sub>g</sub> .....	148
Figure 5.24. Cylinder pressure and AHRR profiles for SOI sweep at 15 bar IMEP <sub>g</sub> , 97% PES, with POMDME/NG combustion. ....	149
Figure 5.25. CA5, CA50, CA90, IFCE, combustion efficiency, MPRR, and COV <sub>IMEP</sub> , for an SOI sweep at 15 bar IMEP <sub>g</sub> , PES = 97% with POMDME/NG .....	150
Figure 5.26. Cylinder pressure and AHRR profiles for an SOI <sub>2</sub> sweep at 15 bar IMEP <sub>g</sub> , SOI <sub>1</sub> = 300 CAD, PES = 97% with POMDME/NG .....	152
Figure 5.27. CA5, CA50, CA90, IFCE, combustion efficiency, MPRR, COV <sub>IMEP</sub> , and emissions for an SOI <sub>2</sub> sweep at 15 bar IMEP <sub>g</sub> , SOI <sub>1</sub> = 300 CAD, and a PES = 97% with POMDME/NG .....	153
Figure 5.28. IFCE, combustion efficiency, and emissions for an injection ratio sweep at 15 bar IMEP <sub>g</sub> , SOI <sub>1</sub> = 300 CAD, SOI <sub>2</sub> = 310 CAD, and a PES = 97% with POMDME/NG .....	155
Figure 5.29. Cylinder pressures for a coupled SOI sweep at 15 bar IMEP <sub>g</sub> , split ratio = 0.45, and PES = 97% with POMDME/NG .....	156
Figure 5.30. AHRR profiles for a coupled SOI sweep at 15 bar IMEP <sub>g</sub> , split ratio = 0.45, and PES = 97% with POMDME/NG .....	157
Figure 5.31. CA5, CA50, CA90, IFCE, combustion efficiency, MPRR, COV <sub>IMEP</sub> , and emissions for a coupled SOI sweep at 15 bar IMEP <sub>g</sub> , split ratio = 0.45, and a PES = 97% with POMDME/NG .....	158
Figure 5.32. Cylinder pressure and AHRR profiles for a rail pressure sweep at 15 bar IMEP <sub>g</sub> , SOI <sub>1</sub> = 305 CAD, SOI <sub>2</sub> = 315 CAD, split ratio = 0.45, and PES = 97% with POMDME/NG .....	160
Figure 5.33. CA5, CA50, CA90, IFCE, combustion efficiency, MPRR, COV <sub>IMEP</sub> , and emissions for a rail pressure sweep at 15 bar IMEP <sub>g</sub> , SOI <sub>1</sub> = 305 CAD, SOI <sub>2</sub> = 315 CAD, split ratio = 0.45, and a PES = 97% with POMDME/NG .....	162
Figure 5.34. Cylinder pressure and AHRR profiles for a boost pressure sweep at 15 bar IMEP <sub>g</sub> , SOI <sub>1</sub> = 305 CAD, SOI <sub>2</sub> = 315 CAD, split ratio = 0.45, rail pressure of 500 bar, and PES = 97% with POMDME/NG .....	164

Figure 5.35. CA5, CA50, CA90, IFCE, combustion efficiency, MPRR, COV<sub>IMEP</sub>, and emissions for a boost pressure sweep at 15 bar IMEPg, SOI1 = 305 CAD, SOI2 = 315 CAD, split ratio = 0.45, rail pressure of 500 bar, and a PES = 97% with POMDME/NG..... 165

Figure 5.36. Exhaust temperatures for both diesel/NG and POMDME/NG as a function of boost pressure..... 167

Figure A.1. Net heat release rate for each HCCI IC engine case..... 188

# I. INTRODUCTION

## 1.1 BACKGROUND AND RATIONALE FOR DUAL FUEL COMBUSTION

Reciprocating internal combustion engines have been a prevalent aspect of society, whether through the movement of goods and people, or through the production of electricity ever since they were first developed in the mid to late 19<sup>th</sup> century [1]. Since their inception they have relied on some form of hydrocarbon fuel to operate. This, in its very nature, poses a problem since with every combustion event that occurs inside the engine there is inevitably harmful pollutants and greenhouse gases (e.g., carbon dioxide) that are released into the atmosphere. Since combustion of typical fossil hydrocarbon fuels will inherently produce harmful emissions, attempts to mitigate the effects that fossil hydrocarbon fuels have on the environment, either by reducing the amount of fossil hydrocarbon fuels used, or through emissions mitigation and cleaner combustion strategies are important.

The Energy Information Administration's (EIA) International Energy Outlook (IEO) for 2021 [2] predicts that demand for travel will increase. Figure 1.1, which was taken from the 2021 IEO, shows that, not only will the passenger-miles increase worldwide through the year 2050, but a large portion of those passenger-miles will be with some form of light-duty vehicles or buses.

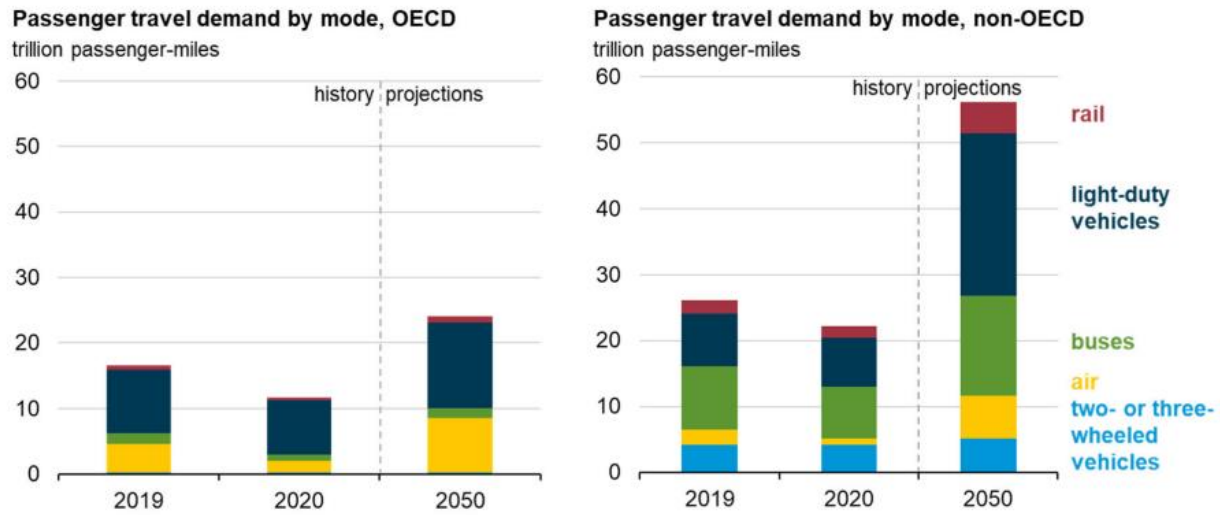


Figure 1.1. Passenger-miles projections for OECD and non-OECD countries through the year 2050. [2]

It is projected in the EIA's Annual Energy Outlook for 2022 [3] that at least 79% of the light duty vehicles sold in the United States in the year 2050 will be powered through conventional IC engines. This number is down from 92% in 2021, but the fact remains that IC engines will continue to be used in vast numbers for decades to come. Since reducing the use of IC engines is clearly not attainable, the best remaining method for emissions mitigation must be through the research of renewable alternative fuels and cleaner combustion strategies.

Typically, to allow for proper emissions mitigation, aftertreatment devices such as diesel particulate filters and selective catalytic reduction devices are used to reduce particulate matter (or soot) and oxides of nitrogen (NO<sub>x</sub>) emissions, respectively. The aftertreatment devices that are currently used, while beneficial for emissions, can be detrimental to engine efficiencies and costly; therefore, a goal of advanced combustion strategies is to reduce the load on aftertreatment devices in meeting future emissions standards by using advanced in-cylinder combustion strategies to reduce formation of the emissions in the first place and thereby avoid the need to

mitigate them in aftertreatment. One such strategy is the low temperature combustion (LTC) concept. Typically, there exists a  $\text{NO}_x$ -soot tradeoff with diesel combustion. This can be visualized by plotting the equivalence ratio ( $\phi$ ) against in-cylinder temperature ( $T$ ), as was shown by Akihama et al. [4]. Neely et al. [5] then built upon this concept to visualize different combustion modes within the  $\phi$ - $T$  space, as shown in Figure 1.2.

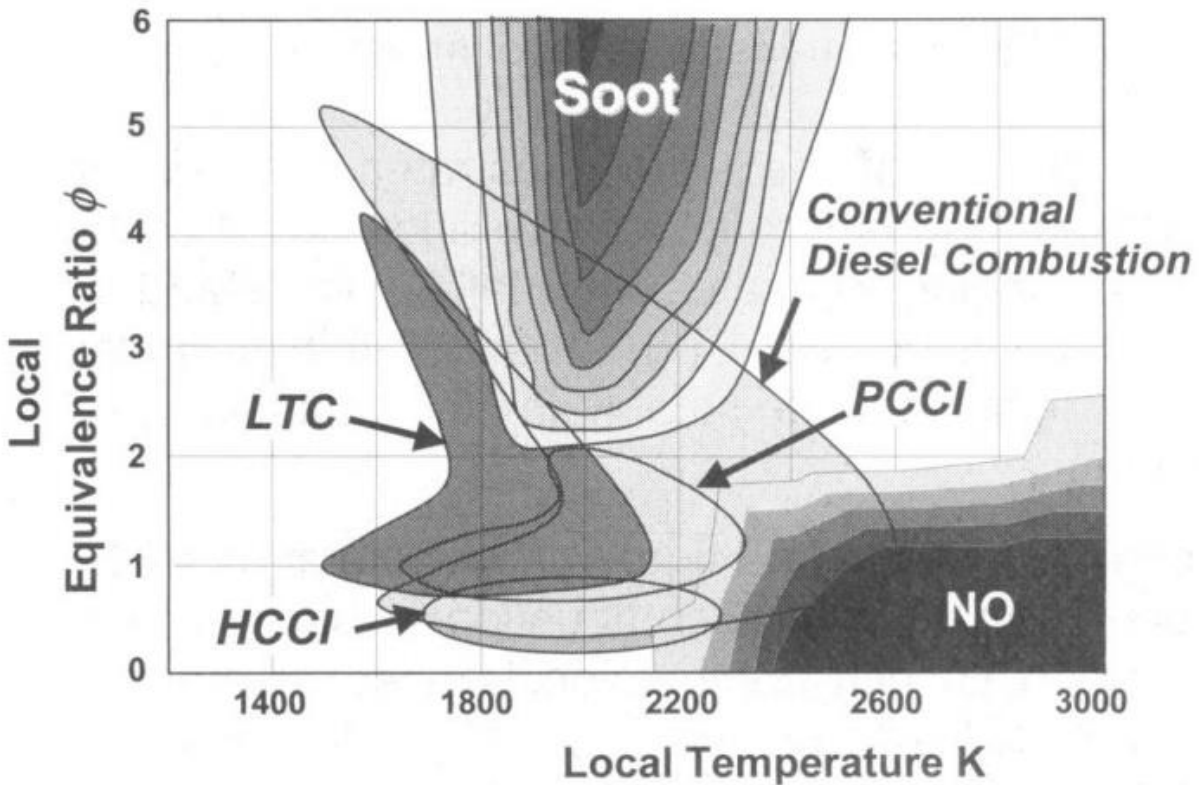


Figure 1.2. Visualization of low temperature combustion regimes within the  $\phi$ - $T$  space. [5]

The tradeoff between soot formation and  $\text{NO}_x$  formation is shown to be a problem that plagues conventional diesel combustion. The LTC concept, though, has the benefit of producing ultra-low  $\text{NO}_x$  emissions, as well as minimal soot emissions by injecting fuel early enough within the engine cycle to allow for sufficient mixing within the combustion chamber. This allows for lower local equivalence ratios to be achieved, which can mitigate the  $\text{NO}_x$ -soot

tradeoff. There are many combustion strategies that can achieve low temperature combustion, such as homogeneous charge compression ignition (HCCI), or premixed charge compression ignition (PCCI), both of which are shown in Figure 1.2. However, this work will focus on the use of dual fueling to achieve LTC.

Dual fueling consists of operating the IC engine on two separate fuels with different levels of reactivity. Usually, a gaseous low reactivity fuel (LRF) is fumigated into the intake manifold, while the high reactivity fuel (HRF) is directly injected into the combustion chamber. The LRF is typically defined as a high octane fuels (i.e. autoignition of the fuel is difficult), whereas the HRF is typically defined as a fuel that has a cetane number that is higher than the LRF chosen (i.e. autoignition of the fuel is easier relative to the higher octane fuel). Dual fueling can be used for a wide variety of applications, including power generation. The advantages that dual fueling has over a combustion strategy such as HCCI include more robust combustion control over a wide range of operating conditions. With HCCI combustion, the start of combustion and combustion phasing is dominated by the chemical kinetic processes within the combustion chamber [6]. Dual fuel strategies, such as reactivity-controlled compression ignition (RCCI), introduce a level of stratification to the fuel-air mixture within the combustion chamber, which aide in providing more control over the start of combustion and the combustion phasing. Figure 1.3, reproduced from Polk et al. [7], illustrates how dual fuel combustion (with diesel as the HRF and propane as the LRF, for example) can be used to achieve LTC, and therefore for emissions mitigation.

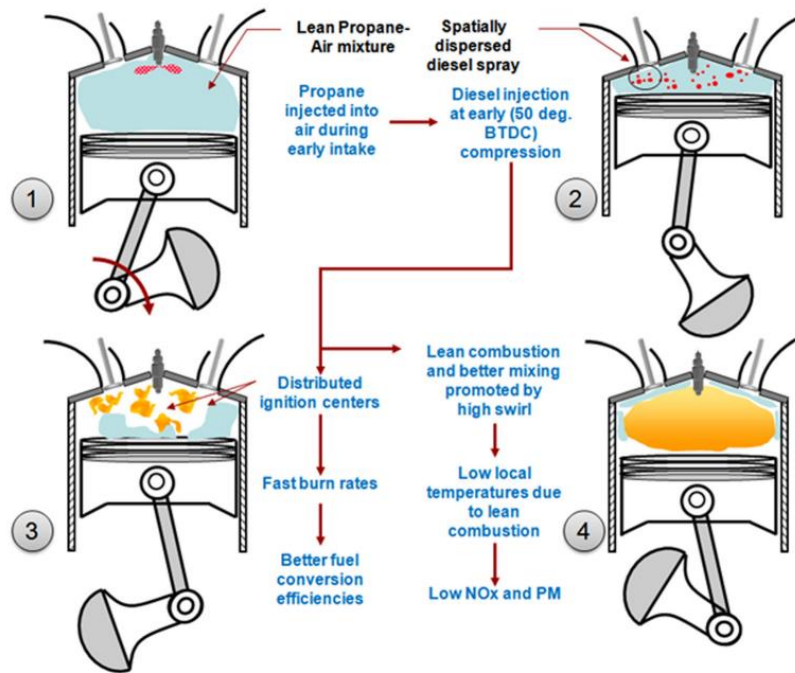


Figure 1.3. Dual fuel LTC concept using propane as the LRF and diesel as the HRF. [7]

To achieve LTC conditions, the HRF needs to be injected early enough to allow for sufficient dispersion throughout the combustion chamber. This allows for distributed ignition centers to form, which leads to better fuel conversion efficiencies and lower soot and NO<sub>x</sub> emissions. The early injection strategy may be beneficial for NO<sub>x</sub> and soot emissions, but is detrimental for carbon monoxide (CO) and unburned hydrocarbon (UHC) emissions, especially at low engine loads. To counteract this, the concept of **Spray Targeted Reactivity Stratification (STARS)** was conceived.

## 1.2 OVERVIEW OF SPRAY TARGETED REACTIVITY STRATIFICATION

The concept of STARS relies on using the dual fuel LTC concept previously mentioned, but instead of using a single injection, multiple injections can be introduced. Figure 1.4 illustrates the process of STARS.

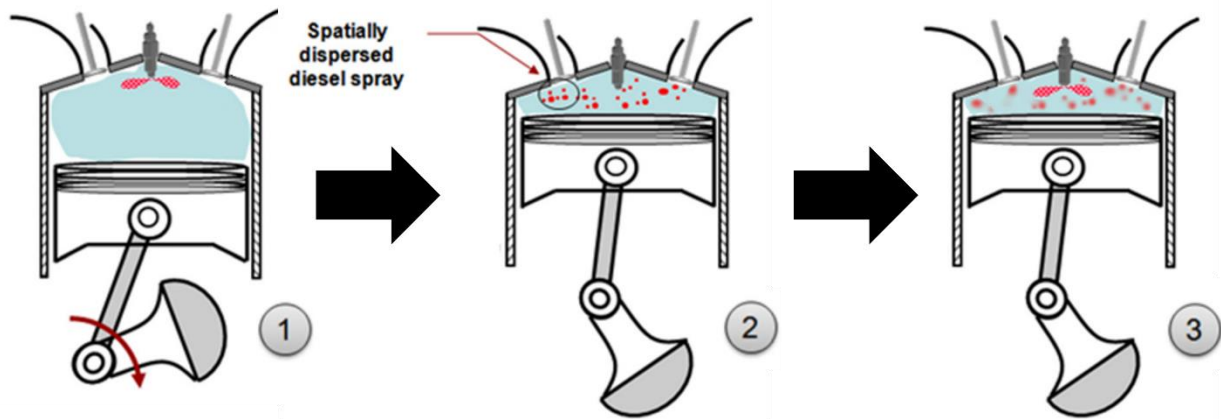


Figure 1.4. STARS combustion concept.

Step 1 of the STARS combustion strategy is the same as step 1 from the LTC concept shown in Figure 1.3, wherein some HRF is directly injected into a lean LRF-fuel air mixture. Similarly, Step 2 of STARS shows the spatially dispersed HRF which is similar to step 2 in the LTC concept as well. In this case, diesel is shown as being the HRF, but other high cetane fuels can be used as well. The differences between the two concepts emerges in Step 3 wherein a second injection of HRF is introduced into the already spatially dispersed spray.

By introducing a second injection in this way, the overall fuel-air mixture becomes further stratified, which is hypothesized to allow for more distributed ignition centers to develop in the combustion chamber. Providing more ignition centers, in theory, allows for more of the LRF-air fuel mixture, which inherently does not want to auto-ignite, to be exposed to these points of ignition thereby decreasing the UHC emissions. It is also posited that CO emissions can decrease, seeing as more distributed ignition centers can provide for even faster burn rates and longer residence times of relatively higher temperature regions compared to traditional dual fuel LTC, thereby allowing for more time for the CO to CO<sub>2</sub> conversion process to take place. The

stratification level within the combustion chamber can be adjusted by using STARS, thereby providing a valuable lever for reducing engine-out emissions in dual fuel combustion.

### 1.3 POLYOXYMETHYLENE DIMETHYL ETHER AS A FUEL IN IC ENGINES

As mentioned previously, the  $\text{NO}_x$  – soot tradeoff is a problem with conventional diesel combustion. LTC concepts attempt to solve this problem by reducing the local combustion temperatures to mitigate the amount of  $\text{NO}_x$  produced, while also using a lean fuel air mixture to mitigate the amount of soot. This works well, but also poses challenges such as higher CO and UHC emissions particularly for low load dual fuel LTC. It is well-known that oxygenated fuels could provide a low sooting alternative to diesel in compression ignition engines [8-11].

Oxygenated fuels can reduce the amount of soot that is produced during combustion by reducing the number of carbon-carbon bonds in the fuel molecule thereby changing the effects of pyrolysis [11], which is one primary mechanisms of soot formation [12,13]. In recent years, polyoxymethylene dimethyl ether (POMDME), which is an oxygenated fuel, has been shown to mitigate soot emissions [14-21], including in single cylinder engine applications at different engine loads [19], as well as multi-cylinder engines [21]. POMDME is typically a combination of six different oxymethylene dimethyl ethers (OMEs). The chemical formula for OME is  $\text{CH}_3(\text{-O-CH}_2)_n\text{-O-CH}_3$ , where  $n$  represents the number of (O-CH<sub>2</sub>) portions of the chain length.

POMDME is especially appealing because, depending on the blend, the mass fraction of oxygen within the molecule of POMDME itself can reach upwards of ~50% [14]. POMDME can also be used in with minor modifications to the injection system, if the right blend is used, due to the higher viscosity and higher boiling point of the fuel [22]. In essence, POMDME remains in the liquid phase under standard conditions of temperature and pressure, similar to typical diesel fuel. The last added benefit of using POMDME is that ongoing research to make POMDME

renewably [23-26] provides avenues to decrease the carbon footprint of any IC engine that uses renewably sourced POMDME for fueling.

#### 1.4 ORGANIZATION OF THE DISSERTATION

The present dissertation is organized in the following manner:

- Chapter II discusses a phenomenon known as the apparent heat release rate (AHRR) transformation region, which has been observed in dual fuel combustion and coincides with a reduction in NO<sub>x</sub> emissions. An experimental analysis, a 0D-chemical kinetic analysis, and a 3D-computational fluid dynamics analysis are combined to elucidate the underlying causes for the AHRR transformation region.

The results of Chapter II are currently under review in the journal *Fuel* under the title “An experimental and computational analysis of combustion heat release transformation in dual fuel combustion” [27].

- Chapter III builds upon the work presented in Chapter II through the observation of the AHRR transformation region on a different SCRE platform with different fuel combinations. The impact that different HRFs had on AHRR transformation was also studied, with diesel and POMDME being considered as the HRFs. City natural gas was used as the LRF, which differs from Chapter II which used pure methane, and the effect that of this change on AHRR transformation is also discussed.
- Chapter IV discusses an experimental framework which was conceived to reduce engine-out HC, CO and NO<sub>x</sub> emissions for low load (5 bar IMEPg) operation utilizing the STARS strategy. Emissions and efficiency data have been published in the *SAE International Journal of Advances and Current Practices in Mobility*. Another journal manuscript, comparing the relative performance and emissions

benefits of utilizing STARS and other strategies with both diesel-NG and POMDME-NG dual fuel combustion, is under review in the *International Journal of Engine Research*.

- Chapter V uses a similar experimental framework to Chapter IV to attempt to increase the indicated fuel conversion efficiency while maintaining low NO<sub>x</sub>, HC, and CO emissions at a high load (15 bar IMEP<sub>g</sub>) condition.
- Chapter VI summarizes the salient conclusions of the present dissertation research and provides recommendations for future work.

## II. AN EXPERIMENTAL AND COMPUTATIONAL ANALYSIS OF COMBUSTION HEAT RELEASE TRANSFORMATION IN DUAL FUEL COMBUSTION

### 2.1 ABSTRACT

Dual fuel diesel-methane combustion, which employs a high-reactivity fuel (diesel) to ignite a low-reactivity fuel (methane), is a widely studied combustion strategy for internal combustion engines, with significant potential for engine-out emissions reductions without the need for major hardware modifications. A phenomenon, which has been reported in the DF literature, but not explained fully, is the transformation of the shape of the apparent heat release rate (AHRR) curve as the start of injection (SOI) of diesel is advanced beyond a certain threshold; coincidentally, this AHRR transformation is usually accompanied by a sharp decrease in engine-out emissions of oxides of nitrogen (NO<sub>x</sub>). The goal of the present work is to establish the underlying physical reason(s) that cause the AHRR transformation. The AHRR transformation was observed on a single cylinder research engine (SCRE) at an indicated mean effective pressure (IMEP) of 5 bar at a speed of 1500 rev/min. The transformation occurred over a range of SOIs from 330 to 320 crank angle degrees (CAD). While the 330 CAD SOI exhibited a typical two-stage AHRR curve, with a clearly definable first-stage peak followed by a second-stage AHRR with little-to-no low temperature heat release (LTHR) present and high engine-out NO<sub>x</sub>, the 320 CAD SOI exhibited a single-stage, Gaussian-like AHRR curve, with noticeable LTHR and at least one order-of-magnitude lower NO<sub>x</sub> emissions. Leveraging analysis of

experimental data, targeted zero-dimensional chemical kinetic simulations, and three-dimensional computational fluid dynamic simulations, the authors show that the AHRR transformation is impacted mainly by differences in local equivalence ratio distributions within the cylinder at ignition onset for different diesel SOIs.

## 2.2 INTRODUCTION

The use of internal combustion engines as movers of goods and people has been a reliable cornerstone of society for decades. In fact, projections from the US Energy Information Administration for 2020 show that vehicle miles will not only increase in the coming decades (up from ~3 trillion vehicle miles traveled in 2019 to ~4 trillion projected vehicle miles traveled in 2050), but also most of those miles traveled will be with some form of IC engine, with over 12 million light-duty vehicles projected to be powered solely by gasoline in the year 2050 [28]. In addition, Class 7-8 heavy-duty trucks will remain powered by diesel engines for the foreseeable future, due to reliability, power output, cost (\$ per ton-mile of freight transported). The drawbacks to continued usage of IC engines, fueled by conventional fossil fuels, are pollutant exhaust emissions and greenhouse gas (GHG) emissions, of which carbon dioxide (CO<sub>2</sub>) is the main culprit. To reduce GHG emissions, increased IC engine efficiencies are vital. Focusing specifically on CO<sub>2</sub>, this would mean that for the same number of miles driven by an IC engine, there would be less fuel used for a higher efficiency engine, meaning less CO<sub>2</sub> produced at the tailpipe.

One method for increasing engine efficiencies is dual fueling, wherein high-reactivity and low-reactivity fuels are used simultaneously within the engine [29-30]. Typically, the low reactivity (i.e., low-cetane) fuel is fumigated into the intake manifold or injected into the intake port, whereas the high reactivity (i.e., high-cetane) fuel is directly injected into the combustion

chamber. Dual fueling can be done with a wide variety of high and low reactivity fuels, but the combination of natural gas with diesel has been widely studied [31-36]. This particular combination is sought, not only because it requires very few engine modifications, but also because methane, which is the primary constituent of natural gas, has the lowest carbon-to-hydrogen ratio of 0.25 among all hydrocarbon fuels.

While the benefits of dual fueling using natural gas and diesel have been studied extensively, of particular interest to the current work is literature that pertains to the transformation of AHRR from a two-stage profile to a single-stage Gaussian profile while injection timing is advanced in dual fuel combustion. Of the literature examined, there were several instances of an AHRR shape transformation occurring with dual fuel combustion. Guerry et al. [37] used a single-cylinder research engine (SCRE) to study the start of injection (SOI) effects on emissions at two different engine loads of 4.1 bar and 12.1 bar indicated mean effective pressure (IMEP). The range of SOIs studied included 260 to 360 CAD (where 360 CAD corresponds to compression TDC). The AHRR shape transformation was observed for 4.1 bar IMEP, but the transformation region itself and its *raison d'être* were not discussed. Interestingly, the AHRR transformation was accompanied by a sharp decrease in engine-out emissions of oxides of nitrogen (NO<sub>x</sub>). The 12.1 bar IMEP load had high maximum pressure rise rates (MPRR) in the AHRR transformation region, and therefore, the transformation itself was not observed. Polk et al. [7] observed a transformation in the AHRR in a 12.9 L heavy duty diesel engine using diesel and propane over a range of SOIs from 10 degrees before top dead center (BTDC) to 50 BTDC at the load of 5 bar brake mean effective pressure (BMEP). Roberts et al. [38] used primary reference fuels such as iso-octane and n-heptane in an optically

accessible SCRE operating on reactivity controlled compression ignition (RCCI) mode and clearly observed the AHRR transformation over the range of SOIs from 335 CAD to 310 CAD.

Wang et al. [39] also observed the AHRR transformation region with dual fueling using compressed natural gas and diesel. The SOI range studied was -5 to 55 degrees BTDC, with the specific AHRR transformation occurring between 30 BTDC and around 17.5 BTDC SOIs. They also mentioned that similar results were found across engine speeds of 1335 rpm, 1655 rpm, and 1975 rpm, with only the 1335 rpm results being shown. RCCI experiments were performed by Willems et al. [40], on a 12.6-liter engine where E85 was fumigated into the intake manifold, and diesel directly injected into the cylinder. The AHRR transformation was observed over a ‘burn ratio’ (i.e., the ratio of the phase-specific burn duration before CA50 to that after CA50) range from 3.04 to 0.53. A clear transformation was observed as the burn ratio decreased. Yousefi et al. [41] examined multiple speed-load combinations at various SOIs. While the full SOI sweep at each speed-load combination was not presented, a change in shape of the AHRR profile was observed when changing speed and load. This could be an artifact of the changing methane/diesel equivalence ratios and not solely due to SOI changes. Yousefi et al. [42] also observed AHRR transformation with SOI in dual fuel experiments at a low load of 4.05 bar BMEP with natural gas and diesel.

The objective of the present work is to study experimentally the AHRR transformation in dual fuel combustion when SOI is varied, consider the parameters affecting this transformation, and present plausible reasons for why such a transformation does occur. To aid in this endeavor, targeted 0-D chemical kinetic simulations, as well as 3-D computational fluid dynamic simulations, were performed.

## 2.3 EXPERIMENTAL SETUP

An SCRE adapted for diesel-methane dual fuel operation was used for the experiments performed in this study. A list of engine specifications is given in Table 2.1. Figure 2.1 shows a detailed schematic of the experimental setup for the engine. The engine was coupled to a 250 horsepower, AC dynamometer and used a Dyne Systems Inter-Loc V controller to control engine speed. The engine torque (load) was set via the fueling rate of the engine. Since the engine utilized the dual fuel operating strategy, the control of both fueling rates was vital. To control the gaseous methane fueling rate into the intake manifold, an electronic needle valve from Hanbay Inc. (Model MCM-50AB) was used. Diesel fuel was injected directly into the cylinder through a solenoid injector, which was connected to a Bosch CP3 common rail system. Diesel injection (timing, duration, and pressure) was controlled via a DRIVVEN (National Instruments) stand-alone diesel injection driver, which was coupled to National Instruments CALVIEW software. Pressurized air was supplied to the engine using an Atlas Copco (Model GA75) external air compressor which, before entering the engine, was conditioned using a heatless desiccant dryer from Atlas Copco (Model CD 250). In-cylinder pressure was measured using a Kistler model 6052C pressure sensor coupled with a Kistler 5010B type charge amplifier. The injector was fitted with a Hall-effect needle lift sensor from Wolff Instruments. A 0.1 crank angle degree (CAD) resolution BEI shaft encoder (Model XH25D-SS-3600-ABZC-28V/V-SM18) was used to phase both the in-cylinder pressure trace as well as the needle lift with respect to crank angle. Intake pressure was measured using a Setra (Model 209) pressure sensor, which was then used to peg the cylinder pressure at intake valve closing (IVC). In a similar fashion, steady state (asynchronous) engine data were collected and averaged over a duration of 60 seconds. Table 2.2

gives more information about the accuracies associated with the sensors used in this engine setup.

Table 2.1. General Engine Specifications.

Engine type	Single cylinder, four stroke
Bore (mm)	128
Stroke (mm)	142
Con. Rod Length (mm)	228
Displaced Volume (L)	1.827
Nozzle dia (mm)/# holes	0.197/8
Compression ratio	17
Intake Valve Timings	IVO – 32 CAD, IVC – 198 CAD
Exhaust Valve Timings	EVO – 532 CAD, EVC – 14 CAD
Diesel Injection System	Bosch CP3 common rail
Operating Speed (rpm)	1500

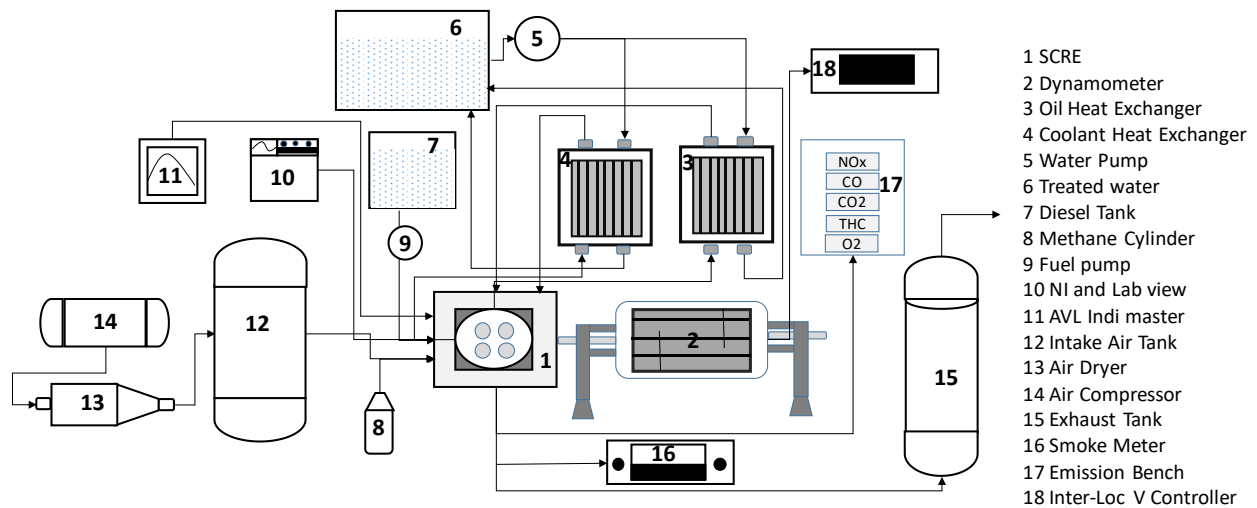


Figure 2.1. Single Cylinder Research Engine Experimental Setup.

Table 2.2. Details of experimental sensors and their accuracies.

Data Type	Make/Model	Type	Unit	Accuracy
Temperature (intake, exhaust, etc.)	Omega	K-type	°C	±0.75% of reading
Air mass flow	Flowmaxx	Sonic orifice	kg/h	±0.1% of reading
Diesel mass flow	Micro Motion	Coriolis	kg/h	0.35% of reading
Methane mass flow	Micro Motion	Coriolis	kg/h	0.56% of reading
Smoke	AVL 415S	Filter	FSN	0.001 of reading
NOx and NO	ESA EGAS 2M	CLD	ppm	<1% of full scale
THC	ESA EGAS 2M	FID	ppm	<0.5% of full scale
CO	ESA EGAS 2M	NDIR	%	<1% of full scale
CO2	ESA EGAS 2M	NDIR	%	<1% of full scale
O2	ESA EGAS 2M	MPA	%	<1% of full scale
Cylinder pressure	Kistler 6052C	Piezoelectric	bar	±0.005 of reading
Pressures (intake, exhaust, etc.)	Setra Model 209	Capacitance	psig	±0.25% of full scale

For the purposes of this paper, all references to crank angles use the absolute crank angle convention, meaning that 0° refers to gas exchange TDC, and 360° refers to compression TDC. One thousand consecutive engine cycles were collected for each operating point, and the subsequent ensemble averages are presented.

## 2.4 EXPERIMENTAL PROCEDURE

The present work focuses on dual fuel combustion, wherein methane was fumigated into the intake manifold, while diesel was directly injected into the combustion chamber. Diesel SOI was the only parameter allowed to vary throughout these experiments, with SOI values of 320, 322, 325, 328, and 330 CAD considered. This allows for the AHRR transformation to be fully characterized. Table 2.3 gives insight into various engine operating conditions at each SOI. A more detailed discussion of the various quantities and equations used in the paper follows.

Table 2.3. Engine Operating Conditions.

Compression Ratio	17:1
SOI	320 CAD, 322 CAD, 325 CAD, 328 CAD, 330 CAD
Gross Indicated mean effective pressure (IMEPg)	5 bar
Percent Energy Substitution (PES)	80%
Absolute Intake Pressure	1.5 bar
Engine Speed	1500 RPM
Rail Pressure	500 bar
Low Reactivity Fuel (LRF) and LRF lower heating value (kJ/kg)	Methane 50,000

Since two different fuels were used, the percent energy substitution (PES), which refers to the percent of total fuel energy substituted by methane, was defined as shown in Equation 2.1 and expressed as a percentage; in this regard, a PES value of 0% indicates pure diesel operation while a PES value of 100% indicates pure methane operation.

$$PES = \frac{\dot{m}_{CH_4} LHV_{CH_4}}{\dot{m}_{Diesel} LHV_{Diesel} + \dot{m}_{CH_4} LHV_{CH_4}} \quad (2.1)$$

Within Equation 2.1,  $\dot{m}$  refers to the mass flow rate and  $LHV$  refers to the lower heating value, with the subscripts identifying diesel or methane. The AHRR is calculated following

Heywood [1]. In Equation 2.2,  $P$  is the in-cylinder pressure at a given crank angle,  $V$  is the instantaneous volume, and  $\frac{dV}{d\theta}$  as well as  $\frac{dP}{d\theta}$  are the derivatives of volume and in-cylinder pressure with respect to crank angle, respectively. The in-cylinder pressure was pegged and smoothed using a lowpass Butterworth filter with a cutoff frequency of 2600 Hz (determined from a qualitative analysis of multiple cutoff frequencies) before performing the heat release analysis. The ratio of specific heats ( $\gamma$ ) was calculated using a correlation proposed by Gatowski et al. [43], as shown in Equation 3. In this regard, it is important to emphasize that the AHRR transformation occurred within the same SOI range, irrespective of the specific approach used for calculating  $\gamma$ .

$$AHRR = \frac{\gamma}{\gamma - 1} P \frac{dV}{d\theta} + \frac{1}{\gamma - 1} V \frac{dP}{d\theta} \quad (2.2)$$

$$\gamma = 1.375 - 6.99 \times 10^{-5} T \quad (2.3)$$

The temperature used within Equation 3 is calculated using the Redlich-Kwong real gas equation of state [44]. This equation uses two constants, given in Equations 2.4 and 2.5, to solve for the temperature. Equation 2.6 gives the governing equation for the Redlich-Kwong equation of state. A MATLAB script was used to solve numerically for the temperature.

$$a = 0.42748 * \frac{R_{Univ}^2 T_{Crit}^{2.5}}{P_{Crit}} \quad (2.4)$$

$$b = 0.08664 * \frac{R_{Univ} T_{Crit}}{P_{Crit}} \quad (2.5)$$

$$P = \frac{R_{Univ} T}{V_{molar} - b} - \frac{a}{\sqrt{T} V_{molar} (V_{molar} + b)} \quad (2.6)$$

The critical temperature ( $T_{Crit}$ ) and critical pressure ( $P_{Crit}$ ) of air were used for both Equations 2.4 and 2.5, and the universal gas constant ( $R_{Univ}$ ) of 8.314 kJ/kmol.K was used in Equation 2.6.

## 2.5 EXPERIMENTAL RESULTS

While the AHRR transformation has been seen in the literature, it has not been previously defined clearly; therefore, it is beneficial to first understand what exactly the transformation region encompasses by observing the experimental results. Figure 2.2 shows the AHRR profiles for the SOIs studied in this work.

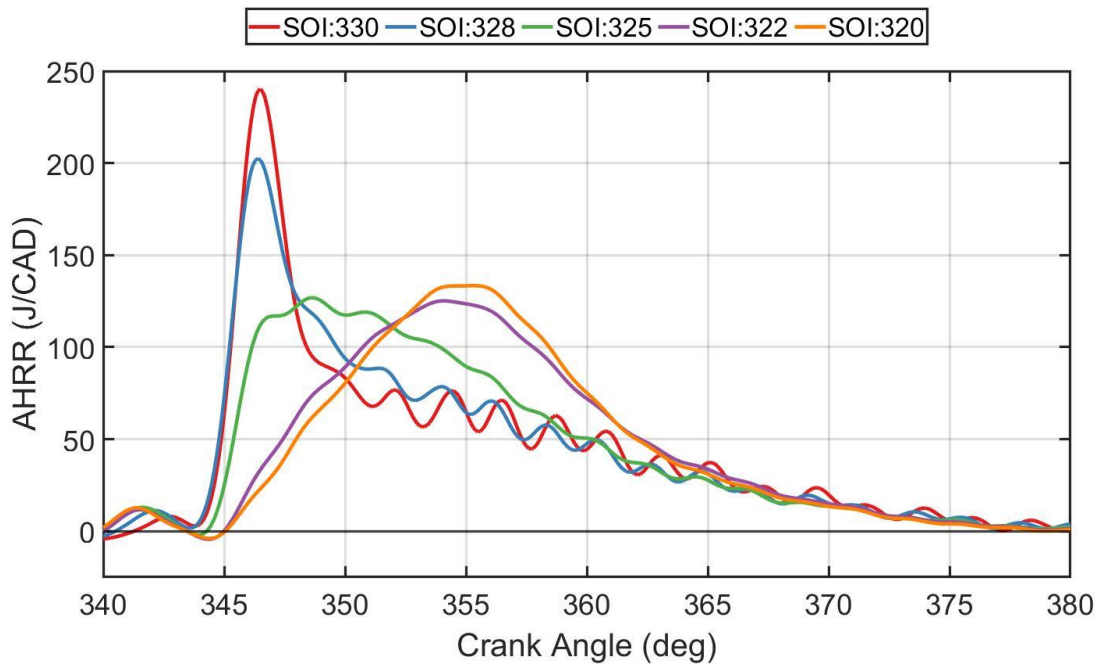


Figure 2.2. AHRR for SOIs of 320, 322, 325, 328, and 330 CAD at 5 bar IMEP<sub>g</sub>, 80% PES.

It is clear from Figure 2.2 that as the SOI advances from 330 CAD to 320 CAD, the AHRR curve changes shape when keeping all other parameters constant. The transformation exhibits itself as a change from a distinct two-stage AHRR profile with a very high peak value followed by a drawn out, but lower value second stage for 330 CAD SOI, to an AHRR profile that is not only smoother in the overall shape, but also has a more ‘Gaussian’ appearance with a lower peak AHRR value occurring later in the cycle for 320 CAD SOI. It is also observed that the LTHR portion of the AHRR curves are more pronounced as the SOI is advanced. This

AHRR shape transformation also manifests in the start of combustion, defined as the location of 5% of total heat release (CA5), the combustion phasing (CA50), and the combustion duration (CA5-90) values, as shown in Figure 2.3 below.

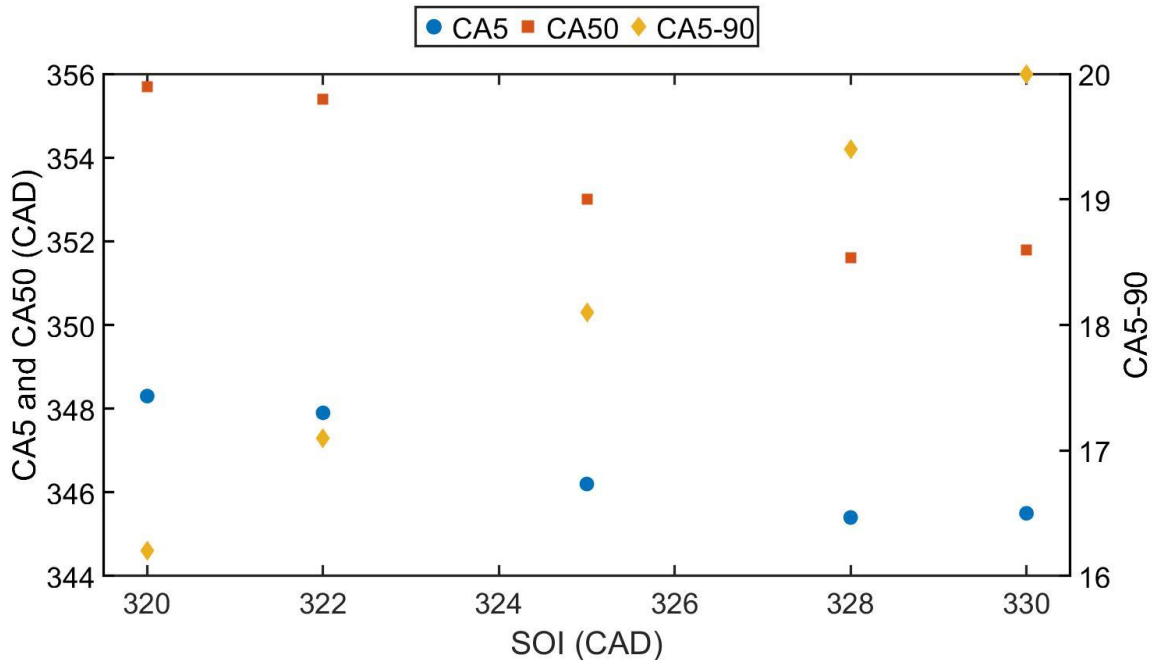


Figure 2.3. CA5, CA50, and CA5-90 values at 5 bar IMEPg, 80% PES.

When the SOI is advanced, the CA5 and CA50 values both move toward TDC slightly, while the combustion duration decreases. The importance of the AHRR transformation region lies in the fact that it is accompanied by significant NO<sub>x</sub> reduction, as evident from Figure 2.4. The indicated specific NO<sub>x</sub> (ISNO<sub>x</sub>) is around 11 g/kWh at 330 CAD SOI and reduces sharply as the SOI is advanced to 320 CAD, where the ISNO<sub>x</sub> is around 1 g/kWh (a nearly 90% reduction). Further advancement of the SOI (e.g., to an SOI of 300 CAD, not shown here) reduces the ISNO<sub>x</sub> even further (< 0.2 g/kWh). This AHRR transformation region is the starting point of the ISNO<sub>x</sub> reduction, and consequently warrants a deeper understanding since it is evident that

whatever phenomenon makes this transformation possible, also makes it possible to reduce engine-out NO<sub>x</sub> emissions at the more advanced SOIs.

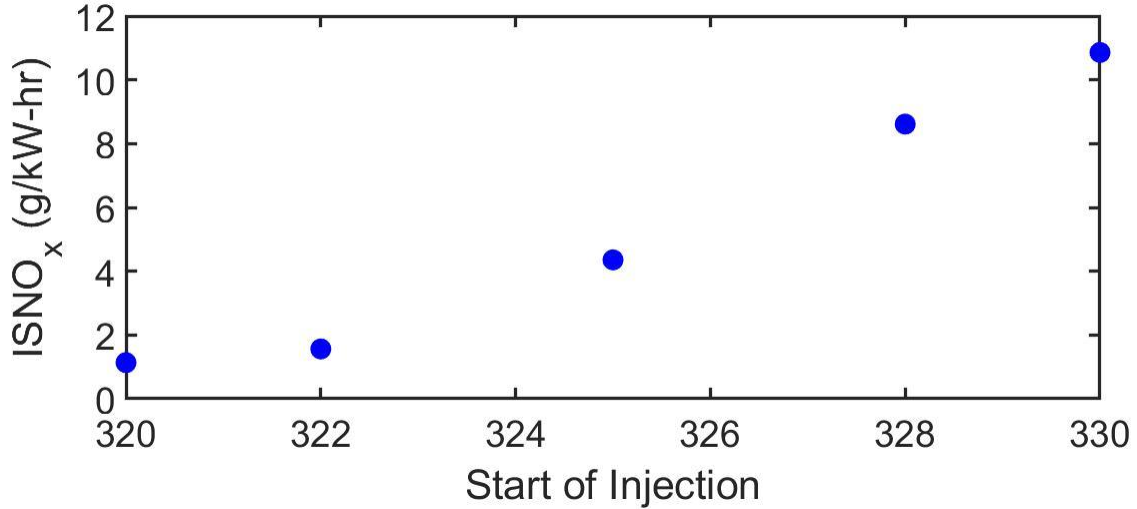


Figure 2.4. Indicated Specific NO<sub>x</sub> Emissions at 5 bar IMEP<sub>g</sub>, 80% PES.

It is also important to note that the ISNO<sub>x</sub> benefit does not come at the sacrifice of engine efficiency. In fact the lower ISNO<sub>x</sub> values show increased efficiencies, which can be seen in Figure 2.5, wherein the ISNO<sub>x</sub> is plotted against the indicated fuel conversion efficiency.

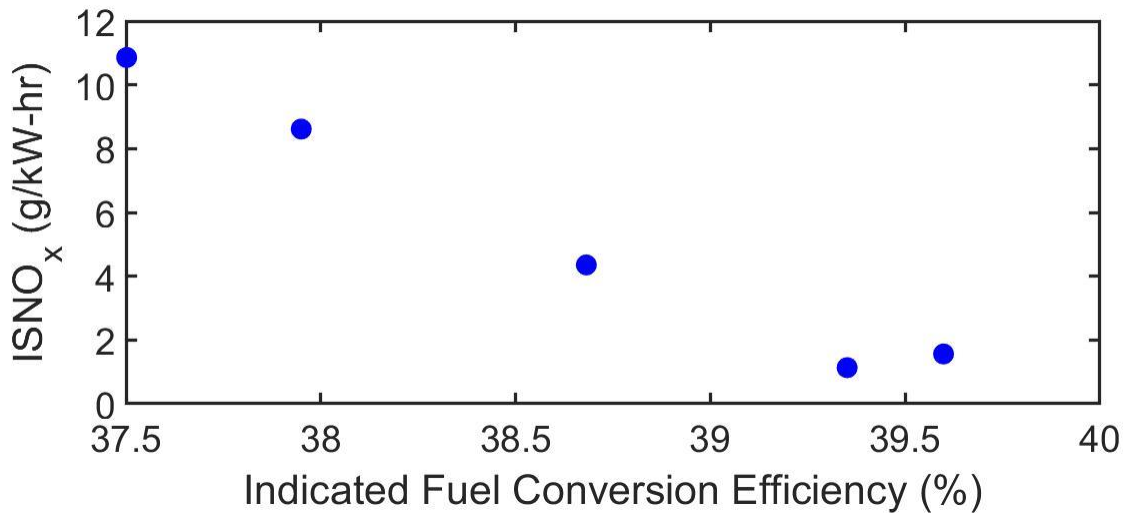


Figure 2.5. Indicated specific NO<sub>x</sub> vs. indicated fuel conversion efficiency.

Since the AHRR transformation has been shown to occur across a range of engine platforms and operating conditions, it is clear that the transformation is not an exception but rather the rule with dual fuel combustion over a certain range of SOIs. Furthermore, since this phenomenon is known to occur over a range of engine types and displacements as well as over a range of at engine speeds and loads, it is likely governed by in-cylinder conditions, including of pressure (P), temperature (T), and equivalence ratio ( $\phi$ ).

Figure 2.6 shows an enhanced view of the LTHR and the start of high-temperature heat release (HTHR) regions (i.e., from 338 to 346 CAD). The start of LTHR and start of HTHR were determined based on a simple first derivative analysis of the AHRR profile and stipulating the CAD when the slope first became positive as the start of LTHR and later of HTHR.

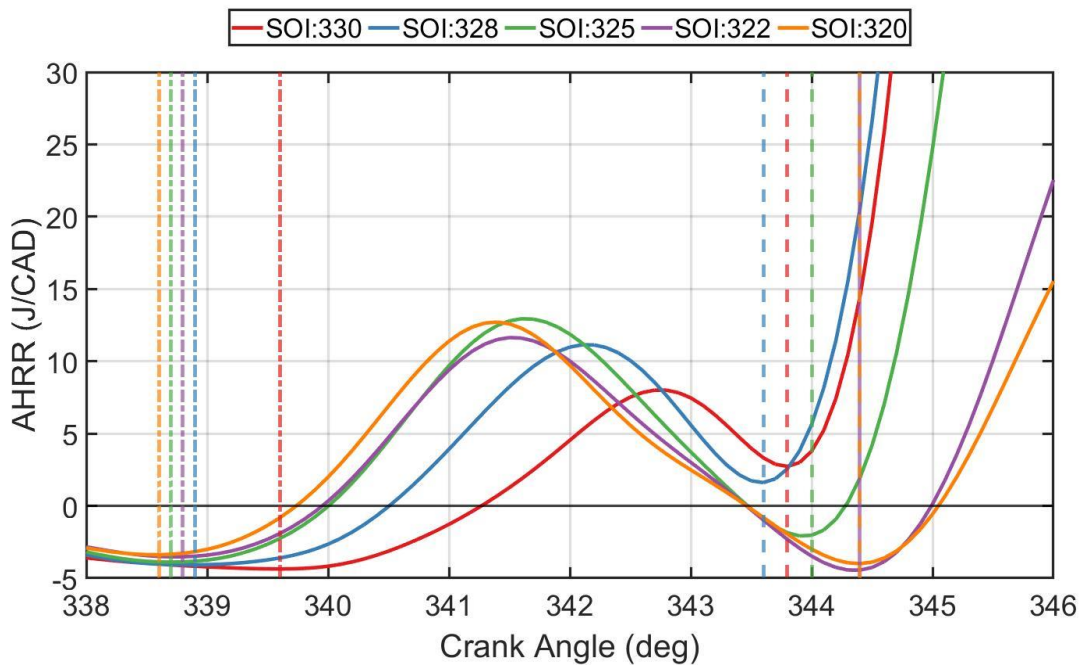


Figure 2.6. Enhanced view of AHRR showing the start of LTHR and HTHR with start of LTHR locations designated with a dot-dashed line and start of HTHR designated with a dashed line, both colored with respect to the corresponding SOI.

Figure 2.6 is useful in determining the key points of the start of LTHR and the start of HTHR within the AHRR profile. As combustion evolves within the cylinder, the thermodynamic history of in-cylinder gases changes temporally; so, it is vital to understand how differences in thermodynamic histories may affect AHRR for different SOIs. It is very important to remember that the only variables that were changed in these experiments were SOI and engine speed, with the SOI being the primary variable of interest regarding the transformation region. Since engine speed was kept constant, the changes to the start of LTHR and start of HTHR are a direct result of the change in the SOI location. The values for these locations, as well as other parameters of interest are given in Table 2.4.

Table 2.4. Start of LTHR and HTHR, end of injection (EOI), and injection duration.

SOI (CAD)	330	328	325	322	320
Start of LTHR (CAD)	339.6	338.9	338.7	338.8	338.6
Start of HTHR (CAD)	343.8	343.6	344	344.4	344.4
EOI (CAD)	338.8	336.8	333.5	330.3	328.6
Injection Duration (CAD)	8.8	8.8	8.5	8.3	8.6

From the locations of LTHR and HTHR found in Table 4, the in-cylinder pressure and in-cylinder temperature at those specific locations could be determined and are shown in Table 2.5. To determine if in-cylinder pressure and temperature have an impact on the AHRR transformation, these values can give insight.

Table 2.5. Pressure and temperature at the onset of LTHR and HTHR for each SOI.

SOI	330	328	325	322	320
Pressure @ start of LTHR (bar)	36.3	35.1	34.8	34.8	34.4
Pressure @ start of HTHR (bar)	44.8	44.6	45.5	46.2	46.1
Temperature @ start of LTHR (K)	859	853	851	850	847
Temperature @ start of HTHR (K)	904	906	911	912	913

To determine from the engine experimental results whether these variables (i.e., pressure and temperature) have any impact on the AHRR transformation, it is important to observe the change in AHRR shape as a function of the SOI. Therefore, the averages across all SOIs were calculated, and the variation about the average was determined by dividing said averages by the standard deviation. The pressure at the onset of LTHR had an average across all SOIs of 35.1 bar and a variation of 2.2%, while the temperature at the onset of LTHR had an average value of 852 K and a variation of 0.5%. Meanwhile, the averages for pressure and temperature at the start of HTHR were 45.5 bar and 909K, with variations of 1.6% and 0.5% respectively. This indicates that, at least from a basic thermodynamic analysis of engine -in-cylinder pressure and AHRR results, pressure and temperature do not vary significantly over the range of SOIs and therefore may not play a dominant role in the AHRR transformation.

While the analysis at the start of LTHR and HTHR for each individual SOI is helpful in identifying that pressure and temperature do not vary at those individual locations, it does not provide a direct comparison of the temporal (CAD) variation of pressure and temperature across all SOIs. It is evident that the chemical reactions take place under varying in-cylinder thermodynamic conditions from one crank angle to the next. Therefore, a more concrete way of comparing the pressure and the temperature across all SOIs is needed. The analysis method chosen was to identify the earliest CAD location of the start of LTHR, and then look at that specific CAD for each SOI. The pressure and temperature at this CAD location was then compared for each SOI. By choosing a location in this way, a comparison of the earliest possible time that low temperature reactions could take place for any of the SOIs studied can be performed. It was found that the earliest start of LTHR was for SOI = 320 CAD, with the location of the start of LTHR occurring at 338.6 CAD. This CAD location occurs after EOI for every SOI, except for SOI = 330 CAD. The importance of the location chosen occurring after EOI becomes apparent when realizing that the combustion chamber becomes, ideally, a thermodynamically closed system with no mass leaving nor entering the system, after EOI. For SOI = 330 CAD, the EOI occurs 0.2 CAD after the 338.6 CAD location of interest. It is important to note that the 0.2 CAD difference between the EOI and the 338.6 CAD location studied only corresponds to 0.02 ms at this engine operation speed of 1500 RPM, which is very small in comparison to the ~1 ms injection durations for all SOIs. Therefore, the 338.6 CAD location was deemed acceptable for comparing across all SOIs, and the values of the pressure and temperature at 338.6 CAD for each SOI are shown in Table 2.6.

Table 2.6. Pressure and temperature at CAD = 338.6.

SOI	330	328	325	322	320
Pressure (bar)	34.7	34.6	34.6	34.5	34.4
Temperature (K)	851	851	850	848	847

As with the previous analysis, the average was taken across all SOIs and the variation about that average determined. Pressure values had an average of 34.6 bar with a variation of only 0.28%, and temperature had an average of 849 K with a variation of only 0.19%. This indicates that, when looking at a point (CAD = 338.6) in the combustion process wherein all of the mass of both the high reactivity and low reactivity fuels was injected, in-cylinder pressure and temperature only varied by a mere fraction of a percent across SOIs.

It is evident from the experimental analysis (Table 2.5) that the variations in pressure and temperature at the onset of LTHR and the onset of HTHR do not vary significantly across the SOI range where the AHRR transformation takes place. Since the variations are small across the SOI range, it is likely that the in-cylinder temperature and pressure do not influence the AHRR transformation as significantly as, perhaps the local equivalence ratio; however, this influence cannot be ruled out completely without further analysis using simulations, mainly 0D chemical kinetic simulations and 3D computational fluid dynamics (CFD) simulations.

## 2.6 0-D CHEMICAL KINETIC STUDY

To analyze the impact of local equivalence ratio, pressure, and temperature on heat release, targeted 0D chemical kinetics simulations were performed using the POLIMI\_TOT\_1407 mechanism, which contains 451 species and 17747 reactions [45], with n-dodecane (representing diesel) and methane as the two fuels. These simulations were performed

in ANSYS® CHEMKIN 2019 R2 [46] for a constant volume, homogeneous reactor. Three individual parameter sweeps were performed: initial pressure, initial temperature, and equivalence ratio. With each parameter sweep, the other two parameters were held constant to independently determine its effect on the reactions occurring. The initial pressures and temperatures for their respective sweeps were determined based on experimental results, and parameters for the Chemkin sweeps can be found in table 2.7. To examine further the conclusions that pressure, and temperature likely do not have an impact on the transformation, the initial pressure and temperature sweeps will be discussed first. It should be noted that, where possible, average values across the SOI sweep were used as the initial conditions that were held constant in these sweeps. In addition, to ensure completeness of the 0D chemical kinetic studies, another set of simulations were run using the same mechanism but using the HCCI IC engine model, built in to Chemkin. More information regarding this simulation can be found in the Appendix, at the end of this dissertation.

Table 2.7. Parameters for Chemkin sweeps.

Parameter	Pressure Sweep	Temperature Sweep
Initial Pressure (bar)	30 - 50	34.5
Initial Temperature (K)	849	830-930
Volume (m <sup>3</sup> )	1	1
Equivalence Ratio	0.313	0.313
Fuel Fraction (mole fraction) of CH <sub>4</sub>	0.974	0.974
Fuel Fraction (mole fraction) of n-C <sub>12</sub> H <sub>26</sub>	0.026	0.026

The volumetric heat release from the initial pressure sweep is given in Figure 2.7.

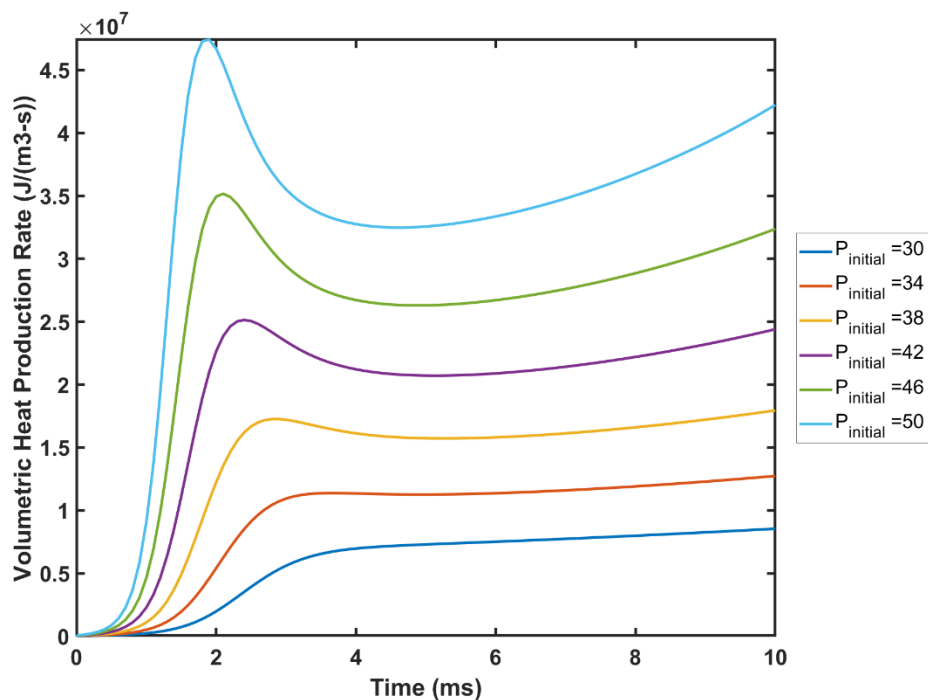


Figure 2.7. Volumetric heat production for an initial pressure of 30 bar to 50 bar.

As the pressure is increased from 30 bar to 50 bar, there is an obvious increase in the volumetric heat production rate. The heat production rate first increases and then decreases, before increasing again with respect to time. This latter increase in heat production rate is not as evident for lower initial pressures but is evident for higher initial pressures. This indicates that the spike in the volumetric heat production rate may be due to low temperature chemical reactions, but this needs further confirmation. The volumetric heat production is also observed to occur sooner at higher initial pressures. To investigate whether the volumetric heat production spike is caused by low temperature reactions, the mole fraction of ketohydroperoxide (NC12OQOOH) radical, which is a key species in the low temperature branching mechanism [47], was plotted in Figure 2.8. It is clear from Figure 2.8, that the peak value from Figure 2.7

corresponds to a peak in the mole fraction of ketohydroperoxide. This indicates that the peak heat release is likely driven by low temperature chemistry. What this means, when comparing to experiments, is that the low temperature pathways, and therefore the LTHR portion of the AHRR curve, are dependent upon the initial pressure. As mentioned previously, the in-cylinder pressure is not affected significantly around the start of LTHR, or around the start of HTHR, nor when looking at a single CAD (338.6 CAD) across all SOIs.

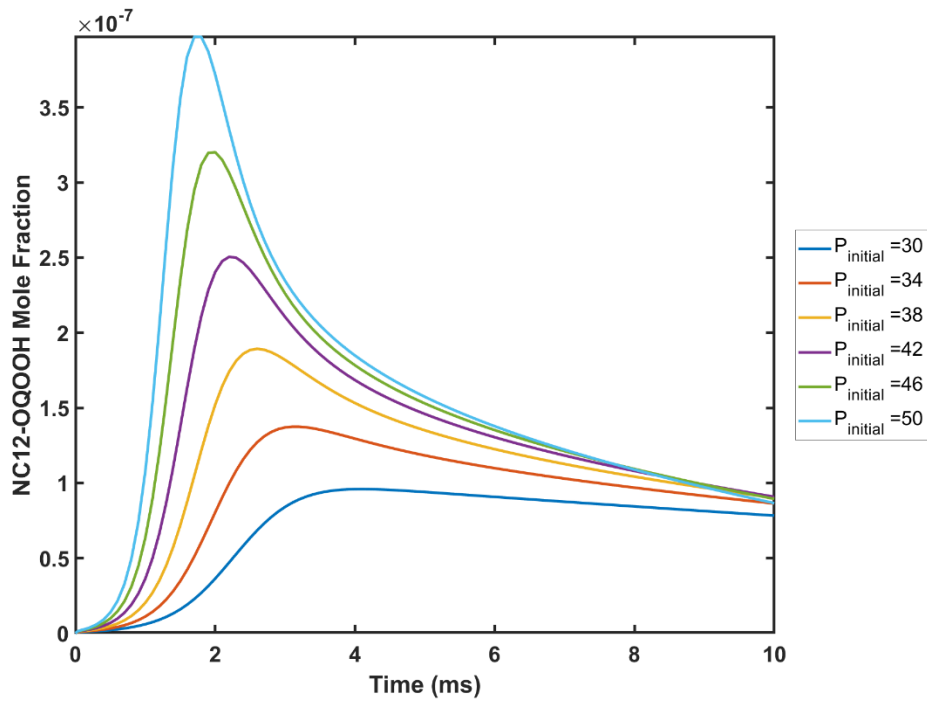


Figure 2.8. Ketohydroperoxide evolution for different initial pressures from 30 bar to 50 bar. Since the change in pressure needed for any appreciable changes in low temperature chemistry is of the order of tens of bars, and the in-cylinder pressure at the start of LTHR for the experimental analysis is only varying at most by 1.95 bar, it is clear that the in-cylinder pressure does not play a key role in causing the AHRR transformation.

A similar observation is seen for the in-cylinder temperature sweep. The volumetric heat production rate is shown in Figure 2.9, and the ketohydroperoxide mole fraction is shown in Figure 2.10. As with the initial pressure sweep, the initial temperature sweep shows that low temperature chemical reactions and associated heat release will increase as the temperature is lowered, from 930 K to 830 K. This falls in line with the typical 550-900 K temperature range when low temperature chemical pathways are favored for most hydrocarbon fuels [22]. When comparing with the experimental analysis, it can be deduced that in-cylinder temperature does not play a governing role in the AHRR transformation, seeing as the average temperature at the onset of LTHR varies at most by 11.85 K, whereas significant changes in the initial temperature (of the order of 50-100K) are needed to see appreciable changes in the low temperature volumetric heat production according to the 0-D chemical kinetic simulations.

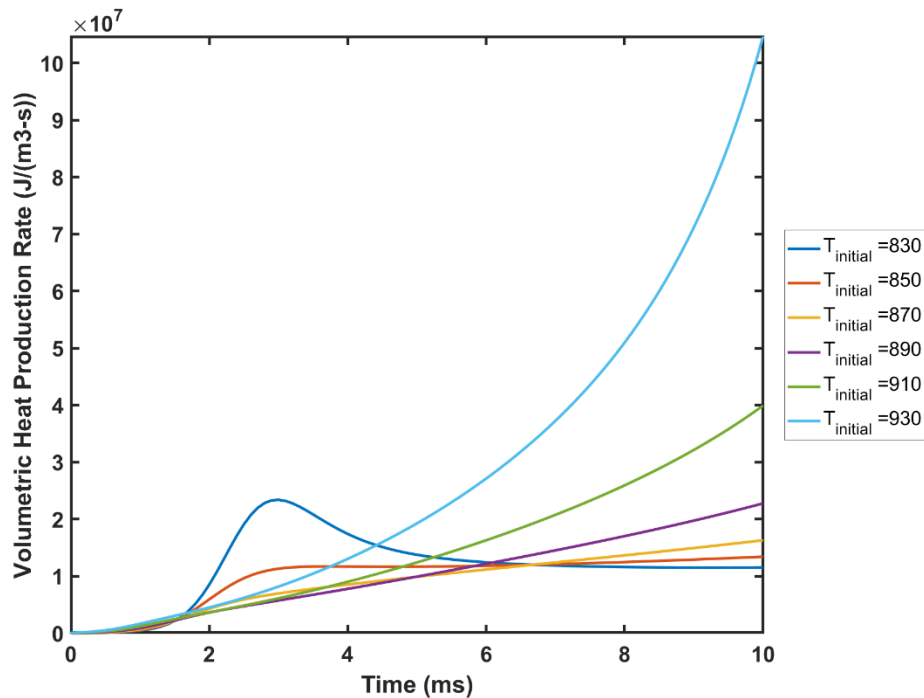


Figure 2.9. Volumetric heat production for an initial temperature of 830 to 930 K.

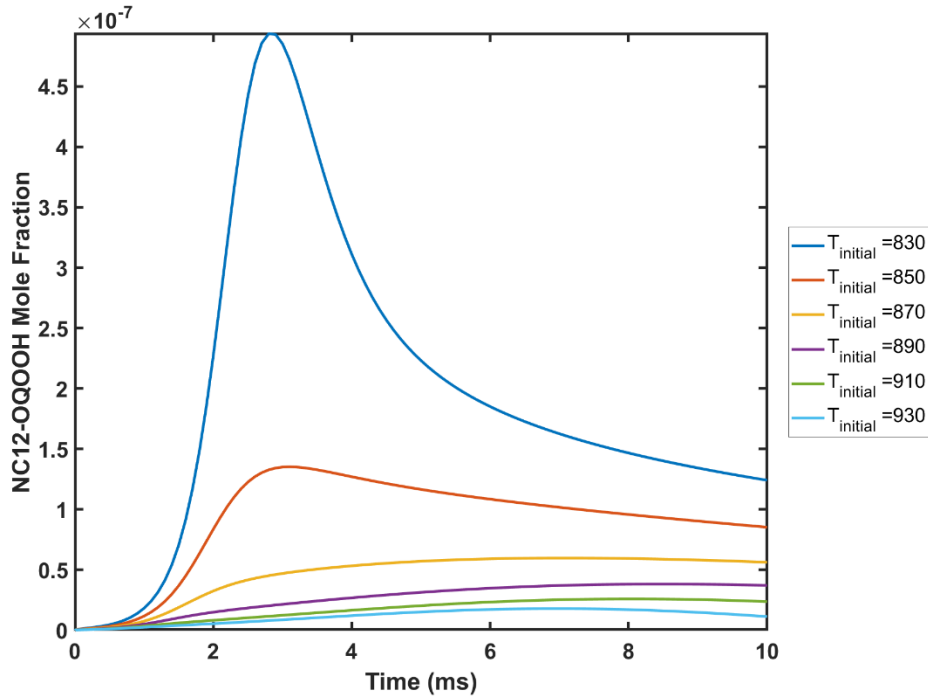


Figure 2.10. Ketohydroperoxide mole fraction for an initial temperature of 830 to 930 K.

With temperature and pressure having been eliminated as unlikely reasons for the AHRR transformation process, the local chemical composition is the next logical variable that may cause the AHRR transformation. Local chemical composition can be described using the equivalence ratio. The impact of local equivalence ratio gradients on AHRR and combustion evolution cannot be observed directly when optical access to the combustion chamber is not available experimentally as in the present scenario. Using 0D chemical kinetic simulations, a preliminary understanding of the impact of equivalence ratios on combustion evolution can be gained. The initialized parameters used for the equivalence ratio sweep within ANSYS® CHEMKIN were an initial pressure of 34.5 bar and an initial temperature of 849 K. The equivalence ratio was swept from a value of 0.253 to 1.2. At this point, it is important to describe the rationale behind how the equivalence ratio was changed. For typical dual fuel combustion,

the mixture of low reactivity fuel and air will be nearly homogeneous since the fuel is usually fumigated into the intake manifold or injected into the intake port. For all experiments performed in this work, methane and diesel fueling rates were kept constant throughout the SOI sweep. This meant that, as the SOI changed, the amount of time available for mixing changes, but the mass of air, methane, and diesel were the same across the board. Since the methane introduction to the cylinder happens only while the intake valve is open and there is sufficient time for the methane-air mixture to virtually homogeneous conditions, the amount of methane and air allowed to locally mix with the diesel as it is injected remains the same. Therefore, a change in the local equivalence ratio would be dictated purely by how much diesel has mixed with the methane-air mixture at a given location; in other words, a higher local equivalence ratio will have higher amounts of diesel and vice versa. For the equivalence ratio sweep with ANSYS<sup>®</sup> CHEMKIN, the mole fractions for methane and n-dodecane (representing diesel) were calculated based on the fueling rates of both fuels and the air flow rate. Average methane fueling rate and average air flow rates for the SOI sweep were used for the equivalence ratio calculations and these quantities were held constant across the equivalence ratio sweep to be consistent with experimental engine measurements and the expectation that methane-air mixtures are nearly homogeneous near the SOIs. However, the n-dodecane fueling rate was varied, and this was expected to capture the variations in local equivalence ratio and its impact on volumetric heat release. The volumetric heat production, as well as the natural log of the volumetric heat production is shown in Figure 2.11 a-b.

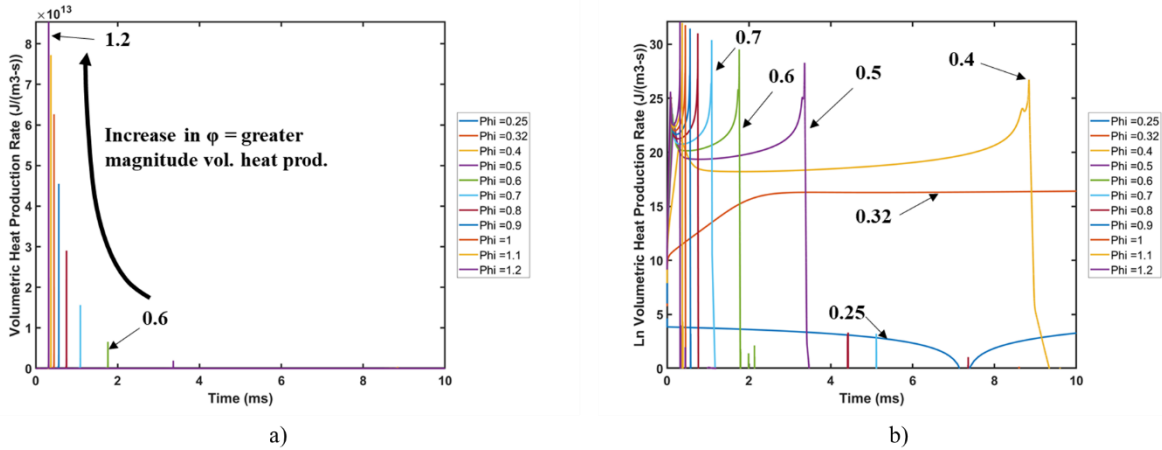


Figure 2.11. (a) Volumetric heat production and (b) natural log of volumetric heat production at different equivalence ratios.

From Figure 2.11 (a), the magnitude of the high temperature volumetric heat production is increasing with an increase in equivalence ratio; a significant peak is not seen until an equivalence ratio of 0.6, and no low temperature heat release is evident from this plot, since the significantly larger high temperature heat release dwarfs any low temperature heat release. Hence, the natural log of the volumetric heat production rate is shown in Figure 2.11 (b) to better discern trends in low temperature and high temperature heat release peaks. In Figure 2.11 (b), the high temperature heat release peaks, as expected, follow the low temperature peaks. Further, the onset of high temperature reactions occurs earlier at higher equivalence ratios, and therefore the time elapsed between the low temperature and high temperature reactions decreases. To get a better picture of low temperature heat release, the “early reaction period” up to 1 ms is examined in Figure 2.12.

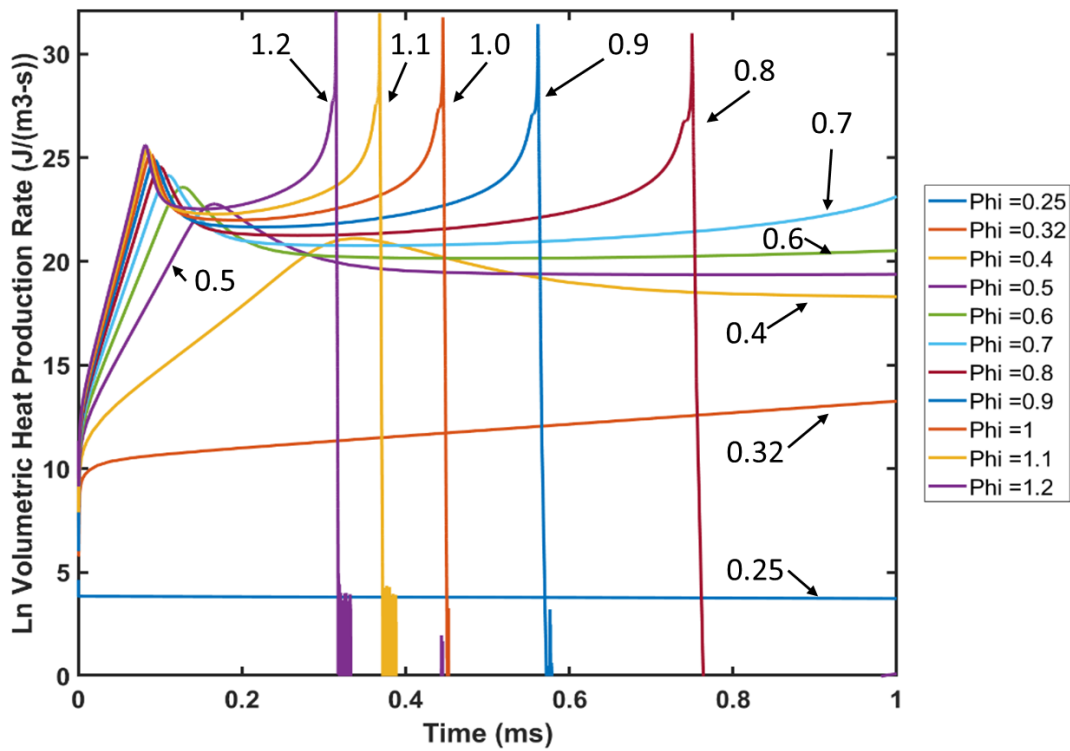


Figure 2.12. Natural log of volumetric heat production rate over the early reaction period (0 to 1 ms) at different equivalence ratios

Within the early reaction period, the high temperature reactions occur faster at higher equivalence ratios but with diminishing impact as equivalence ratio is increased from 0.7. For example, while high temperature reactions occur after 1 ms for the equivalence ratio of 0.7, but they occur just under 0.8 ms for the equivalence ratio of 0.8. This jump is far greater compared to the nearly negligible difference in the onset of high temperature reactions between the equivalence ratios of 1.1 and 1.2. Similarly, low temperature heat release peaks increase and occur quicker as equivalence ratio is increased but again with diminishing returns at very high equivalence ratios. Recall that the equivalence ratio increase is directly coupled with an increase in the amount of n-dodecane that is present within the reactor. Also, since n-dodecane exhibits two stage heat release characteristics whereas methane does not, a greater quantity of high

reactivity fuel will inevitably cause the rate of both low and high temperature reactions to occur faster. The ANSYS® CHEMKIN simulation results shown here are meant to be representative of the differences in local chemical reaction rates due to local equivalence ratio stratification within the engine's combustion chamber. For instance, for an earlier injection timing such as SOI = 320 CAD, there is more time for the diesel to mix with the surrounding methane/air environment, meaning that there will be more local regions within the combustion chamber that have lower equivalence ratios than high equivalence ratios. Conversely, for SOI = 330 CAD, there will likely be a greater number of locally richer regions. This change in local equivalence ratio stratification with SOI clearly has an impact on both the magnitude of the heat production as well as the rate at which the reactions take place. However, to prove that local equivalence ratio stratification variation between SOIs of 330 CAD and 320 CAD is the true governing factor in the transformation of AHRR, further analysis is needed to prove that the local equivalence ratio stratification is indeed significantly different between the two SOIs, which are only 10 CAD apart. Therefore, a more detailed examination of the local equivalence ratio stratification and the associated combustion processes was performed using 3D computational fluid dynamics simulations.

## **2.7 3D COMPUTATIONAL FLUID DYNAMIC SIMULATIONS**

CONVERGE [48] 3D CFD software was used to perform simulations of three consecutive engine cycles, and a portion of the last engine cycle (specifically from ~ 300 CAD to ~ 400 CAD) was analyzed for the present work, so as to capture the start of LTHR and the start of HTHR. A Reynolds averaged Navier-Stokes (RANS) approach (specifically the renormalization group (RNG)  $k$ - $\epsilon$  turbulence model) was used for this work. More detailed information on the model specifics is presented in previous work [49]. Good agreement between

experimental and computation results was obtained and is presented by Jha et al [49]; consequently, there is high confidence in the spatial and temporal results from the experimentally validated CFD model. A reduced mechanism based on the POLIMI\_TOT\_1407 mechanism, which has 96 species with 993 reactions [50], was used in the CFD simulations. In other words, the same fundamental reaction mechanism (the “full version” with CHEMKIN and “reduced version” with CONVERGE) and similar species were used with the CFD simulations and the chemical kinetics simulations to ensure as much consistency as possible.

The aim of the CFD study is to ascertain local equivalence ratio ( $\phi$ ) and local temperature stratification levels within the cylinder, especially across the SOI range spanning the AHRR transformation region. With CFD simulations of the in-cylinder engine processes, the effect of in-cylinder turbulence on fuel-air mixing and the ensuing combustion process is important. Using the RNG k- $\epsilon$  turbulence model, coupled with the low-swirl engine platform used for developing the validated model [51], the validated model is deemed to have captured fuel-air mixing adequately for the purposes of this study. Temperature and equivalence ratio ( $\phi$ ), when plotted against each other, can elucidate certain temporal trends in the combustion process, for example, the NO<sub>x</sub>-soot tradeoff [52, 53]. With CFD, there is the added benefit of being able to track local species temporally through the combustion process, in addition to the local temperature and the local  $\phi$ . It is important to note that the “equivalence ratio” defined in CONVERGE includes all species within the defined region, including carbon dioxide (CO<sub>2</sub>) and water vapor (H<sub>2</sub>O). A more appropriate measure of the composition of fresh fuel-air mixture within each region would be to calculate equivalence ratio after excluding CO<sub>2</sub> and H<sub>2</sub>O. CONVERGE outputs this parameter as “reaction ratio” ( $\phi_{\text{React}}$ ), which is calculated using the

same equation as  $\phi$ , but excludes  $\text{CO}_2$  and water ( $\text{H}_2\text{O}$ ). Reaction ratio is defined in CONVERGE using Equation 2.7, which includes all species except  $\text{CO}_2$  and  $\text{H}_2\text{O}$ .

$$\Phi_{React} = \frac{2 \sum N_{C_i} + \frac{1}{2} \sum N_{H_i}}{\sum N_{O_i}} \quad (2.7)$$

Various  $\phi_{\text{React}}\text{-T}$  plots can be made with data points colored by mass fractions of certain key species. One such species is the ketohydroperoxide radical, which as mentioned previously, is a good indicator of low temperature chemical reactions and heat release [47]. Figures 2.13 and 2.14 show the  $\phi_{\text{React}}\text{-T}$  plots for SOIs of 320, 325 and 330 CAD at engine CAD locations of 337-339 and 340-342, respectively. The individual points on the plot represent the ordered pairs of  $\phi_{\text{React}}$  and T values for each individual cell within the instantaneous CFD domain, and each point is colored with the ketohydroperoxide mass fraction (denoted by NC12-OQOOH) for that individual cell within the domain. Before discussing the  $\phi_{\text{React}}\text{-T}$  plots from CFD simulations further, a word of caution is appropriate vis-à-vis the interpretation of these plots. The data points provide instantaneous snapshots of  $\phi_{\text{React}}$  and T values in each cell and species mass fractions (e.g., NC12-OQOOH in Figs. 16 and 17). Clearly, with CFD simulations, species mass fractions in each cell can be affected by both species transport (e.g., by diffusion or turbulent mixing) and chemical reactions (leading to production or consumption of certain species). Given this scenario, it is not easy to separate temporal differences in species mass fractions in a given computational cell from one CAD to another arising due to species transport or chemical reactions. Consequently, it is helpful to focus on instantaneous differences in species mass fraction distributions between different SOIs to accurately interpret differences in the evolution of a given species.

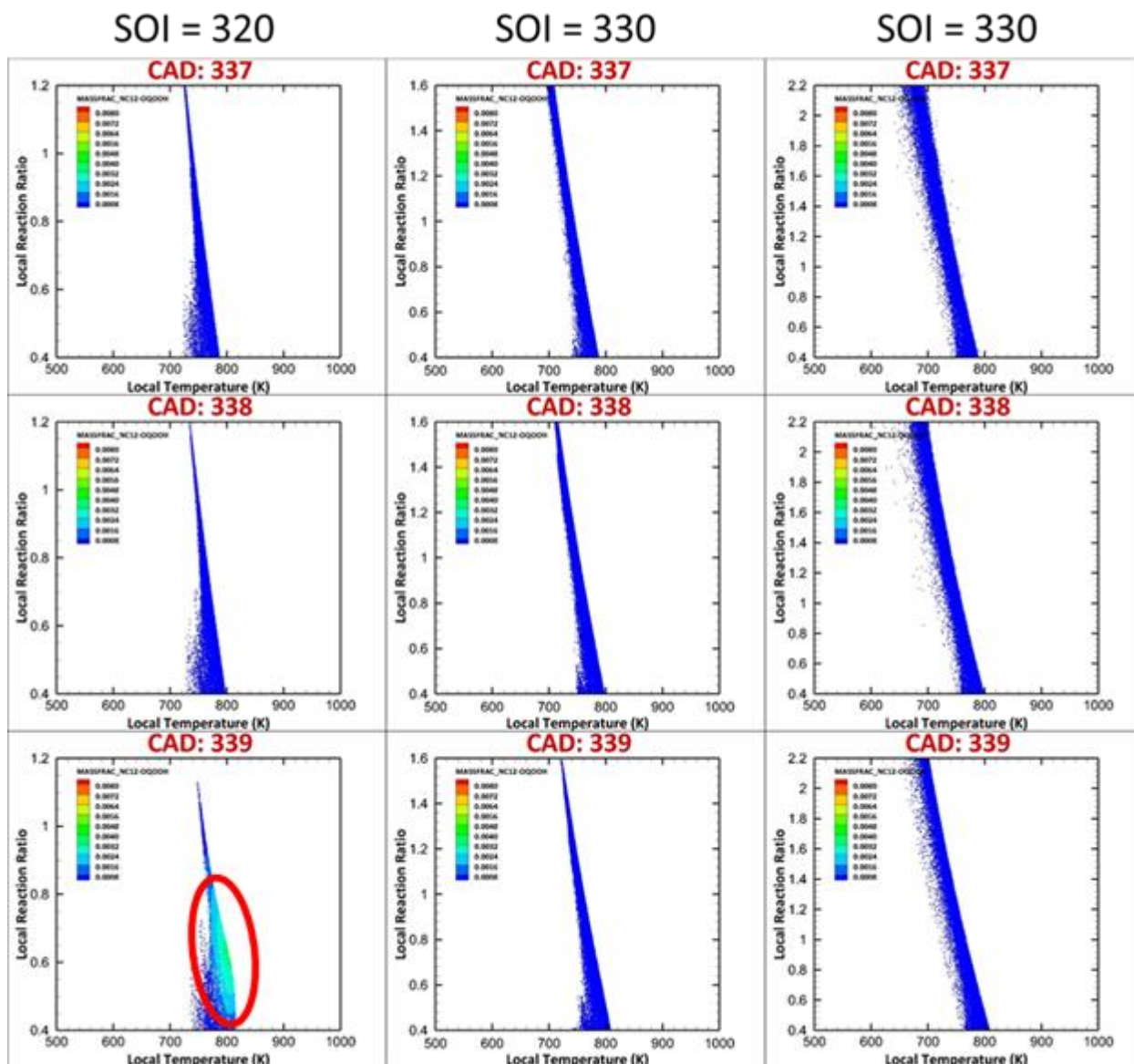


Figure 2.13. Local reaction ratio vs. local temperature colored by ketohydroperoxide mass fractions for SOIs = 320, 325, and 330; CAD = 337-339.

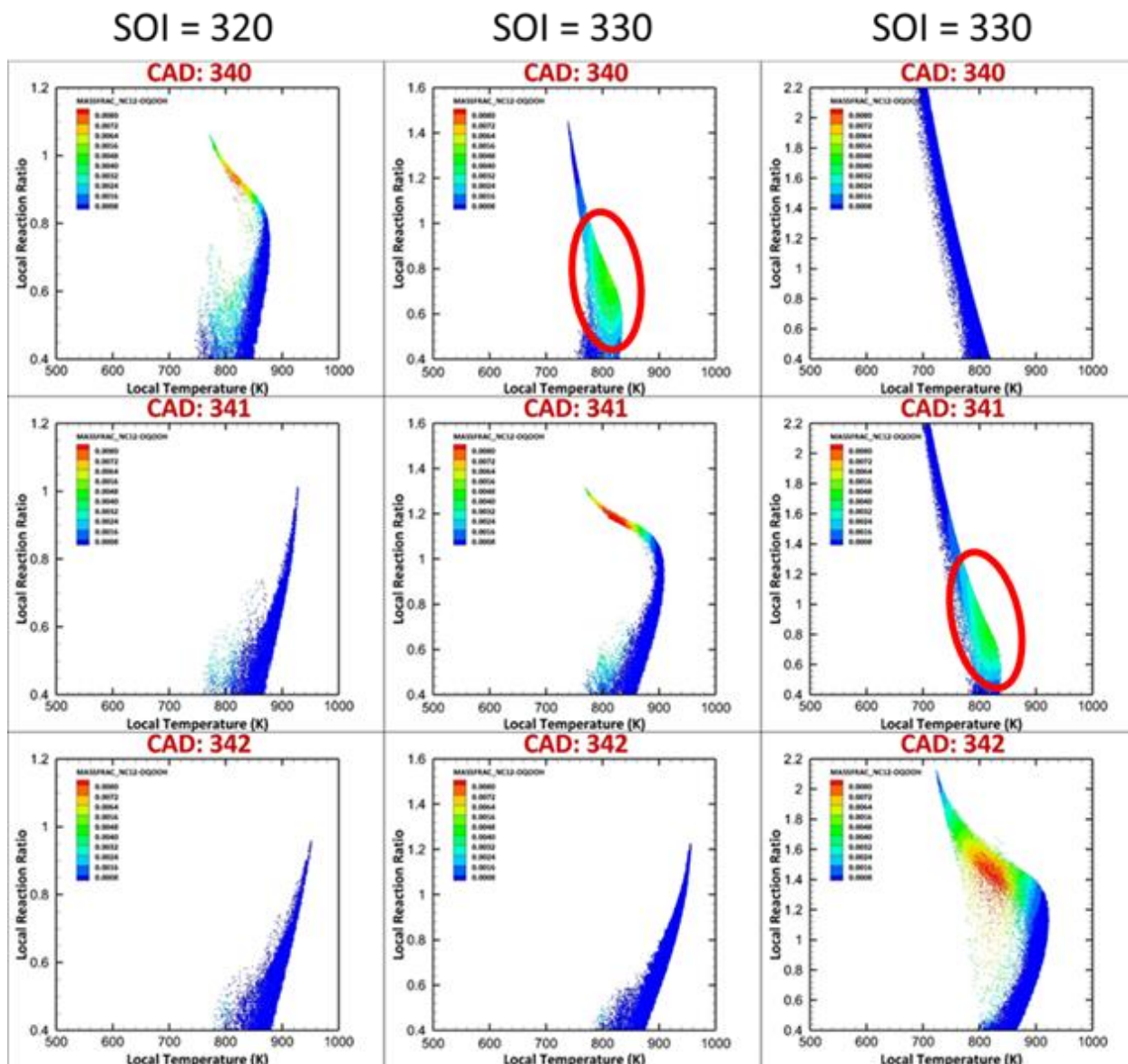


Figure 2.14. Local reaction ratio vs. local temperature, with colored by ketohydroperoxide mass fractions for SOIs = 320, 325, and 330; CAD = 340-342.

The temperature range shown in Figures 2.13 and 2.14 correspond to the expected range of low temperature chemical reactions to clearly identify the temperature and  $\phi_{\text{React}}$  at which ketohydroperoxide forms and/or gets consumed within the cylinder. In these figures, the first presence of ketohydroperoxide within the cylinder corresponds to a slight increase in

temperature for those regions; this manifests itself in the  $\phi_{\text{React}} - T$  plots as a small inflexion bump (circled in red on Figures 2.13 and 2.14), skewing the data points toward slightly higher temperatures on the  $\phi_{\text{React}} - T$  distributions. These can be seen at CAD locations of 339 for SOI = 320, 340 for SOI = 325, and 341 for SOI = 330. At these CAD locations, the first presence of ketohydroperoxide occurs at a temperature range of ~800-850K for each SOI. The  $\phi_{\text{React}}$  at which the first presence of ketohydroperoxide is observed is within 0.6 – ~1.1 for all of the SOIs, with SOI=330 having a wider range than SOI=320. It appears that ketohydroperoxide is formed earlier for more advanced SOIs, but at a more rapid pace for later SOIs, with SOI = 330 showing qualitatively more intense ketohydroperoxide formation (note same scales for all plots) not only at the start of the LTHR phase (CAD = 341), but also as the combustion proceeds temporally. A clearer visualization of this is shown in Figure 2.15, wherein results for SOI = 320 and SOI = 330 are compared at the start of LTHR for each SOI. The color scale for the ketohydroperoxide mass fraction was chosen based on the maximum value (0.0048) between the two SOIs. It is clear from Figure 2.15 that, not only is the amount of ketohydroperoxide formed at the start of LTHR higher for the later SOIs but also the  $\phi_{\text{React}}$  is higher at the highest concentrations of ketohydroperoxide. This shows the importance of the level of local fuel stratification level on the low-temperature chemical kinetics, which directly impacts subsequent high temperature reactions as well. This is consistent with the volumetric heat release results from the 0D chemical kinetics study shown in Figure 2.12, which demonstrated that an increase in the magnitude of LTHR (i.e., a greater presence of ketohydroperoxides) results in earlier and faster high temperature reactions.

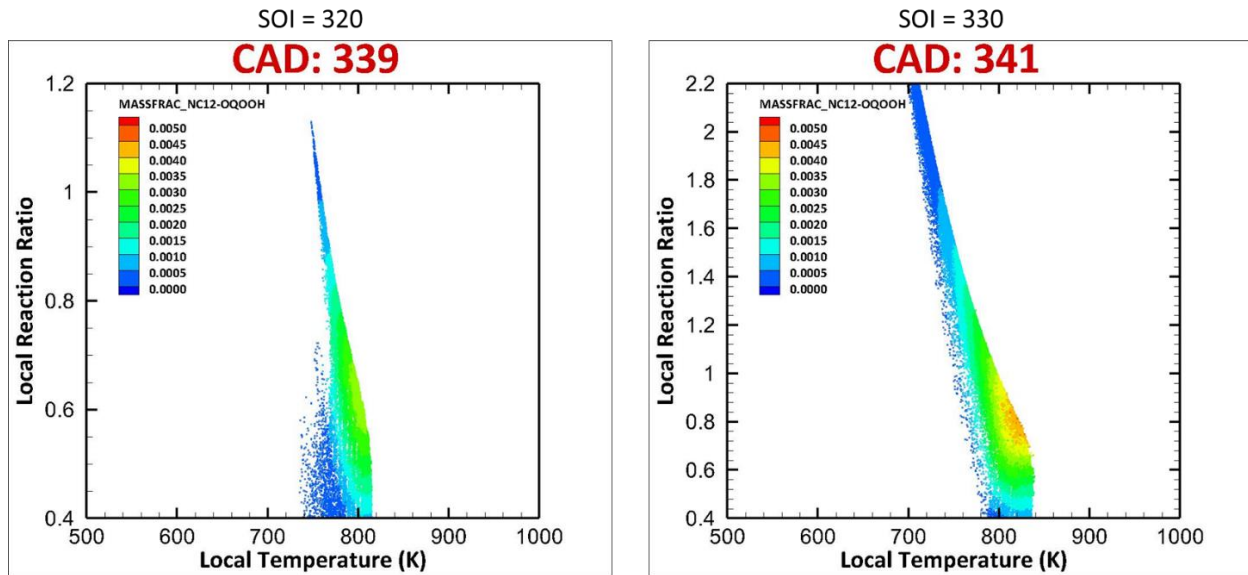


Figure 2.15. Local reaction ratio vs. local temperature colored by ketohydroperoxide mass fractions for SOIs = 320 and 330 and a range of 0 - 0.005 mass fraction.

To understand the distribution of  $\phi_{\text{React}}$  better, a histogram of  $\phi_{\text{React}}$  values across the entire computational domain was developed at the CAD locations where ketohydroperoxide is first observed. This corresponds to the aforementioned locations of 339 CAD, 340 CAD, and 341 CAD for SOIs of 320, 325, and 330 respectively. Figure 2.16 shows these individual histograms overlaid on each other to ascertain differences in the  $\phi_{\text{React}}$  distribution at the start of LTHR for each SOI. The  $\phi_{\text{React}}$  distribution within the cylinder is dramatically different at the start of LTHR for each of the three different SOIs. For SOI = 320, there is more time for the diesel to mix with the surrounding environment (19 CAD to be precise), leading to more areas of leaner  $\phi_{\text{React}}$  values. For SOI = 330, there is less time for mixing before the start of LTHR (~9 CAD), leading to a  $\phi_{\text{React}}$  distribution that is much more stratified (as seen from more cells with  $\phi_{\text{React}} > 1.5$ ). As shown in the  $\phi_{\text{React}}-T$  plots, and as previously stated, LTHR starts earlier for advanced SOIs. This, combined with the experimental analysis for pressure and temperature as well as the

0D chemical kinetic study, shows that the time allowed for mixing, and therefore the local  $\phi_{\text{React}}$ , is likely a vital factor in determining the timing, nature, and intensity of the start of the combustion process. Subsequently, the differences in start of combustion impact the rest of the combustion process, thereby impacting the AHRR transformation phenomenon observed.

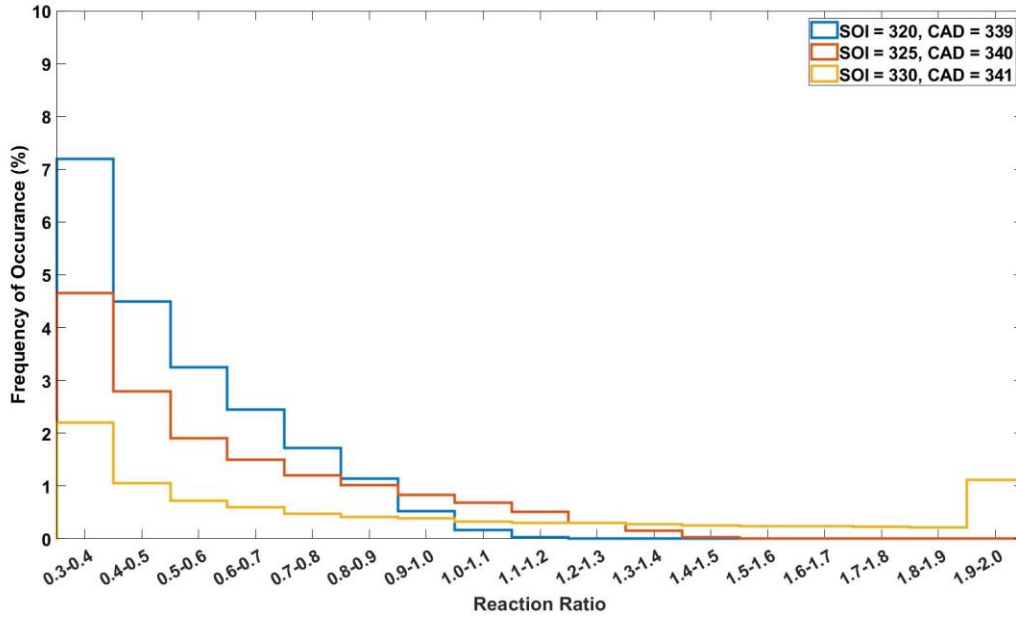


Figure 2.16. Reaction ratio histogram for each SOI at the respective start of LTHR locations.

To further explore the progression of combustion, the transition from low temperature chemical reactions to high temperature reactions is examined using the same  $\phi_{\text{React}}-T$  plots. Figures 2.17 and 2.18 show the  $\phi_{\text{React}}-T$  plots for SOIs of 320, 325 and 330 at CAD locations of 343-345 and 346-348, respectively, with each data point colored by the mass fraction of  $\text{CO}_2$ .  $\text{CO}_2$  was chosen as the species of interest in these plots to indicate “completeness” of the combustion process. As is well known, the reaction of  $\text{CO} + \text{OH} \rightarrow \text{CO}_2 + \text{H}$  is the main reaction for high temperature heat release in hydrocarbon combustion [54], and therefore any presence of  $\text{CO}_2$  would indicate high temperature reactions have occurred.

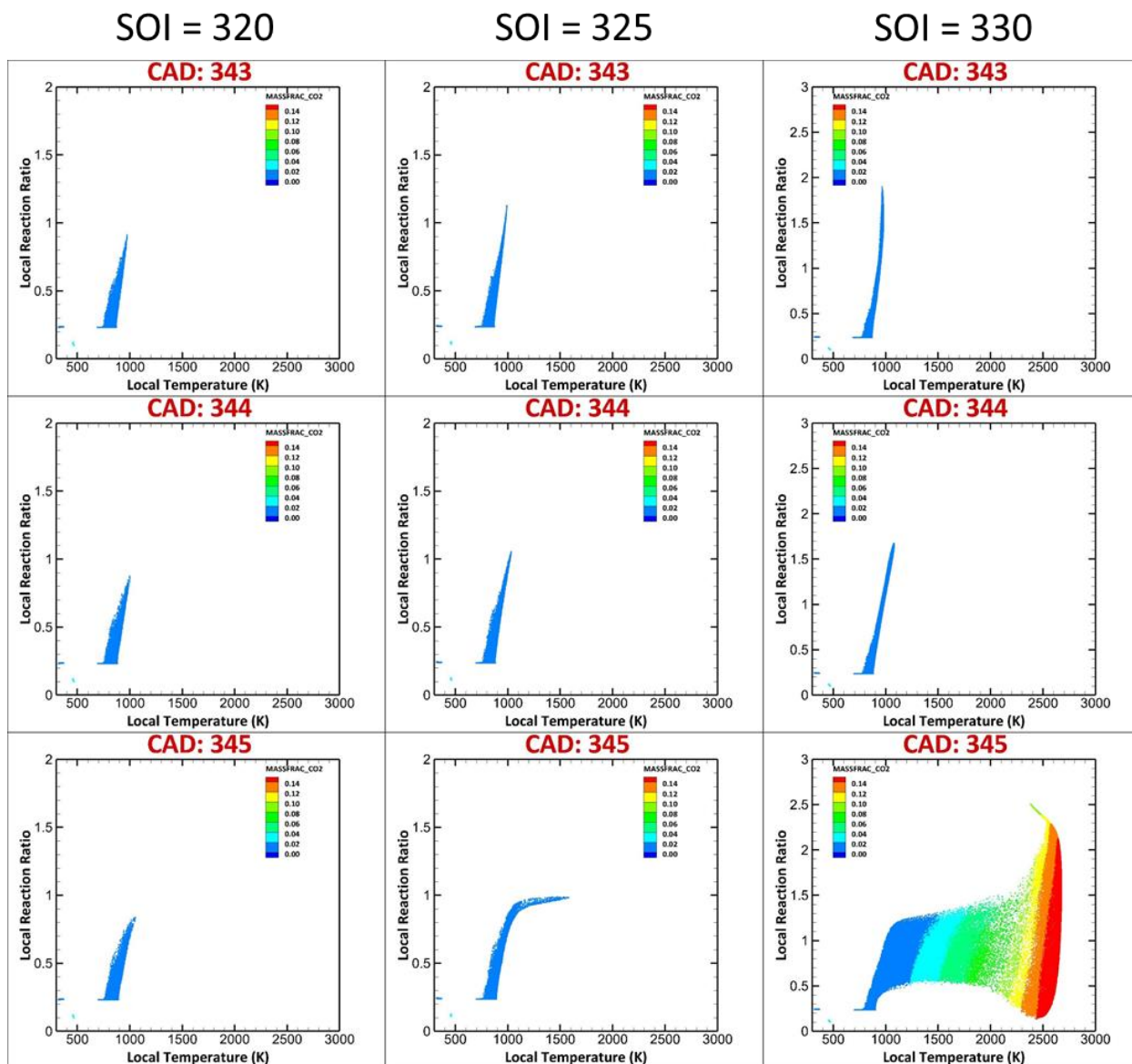


Figure 2.17. Local reaction ratio vs. local temperature colored by CO<sub>2</sub> mass fractions for SOIs = 320, 325, and 330; CAD = 343-345.

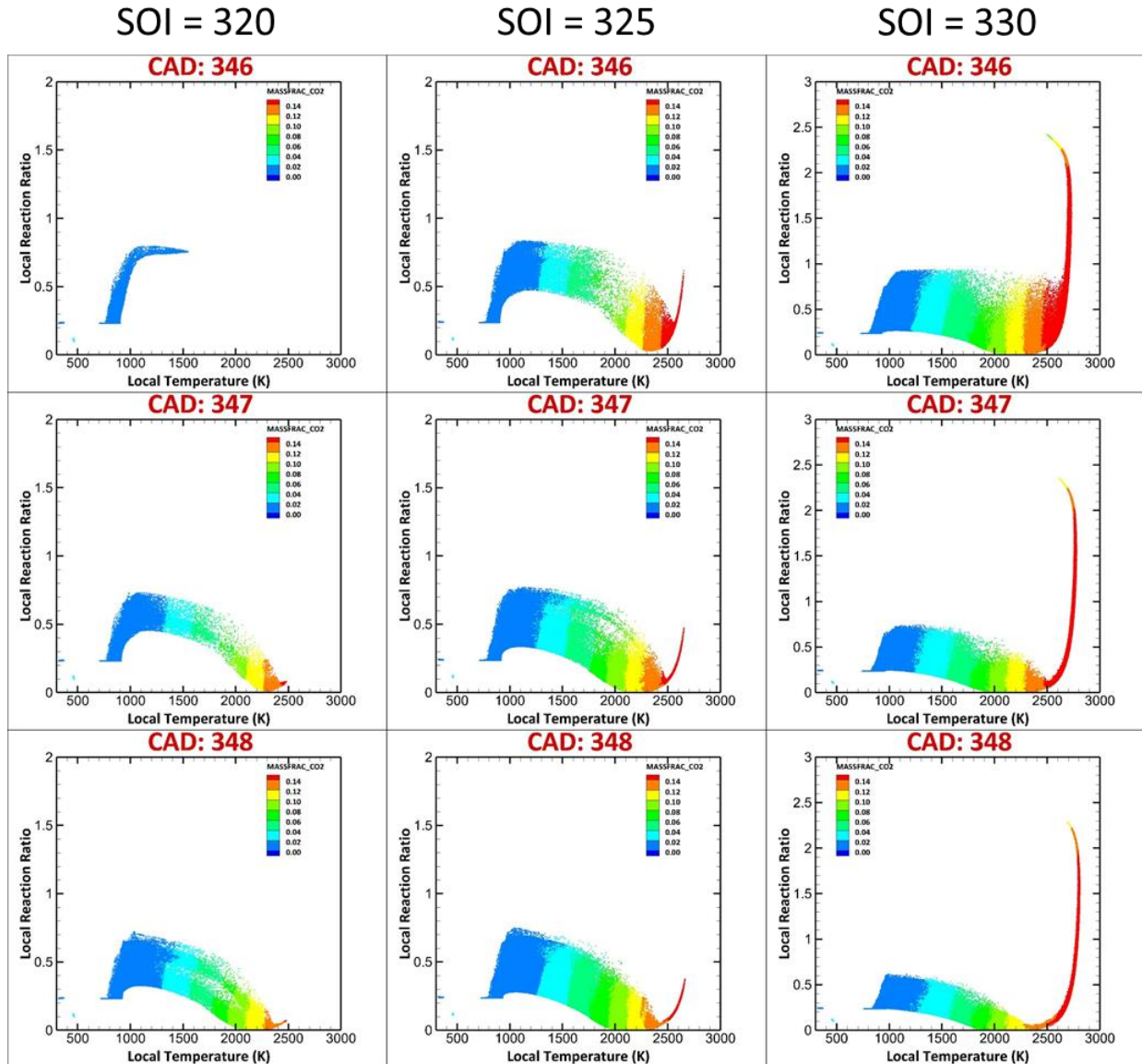


Figure 2.18. Local reaction ratio vs. local temperature colored by CO<sub>2</sub> mass fractions for SOIs = 320, 325, and 330; CAD = 346-348.

In Figures 2.17 and 2.18, high temperature heat release manifests itself in the  $\phi_{\text{React}} - T$  space as an abrupt shift of cells that are initially clustered over a range of  $\phi_{\text{React}}$  and temperatures below 1000 K to lower  $\phi_{\text{React}}$  and higher temperatures (2500-2600 K) upon combustion. From the specific definition of  $\phi_{\text{React}}$  (see Equation (2.7)) adopted in CONVERGE,  $\phi_{\text{React}}$  decreases upon combustion in a given cell because more of the hydrogen and carbon atoms arising from

the fuel and fuel fragments become bound in H<sub>2</sub>O and CO<sub>2</sub> molecules, which are excluded in the calculation of  $\phi_{\text{React}}$ . For the same reason, in some very high temperature (>2500 K), oxygen-deficient cells, in which combustion is virtually complete (high CO<sub>2</sub> and H<sub>2</sub>O levels), the  $\phi_{\text{React}}$  tends to increase again because the denominator in Equation (5) assumes very small values. This is manifested as “increasing red tails,” for example, at 348 CAD for both SOI = 325 CAD, and SOI = 330 CAD. The shift from low temperature cells with the lowest CO<sub>2</sub> mass fractions to increasingly higher temperature cells with higher CO<sub>2</sub> mass fractions (evident, for example, from the spatial spread of colors at 348 CAD for all SOIs) captures the overall evolution of combustion in different cells at a given CAD.

When combining Figures 2.14, 2.15, 2.17 and 2.18 together, it is shown that the transition from low temperature to high temperature reactions occurs faster for SOI = 330 compared to SOI = 325 and 320. The dwell between the start of LTHR and the start of HTHR for SOI = 320 CAD is 7 CAD (349 – 346 CAD) whereas the dwell for SOI = 330 CAD is 4 CAD (341 – 345 CAD). This trend agrees with the experimental SCRE results, in which the advanced SOIs had a shorter dwell between the start of LTHR and the start of HTHR than for the later SOIs, with SOI = 330 having a 4.2 CAD difference between the start of LTHR to the start of HTHR while SOI = 320 had a 5.8 CAD difference. This trend could be a result of the more intense low temperature reactions occurring for the later SOIs, thereby creating an environment that has a higher quantity of the necessary reactants needed for high temperature reactions to occur. To verify this hypothesis, the mass fractions of CO and OH were examined for the extreme SOIs of 320 and 330 CAD at CAD = 344, which occurs just before the start of high temperature reactions for both SOIs. These comparisons are shown in Figure 2.19. Both CO and

OH were chosen because of their importance for the  $CO + OH \rightarrow CO_2 + H$  high temperature heat release reaction.

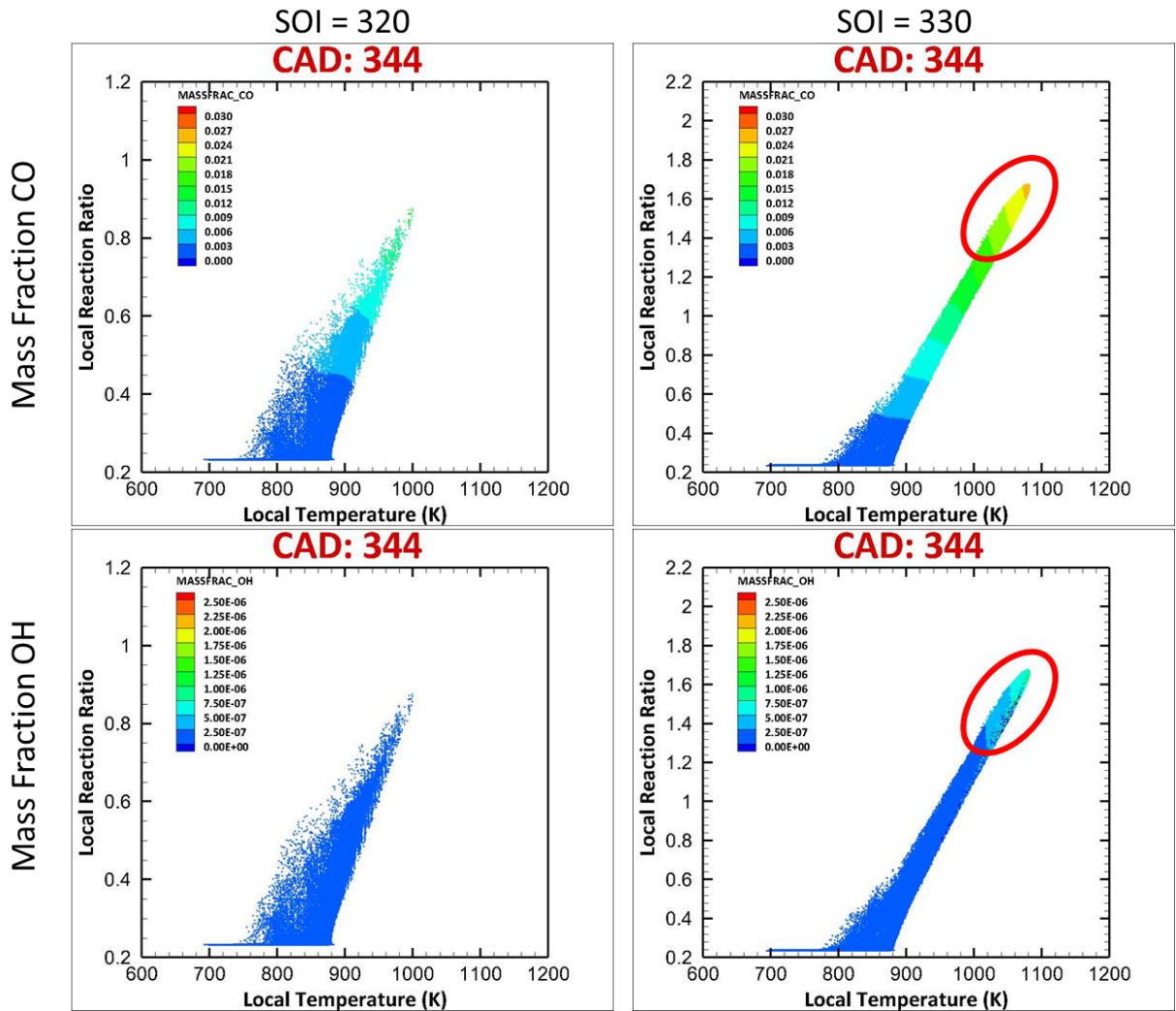


Figure 2.19. Mass fraction of CO and OH at CAD = 344 for SOIs of 320 and 330 CAD.

The CO mass fractions for SOI=330, are clearly higher within the circled area compared to SOI = 320. Again, since the same color scale (0-0.03) used for both SOIs, the higher mass CO fractions obtained at the same 344 CAD with SOI=330 implies that the higher local equivalence ratio stratification leads to faster high temperature reactions at the more later SOI. Similar observations can be made when comparing OH, again with the same color scale of 0-2.5E-6 for

both SOIs. The OH mass fraction for SOI = 330 ( $\sim 2E-6$ ) is an order of magnitude higher compared to the OH mass fraction for SOI = 320 ( $1.6E-7$ ). Since OH is well known as an important marker of reacting zones in combustion [55] as well as an important initiator of high temperature ignition [56], the fact that SOI = 330 has an order of magnitude more OH than SOI = 320 shows that the intensity of the low temperature reactions are allowing for more OH formation, thereby leading to a faster onset of more intense high temperature reactions.

Recalling the goal of the present work to unravel the reasons for AHRR shape transformation over a narrow range of SOIs in dual fuel combustion, all of these results further support the conclusion that the local equivalence ratio plays a dominant role in how reactions progress temporally through the combustion process. While it seems implausible for a small change in the injection timing ( $\sim 10$  CAD), to have such a significant impact, the CFD simulations clearly show that the extra time allowed for mixing with the slightly earlier SOI of 320 CAD allows for drastically different stratification levels. These differing stratification levels lead to either more intense low temperature reactions to occur, as is the case for more stratified mixtures like SOI = 330, or a more gradual low temperature combustion process, as for the more homogeneous SOI = 320 case. This directly impacts the temporal progression of combustion by changing how many reactant species are available, such as CO and OH, which leads to drastically different AHRR profiles, as evidenced in the experimental results. Therefore, by combining the experimental results, along with detailed 0D chemical kinetic simulations, and 3D CFD simulations, it can be concluded that variations in local equivalence ratio distributions is the most likely explanation for not only how the AHRR shape transformation occurs but also for why an order-of-magnitude decrease in  $NO_x$  emissions is observed when SOI is advanced over a narrow range (typically  $\sim 10$  CAD). While experimental and simulation results from a specific

SCRE operating at a specific set of operating conditions (speed, load, boost pressure, rail pressure, fuel combination (diesel-methane), etc.) were leveraged to explain the AHRR shape transformation in this study, it is well known (*cf.* Section 2.2) that similar AHRR shape transformations occur for SOI sweeps with dual fuel combustion with other engines and at other operating conditions. Consequently, even for other engines and under other operating conditions (including different fuel combinations), it is likely that differences in local equivalence ratio stratification drive the AHRR shape transformation and the associated sharp decrease in NO<sub>x</sub> emissions.

## **2.8 SUMMARY AND CONCLUSIONS**

Engine experiments were performed on a single cylinder research engine (SCRE) at fixed engine load, engine speed, rail pressure, and the percent energy substitution of the low reactivity fuel as the start of injection (SOI) was varied from 320 CAD to 330 CAD. This narrow SOI range exhibited a significant transformation of the shape of the AHRR profile, with SOI = 320 CAD exhibiting a more Gaussian-like profile, and SOI = 330 CAD exhibiting a more distinct two-stage heat release. Experimental analysis was performed on the AHRR profiles, including identifying the starting points of LTHR and HTHR. This was then coupled with 0-D chemical kinetic simulations, performed in ANSYS® CHEMKIN 2019 R2, as well as 3-D CFD simulations, performed in CONVERGE 3.0, to discern the specific influence of local thermodynamic conditions (i.e., pressure, temperature, equivalence ratio) on the AHRR transformation. The following conclusions were obtained from the combined experimental and computational analyses:

- The AHRR shape transformation occurs over a narrow range of SOIs (from 330 CAD to 320 CAD in the present case) and coincides with a significant reduction in NO<sub>x</sub> emissions, from 16.56 g/kWh at SOI = 330 to 1.74 g/kWh at SOI = 320 (~90% reduction).
- The start of LTHR advanced as SOI is advanced, with SOI = 330 having a start of LTHR of 339.6 CAD and SOI = 320 having a start of LTHR of 338.6 CAD. This phenomenon was captured in the 3D CFD results.
- In-cylinder pressure and in-cylinder bulk gas temperature do not vary significantly at the start of LTHR and the start of HTHR over the range of SOIs from 330 CAD to 320 CAD. The average pressure at the start of LTHR was 35.1 bar and the average temperature was 852 K, with variations of 2% and 0.53% respectively. At the start of HTHR, the average pressure was 45.5 bar and the average temperature was 909 K, with variations of 1.6% and 0.45%, respectively. The minimal variations in in-cylinder pressure and temperature indicated that they may not be important causes for the AHRR shape transformation and NO<sub>x</sub> reductions.
- From 0-D kinetic simulations, it is evident that large changes in the initial pressure (~ 20 bar) and initial temperature (~100 K) are needed to significantly impact heat release rates. Combining experimental and 0D chemical kinetic simulation results, it can be concluded that the minor variations in-cylinder pressure and bulk gas temperature across the SOI range are insufficient to cause the significant AHRR shape transformation observed experimentally.
- By comparison, smaller changes in the equivalence ratio can lead to larger changes in heat release rates. Combining 0D chemical kinetic and 3D CFD simulation results (including in-cylinder T, reaction ratio, CO, OH, and CO<sub>2</sub> distributions), the authors conclude that local

equivalence ratio stratification differences are the most likely cause for not only the AHRR shape transformation but also for the sharp decrease in  $\text{NO}_x$  emissions when SOI is advanced over a narrow range ( $\sim 10$  CAD).

- Finally, since local equivalence ratio stratifications are dependent only on the fuel-air mixing process (governed by in-cylinder turbulence) at different SOIs and not necessarily on other operating conditions, it is likely that differences in local equivalence ratio stratification drive the AHRR shape transformation and the associated sharp decrease in  $\text{NO}_x$  emissions observed in the literature across a narrow SOI range for other engines and under other operating conditions (e.g., specific combination of high reactivity and low reactivity fuels)

III.  
EXPERIMENTAL ANALYSIS OF COMBUSTION HEAT RELEASE TRANSFORMATION  
FOR DIESEL-NATURAL GAS AND POMDME-NATURAL GAS DUAL FUEL  
COMBUSTION ON A HIGH COMPRESSION RATIO SINGLE-CYLINDER ENGINE

### 3.1 ABSTRACT

Dual fuel combustion uses two different fuels, typically a high reactivity fuel (HRF) and a low reactivity fuel (LRF), to attempt to reduce the harmful emissions that are produced by combustion. One of those emissions, oxides of nitrogen ( $\text{NO}_x$ ), is a contributor to smog problems. Previous research has shown that, in dual fuel combustion,  $\text{NO}_x$  emissions reduce when the start of injection (SOI) of HRF occurs relatively early in the compression stroke. Separately, a phenomenon wherein the apparent heat release rate (AHRR) changes shape from a two-stage type heat release to a single stage Gaussian like heat release profile has been observed. The SOI range over which this transformation occurs coincides with significant engine out  $\text{NO}_x$  reduction. Therefore, further study needs to be done to understand the governing principles of the transformation region, so as to better understand how it can help reduce  $\text{NO}_x$  values. The AHRR transformation was observed on a single cylinder research engine platform with a compression ratio of 18.5:1, and a gross indicated mean effective pressure (IMEPg) of 5 bar, at a speed of 1339 RPM. Two different HRFs of differing reactivities, diesel and polyoxymethelene dimethyl ether (POMDME), were studied over an SOI range of 320 CAD to 330 CAD. The results of the experimental study were compared to previous results from a different engine platform to

ascertain if changes in speed, compression ratio, as well as different fueling combinations were a factor in the transformation process. It was deemed that the transformation process occurs irrespective of the changes in speed and engine platform and is purely a thermodynamic related phenomenon, which therefore must be governed by some parameter such as pressure, temperature, or local stratification. When comparing diesel-NG and POMDME-NG combustion, it was found that pressures and temperatures at key areas of the AHRR profile, mainly the start of low temperature heat release (LTHR) and start of high temperature heat release (HTHR), were comparable, yet there was a difference in how the transformation region manifested itself. Since the only difference between the two SOI sweeps studied was the different reactivity of the HRF, it was determined that the local stratification is the key governing parameter in how the transformation region manifests, which is supported by previous studies on the 17:1 compression ratio engine platform.

### **3.2 INTRODUCTION**

Internal combustion (IC) engines have been a key factor in how society has evolved throughout the years, since without IC engines, it would be nearly impossible to remain as interconnected as society has become today. A continuing problem with IC engines is the emissions that are output by the combustion process, mainly greenhouse gas emissions such as CO<sub>2</sub>. In fact, the transportation sector accounts for ~11% of the total greenhouse gas emissions produced as of 2016 [57]. There have been a multitude of strategies researched to reduce the emissions that are output by IC engines, including gasoline compression ignition [58-61], homogeneous charge compression ignition (HCCI) [62-65], pre-chamber ignition [66-68], thermally stratified compression ignition (TSCI) [69], and reactivity-controlled compression ignition (RCCI) [70-73]. The current work focuses on dual fuel combustion, wherein a low-

reactivity fuel (LRF) is fumigated into the intake manifold, in which a small amount of high reactivity fuel (HRF) is used to ignite the fuel-air mixture. The physical modifications needed to implement dual fuel combustion on an IC engine are minimal because in its simplest form the LRF can be directly fumigated into the intake manifold.

Dual fuel combustion can be utilized to reduce engine out oxides of nitrogen emissions ( $\text{NO}_x$ ) by utilizing advanced SOIs of the HRF in the engine, such as demonstrated in the advanced low pilot ignited natural gas (ALPING) strategy [74-76]. An interesting phenomenon can be observed with changing SOI, wherein the shape of the apparent heat release rate (AHRR) profile changes from a typical two-stage heat release to a more single stage “Gaussian”-like heat release rate with prominent low temperature heat release (LTHR). This change in the AHRR profile is accompanied by a steep reduction in engine-out  $\text{NO}_x$  emissions. While this AHRR transformation has been observed in several previous studies [7,37-42], the possible underlying reason for the transformation have only been recently elucidated for the specific case of diesel-methane dual fuel combustion [27]. Consequently, it is important to study the impact of other HRF fuels (e.g., POMDME) and a more practical LRF fuel (natural gas instead of methane) on the AHRR transformation.

The current work builds upon Partridge et al. [27] by examining the transformation region for a different single cylinder research engine (SCRE) platform. The same SOI range was examined as in Partridge et al. [27] (i.e. SOI = 320 to SOI = 330 CAD), and two different HRFs (diesel and POMDME) were studied. POMDME has previously been used as a compression ignition engine fuel in multiple studies by Pellegrini et al. [16-18] and has shown improvement in engine out particulate matter emissions since it is an oxygenated fuel. POMDME also has a higher cetane number compared to diesel, thereby allowing for a fuel with a higher reactivity to

be studied in terms of the transformation region. The goals of the present work is to further add to the body of literature available on the transformation region, determine if the use of a different HRF impact the transformation region, determine if the use of natural gas as an LRF has any impact on the transformation, and determine the impacts of engine hardware on the transformation region.

### 3.3 EXPERIMENTAL SETUP

The present work focuses on a single cylinder research engine (SCRE) platform that has a compression ratio (CR) of 18.5:1. Details of the SCRE are provided in Table 3.1.

Table 3.1. Single cylinder research engine specifications.

Engine type	Single cylinder, four stroke
Bore (mm)	123
Stroke (mm)	152
Con. Rod Length (mm)	244.5
Displaced Volume (L)	1.806
Nozzle dia (mm)	0.1905
Number of nozzle holes	7
Compression ratio	18.5
Intake Valve Timings	IVO – 710 CAD, IVC – 210 CAD
Exhaust Valve Timings	EVO – 490 CAD, EVC – 5 CAD
Diesel Injection System	Delphi DFP5 common rail
Operating Speed (rpm)	1339

The SCRE utilizes NG as the LRF, which is fumigated into the intake manifold to achieve dual fuel combustion. A detailed diagram of the SCRE experimental setup can be seen in Figure 3.1.

The engine was coupled to a 393 hp, AC dynamometer, with a Dyne Systems InterLok (IL5) used to control the engine speed. The load was controlled via the fueling rates of HRF and LRF. A pressure regulator was used to meter the LRF flowrate (in this case, natural gas), with a Micromotion Coriolis flow meter (Model CMFS015M319N0A2ECZZ) being used to measure the fuel flow rate. The HRF (diesel or POMDME) was injected directly into the cylinder using the stock solenoid injector, which was connected to a common rail injection system capable of achieving up to 2500 bar rail pressure. Diesel injection timing, duration, and rail pressure were controlled via a National Instruments Direct injector Control and Measurement (DCM) device interfacing with Vieletech Calibration Viewer software. The HRF flowrate was measured with a Micromotion Coriolis flow meter (Model CMFS010M319N0A2ECZZ). Pressurized air was supplied to the intake using an external air compressor, which was conditioned using a heatless desiccant dryer before entering the engine. The air flow rate was measured using a sonic (choked) nozzle from FlowMaxx (Model SN16-SA-345). In cylinder pressure was measured using a Kistler model 6124A pressure sensor, with a Kistler 5018 type charge amplifier used to amplify the signal. A 0.1 CAD resolution BEI shaft encoder was used to phase the in-cylinder pressure trace. Steady state intake pressure ( $P_{\text{intake}}$ ) was measured with a Setra model 206 pressure transducer, and a Kistler 4624A pressure transducer was used to measure crank-angle resolved intake pressure to peg each engine cycle's cylinder pressure trace.

Diesel and POMDME were used as the HRFs, and both were directly injected into the combustion chamber. The SOI was the only parameter allowed to vary throughout the

experiments, except the different fuels. For the purposes of these experiments, the SOI ranges from Chapter II of this dissertation were used as the framework for the SOIs studied, with the SOI values of 320, 322, 324, 326, 328, and 330 CAD being considered. Table 3.2, below, details the operating conditions considered for both POMDME and diesel operation.

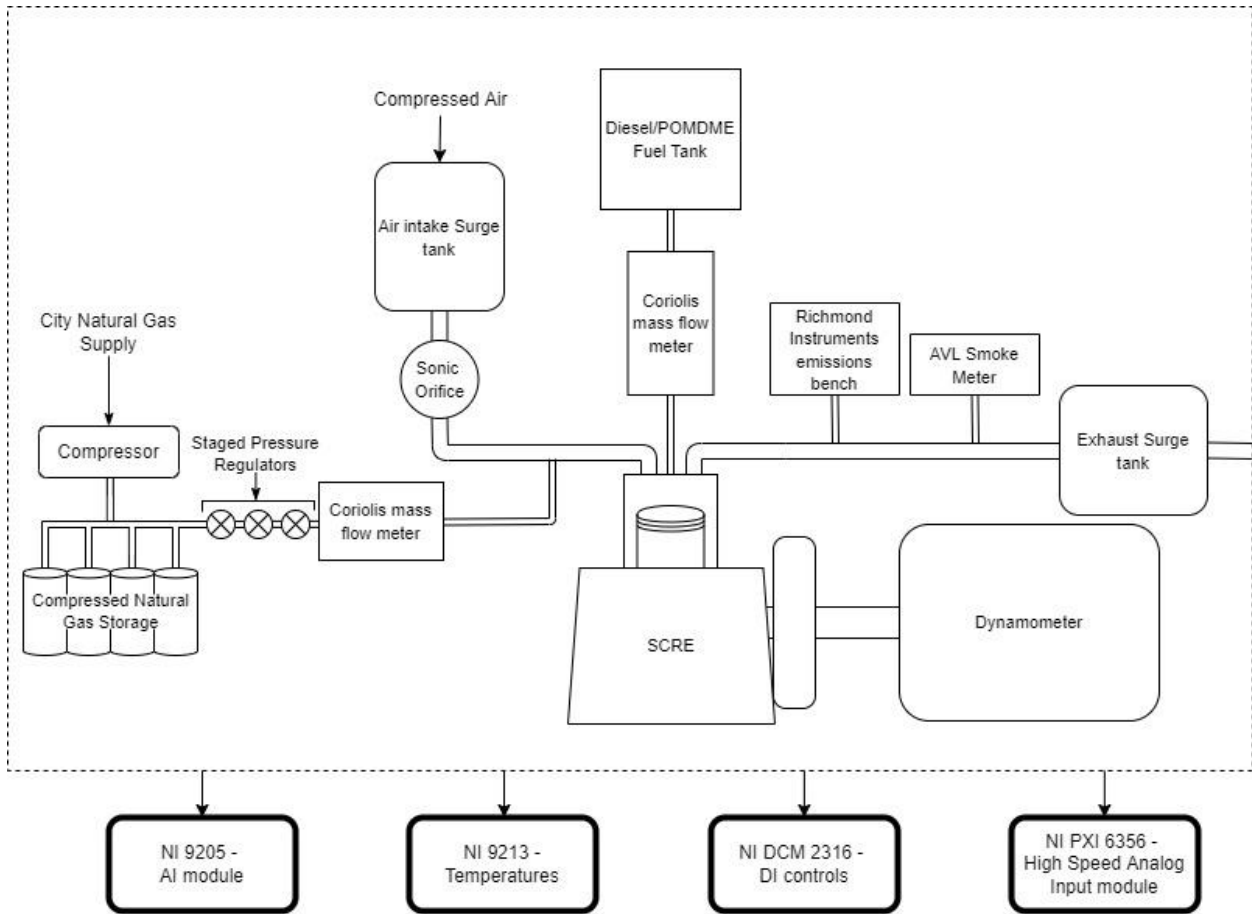


Figure 3.1. Detailed engine layout.

Table 3.2. Engine operating conditions for both diesel and POMDME.

	320 CAD, 322 CAD, 324
SOI	CAD, 326 CAD, 328 CAD, 330 CAD
Gross Indicated Mean Effective Pressure (IMEPg)	5 bar
PES	80%
Intake Pressure	1.5 bar
Engine Speed	1339 RPM
Rail Pressure	500 bar
LRF type LRF lower heating value	Natural Gas 49,229 (kJ/kg)

Since this work is discussing the transformation region, which has been defined previously in Chapter II, all the equations and terminology used throughout the present work are identical to those used in Chapter II. Therefore, for brevity, for more information on the equations and terminology used, refer to Chapter II within this dissertation. Details of the experimental sensors used in the current work are detailed in Table 3.3, below.

Table 3.3. Details of sensors used on CR = 18.5 engine platform.

Data Type	Make/Model	Type	Unit	Accuracy
Temperature (intake, exhaust, etc.)	Omega	K-type	°C	±0.75% of reading
Air mass flow	Flowmaxx	Sonic orifice	kg/h	±0.25% of reading
Diesel mass flow	Micro Motion	Coriolis	kg/h	0.1% of reading
Natural Gas mass flow	Micro Motion	Coriolis	kg/h	0.25% of reading
Smoke	AVL 415S	Filter	FSN	0.001 of reading
NOx and NO	Rosemount Analytical	CLD	ppm	+/-1% of full scale
THC	Rosemount Analytical	HFID	ppm	+/-1% of full scale
CO	Rosemount Analytical	NDIR	%	+/-1% of full scale
CO2	Rosemount Analytical	NDIR	%	+/-1% of full scale
O2	Rosemount Analytical	NDIR	%	<1% of full scale
Cylinder pressure	Kistler 6124A	Piezoelectric	bar	±0.3% of reading
Dynamic pressures (intake, exhaust)	Kistler 4049A	Piezoresistive	Bar	±0.1% of full scale
Steady state pressures (intake, exhaust, etc.)	Setra Model 206	Capacitance	psig	±0.13% of full scale

A key difference between the results shown in the present work, and those of Chapter II is the absence of a needle lift sensor on the injector used. Because of the injector type on this SCRE, it was not possible to install a needle lift sensor on the injector. Therefore, the commanded injection current is used for the analysis in this work. Injection line pressure was measured using a piezoresistive sensor installed on the high-pressure injection line connecting the rail to the injector. Apparent injection delays were calculated as the crank angle difference between the commanded injection current (commanded SOI) and the first instance when the injection line pressure decreased from its average value by 1%. For reference, the apparent injection delays calculated for these operating conditions were in the range of 7-8 CAD.. Thus, while the apparent delay in injection between the commanded SOI and the actual SOI must be considered while observing the results in this work, the trends themselves are valid (perhaps with an offset) since the injection delay remained virtually constant across the SOIs studied here.

### **3.4 DIESEL-NATURAL GAS RESULTS**

The apparent heat release (AHRR) profiles for the SOI sweep on the 18.5:1 compression ratio engine is shown in Figure 3.2.

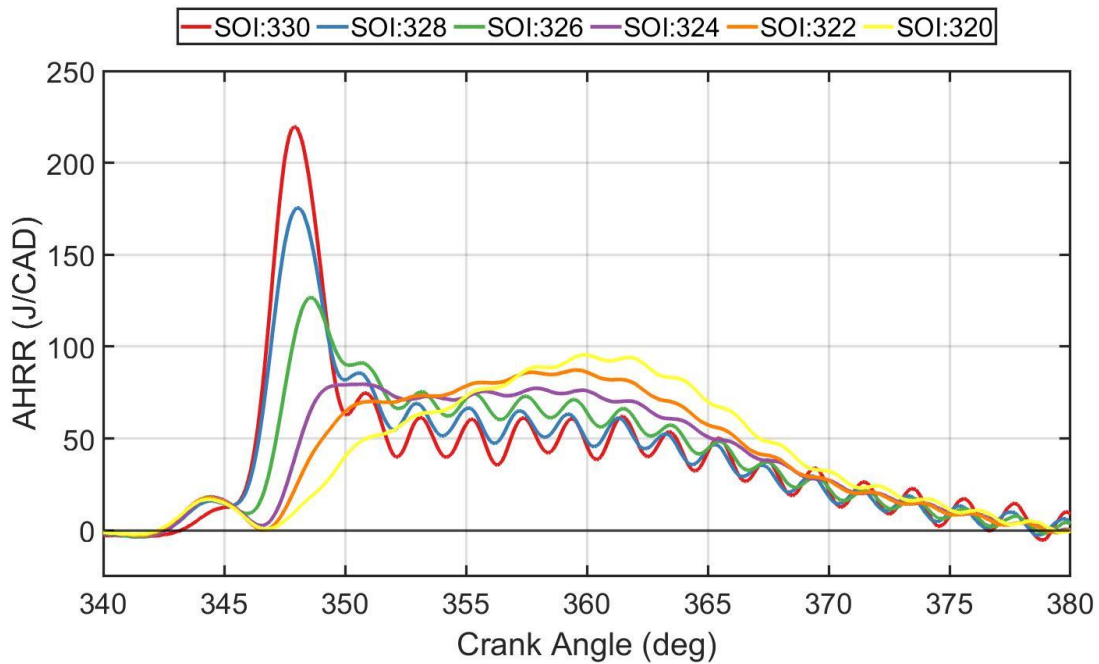


Figure 3.2. AHRR for SOIs of 320, 322, 324, 326, 328, and 330 CAD for CR = 18.5 engine at 5 bar IMEP<sub>g</sub>, 80% PES.

It is clear from Figure 3.2 that the transformation region occurs over the same commanded injection timing range as for diesel/natural gas combustion shown in Chapter II, which used needle lift data to for the SOIs on a 17:1 compression ratio engine. The clear transformation from a distinct two-stage AHRR profile at later commanded SOIs to the more Gaussian AHRR shape at advanced SOIs is evident. This transformation is again accompanied by a reduction in indicated specific oxides of nitrogen (ISNO<sub>x</sub>) emissions, and as the ISNO<sub>x</sub> is decreased, an increase in the IFCE is also observed, as shown in Figure 3.3. This is significant because it shows the importance of understanding the transformation region phenomenon.

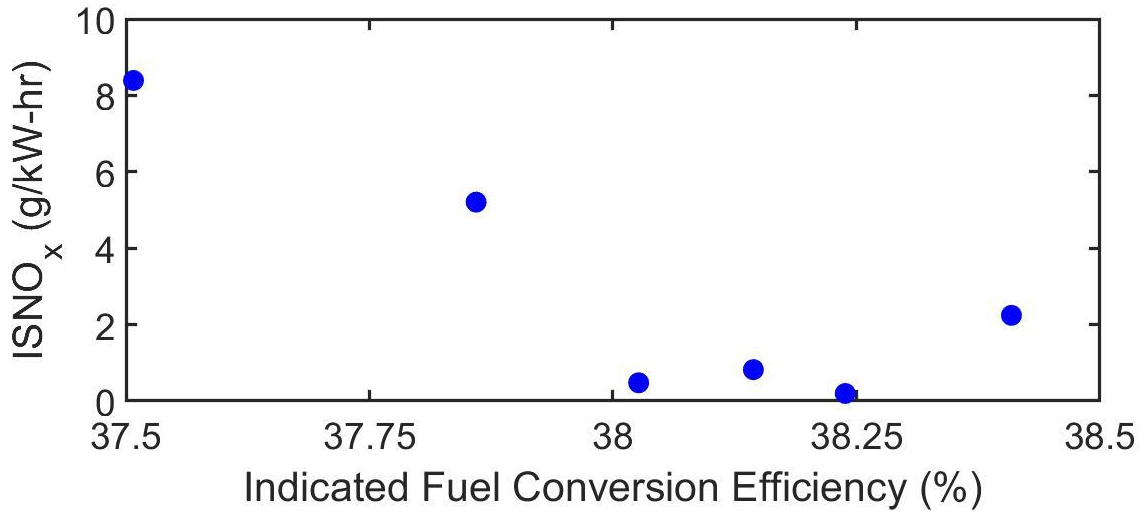


Figure 3.3. Indicated specific NO<sub>x</sub> values vs. IFCE for diesel/natural gas on the CR = 18.5 engine.

The fact that the transformation region was observed for dual fuel combustion on another SCRE with a compression ratio of 17:1, as shown in Chapter II as well as on the 18.5:1 SCRE as evident from Figure 3.2, in addition to many other engine platforms as evident from the literature, shows that the AHRR transformation is not an exception, but rather the rule with dual fuel combustion. Furthermore, as shown in Chapter II, the transformation is governed by the in-cylinder thermodynamic conditions, mainly pressure, temperature, and equivalence ratio ( $\phi$ ). To determine if the different engine platform, as well as changes to the LRF has an impact on the transformation region, a similar analysis is performed as shown in Chapter II, wherein the in-cylinder pressure and in-cylinder temperature are analyzed at the start of low temperature heat release (LTHR) as well as at the start of high temperature heat release (HTHR).

A zoomed-in portion of the AHRR curve is shown in Figure 3.4. Included in the figure are vertical lines corresponding to the start of LTHR (which is denoted by a dotted-dashed line) as well as the start of HTHR (denoted by the dashed line), with each vertical line being color-coded to match with the corresponding SOI. The start of LTHR is invariant for SOIs 320-328,

with all the start of LTHR's occurring at 341.7 CAD. It was determined that SOI 330 did not have any LTHR, as there is not a significant difference between the slight rise in AHRR value that occurs around 344-345 CAD and the subsequent high temperature heat release spike. It should also be noted that the LTHR portions of the AHRR curve for all SOIs except SOI = 330 have very similar profiles, comprising comparable peak LTHR values (with the peak occurring consistently between 15 to 20 J/CAD) as well as a consistent CAD location of the peak LTHR, with peak locations consistently occurring at the value of 344.5 CAD. If SOI = 330 had any LTHR, it would be occurring as an outlier from the rest of the SOIs; consequently, it is safe to assume that SOI = 330 has no LTHR component. The CAD values of start of LTHR and start of HTHR are listed in Table 3.4 for reference.

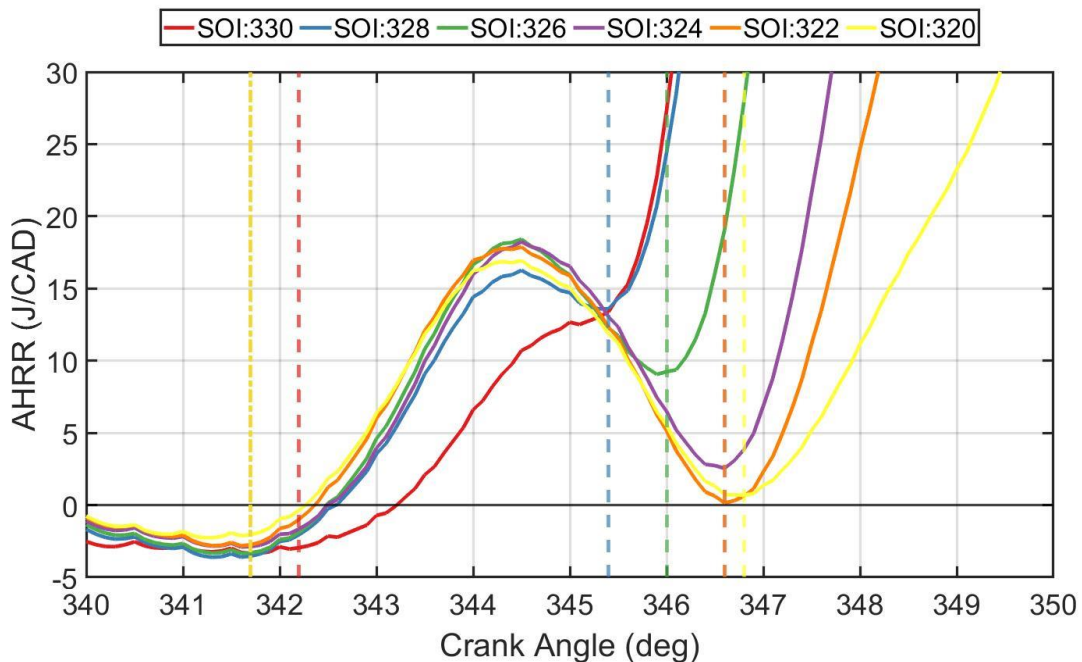


Figure 3.4. LTHR portion of the AHRR curve for diesel/natural gas on the CR = 18.5:1 engine with dashed vertical lines representing the onset of HTHR and dot-dashed vertical lines representing the onset of LTHR, both colored with respect to the corresponding SOI.

Table 3.4. Start of LTHR and start of HTHR for diesel/natural gas combustion on the 18.5:1 compression ratio SCRE.

SOI (CAD)	330	328	326	324	322	320
Start of LTHR (CAD)	N/A	341.7	341.7	341.7	341.7	341.7
Start of HTHR (CAD)	342.2	345.4	346	346.6	346.6	346.8

To determine if there are any differences with this engine platform in the governing phenomenon, the pressure and temperature at the start of LTHR and start of HTHR are determined based on the respective starting locations and are given in Table 3.5.

Table 3.5. Pressure and temperature @ start of LTHR and HTHR for diesel/natural gas combustion on the 18.5:1 CR engine platform.

SOI (CAD)	330	328	326	324	322	320
Pressure @ Start of LTHR (bar)	N/A	45.95	45.87	45.88	45.90	45.86
Pressure @ Start of HTHR (CAD)	47.07	56.03	57.81	59.50	59.56	60.06
Temp. @ Start of LTHR	N/A	771.3	769.7	768.8	769.4	769.2
Temp @ Start of HTHR	774.8	814.6	821.7	826.4	827.4	828.9

It is observed that the pressure at the onset of LTHR is practically constant across the SOI range. Without any combustion occurring, the differences in pressure curves between SOIs will be minimal, so this observation makes sense. The temperatures at the start of LTHR, subsequently, are also consistent across the SOIs. To visualize this better, a plot of AHRR vs. in-cylinder bulk gas temperature is shown in Figure 3.5.

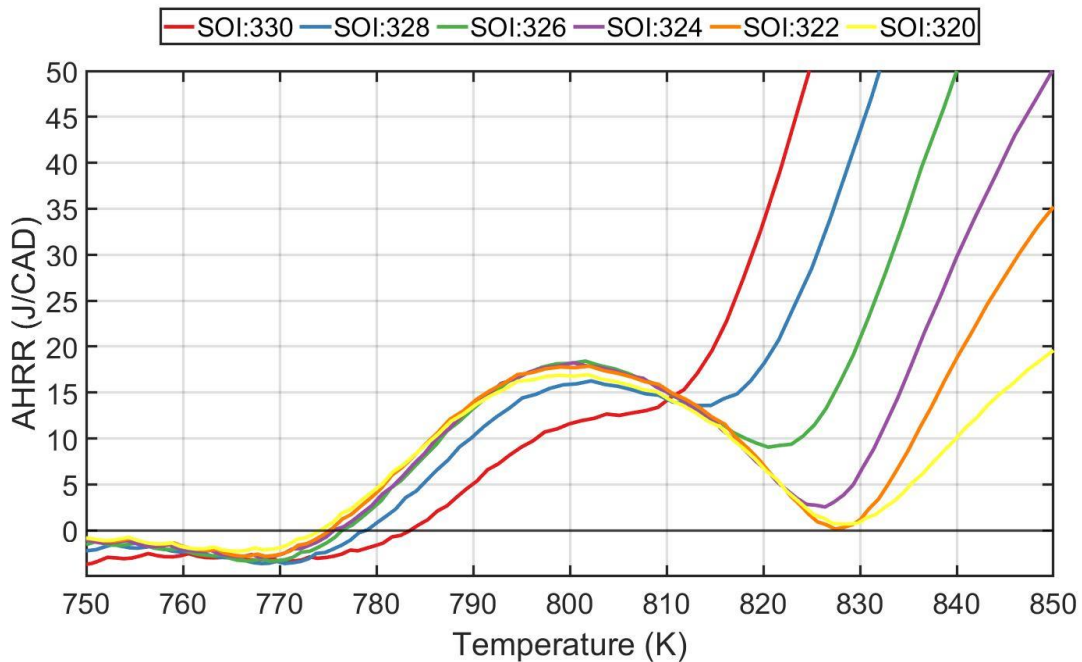


Figure 3.5. AHRR vs. Temperature for diesel-natural gas combustion on the 18.5 CR engine platform.

When performing the 0D chemical kinetic simulations, variable including temperature and pressure were independently varied while keeping other parameters a constant. When varying the pressure and keeping the temperature and  $\phi$  a constant (*c.f. Figure 2.6 & Figure 2.7*), it was found that increasing the initial pressure increases the speed at which low temperature reactions occur even when starting from the same initial temperature. Therefore, it could be surmised that for the higher 18.5 CR engine platform, since pressures are consistently higher due to the higher compression ratio, that low temperature chemistry could occur earlier and at a lower temperature than for the 17:1 CR engine platform.

Nonetheless, the results of the experimental analysis further bolster the hypothesis that the local reactivity influences the transformation region, as was concluded in Chapter II, seeing

as the temperature and pressure at the start of LTHR and start of HTHR across all SOIs do not vary significantly enough to drastically impact the temporal progression of combustion which would result in such stark differences as seen in the transformation region. To further test this theory, the reactivity of the fuels must be changed, keeping all else the same (as much as possible). This can be achieved by using a different fuel for the HRF, such as polyoxymethylene dimethyl ether (POMDME). It should be noted that the LRF used throughout the current work differs from that presented in Chapter II, seeing as this work uses city natural gas, whereas Chapter II used 99.9% pure methane. This can also influence the transformation region; however, since the same LRF is being used consistently throughout the present work, any conclusions drawn as to the changes in the transformation region when changing to POMDME can be concluded to arise solely from the different reactivities of POMDME and diesel.

### 3.5 POMDME-NATURAL GAS RESULTS

Before discussing the results of to the impact of POMDME as the HRF in dual fuel combustion, it is important to first understand the differences between the POMDME and the diesel that was used previously. POMDME is typically a combination of six different oxymethylene dimethyl ethers (OMEs). The chemical formula for OME is  $\text{CH}_3(-\text{O}-\text{CH}_2)_n-\text{O}-\text{CH}_3$ , where  $n$  represents the number of  $(\text{O}-\text{CH}_2)$  portions of the chain length. The composition of the fuel used in this study was: 0.02% OME1, 0.12% OME2, 47.76% OME3, 29.58% OME4, 16.38% OME5, and 5.37% OME6. More details of the fuel properties can be found in Table 3.6.

Table 3.6. POMDME and diesel fuel properties.

	<b>Diesel</b>	<b>POMDME</b>
Octane Number/Cetane Number	Cetane = ~42	Cetane = 70
Lower Heating Value (MJ/kg)	43.4	19.204
Oxygen (m/m) %	0	47
Hydrogen/Carbon Ratio	1.8	2.35
Oxygen/Carbon Ratio	0	0.83

The main differences in the diesel and POMDME are in the change in reactivity (higher cetane number of POMDME compared to diesel) and in the significantly reduced lower heating value (LHV) of POMDME. Because of the reduced lower heating value (by about 2.25 times), a larger amount of POMDME will be required for the same load output from the engine. In the context of the transformation region, as discussed in Chapter II and the diesel-NG results discussed above, there will be more POMDME fuel that needs to mix with the surrounding NG-air mixture within the cylinder. This could mean longer required mixing times, and consequently, higher local equivalence ratios. To add to this, the cetane number of POMDME is 70, as opposed to approximately 42 for diesel. This means that POMDME will auto ignite easier than diesel. All other parameters from the diesel-NG section will be kept constant, meaning the SOI range of 320 to 330 will be studied at a 5 bar IMEPg, and a PES of 80%. The AHRR profiles for POMDME-NG operation over this range are shown in Figure 3.6.

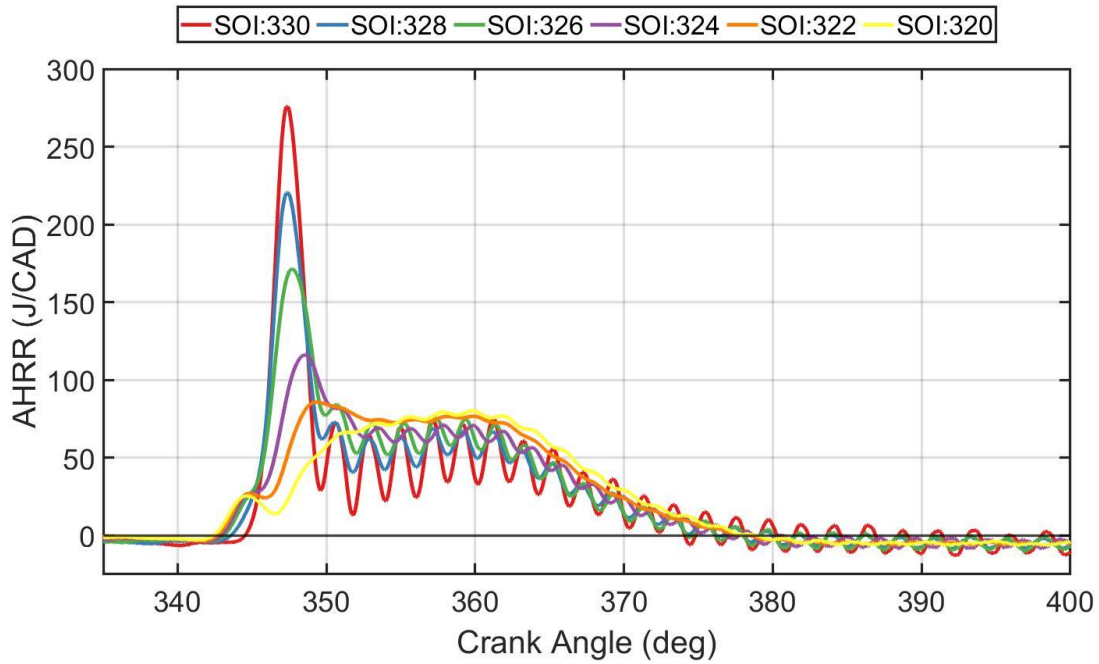


Figure 3.6. AHRR profiles for POMDME/natural gas operation on the 18.5 CR engine platform.

It is observed in Figure 3.6 that the AHRR transformation region occurs within the range of SOIs studied, however there are some differences between POMDME-NG operation and diesel-NG operation (*c.f. Figure 3.2*). First, the peak AHRR values are higher for 330 CAD SOI in POMDME-NG operation than for diesel-NG operation. This could be due to the higher mass of HRF that is required to maintain load and 80% PES, combined with the higher cetane number. These two factors result in more locally stratified regions in the combustion chamber (due to the increased HRF mass) that are primed for ignition (due to the increased cetane number), meaning that more HRF fuel takes part in the initial stage of high temperature heat release. Another observation is that the AHRR transformation is occurring differently from diesel over the range of SOIs studied. To explain this further, a zoomed-in view of the onset of LTHR and onset of HTHR is shown in Figure 3.7.

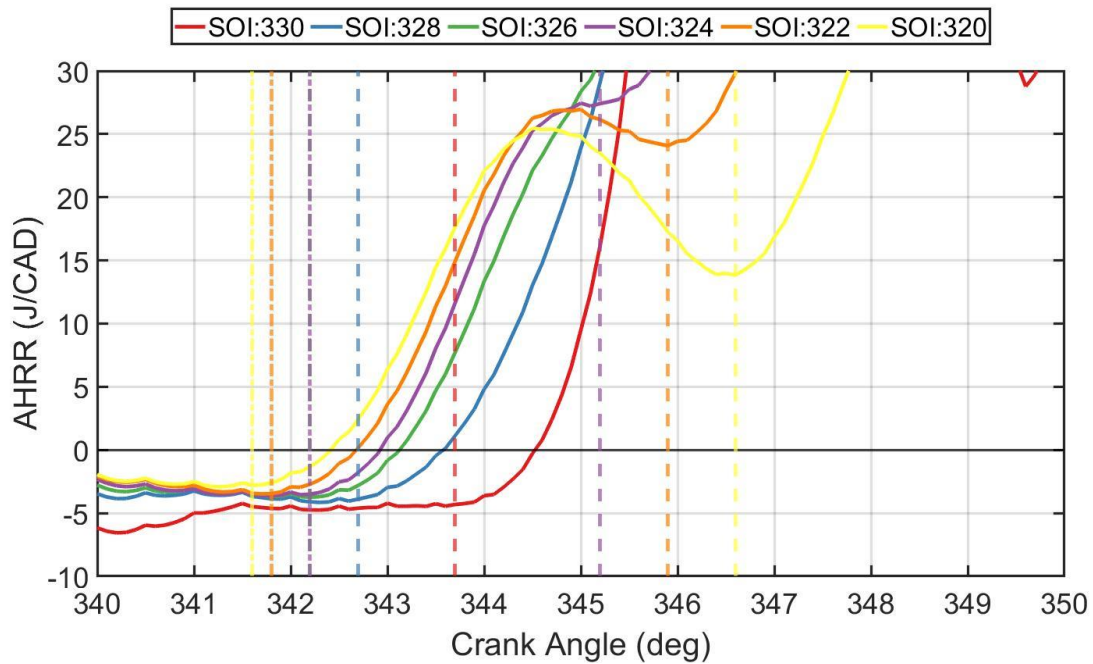


Figure 3.7. LTHR portion of the AHRR profiles for POMDME/natural gas on the 18.5:1 CR engine platform.

The LTHR portion of the AHRR profiles show a stark contrast to those from the diesel/natural gas cases (*c.f.* Figure 3.4). Firstly, the LTHR portions of the curves do not align nearly as well as for diesel operation, with the onsets of LTHR continually advancing with advancing SOI. Secondly, three of the SOIs did not exhibit any LTHR (SOI = 330, SOI = 328, and SOI = 326). All three of these SOIs also had prominent two stage AHRR profiles. This indicates that the AHRR transformation region is occurring over a shorter period of SOIs than for diesel-NG operation. This is likely due to the differences in reactivity that arise from using a higher cetane fuel such as POMDME, as compared to diesel. This also indicates that the local reactivity of the fuel-air mixture is important in influencing the transformation region.

The start of LTHR and start of HTHR CAD locations are given in Table 3.7, below. To ascertain if the values of pressure and temperature align with trends shown in diesel-NG

operation, the pressure and temperature at the start of LTHR and start of HTHR are determined based on the onset locations in Table 3.7. These values are presented in Table 3.8, below.

Table 3.7. Onset of LTHR and onset of HTHR locations for POMDME/natural gas on the 18.5:1 CR engine platform.

SOI (CAD)	330	328	326	324	322	320
Start of LTHR (CAD)	N/A	N/A	N/A	342.2	341.8	341.6
Start of HTHR (CAD)	343.7	342.7	342.2	345.2	345.9	346.6

Table 3.8. Pressure and temperature at the onset of LTHR and HTHR for POMDME/natural gas on the 18.5:1 CR engine platform.

SOI (CAD)	330	328	326	324	322	320
Pressure @ Start of LTHR (bar)	N/A	N/A	N/A	45.26	44.30	43.76
Pressure @ Start of HTHR (CAD)	49.11	46.61	45.42	53.46	55.74	57.75
Temp. @ Start of LTHR	N/A	N/A	N/A	779	775	771.6
Temp @ Start of HTHR	795.5	785.3	781	819	832.4	840.7

For POMDME-NG, the pressure at the start of HTHR is nowhere near as consistent as it is for diesel combustion because HTHR occurs earlier for SOIs of 330 328 and 326 CAD due to their lack of LTHR. For cases that do exhibit LTHR, the pressure at the onset of LTHR happens around the same pressure as for diesel-NG combustion. To understand the differences between POMDME and diesel better, the temperature at the onset of HRHR is compared for each SOI, and is plotted in Figure 3.8, below.

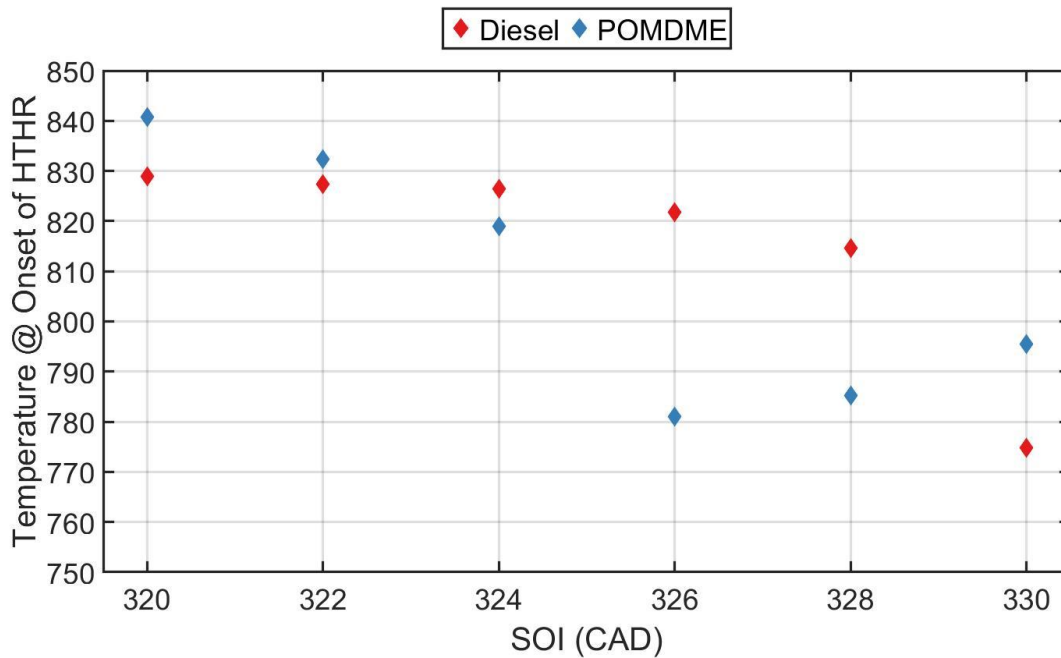


Figure 3.8. Temperature at the onset of HTHR for both diesel and POMDME on an 18:1 CR engine platform.

The rationale behind comparing the onset of HTHR temperatures stems from both diesel and POMDME having complete data sets to compare for the SOIs considered, seeing as POMDME only has three SOIs which exhibit LTHR. From Figure 3.8, for diesel operation, as the SOI is advanced, the temperature of the onset of HTHR increases gradually. For POMDME, on the other hand, the temperature does not increase gradually over the entire range of SOIs; rather the temperature only gradually starts to increase when advancing from SOI = 326 CAD. This could be because of the differences in cetane number of the fuels, with POMDME having a higher cetane number, which could lead to easier autoignition at lower temperatures, and therefore the transformation may not start occurring until a more advanced SOI, such as 326 CAD. This further bolsters the hypothesis presented in Chapter II that the local equivalence ratio is the predominant governing factor in the transformation region, and therefore plays a key role

in  $\text{NO}_x$  reduction, seeing as changing only the fuel's reactivity and LHV had an impact on how wide of an SOI range was needed for the transformation from a two-stage type heat release to a single stage Gaussian heat release to occur.

### 3.6 SUMMARY AND CONCLUSIONS

The transformation region was studied on a single cylinder research engine (SCRE) with a compression ratio of 18.5:1 at the same engine load, percent energy substitution (PES), rail pressure, and injection timing range as studied previously on an engine platform with a 17:1 compression ratio. The goal of the experiments were to not only collect more data within the transformation region using a different engine platform, but also to further attempt to verify the hypothesis that the local reactivity stratification within the combustion chamber is the governing factor of the transformation region. To accomplish this, two different high reactivity fuels (HRF) were studied, including diesel and POMDME, which has a higher reactivity than that of diesel. The following conclusions were made from this study:

- The transformation region for diesel-natural gas combustion on the 18.5:1 compression ratio engine operating at a speed of 1339 RPM occurred over the same SOI range as studied previously on the 17:1 compression ratio engine. This indicates that the transformation region is not engine-specific but is rather dictated by in-cylinder thermodynamic conditions that occur within the combustion chamber.
- The onset of low temperature heat release (LTHR) occurred at higher pressures for the CR = 18.5:1 engine studied as compared to the CR = 17:1 engine previously studied. The temperatures at onset of LTHR were lower for the 18.5:1 CR engine, which could be due to the pressures being higher, leading to a lower required temperature needed for low temperature chemistry to occur.

- By using POMDME as the HRF, the effective SOI range over which the transformation region occurred diminished in size. Diesel operation showed the transformation occurring over the entire SOI= 320 to 330 range, whereas POMDME only showed significant transformation to occur from SOI = 320 to 326 CAD.
- The use of natural gas as opposed to methane did not show significant impacts on the transformation region phenomenon.
- When comparing diesel and POMDME operation, the pressures and temperatures at the onset of LTHR (for cases that had LTHR) were comparable, meaning that the pressure and temperature need not be the main governing factors in the transformation process. This aligns conclusions from Chapter II.

IV.  
COMBUSTION ANALYSIS FOR DUAL FUEL STRATEGIES APPLIED TO REDUCE  
ENGINE OUT HC, CO, AND NO<sub>x</sub> EMISSIONS USING DIESEL-NATURAL GAS AND  
POMDME-NATURAL GAS

#### 4.1 ABSTRACT

Dual fuel low temperature combustion (DFLTC) has been studied as a possible solution to the emissions problems that plague conventional diesel engines, specifically in alleviating the oxides of nitrogen (NO<sub>x</sub>) - soot tradeoff that is present in diesel combustion. At low engine loads DFLTC exhibits challenges in combustion stability, which can manifest as high engine-out carbon monoxide (CO) and unburned hydrocarbon (UHC) emissions. The present work compares CO, UHC, and combustion benefits from both diesel and poly-oxy methylene dimethyl ether (POMDME) as high reactivity fuels to ignite natural gas. The experimental procedure involved the completion of six steps: 1) A start of injection (SOI1) timing sweep to fix an SOI1 based on low emissions values, 2) Introduce a second injection (SOI2), and sweep SOI2 to determine an optimal SOI2 for low emissions, 3) A percent energy substitution (PES) sweep to determine an optimal PES, 4) An injection ratio sweep, wherein the ratio of the commanded injection duration of SOI1 to SOI2 is swept, 5) A rail pressure sweep to determine an optimal rail pressure for low emissions, and finally 6) An intake boost pressure sweep to reduce CO emissions. This experimental procedure was performed on a 1.8-liter single cylinder research engine (SCRE) platform operating at a speed of 1339 rev/min. Not-to-exceed limits for indicated specific NO<sub>x</sub> (ISNO<sub>x</sub>) emissions, maximum pressure rise rate (MPRR), and coefficient of

variation of indicated mean effective pressure ( $COV_{IMEP}$ ) were set to 1 g/kWh, 10 bar/CAD, and 10%, respectively. Indicated specific carbon monoxide (ISCO) and indicated specific unburned hydrocarbons (ISHC) emissions were shown to decrease for both fueling combinations when the experimental procedure was applied. The present work includes a detailed comparative analysis of dual fuel LTC with both diesel and POMDME, leveraging apparent heat release rate (AHRR) histories and other combustion metrics to explain the observed emissions trends.

## 4.2 INTRODUCTION

Internal combustion engines (ICE) have been a predominant factor in the growth and interconnectivity of society [77] ever since their introduction nearly 145 years ago [78]. ICEs are integral to our everyday life, with over 99% of all global transport powered by ICEs [79], thus they will remain essential for the movement of people and goods for the coming decades [80]. While light duty ICEs may have some form of hybridization or electrification in the near future, heavy duty vehicles (mainly Class 7 and 8 trucks) will be powered using ICEs. Heavy duty vehicles will see a continual increase in vehicle miles traveled according to the US Energy Information Administration's (EIA) latest Annual Energy Outlook [81], with heavy duty trucks estimated to travel approximately 500 billion vehicle miles by 2050. An increase in the vehicle miles traveled inevitably leads to more emissions associated with combustion, mainly carbon dioxide ( $CO_2$ ), oxides of nitrogen ( $NO_x$ ), carbon monoxide (CO), and unburned hydrocarbons (UHC). Emissions, which are harmful to the environment and to public health, are heavily regulated globally. For example, the California Air Resources Board recently implementing amendments to Title 13 of the California Code of Regulations [82], which state that the  $NO_x$  limits for heavy duty diesel engines cannot exceed 0.05 grams per brake horsepower-hour (g/bhp-hr) for model years 2024-2026. The  $NO_x$  limit is further restricted to 0.02 g/bhp-hr for

any 2027 model year and newer vehicles. UHCs and CO emissions are also restricted to 0.14 and 15.5 g/bhp-hr, respectively. To meet the needs of these stringent regulations, advanced combustion engine strategies will need to be researched and implemented. Strategies such as dual-fuel low temperature combustion (DFLTC) and reactivity-controlled compression ignition (RCCI) are potential pathways to maintain compliance with emissions regulations.

The concept of using two fuels at the same time in an ICE is not inherently novel, with studies from Boyer [83] and Elliot et al. [84] showcasing it as early as the 1950s. DFLTC and RCCI take advantage of using two fuels, a low-reactivity fuel (LRF) which has a high resistance to auto-ignition (low cetane number) and a high-reactivity fuel (HRF), which has a high cetane number to achieve low engine-out  $\text{NO}_x$  and soot emissions. DFLTC and RCCI are not the only LTC concepts, with homogenous charge compression ignition (HCCI) [85,86] and gasoline compression ignition (GCI) [59,60] being two examples of other concepts that have been considered due to their emissions benefits. An advantage that DFLTC and RCCI have over these other strategies include the ability to control combustion phasing through the inherent reactivity stratification levels achieved while requiring minimal modifications to existing compression ignition engines. Another benefit is the wide variety of LRF and HRF fuels that can be used together, including renewable fuels; fuel combinations such as diesel/ammonia [87,88], diesel/natural gas (NG) [36,42,89,90], diesel/propane [91,92], diesel/methanol [93], diesel/gasoline [93,94], and primary reference fuels (n-heptane and isooctane) [38,95] have been used.

The low  $\text{NO}_x$  and soot emissions with DFLTC are accompanied by higher CO and UHC as well as higher cycle to cycle variations in the combustion process [96]. One strategy that could be implemented to address these challenges is to use multiple HRF injections instead of

single HRF injection. Carlucci et al. [97] used a biodiesel-syngas fuel combination and split the pilot injection into two separate injections on a 510.1 cc displacement engine. They concluded that a second injection that occurs 10 to 30 crank angle degrees (CAD) after the first injection, with the first injection occurring within 35 to 20 degrees before compression top dead center (dBTDC) can ensure highest fuel conversion efficiencies for biodiesel-syngas dual fuel combustion. Yadav et al. [98] used diesel and butanol on a three-cylinder 1.5 L turbocharged engine at an engine speed of 1800 RPM. It was found that by introducing a post injection, the brake thermal efficiency increased as compared to a single injection case at the same load, and the smoke measurements were also lower. A post injection quantity of 1.5 mg/cycle, with the injection occurring 9.7 CAD after the main injection were found to be optimal. Bartolucci et al. [99] numerically investigated the benefits that using a split injection strategy with diesel and natural gas could provide at a 5 bar brake mean effective pressure (BMEP) case on a 1.8 L single cylinder research engine (SCRE) operating at 1500 RPM. After validating an early injection timing of 310 CAD with experimental results, the effects of using multiple injections and different rail pressures were studied. The second injection was added 65 degrees after the first injection (i.e., after TDC). Adding in the second injection without increasing the rail pressure showed a higher amount of CO and UHC than for the single injection case alone, and this was corroborated by experimental results. However, increasing the rail pressure from 500 bar to 1200 bar significantly decreased the CO and HC, while also maintaining a NO<sub>x</sub> value less than 1 gram per kilowatt hour (g/kW-hr), because of a greater number of observed ignition locations which results in faster methane reaction rates. Hariharan et al. [100] specifically targeted the reduction in UHC and CO emissions on a 1.8-liter single cylinder engine operating at 1500 RPM through the use of a split injection strategy. Parameters such as the second injection duration, the percent

energy substitution (PES), and the rail pressure were studied. Close-coupled injections (injections events whose starts were within 15 CAD of one another) showed advanced combustion phasing, as well as increased combustion efficiency. The NO<sub>x</sub> emissions with close-coupled injections were six times as high as the baseline diesel-methane dual fuel point. It was also shown that rail pressure had a significant impact on the efficiency emissions tradeoffs, and the indicated fuel conversion efficiency increased with rail pressure, with a maximum value of ~50% being observed.

Split injection may be a possible solution to DFLTC's cyclic variation problem at low loads, however there is still the issue of possible soot formation, or particulate matter (PM), with near-TDC second injection of diesel. The use of oxymethylene dimethyl ether (OME) fuel blends has become a growing area of research interest to mitigate PM emissions [16-21,101]. OME fuels can help reduce PM because they are an oxygenated fuel, and they lack carbon-carbon bonds [19]. García et al. [20] numerically showed the benefits of using OME with dual fuel combustion, with gasoline as the LRF, on a series-hybrid setup using a 0-D vehicle model. The well-to-wheel CO<sub>2</sub> analysis showed that the use of an optimized series-hybrid architecture along with OME-gasoline dual fuel combustion improves upon the current commercial truck by 25%. Garcia et al. [21] demonstrated the use of OME fuels in a four-cylinder 1.6 L engine. The engine was fueled with three different fuel blends, each with a different amount of OME fuel and Fischer-Tropsch diesel on a volume basis; three different speed/load points were considered for the study. It was found that the fuel blends with higher OME amounts reduced PM by at least 5 mg/kWhr, as compared to diesel when using baseline engine calibrations. The fuel consumption for these higher OME fuel blends increased due to the reduced lower heating value (LHV) of the blend accompanying higher percentages of OME fuels in the blends. NO<sub>x</sub> emissions could not be

directly correlated with the decreased soot, seeing as they could either be lower or higher than the baseline diesel reference depending on the engine load, however NO<sub>x</sub> could be reduced with respect to the diesel baseline (at the expense of PM, UHC, and CO emissions) if the engine calibration were optimized. Overall, the well-to-wheel brake specific CO<sub>2</sub> were reduced for the fuel blend that was entirely composed of OME and Fischer-Tropsch diesel. Tong et al. [101] successfully demonstrated the use of polyoxymethylene dimethyl ether (POMDME) in a dual fuel RCCI configuration with gasoline as the LRF. The experiments were conducted on a modified six-cylinder heavy duty diesel engine, where one of the six cylinders was isolated from the rest for the purposes of testing. Low PM values were obtained for the POMDME-gasoline combustion regardless of the POMDME injection timing and the amount of POMDME to gasoline fuel proportion. A slight penalty in NO<sub>x</sub> emissions was observed compared to diesel-gasoline operation. Stoichiometric equivalence ratios were also deemed to be achievable with the POMDME dual fuel method, meaning the use of three-way catalysts could be explored in the future.

The present work leverages the **Spray Targeted Reactivity Stratification (STARS)** concept introduced by Narayanan et al. [102] for DFLTC along with other control parameters to reduce UHC and CO emissions and to improve efficiency and combustion stability. The STARS concept utilizes a split injection strategy to minimize the cycle-to-cycle variations that are inherent in dual fuel combustion, by allowing for a more distributed ignition within the cylinder (due to higher stratification levels) which lead to faster burn rates, higher combustion efficiencies, and lower UHC and CO emissions. The present study builds upon previous research by Hariharan et al. [103] which studied pathways for reducing UHC and CO emissions using both diesel-natural gas as well as POMDME-natural gas DFLTC, which showed that by

strategically vary six control parameters, UHC and CO reductions of ~85% and ~92%, respectively, can be achieved

### 4.3 EXPERIMENTAL SETUP

The engine used for the experiments is an SCRE platform, based on a PACCAR MX-11 multi-cylinder engine. The engine specifications can be found in Table 4.1, and a detailed schematic of the experimental setup is presented in Figure 4.1. The engine was coupled to a 393 hp, AC dynamometer, with a Dyne Systems InterLok (IL5) used to control the engine speed. The load was controlled via the fueling rates of HRF and LRF. A pressure regulator was used to meter the LRF flowrate (in this case, natural gas), with a Micromotion Coriolis flow meter (Model CMFS015M319N0A2ECZZ) being used to measure the fuel flow rate. The HRF (diesel or POMDME) was injected directly into the cylinder using the stock solenoid injector, which was connected to a common rail injection system capable of achieving up to 2500 bar rail pressure. Diesel injection timing, duration, and rail pressure were controlled via a National Instruments Direct injector Control and Measurement (DCM) device interfacing with Vieletech Calibration Viewer software. The HRF flowrate was measured with a Micromotion Coriolis flow meter (Model CMFS010M319N0A2ECZZ). Pressurized air was supplied to the intake using an external air compressor, which was conditioned using a heatless desiccant dryer before entering the engine. The air flow rate was measured using a sonic (choked) nozzle from FlowMaxx (Model SN16-SA-345). In cylinder pressure was measured using a Kistler model 6124A pressure sensor, with a Kistler 5018 type charge amplifier used to amplify the signal. A 0.1 CAD resolution BEI shaft encoder was used to phase the in-cylinder pressure trace. Steady state intake pressure ( $P_{\text{intake}}$ ) was measured with a Setra model 206 pressure transducer, and a Kistler 4624A pressure transducer was used to measure crank-angle resolved intake pressure. Since in-cylinder

pressure measurements are taken with a piezo-electric pressure transducer, it is important to properly reference, or peg, each engine cycle's cylinder pressure trace using the crank-angle resolved intake pressure. Table 4.2 shows more information on the accuracies associated with the sensors used in this engine setup.

Table 4.1. General engine specifications.

Engine type	Single cylinder, four stroke
Bore (mm)	123
Stroke (mm)	152
Con. Rod Length (mm)	244.5
Displaced Volume (L)	1.806
Nozzle dia (mm)/# holes	0.1905/7
Compression ratio	18.5
Intake Valve Timings	IVO – 710 CAD, IVC – 210 CAD
Exhaust Valve Timings	EVO – 490 CAD, EVC – 5 CAD
Diesel Injection System	Delphi DFP5 common rail
Operating Speed (rpm)	1339

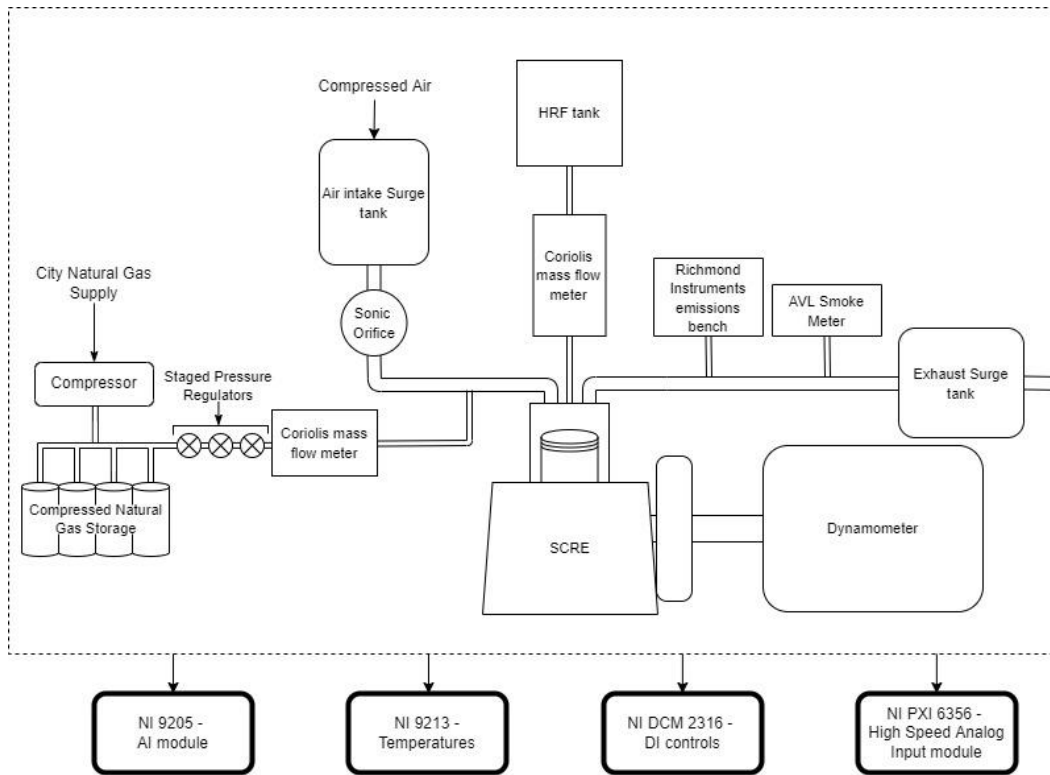


Figure 4.1. Detailed experimental setup.

Table 4.2. Details of experimental sensors and their accuracies.

Data Type	Make/Model	Type	Unit	Accuracy
Temperature (intake, exhaust, etc.)	Omega	K-type	°C	±0.75% of reading
Air mass flow	Flowmaxx	Sonic orifice	kg/h	±0.25% of reading
Diesel mass flow	Micro Motion	Coriolis	kg/h	0.1% of reading
Natural Gas mass flow	Micro Motion	Coriolis	kg/h	0.25% of reading
Smoke	AVL 415S	Filter	FSN	0.001 of reading
NOx and NO	Rosemount Analytical	CLD	ppm	+/-1% of full scale
THC	Rosemount Analytical	HFID	ppm	+/-1% of full scale
CO	Rosemount Analytical	NDIR	%	+/-1% of full scale
CO2	Rosemount Analytical	NDIR	%	+/-1% of full scale
O2	Rosemount Analytical	NDIR	%	<1% of full scale
Cylinder pressure	Kistler 6124A	Piezoelectric	bar	±0.3% of reading
Dynamic pressures (intake, exhaust)	Kistler 4049A	Piezoresistive	Bar	±0.1% of full scale
Steady state pressures (intake, exhaust, etc.)	Setra Model 206	Capacitance	psig	±0.13% of full scale

As mentioned before, two different HRFs were used in this work: diesel, and POMDME. POMDME is typically a combination of six different OMEs. The chemical formula for OME is  $\text{CH}_3(-\text{O}-\text{CH}_2)_n-\text{O}-\text{CH}_3$ , where  $n$  represents the number of (O-CH<sub>2</sub>) portions of the chain length. The composition of the fuel used in this study is: 0.02% OME1, 0.12% OME2, 47.76% OME3, 29.58% OME4, 16.38% OME5, and 5.37% OME6. More details of the fuel properties can be found in Table 4.3.

Table 4.3. Fuel properties.

	<b>Diesel</b>	<b>POMDME</b>	<b>City Natural Gas</b>
Octane Number/Cetane Number	Cetane = ~42	Cetane = 70	Octane = ~110-120
Lower Heating Value (MJ/kg)	43.4	19.204	49.229
Oxygen (m/m) %	0	47	0
Hydrogen/Carbon Ratio	1.8	2.35	3.8655
Oxygen/Carbon Ratio	0	0.83	0.0029
Nitrogen/Carbon Ratio	0	0	0.0076

In the current work all references to crank angles use the absolute crank angle convention, meaning that 0° refers to gas exchange TDC, and 360° refers to compression TDC. For each operating point recorded, 1000 consecutive engine cycles were collected. These data were then post-processed using an in-house MATLAB code.

#### 4.4 EXPERIMENTAL PROCEDURE

The experiments performed for this study were carried out in accordance with the flowchart shown in Figure 4.2. This flowchart was designed as one potential pathway towards reducing UHC and CO emissions at an indicated mean effective pressure (IMEP) of 5 bar and an

engine speed of 1339 rev/min. Equation 4.1 shows the IMEP calculation, where  $P_i$  is indicated power in kW,  $V_d$  is displaced volume in liters, and  $N$  is engine speed in revolutions per second. The not-to-exceed limits for the entire set of experiments were:  $MPRR < 10$  bar/CAD, coefficient of variation of IMEP ( $COV_{IMEP} < 10\%$ ), and indicated specific  $NO_x$  ( $ISNO_x < 1$  g/kWhr. Equation 4.2 shows the  $COV_{IMEP}$  calculation, where  $\sigma$  is the standard deviation of IMEP, and  $\mu$  is the mean of the IMEP over the 1000 consecutive cycles of recorded data. It is important to note that these experiments were completed without the use of exhaust gas recirculation (EGR), which is typically relied on to reduce  $NO_x$  emissions.

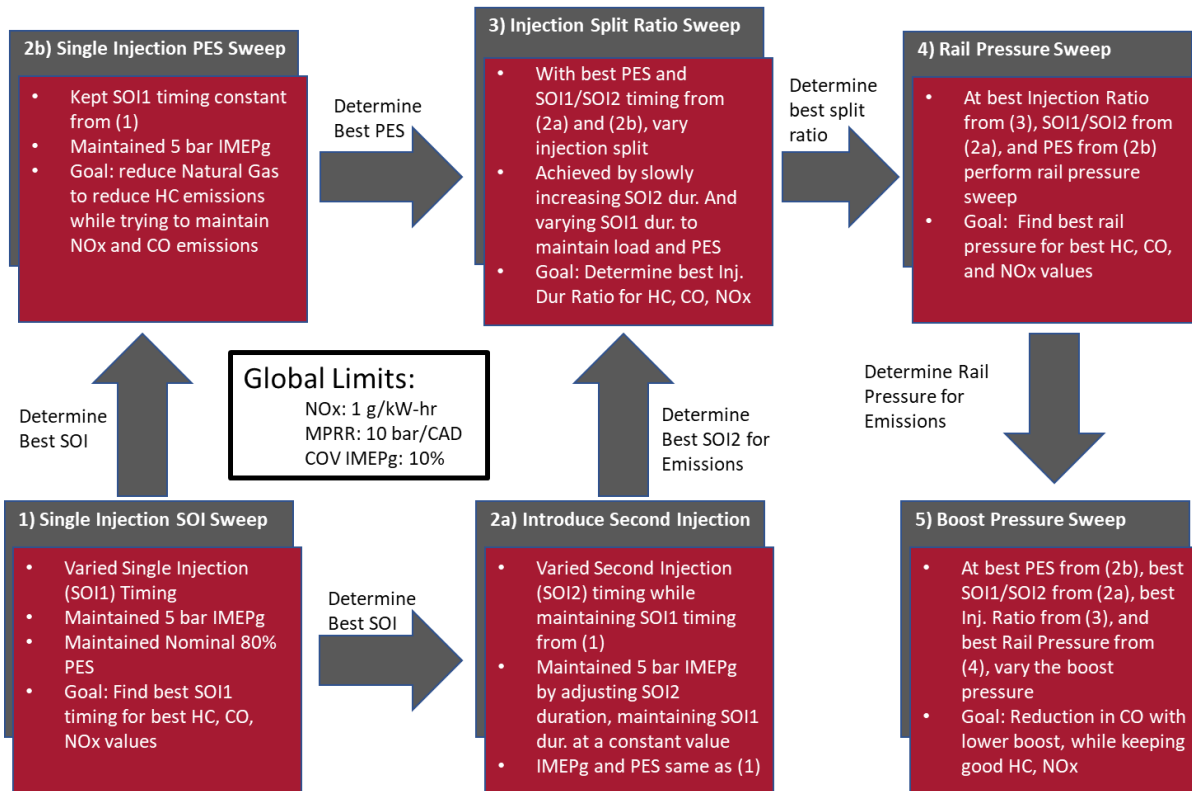


Figure 4.2. Detailed experimental procedure.

$$IMEP = \frac{2P_i 10^3}{V_d * N} \quad (4.1)$$

$$COV_{IMEP} = \frac{100\sigma}{\mu} \quad (4.2)$$

Step 1 in the experimental procedure is to perform a start of injection (SOI1) timing sweep at a constant percent energy substitution (PES) of natural gas and a constant  $P_{intake}$  of 1.5 bar. The PES is calculated using Equation 4.3, where  $\dot{m}$  is defined as the mass flowrate, and both  $\dot{m}$  and LHV have subscripts denoting which fuel is being considered. The value of PES is used as a metric for the proportion of the fuel energy input into the engine originating from the LRF, and therefore, a higher number for PES means higher LRF substitution rates. The optimal operating point for the SOI sweep is then determined based on the criterion of ultra-low  $NO_x$  emissions along with reasonable UHC and CO values. The goal for SOI sweep was to prioritize  $NO_x$  reduction so that the remainder of the tests could be leveraged to reduce UHC and CO while keeping  $NO_x$  below the self-imposed 1 g/kWhr limit.

$$PES = \frac{\dot{m}_{LRF}LHV_{LRF}}{\dot{m}_{LRF}LHV_{LRF} + \dot{m}_{HRF}LHV_{HRF}} \quad (4.3)$$

Step 2 is divided into two parts; part (a) consists of introducing a second injection (SOI2), following the STARS idea, and part (b) consists of a PES sweep. In part (a), the SOI from step 1 (henceforth known as SOI1) was kept constant. The injection duration of SOI1 was reduced until the  $COV_{IMEP}$  limit of 10% was reached, at which point a second injection (SOI2) was added to stabilize the combustion. This injection duration for SOI1 was then kept constant for the remainder of part (a) testing, as the SOI2 timing was changed. Load was maintained by changing only the injection duration of SOI2 at each injection timing, and the PES was maintained at 80%. Part (b) only utilized the best single injection timing from Step 1, and the effects of changing PES were observed. Both parts (a) and (b) of step two were completed parallelly, and both were combined to choose the operating point that would be considered for the remainder of the testing

procedure based on optimal UHC and CO emissions while maintaining reasonable NO<sub>x</sub> emissions.

Step 3, as mentioned previously, used the SOI2 timing from step 2(a) and the PES value from step 2(b) that were determined to be the best operating points for those conditions and changed the injection split ratio. In the present work, the injection split ratio is defined as the commanded injection duration of SOI1 divided by the commanded injection duration of SOI2. While it would be more appropriate to determine the actual injection duration from needle lift data, the injector could not be instrumented for needle lift data acquisition. As with previous steps, the optimal point for these operating conditions was determined based on emissions values. In step 4, the optimal rail pressure (again, based on emissions) was chosen before performing the boost pressure sweep in step 5.

The apparent heat release rate (AHRR) was calculated using Equation 4.4, in which  $\gamma$  is the ratio of specific heats,  $P$  the crank resolved cylinder pressure,  $V$  the crank resolved volume, and  $\theta$  the instantaneous crank angle. To find  $\gamma$  at each crank angle, an in-house chemical equilibrium code was used to determine composition and NASA polynomials [104] were used for determining specific heats as functions of temperature.

$$AHRR = \frac{\gamma}{\gamma-1} P \frac{dV}{d\theta} + \frac{1}{\gamma-1} V \frac{dP}{d\theta} \quad (4.4)$$

The cumulative heat release is then calculated by integrating the AHRR with respect to  $\theta$ , and the start of combustion (CA5), combustion phasing (CA50) and end of combustion (CA90) are determined by determining the CAD locations where the cumulative heat release achieves 5%, 50%, and 90% of the maximum cumulative heat release. In cylinder temperature is also calculated on a crank angle basis using the Redlich-Kwong real gas equation of state [44]. Using

these calculated in-cylinder temperatures, CAD-based residence times for which the in-cylinder gases remain above a certain temperature can be determined. Combustion efficiency ( $\eta_{Comb}$ ) and indicated fuel conversion efficiency (IFCE) are also calculated based on definitions presented by Heywood [1] and are provided in Equations 4.5 and 4.6, respectively.

$$\eta_{Comb}(\%) = 100 - 100 * \left[ \frac{(y_{UHC}LHV_{UHC} + y_{CO}LHV_{CO} + y_{H_2}LHV_{H_2}) * (\dot{m}_{air} + \dot{m}_{LRF} + \dot{m}_{HRF})}{\dot{m}_{LRF}LHV_{LRF} + \dot{m}_{HRF}LHV_{HRF}} \right] \quad (4.5)$$

$$IFCE(\%) = \frac{\int_{180\text{ CAD}}^{540\text{ CAD}} PdV}{\dot{m}_{LRF}LHV_{LRF} + \dot{m}_{HRF}LHV_{HRF}} \quad (4.6)$$

Finally, the MPRR is defined as the maximum of the first derivative of the ensemble-averaged cylinder pressure with respect to CAD.

## 4.5 SUMMARY AND CONCLUSIONS

This section is divided into each individual step of the experimental procedure that is described in Figure 4.2. For each step, both diesel-natural gas and POMDME-natural gas operation are discussed.

### 4.5.1 STEP 1: SOI SWEEP

A wide SOI range, with SOIs as advanced as 310 CAD and as late as 355 CAD, was considered for both fuel combinations. Injection timings earlier than 310 CAD resulted in  $COV_{IEMP}$  values greater than the 10% limit. Figure 4.3 shows the cylinder pressure curves, AHRR profiles, and emissions for both diesel-NG and POMDME/NG operation. As the SOI is advanced from 355 to 330 CAD for diesel-NG, the location of peak AHRR advances and  $ISNO_x$  increases, while ISHC decreases. The same phenomenon occurred with POMDME/NG. For both fuels, as well, the peak cylinder pressure increases until the MPRR limit is reached, at which point the SOI1 must be moved earlier. After this movement to avoid the MPRR limited region,

further advancement of SOI1 results in lower peak cylinder pressures. Further advancement of SOI1 to 310 CAD also moves the location of peak AHRR later. Correspondingly, the ISNO<sub>x</sub> decreases dramatically as the SOI is advanced toward 310 CAD. This phenomenon has been seen previously in various studies [30,105,106]. There is also a change in the shape of the AHRR profile, which has been discussed in previous literature [107]. The lower ISNO<sub>x</sub> at earlier SOIs is possibly due to the increased amount of time for fuel-air mixing, meaning there are likely fewer regions in the combustion chamber for which the equivalence ratio ( $\phi$ ) is near stoichiometric, leading to lower local temperatures. The avoidance of high temperatures is key to the reduction of NO<sub>x</sub>, since the main mechanism for NO<sub>x</sub> formation (the Zel'dovich mechanism) requires temperatures  $> 1900$  K [46]. It is important to note, though, that the Zel'dovich mechanism is not the only mechanism for NO formation, with prompt NO and fuel bound NO formation being other pathways. However, the Zel'dovich mechanism is the overwhelmingly predominant mechanism in combustion, and is it is therefore why decreased combustion temperatures are desired.

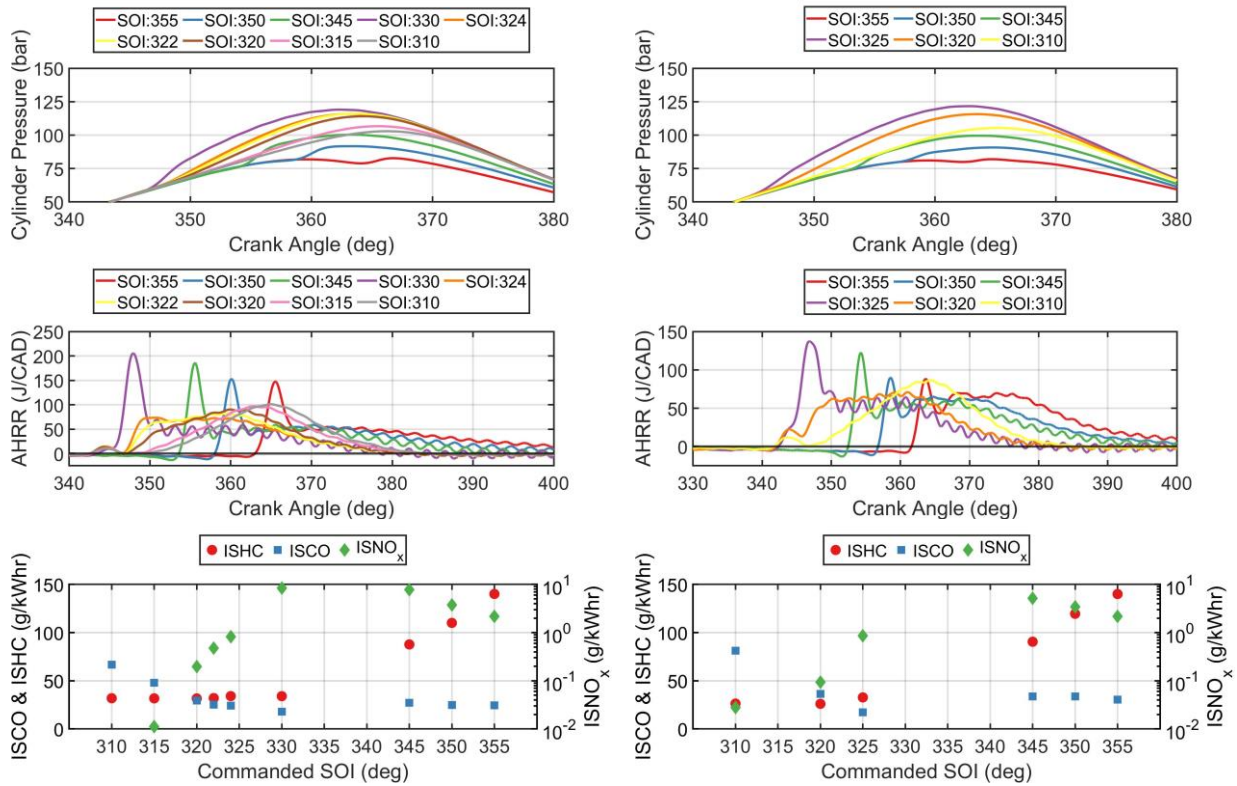


Figure 4.3. Cylinder pressure (top), AHRR (middle), and emissions values (bottom) for diesel-NG (left) and POMDME-NG (right).

The SOI advancement from 330 to 310 CAD increases ISCO emissions, but the ISHC emissions stay consistent. To explain this, the  $COV_{IMEP}$  is presented in Figure 4.4, along with MPRR for both fuel combinations. At the very advanced SOIs, the  $COV_{IMEP}$  for diesel-NG was 6.5%, and for POMDME-NG it was 6.2%. This indicates that the combustion is very unstable at these conditions due to high cycle to cycle variability. This variability could mean that the fuel is being partially oxidized into CO, but not being fully oxidized into CO<sub>2</sub>, seeing as there are more cycles of partial combustion at these SOIs than for other SOIs. This would explain the leveling off of ISHC, as well, since further advancement of the SOI timing may not lead to more distributed ignition, meaning the amount of fuel that remains unburned, on a global basis, remains consistent.

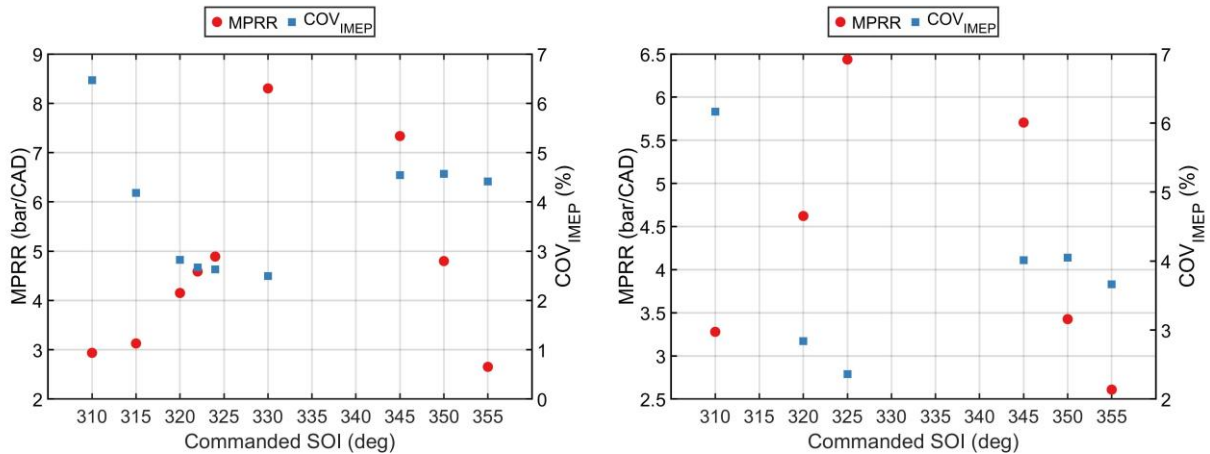


Figure 4.4. MPRR and COV<sub>IMEP</sub> values for diesel/natural gas (left) and POMDME/natural gas (right).

The SOI<sub>1</sub>s of 310 CAD and 320 CAD were chosen for subsequent steps for diesel-NG and POMDME-NG operation, respectively. The 310 CAD SOI for diesel-NG was chosen due to virtually zero ISNO<sub>x</sub> emissions (unmeasurable by emissions bench, and hence not represented on the log scale for ISNO<sub>x</sub> in Figure 4.3 for diesel). When performing the POMDME-NG experiments, the 320 CAD SOI was chosen due to its higher IFCE compared to the 310 SOI (39.8% vs. 38.2%), which offered a better starting point for performing the remainder of the experiments.

#### 4.5.2 STEP 2(a): SPLIT INJECTION (STARS) SWEEP

The goal of STARS is to improve the combustion stability (lower COV<sub>IMEP</sub>) using multiple injections. This will, in theory, show an improvement in ISCO emissions and possibly also ISHC emissions. Figure 4.5 shows COV<sub>IMEP</sub> along with the MPRR for both fuel

combinations at each SOI2 value.

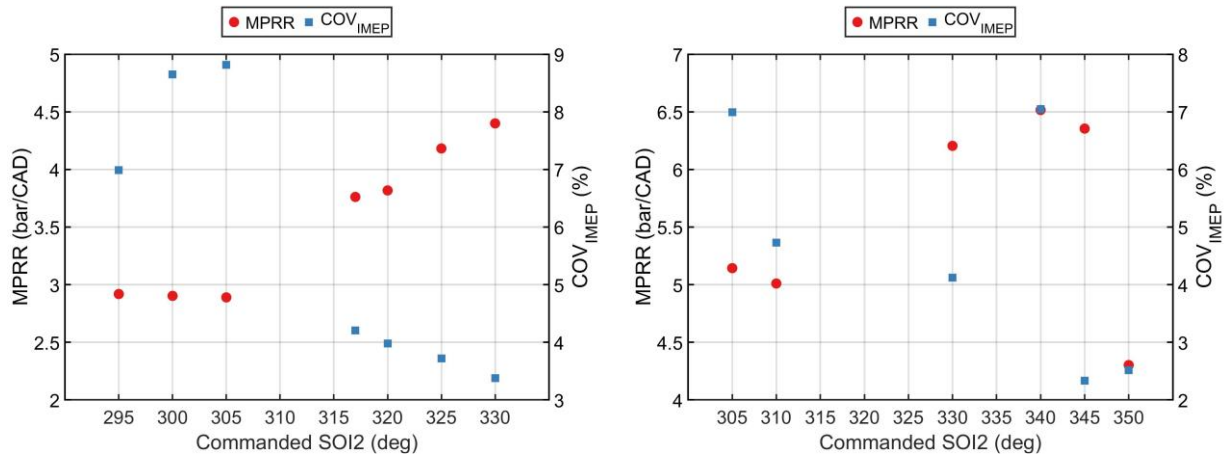


Figure 4.5. MPRR and COV<sub>IMEP</sub> for the SOI2 sweep for diesel/NG (left) and POMDME/NG (right).

For diesel-NG dual fuel LTC, which had a COV<sub>IMEP</sub> of 6.5% for the baseline single injection case, introducing a second injection after the 310 CAD SOI from step 1 reduced the COV<sub>IMEP</sub>, whereas SOI2s earlier than 310 CAD increased the COV<sub>IMEP</sub>. The COV<sub>IMEP</sub> results for POMDME-NG combustion were less conclusive, seeing as injections that occurred before or after the fixed 320 CAD SOI from step 1 produced both higher and lower COV<sub>IMEP</sub> values compared to the 6.2% value. To determine what impact this has on the combustion, the cylinder pressure, AHRR, and emissions results for each SOI2 are presented in Figure 4.6.

Injections occurring after the fixed 310 CAD injection timing have lower ISCO values than those that occur before the 310 CAD timing, for diesel-NG combustion. The ISCO values for all SOI2s considered in the diesel-NG sweep were lower than the ISCO for the single injection baseline from step 1, which had an ISCO value of 66.7 g/kWhr. A similar trend is observed for POMDME-NG, where the ISCO values for each SOI2 timing are less than the ISCO value for the baseline single injection of 320 CAD considered from step 1. Similarly, the

ISNO<sub>x</sub> trends are also similar to the SOI1 trends seen in step 1, which is likely due to the increased mixing times available for early injection timings, thereby allowing for lower local equivalence ratios and therefore lower local temperatures.

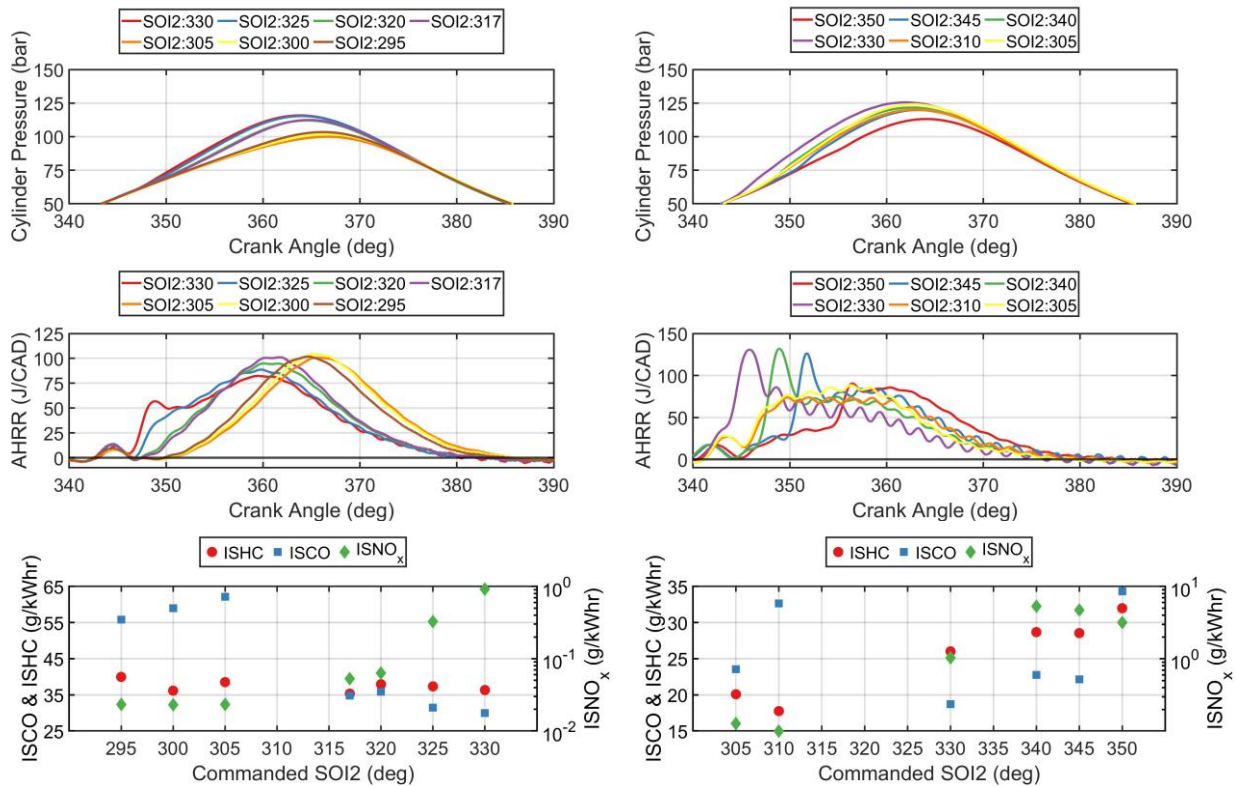


Figure 4.6. Cylinder pressure (top), AHRR (middle), and emissions (bottom) results for SOI2 sweep at each SOI2 timing for both diesel-NG (left) and POMDME-NG (right).

The AHRR curves for diesel-NG show that changing the location of the second injection has an impact on the location of the peak AHRR, with SOI2 timings of 295, 300, and 305 (all of which occur before the fixed 310 injection timing from step 1) having the latest locations of peak AHRR with respect to TDC of 364.6, 365.2, and 365.5 CAD, respectively. Once the SOI2 occurs after the 310 fixed injection timing, the peak AHRR location shifts to near TDC for SOI2 timings of 317, 320, 325, and 330 CAD. A similar phenomenon occurs with POMDME-NGs, with the exception that the peak AHRR location starts to move closer to TDC as the SOI2

location is moved closer to TDC. To observe these trends better, the CA5, CA50, and CA90 locations at each SOI2 are plotted for both fuel combinations in Figure 4.7.

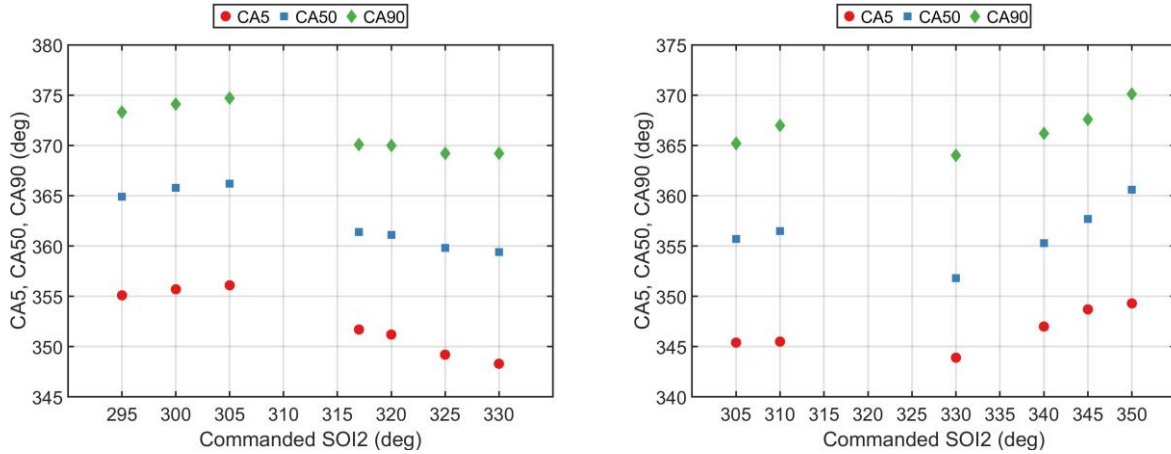


Figure 4.7. CA5, CA50, and C90 for diesel/NG (left) and POMDME natural gas (right) at each SOI2 injection timing.

The location of CA5, CA50, and CA90 occurs earlier in the cycle as soon as SOI2 occurs after SOI1 for diesel-NG; for POMDME-NG, there is a similar trend for SOI2 = 330. However, when the SOI2 was commanded later, the CA5, CA50, and CA90 values occur later in the cycle. This can be attributed to the time allowed for fuel-air mixing, as SOI2 timings that occur before SOI1 will inevitably have more time for mixing than for later SOI2s, which leads to more homogenization of the fuel/air mixture.

Another interesting observation is how the low temperature heat release (LTHR) portion of the AHRR profile manifests for both diesel-NG, and POMDME-NG combustion. Figure 4.8 shows this LTHR region for both fuel combinations. There is a stark contrast within the LTHR region between diesel and POMDME. Diesel-NG has a consistent LTHR profile, with peak LTHR values that never exceeds 15 J/CAD; POMDME-NG, on the other hand, has an erratic

LTHR profile, with the SOI2 timings that occur before the fixed 320 SOI having higher LTHR than for SOI2s that occur after the fixed 320 injection timing.

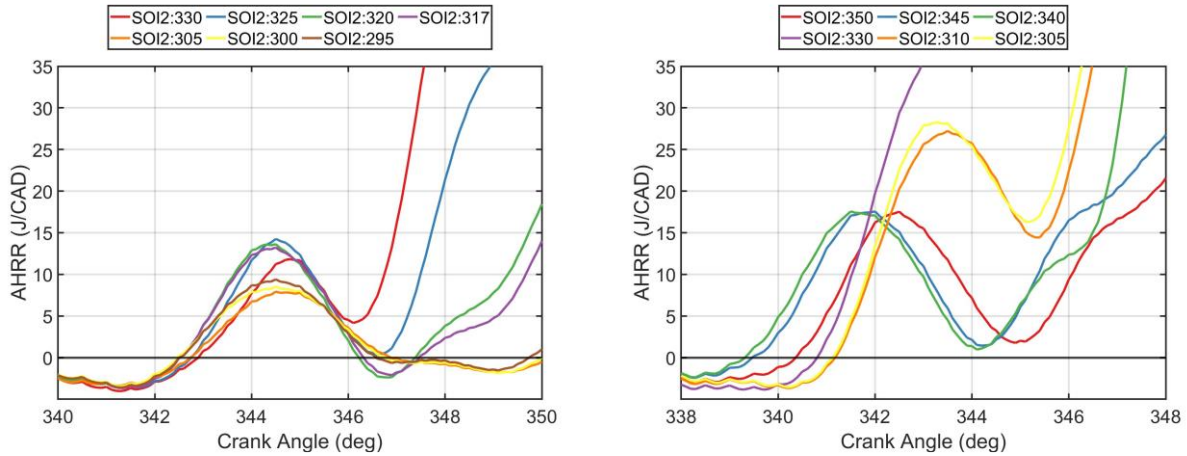


Figure 4.8. LTHR portion of the AHRR curve for diesel/NG (left) and POMDME/natural gas (right).

The differences in LTHR profiles for both fueling combinations could be because of a few different parameters. First, the timing of SOI1 could impact LTHR, with diesel having a fixed SOI1 timing of 310 CAD and POMDME having a fixed SOI1 timing of 320 CAD. This means that diesel-NG combustion will have at least 10 CAD more time for mixing than for POMDME. In addition to this effect, POMDME requires much higher fueling rates compared to diesel, as evident from Figure 4.9, due to the decreased LHV of POMDME. This likely leads to higher local stratification levels for POMDME than for diesel simply due to the increased mass of POMDME available locally.

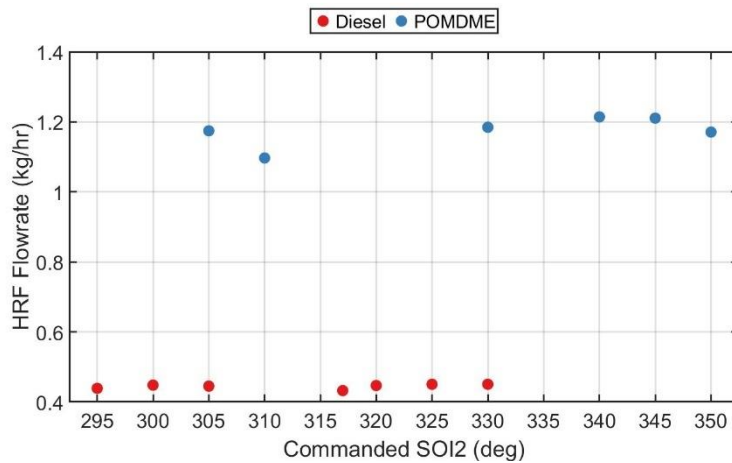


Figure 4.9. HRF flow rates for each SOI2.

It is also noteworthy to compare the differences between the LTHR curves for SOI2s that occur before their respective SOI1s for both diesel and POMDME. In Figure 4.8, as mentioned previously, the LTHR seems consistently having similar peak LTHR values as well as similar onset of LTHR locations for all diesel SOI2s, whereas for POMDME, 310 and 305 SOI2s had significantly different LTHR curves. To further understand the possible reasons for this behavior, the LTHR was plotted against the calculated in-cylinder real gas temperature (Figure 4.10).

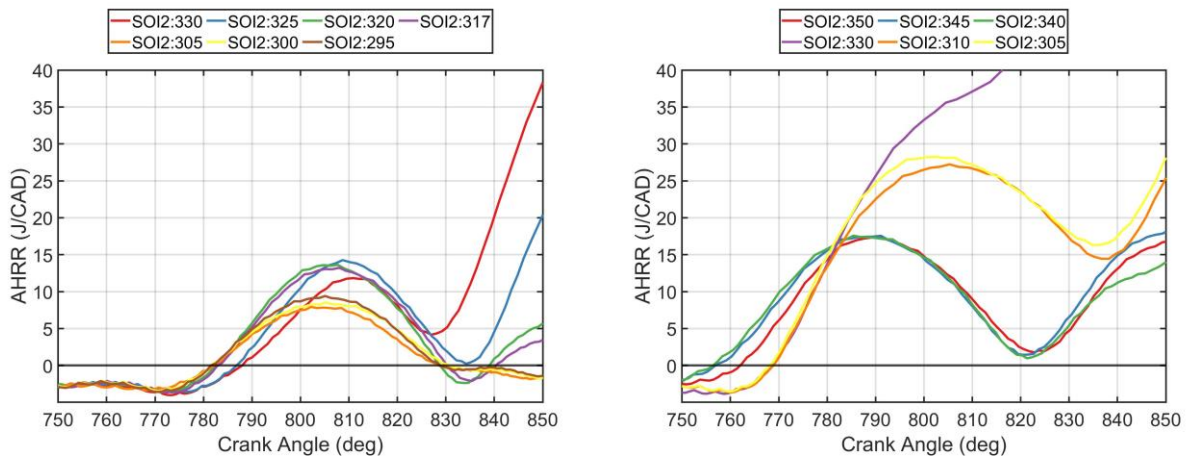


Figure 4.10. LTHR vs. in-cylinder temperature for diesel/NG (left) and POMDME/natural gas (right).

It is evident from Figure 4.10 that for diesel-NG combustion, there are only minor differences between the different SOI2 conditions, with the start of LTHR occurring consistently between 770 and 780 K. POMDME operation shows LTHR onset temperatures between 760 K and 770 K for SOI2s of 305, 310, and 330, but shows temperatures that are near 750 K or lower for SOI2s of 340, 345, and 350. Firstly, it is clear from these plots that POMDME's increased cetane number has an impact on the low temperature chemistry, seeing as all the temperatures at the onset of LTHR are lower compared diesel, indicating the impact of POMDME's higher reactivity. Secondly, the changes in behavior of the LTHR curve seen in POMDME operation can be attributed to a phenomenon that is occurring locally within the cylinder. It is posited that for SOI2 values of 340, 345, and 350 CAD in POMDME operation the LTHR component is mostly due to the fuel which has been properly mixed from the SOI 320 CAD injection event. Conversely, the SOI2s that occur before the SOI1 of 320 CAD show more intense LTHR. This could mean that more of the overall fuel mixture is taking part in the low-temperature chemical reactions. Without detailed chemical kinetic simulations, nor without knowing the local thermodynamic conditions within the combustion chamber, no definitive explanations can be put forth for these LTHR trends for POMDME compared to diesel.

Finally, the reduction in ISCO that occurs with introducing a second injection needs to be addressed. Not only did the cycle-to-cycle variability decrease for some injection timing combinations, but also the bulk in-cylinder temperatures were higher for longer durations of time. To visualize this, residence times above a threshold temperature were calculated and plotted in Figure 4.11. It has been shown that, in HCCI combustion engines for example, the lowest peak temperature for complete CO oxidation is 1500 K [108]. This would be a reasonable threshold temperature to study residence times; for the low-load DFLTC studied here,

temperatures within the cylinder for the SOI2 sweep considered never approached 1500 K. In fact, the maximum temperature calculated within the cylinder was 1296 K for diesel-NG and 1351 K for POMDME. It should be noted that these temperatures are bulk gas temperatures, not local temperatures, which can exceed 1500 K, leading to CO to CO<sub>2</sub> conversion within the cylinder. Bulk gas temperatures, and the residence times at high bulk gas temperatures, can be important in comparing the trends between different operating conditions, since local temperatures cannot be determined experimentally. Two residence time threshold temperatures were considered, and they were calculated as 10% of the maximum temperature achieved throughout the SOI2 sweep, and 20% of the maximum temperature achieved throughout the SOI2 sweep, both of which were rounded to the nearest integer and to two significant digits. For example, in the diesel-NG SOI2 sweep, the maximum temperature for any SOI2 was 1296 K, therefore the cutoff temperatures were set at 1200 K and 1000 K for 10% and 20% respectively. This process is repeated for each different sweep, for both fuels. In general, the longer the residence times at high temperatures, the greater the opportunity for oxidizing CO to CO<sub>2</sub> within the combustion chamber.

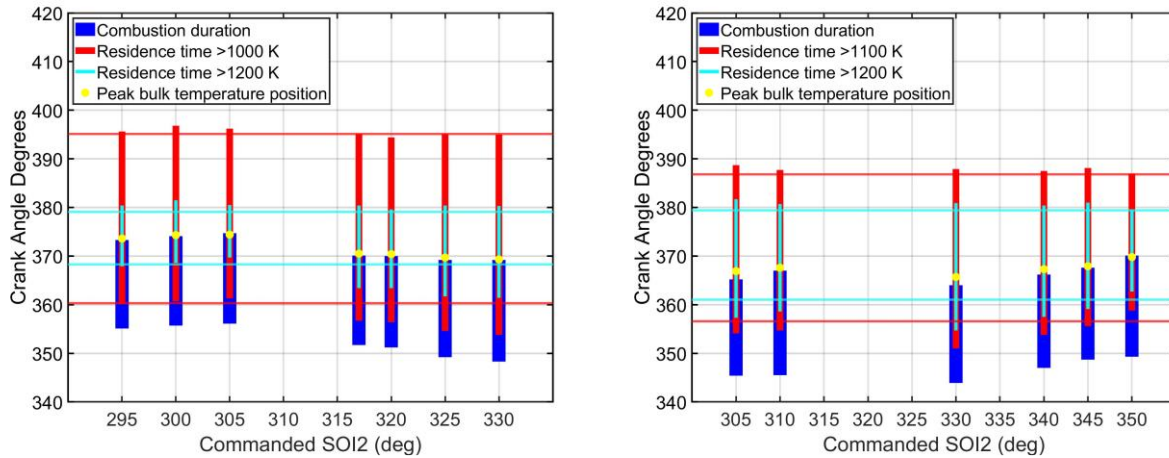


Figure 4.11. Residence time above 10% peak temperature and 20% peak temperature in CAD for diesel-NG (left) and POMDME-NG (right) with the residence times for the ‘best’ operating point from SOI1 being shown as horizontal lines.

Within Figure 4.11, the residence time for the ‘best’ operating point chosen from SOI1 sweep is also shown, for comparison, as horizontal lines, with red corresponding to the 20% threshold and cyan corresponding to the 10% threshold. It is clear from Figure 4.11 that the residence times for every SOI2, for both diesel/natural gas as well as POMDME-NG are longer at the given threshold temperatures. For diesel-NG, the 295, 300 and 305 SOI2 timings were close to the residence times of that observed from the SOI1 sweep in step 1 the ISCO was still lower than the 310 CAD SOI1 chosen from step 1, but were higher than for the 317, 320, 325, and 330 SOI2 timings. This indicates that the residence time plots and the respective thresholds that were used in Figure 4.11 can be correlated to the reduction in ISCO emissions.

#### 4.5.3 STEP 2(b): PES SWEEP

As with Step 2a, the single injection timings of 310 CAD and 320 CAD for diesel-NG and POMDME -NG operation, respectively, will be considered for the PES sweep. The goal of the PES sweep is to determine, at these injection timings, the impact of PES on emissions,

specifically UHC and CO emissions. Figure 4.12 shows the cylinder pressure, AHRR, and emissions for each PES for both fueling combinations.

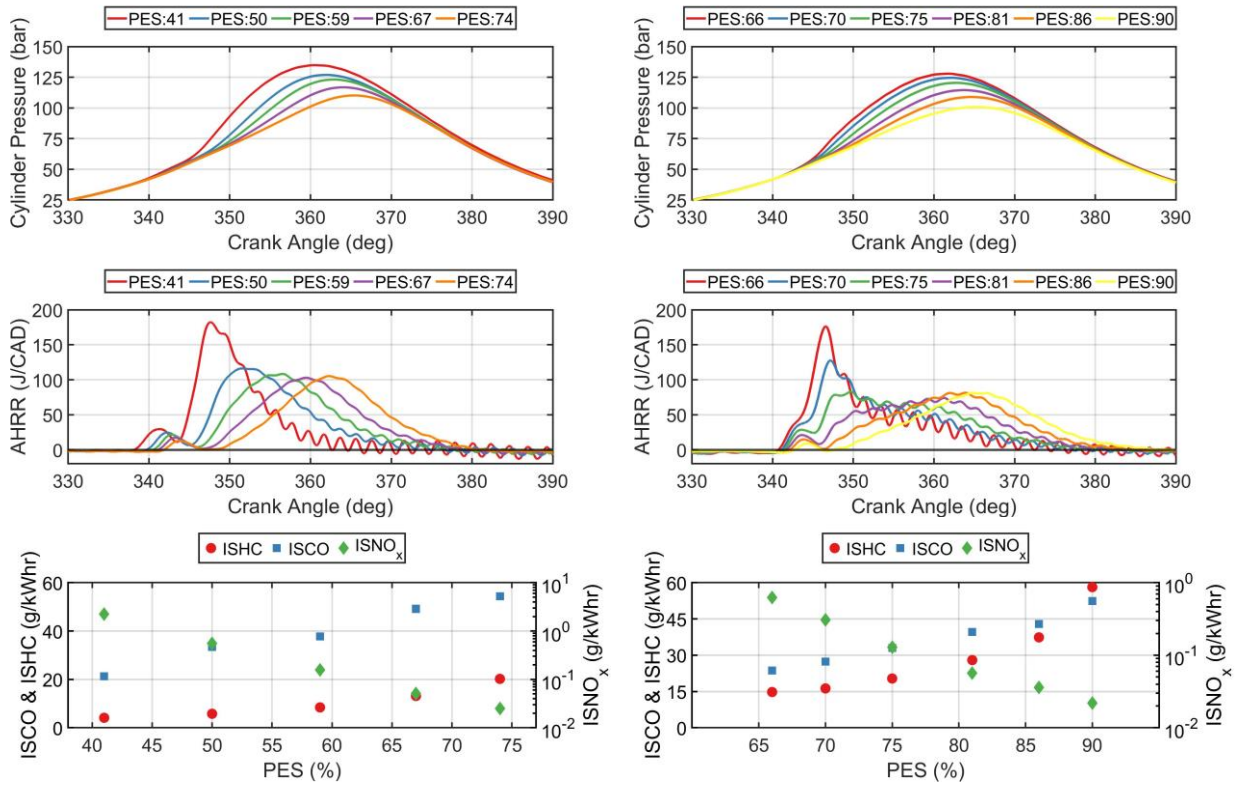


Figure 4.12. Cylinder Pressure (top), AHRR (middle), and emissions (bottom) results from a PES sweep for both diesel/NG (left) and POMDME/NG (right).

As PES is decreased, for both fueling combinations, the peak cylinder pressure is increased, and the location of peak cylinder pressure is advanced. AHRR profiles also show this advancement in the location of peak AHRR and increased peak AHRR values with decreasing PES. This phenomenon can be seen in the CA5, CA50, and CA90 trends shown in Figure 4.13. As PES is decreased, the CA5, CA50, and CA90 all advanced linearly, with diesel-NG and POMDME-NG showing an advancement in combustion phasing. The combustion advancement with decreasing PES is accompanied by ISCO and ISHC reductions and ISNO<sub>x</sub> increase due to increasing bulk gas temperatures, which will inherently increase the local temperatures as well.

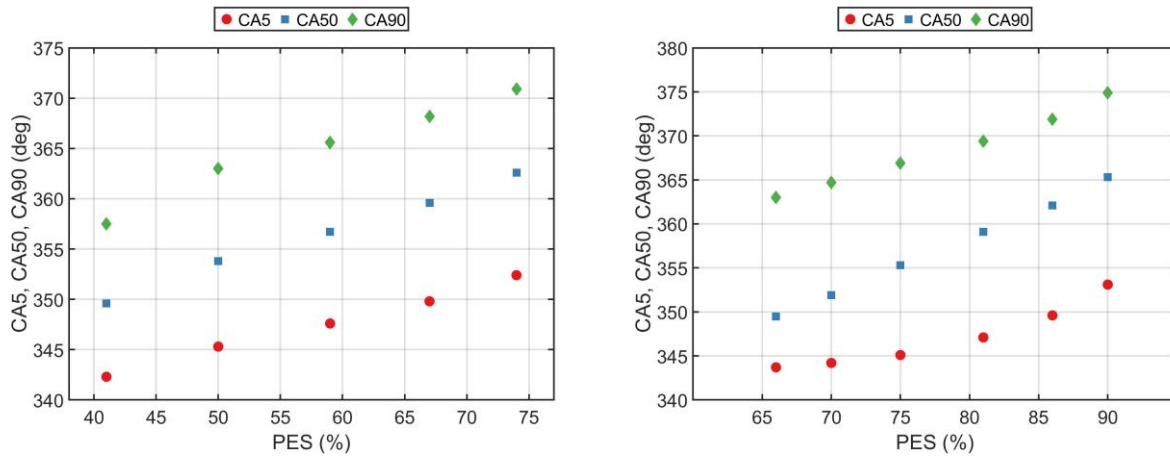


Figure 4.13. CA5, CA50, and CA90 results from a PES sweep for both diesel/NG (left) and POMDME/NG (right).

By reducing the PES, multiple outcomes arise that helps reduce the ISHC and ISCO emissions. First, the advancement of the combustion phasing for both fuel combinations facilitate the reduction in the total combined HRF and LRF quantities needed to achieve 5 bar IMEP, thereby increasing IFCEs as seen in Figure 4.14. In fact, IFCE increased from 41.2% at ~75% PES to as high as 44 % at ~60% PES for diesel-NG and increased from 33.6% at 90% PES to as high as 41.3 % at 70% PES for POMDME-NG combustion. Second, the combustion efficiency (also shown in Figure 4.14) increased, due in part to the more robust distributed ignition centers likely with a higher quantity of HRF fuel dispersed throughout the combustion chamber at lower PES values. Combustion efficiencies approached 95% for diesel-NG operation and exceeded 90% for POMDME-NG operation.

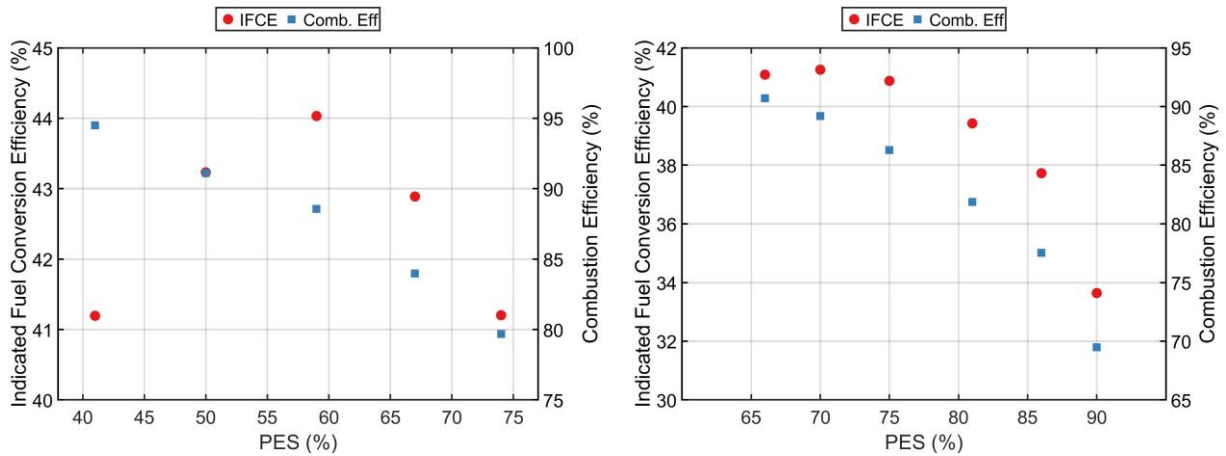


Figure 4.14. IFCE and combustion efficiency for results from a PES sweep for diesel/NG (left) and POMDME/NG (right) operation.

Finally, the residence time plots are shown in Figure 4.15 for diesel-NG, and for POMDME-NG. As done previously, the lower threshold was taken as 20% of the peak temperature that occurred for any PES within the sweep, and the upper threshold was 10%. As PES decreases for each fueling combination, the residence time that is spent above these threshold values increases. This indicates that there is a longer duration of time within the cycle for which higher temperatures occur, resulting in greater CO oxidation as evident from Figure 4.12.

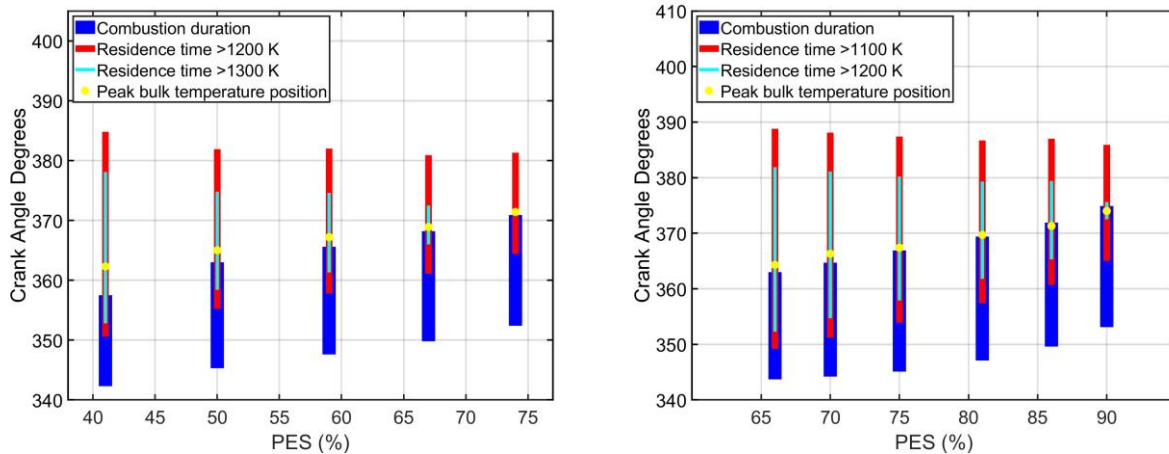


Figure 4.15. Residence time results from a PES sweep for diesel/NG (left) and POMDME/NG (right) operation.

#### 4.5.4 INJECTION SPLIT RATIO SWEEP

When performing the injection split ratio sweep, the results from Steps 2(a) and 2(b) were combined to set SOI1 and SOI2, as well as a PES value to hold constant during the experiments. For diesel-NG operation, the SOI2 of 300 CAD was chosen. This falls before the SOI1 timing of 310, which was set from step 1, however the nomenclature of SOI2 will still be used since it was introduced as the second injection within the framework presented in this study. The SOI2 of 300 CAD was chosen mainly due to its low  $\text{NO}_x$  compared to SOI2s that had longer injection dwells.  $\text{NO}_x$  was expected to be a limiting factor when the boost pressure sweep was performed and consequently, it was decided to minimize  $\text{NO}_x$  at this stage. A PES of 50% was chosen from step 2b, due to the high IFCE as well as low  $\text{NO}_x$  values. While the  $\text{NO}_x$  values for this point were near the cutoff of 1 g/kWhr, the results were for a single injection case; therefore, by combining this with the STARS strategy from step 2a, it was thought that  $\text{NO}_x$  values could be reduced.

For POMDME-NG operation, an SOI2 of 310 was chosen. Once again, this is before the SOI1 timing of 320, which was set from step 1, but the nomenclature of SOI2 will remain the same. The rationale behind choosing an SOI2 of 310 CAD is much the same as for diesel-NG operation, in that the NO<sub>x</sub> values were very low. A PES of 75% was chosen due to its good IFCE and NO<sub>x</sub> value.

For the injection split ratio sweep, the SOI1 and SOI2 timings were fixed from step 1 and step 2(a), respectively, while allowing for the injection durations to vary at constant IMEP and PES. It was hypothesized that the injection split ratio could give finer control over the stratification level inside of the cylinder, which could lead to greater reduction in ISCO and ISHC. The injection split ratio is defined as the ratio of the commanded injection duration of SOI1 to that of SOI2. This was varied for both diesel-NG and POMDME-NG combustion. The AHRR and emissions curves for this sweep are shown in Figure 4.16, below.

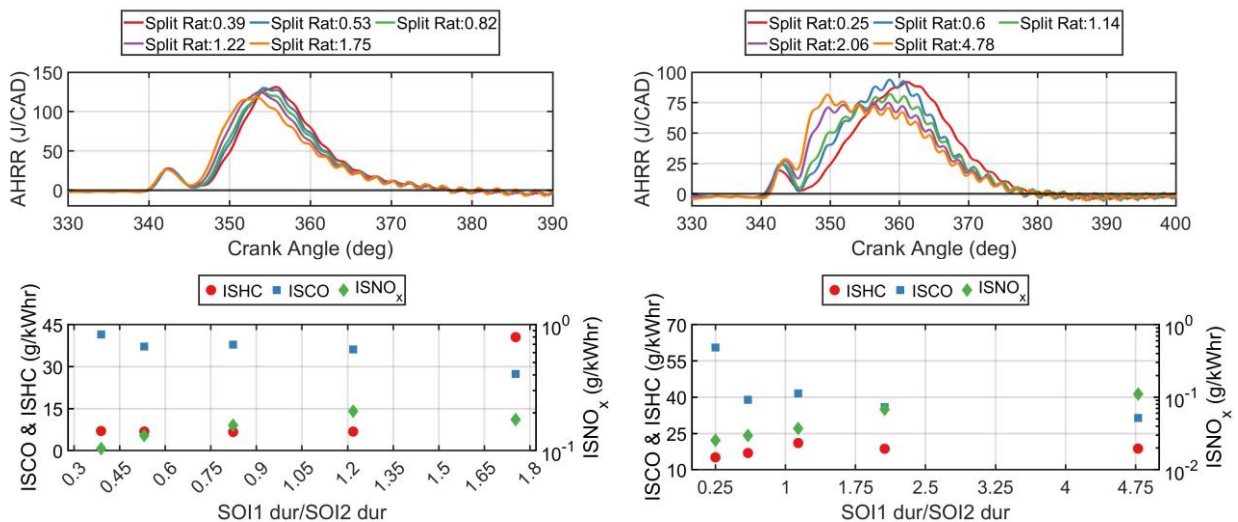


Figure 4.16. AHRR and emissions results at different injection ratios for diesel/NG (left) and POMDME/NG (right) operation.

Diesel-NG operation shows a consistent heat release profile regardless of the injection split ratio. The emissions are relatively invariant as well, with the exception being an increase in ISHC emissions to over 40 g/kWhr at a split ratio of 1.75. This point was deemed to be an outlier within the dataset. The changes in the shape of AHRR in POMDME-NG operation may be attributed to the fact that the coupled injections occur later compared to diesel-NG operation, meaning there is less time for mixing, and there is a larger amount of mass of fuel for POMDME compared to diesel, which compounds the mixing limitation. It is evident, though, that for POMDME operation the higher injection split ratio did improve the ISCO emissions, bringing them down from ~60 g/kWhr to just over 30 g/kWhr. This, once again, can be explained with the residence time plot shown in Figure 4.17.

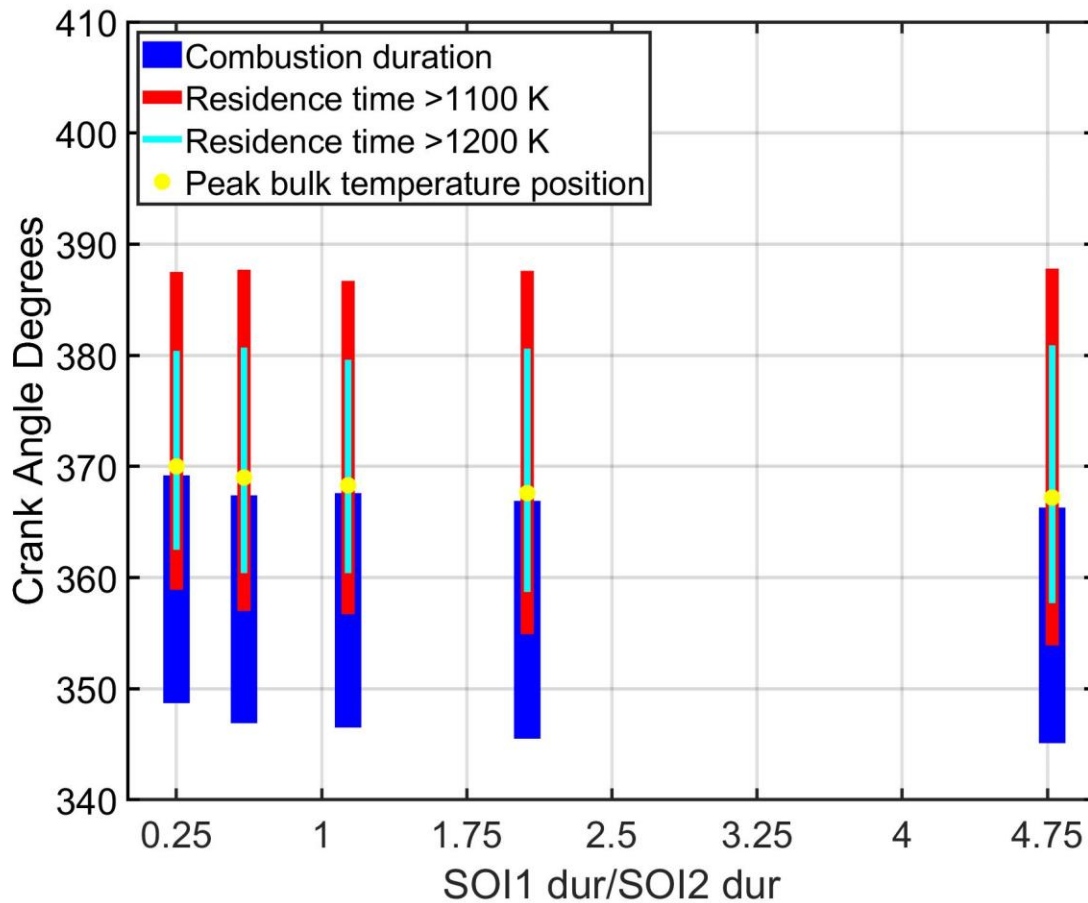


Figure 4.17. Residence time results for injection split ratio sweep of POMDME/NG.

The combustion duration shifts to starting earlier in the cycle for higher injection split ratios, and the temperature exceeds 1200 K sooner than for other injection split ratios. The time for which the temperature stays above 1200 K is also prolonged at the 4.75 injection split ratio. This resulted in lower ISCO, but only slightly higher ISNO<sub>x</sub> emissions, and therefore the injection split ratio of 4.75 was chosen for POMDME to move forward. For diesel operation, the injection ratio sweep did not produce any significant emissions reductions. Therefore, the 0.82 injection split ratio was chosen as it was close to equal weighting between the injection durations.

#### 4.5.5 RAIL PRESSURE SWEEP

Rail pressure has been shown to impact dual fuel emissions in the literature [28, 29]. The AHRR and emissions values for both fueling combinations are shown in Figure 4.18.

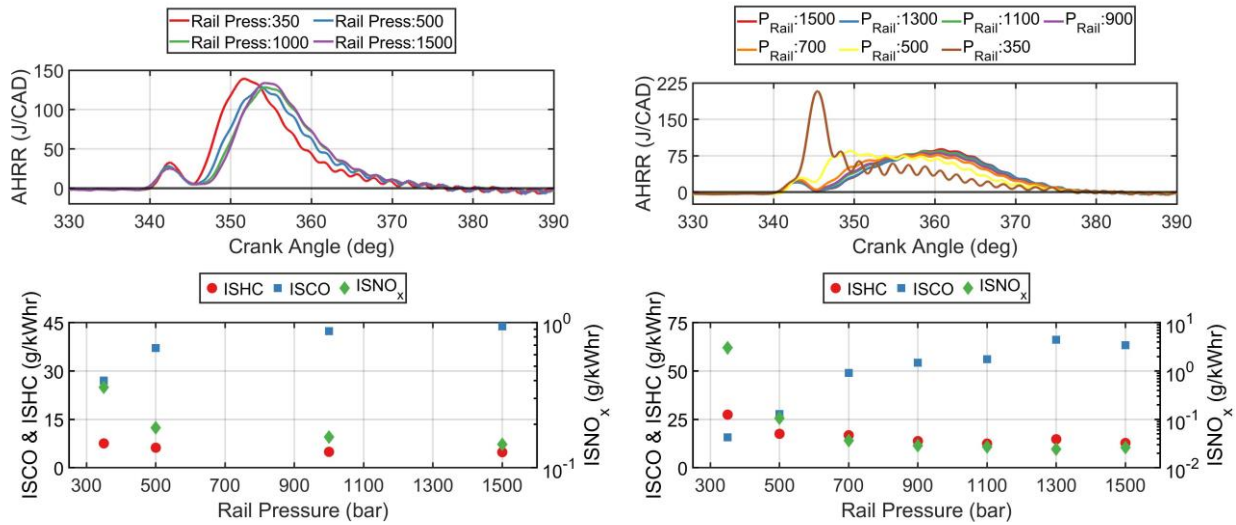


Figure 4.18. AHRR (top) and emissions (bottom) results for a rail pressure sweep using diesel/NG (left) and POMDME/NG (right) fueling combinations.

Interestingly, the rail pressure effects on dual fuel emissions observed in this work are different from trends previously observed in the literature. The differences may have been caused by the close coupled (or short dwell) strategy chosen in the present work for multiple injections and the relatively lower PES conditions chosen for the rail pressure sweep. For example, Bartolucci et al. [28] observed a decrease in the CO emission emissions for higher rail pressures, albeit for a long dwell between the multiple injections as opposed to close coupled multiple injections used in the present work. In a similar fashion, Hariharan et al. [29] showed an improvement in the efficiency-emissions tradeoffs when increasing the rail pressure. By comparison, as shown in Figure 4.17, the ISCO decreases when rail pressure is decreased for both fueling combinations. The explanation for the differences from this study and literature could come from the differences in PES between the studies and possibly from the use of long dwell injections from literature compared to short dwells in the present study. The literature

examples used PES values of 75% or higher for diesel, whereas for diesel operation in this study, a PES of 50% was used. The higher amount of diesel, combined with close coupled early injections, likely resulted in some spray impingement on the walls of the combustion chamber at higher rail pressures. This would lead to partial burning of the diesel and less active combustion spread in the surrounding NG-air mixture, potentially leading to higher CO emissions. The higher rail pressures could also be contributing to an over-leaning of the local fuel-air mixture, which can inhibit the complete combustion process.

Differences are also evident in how rail pressure affects the AHRR curves when comparing diesel-NG and POMDME-NG operations. For diesel natural gas, the AHRR curve is minimally affected when rail pressure is changed from the baseline pressure of 500 bar. POMDME-NG shows a much more pronounced change in the shape of the AHRR, with the 350-bar rail pressure case exhibiting a very high peak AHRR as compared to the other rail pressures. This likely explains why ISNO<sub>x</sub> increases, since there are likely higher local temperatures realized due to the more intense AHRR profile for 350 bar rail pressure.

As noted previously, the residence time plots (shown in Figure 4.19) for diesel and POMDME operation can give insight into the ISCO emission reduction at low rail pressure, but no improvement for higher rail pressures. For both fueling combinations, the calculated threshold temperatures were the same, with the 10% and 20% cutoffs being 1200 K and 1100 K, respectively.

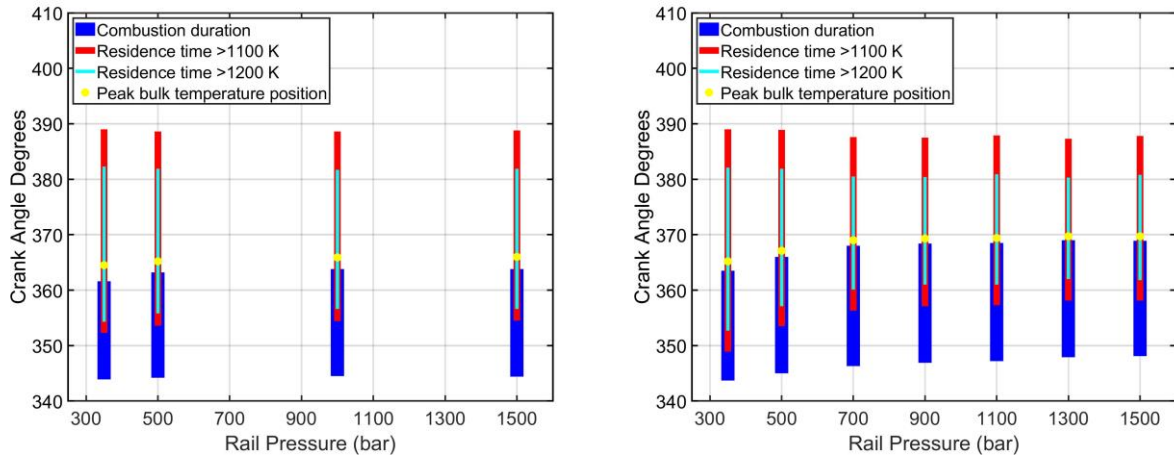


Figure 4.19. Residence time results for a rail pressure sweep using diesel/NG (left) and POMDME/NG (right) fueling combinations.

The rail pressures of 1000 bar and 1100 bar were chosen for diesel-NG and POMDME-NG, respectively, for the subsequent boost pressure sweep. Even though these rail pressures actually led to higher ISCO emissions compared to 500 bar, which was used in step 3, the ISNO<sub>x</sub> decreased slightly, and the ISHC also improved for the POMDME case. Therefore, the higher injection pressures were preferred.

#### 4.5.6 ABSOLUTE BOOST PRESSURE SWEEP

The intake boost pressure is an important lever that is known to affect dual fuel LTC. By reducing the boost pressure, the air flow rate will decrease, which will lead to higher global  $\phi$  values, resulting in higher in-cylinder temperatures. The cylinder pressure, AHRR, and emissions for the boost pressure sweep from nearly naturally aspirated conditions (~1.02-1.07 bar) to 1.6 bar are shown in Figure 4.20 for both fueling combinations.

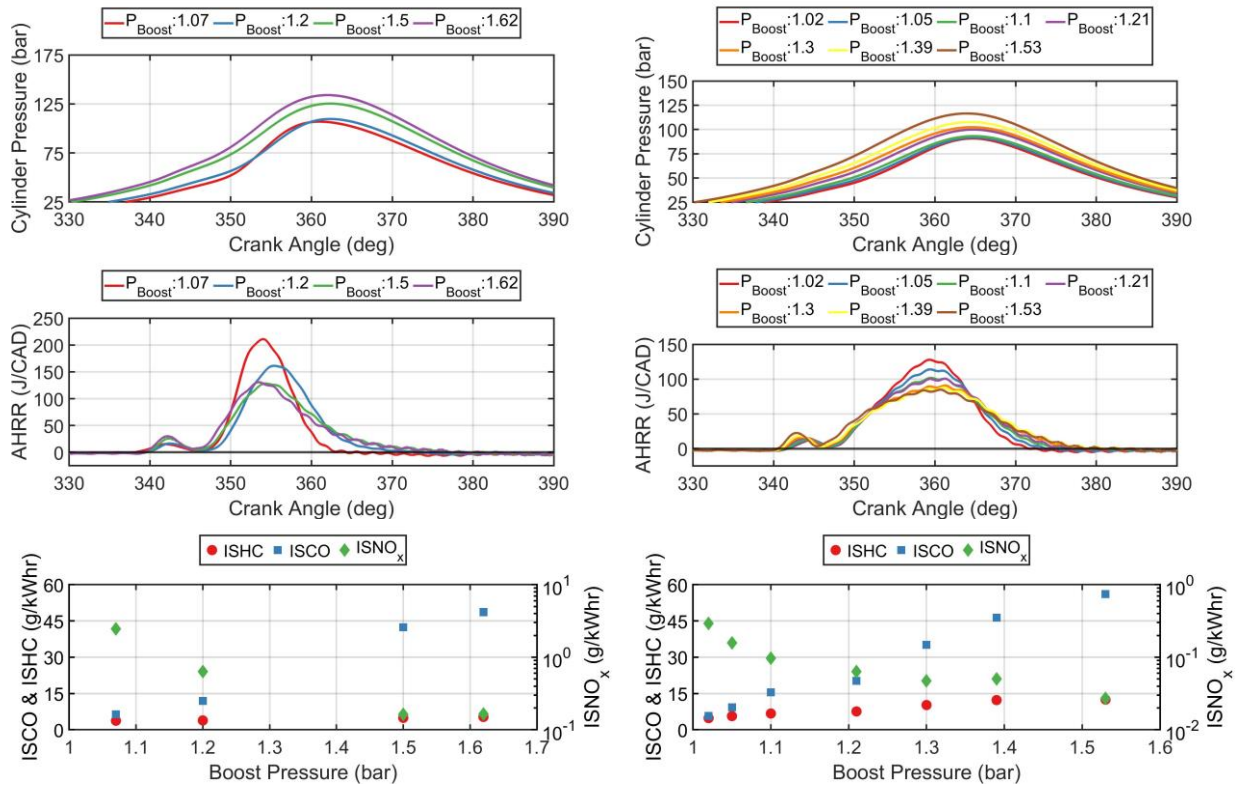


Figure 4.20. Cylinder pressure (top), AHRR (middle), and emissions (bottom) for a boost pressure sweep using diesel/NG (left) and POMDME/NG (right).

The cylinder pressures, including the peak cylinder pressures, decrease as the intake pressure decreases. This is intuitive since the pressure at TDC is dependent on the compression ratio and the pressure at the start of the closed portion of the cycle, which is decreased as intake pressure decreases. The peak AHRR, on the other hand, increases as the boost pressure is decreased for both fuels. As boost pressure is reduced the air flow into the cylinder is reduced leading to higher overall equivalence ratios and the increased likelihood of locally rich areas within the cylinder. This ultimately results in higher local temperatures, faster rates of heat release, and higher peak AHRR values. The ISCO emissions dramatically decrease for both fuels combinations with decreasing boost pressures, with ISCO values under 10 g/kWhr at low boost pressures. This ISCO reduction is accompanied by higher ISNO<sub>x</sub> emissions, and this tradeoff can

be explained better using the in-cylinder bulk gas temperature and residence time trends shown in Figure 4.21.

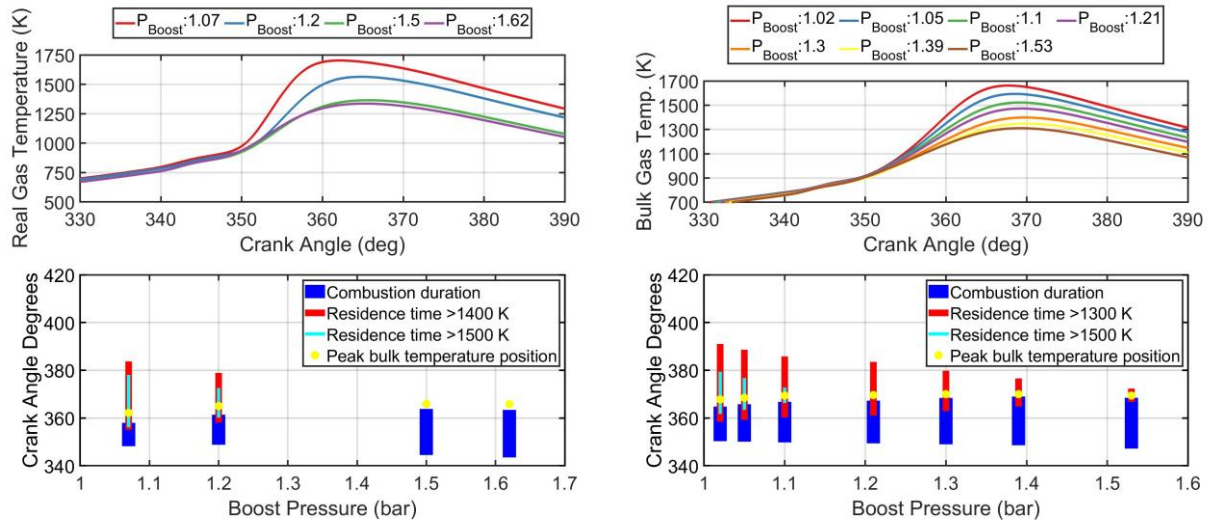


Figure 4.21. Calculated real gas temperature(top) and residence time (bottom) for a boost pressure sweep using diesel/NG (left) and POMDME/NG (right).

Peak bulk gas cylinder temperatures increased as the boost pressure was decreased. This inevitably led to longer residence times for which high temperatures persisted. For the baseline 1.5 bar boost pressure, with baseline diesel-NG operation, never registered any residence time above the calculated thresholds. For POMDME-NG operation finite residence times were observed above the 20% threshold at the higher boost pressures. The longer residence times allowed for more complete CO oxidation within the cylinder, thereby reducing the ISCO emissions. The increased bulk gas temperatures and faster AHRR likely led to higher local temperatures, resulting in higher ISNO<sub>x</sub> emissions. ISHC emissions decreased slightly (for POMDME-NG) or remained nearly invariant (for diesel-NG) throughout the boost pressure sweep. With fumigation of NG as the LRF in dual fuel LTC, most of the ISHC emissions may be expected to be unburned NG arising either from the cold crevice regions or from bulk gas quenching. With the lower in-cylinder densities accompanying lower boost pressures, the mass

of unburned NG-air mixture trapped within the crevices may be expected to decrease, leading to lower ISHC emissions. The relative invariance in ISHC emissions with boost pressure for diesel-NG combustion indicates that the impact of reducing crevice trapped mass on ISHC at lower boost pressures is minimal for this engine at these specific operating conditions.

Emissions values for the final boost pressure sweep were lower than for the single injection case for both fuels. However, these emissions were recorded without the use of aftertreatment devices. After treatment devices could get emissions values even lower than the current reported values, but would require the use of catalysts which have minimum operating temperature requirements. For reference, the exhaust temperature of the boost pressure sweep (which produced the best emissions point) is shown in Figure 4.22, below, as a means for future researchers to determine the applicability of certain catalysts with this combustion strategy.

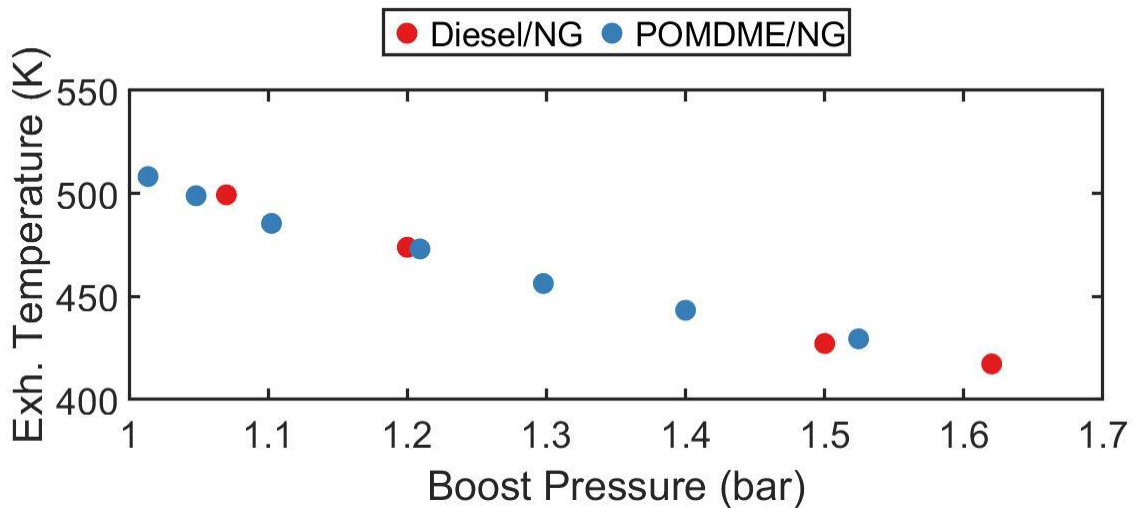


Figure 4.22. Exhaust temperatures for each boost pressure point for both diesel/NG and POMDME/NG.

## 4.6 CONCLUSIONS

A detailed set of experiments was performed on a single cylinder research engine involving multiple strategies to reduce ISHC and ISCO emissions at a low load (5 bar IMEPg) and constant engine speed (1339 rev/min) with both diesel-natural gas and POMDME-natural gas dual fuel combustion. With not-to-exceed limits of 10 bar/CAD for MPRR, 10%  $COV_{IMEP}$ , and 1 g/kWhr  $ISNO_x$ , and employing multiple injections, percent energy substitution (PES) of natural gas, rail pressure, injection split ratio, and boost pressure as the control parameters, significant performance and emissions benefits were demonstrated. The salient conclusions are as follows:

- Indicated specific carbon monoxide trends are strongly correlated with the amount of time, in crank angle degrees, that the bulk gas temperature stays at high temperatures within the cylinder.
- Utilizing STARS increased the combustion stability at advanced injection timings, which is shown in the reduction in  $COV_{IMEP}$  for second injections that occurred after the first injection.
- ISHC emissions decreased the most during the PES sweep for both diesel and POMDME. This can be attributed to more diesel or POMDME being utilized to achieve a better distributed ignition, leading to faster burn rates and less unburned hydrocarbons.
- Indicated fuel conversion efficiencies as high as 45% were achieved for both fueling combination after the experimental framework was implemented. This value increased from baseline values of around 37% for both fueling combinations. Most of this IFCE improvement resulted from an increase in combustion efficiency, which resulted in values over 95% for both fueling combinations.

- Injection split ratio experiments did not provide any significant improvement in the emissions or efficiency values across any split ratio studied.
- A decrease in the boost pressure had the most profound impact on ISCO emissions, due to the increased residence times at higher temperatures, allowing for more time for CO oxidation to occur.

V.  
A COMPARATIVE ANALYSIS OF HIGH LOAD NATURAL GAS DUAL FUEL  
COMBUSTION IGNITED BY DIESEL AND POMDME

## 5.1 ABSTRACT

Dual fuel combustion has been used to achieve low temperature combustion (LTC) at low loads and has been shown to decrease engine out oxides of nitrogen ( $\text{NO}_x$ ). In high load applications, early injection timings can be used to mitigate engine out  $\text{NO}_x$  emissions. Utilizing advanced injection timings comes at the detriment of higher maximum pressure rise rates (MPRR). Typically, to avoid the MPRR-limited region, the injection timings must be advanced even further, which leads to lower indicated fuel conversion efficiency (IFCE). In the present study, an experimental framework for improving the IFCEs of natural gas dual fuel combustion operating at a relatively high load of 15 bar gross indicated mean effective pressure (IMEPg) with both diesel and polyoxymethylene-dimethyl ether (POMDME) as the high reactivity fuels. First, a single injection and percent energy substitution (PES) sweep are performed. This is followed by introducing a second injection leading to Spray Targeted Reactivity Stratification (STARS) within the combustion chamber. Next, an injection ratio sweep, wherein the ratio of the commanded injection duration of SOI1 to SOI2, is swept over a range of values. A coupled injection sweep (wherein both the injection timings are moved together), a rail pressure sweep, and a boost pressure sweep are then performed. This framework is performed on a 1.8-liter single cylinder research engine (SCRE) platform operating at 1339 RPM. It was shown that the MPRR limited range, when using the STARS combustion

strategy, decreased for both diesel-natural gas combustion as well as for POMDME-natural gas combustion. It was also shown that the coupled injection sweep was immensely effective at improving IFCEs, with diesel-natural gas achieving upward of 51% IFCE, with ISHC and ISCO decreasing at this point to 15 g/kWhr and 4 g/kWhr, respectively; ISNO<sub>x</sub>, however, increased at this high efficiency point to just under 1 g/kWhr. The present work includes a detailed comparative analysis of dual fuel LTC with both diesel and POMDME, leveraging apparent heat release rate (AHRR) histories and other combustion metrics to explain the observed emissions trends.

## 5.2 INTRODUCTION

The use of internal combustion as a main source of energy production and for use in transportation has been pivotal for humankind. Internal combustion engines also lead to harmful pollutant emissions such as unburned hydrocarbons (UHC), carbon monoxide (CO), and oxides of nitrogen (NO<sub>x</sub>). In addition, the reduction of greenhouse gas emissions, such as carbon dioxide (CO<sub>2</sub>), is increasingly important for many countries across the world, as limiting CO<sub>2</sub> emissions is key in the fight against climate change [109]. For internal combustion engines, this means increasing the fuel conversion efficiency (FCE) of the engines, seeing as a direct increase in FCE means that there is less fuel being used per mile traveled. Typically, the fuel used is some sort of hydrocarbon, and therefore a decrease in the amount of carbon that is input into the combustion chamber with improved FCEs results in a direct reduction in CO<sub>2</sub> emissions.

Improving the FCE of engines has always been a focus for engine researchers. Techniques such as thermal barrier coatings to minimize losses from heat transfer [110,111], variable valve timing strategies [112,113], waste energy recovery [114], and spark assisted compression ignition [115-117], to name a few, have widely explored. Specifically, in the heavy-

duty, long haul tractor trailer market, the United States Department of Energy's Super Truck program [118] was able to demonstrate brake thermal efficiencies (BTE) in excess of 50% on a dynamometer. Increased engine efficiencies are not the only goal, with emissions mitigation also being an important regulatory requirement. Specifically, tailpipe NO<sub>x</sub> emissions are of key importance and current on-road heavy-duty trucks typically utilize selective catalytic reduction (SCR) catalysts with urea injection to mitigate tailpipe NO<sub>x</sub> emissions. Future proposed NO<sub>x</sub> emissions standards are even more stringent, approaching limits of 0.02 g/bhp-h [82]. To achieve such low tailpipe NO<sub>x</sub> emissions, the engine-out NO<sub>x</sub> emissions must also be reduced. For this purpose, several low-temperature combustion (LTC) techniques have been considered, including homogeneous charge compression ignition (HCCI) [119,120], and reactivity-controlled compression ignition (RCCI) [121,122] to name a few. Dual fuel combustion can also be used to achieve LTC. Dual fuel combustion uses two fuels with different reactivities simultaneously in the combustion chamber. Typically, the fuel with the higher reactivity is directly injected into the combustion chamber, whereas the lower reactivity fuel is fumigated into the intake manifold or injected into the port. Dual fuel combustion can be achieved at low loads successfully, but typically faces challenges with high UHC and CO emissions as well as high engine instability. Chapter IV contains literature that covers this area specifically, therefore, for brevity, this will not be repeated here. High load engine conditions pose a different issue for dual fuel combustion, mainly in the form of increased maximum pressure rise rates (MPRR) and NO<sub>x</sub> emissions [123].

Several studies [124-128] have addressed the issues of using LTC in the high load region of an internal combustion engine. Yousefi et al. [125] performed diesel-natural gas (NG) experiments on a 2.4L engine at an engine load of 12.15 bar. A post-injection strategy was used and the maximum IFCE observed was 41.5%. Walker et al. [126] studied both diesel-gasoline

and diesel-methane combustion on a 2.4L engine to determine how the load limit could be expanded with the use of methane instead of gasoline. It was observed that the load limit could be extended from a maximum of 7 bar gross indicated mean effective pressure (IMEPg) for gasoline to a maximum of 17.3 bar IMEPg for methane.

The current study focuses on the implementation of STARS, which has been detailed in Chapter IV, at a high load of 15 bar IMEPg. The experimental framework is similar to that of Chapter IV. The goal of the present study is to improve the IFCE while also maintaining low engine-out emissions at high loads.

### **5.3 EXPERIMENTAL SETUP**

The same engine was used for this study as in Chapter IV. The engine specifications can be found in Chapter IV (*c.f. Table 4.1*). Similarly, a detailed engine schematic can also be found in Chapter IV (*c.f. Figure 4.1*). For brevity, details of the experimental setup, will not be repeated here.

### **5.4 EXPERIMENTAL PROCEDURE**

The experiments were performed with diesel-NG and POMDME-NG fueling combinations. Diesel-NG experiments were carried out in accordance with the flowchart shown in Figure 5.1, whereas POMDME/natural gas experiments were performed in accordance with the flowchart shown in Figure 5.2. The flowcharts are similar in scope to those found in Chapter IV, with three exceptions: 1) the experiments performed with the current procedure has a higher gross indicated mean effective pressure (IMEPg) of 15 bar, and consequently, started with a higher intake boost pressure of 2.25 bar; 2) a ‘coupled SOI sweep’ that was not used previously, and 3) the SOI sweep and PES sweep are performed simultaneously. All relevant equations and definitions are described in Chapter IV.

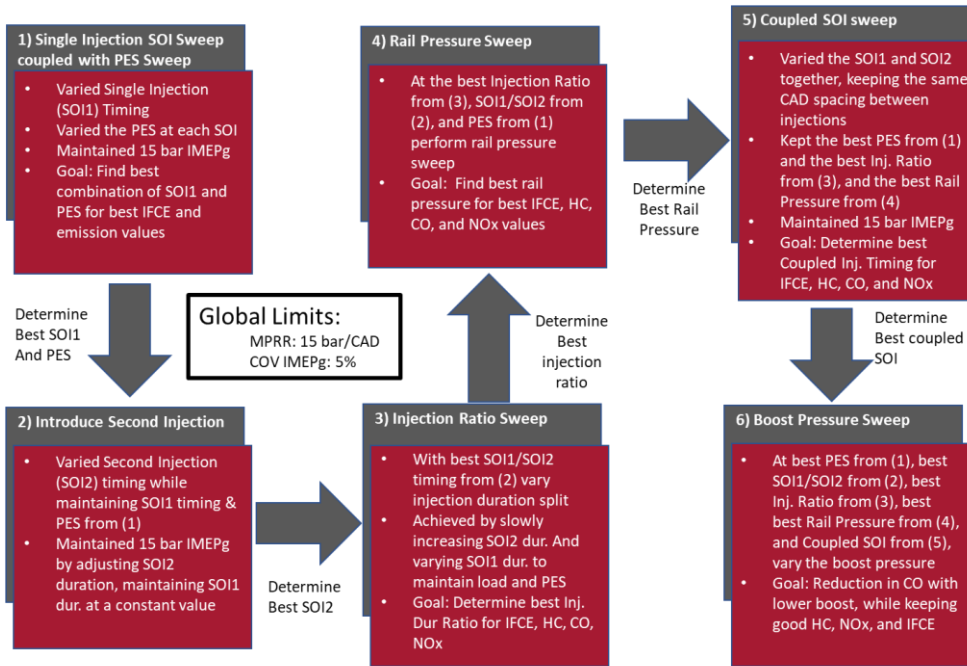


Figure 5.1. Detailed experimental procedure for diesel/NG operation.

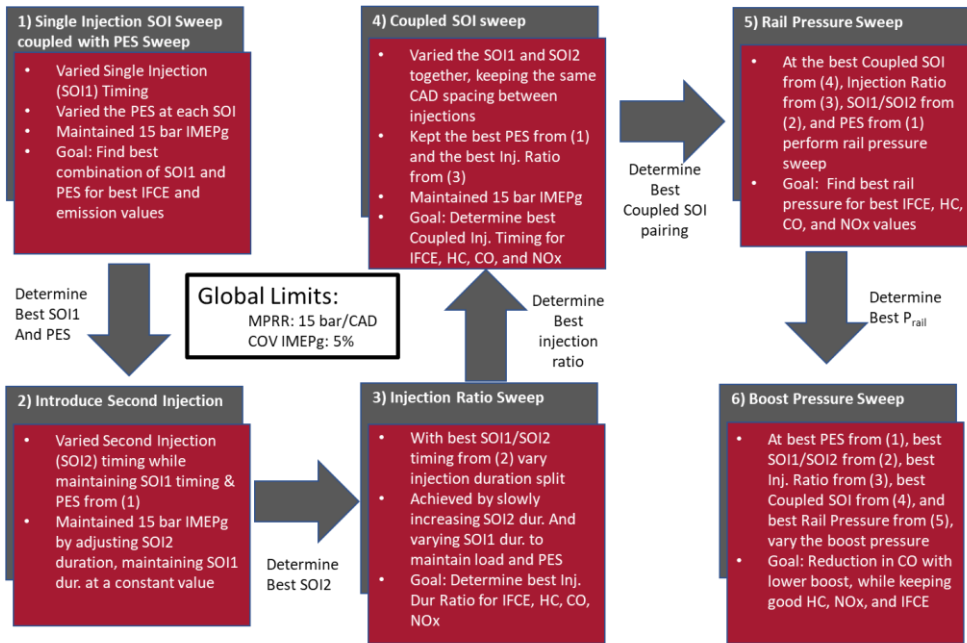


Figure 5.2. Detailed experimental procedure for POMDME/NG operation.

Details about each step will not be provided in the current chapter since they have been covered in depth in Chapter IV. However, since the coupled SOI sweep has not been discussed,

the details of it are provided. The coupled SOI sweep is inserted into the flowchart between the rail pressure sweep (step 4) and the boost pressure sweep (step 5) for diesel/natural gas, and between the Injection Ratio sweep (step 3) and the rail pressure sweep (step 5) for POMDME/natural gas. The coupled SOI sweep for POMDME-NG combustion was performed before the rail pressure sweep, as opposed to the order in which the experiments were performed in the diesel-natural gas experimental framework. This was done because, with diesel-natural gas combustion, the rail pressure did not have a significant operating range, nor did it show any significant changes to the combustion characteristics. It was hypothesized that, if the order in which the experiments were performed was switched, that the rail pressure sweep could have more of an impact than for the diesel-natural gas experiments

The coupled SOI sweep actively moves both SOI1 and SOI2 together, keeping the commanded injection split ratio, the load, and the PES constant. The dwell between the injections is also kept a constant during this sweep. The goal is to study if moving the injection timing pair can provide better emissions and efficiency tradeoffs, after having set the PES and injection split ratio.

## **5.5 EXPERIMENTAL RESULTS – DIESEL/NATURAL GAS**

The experimental results for diesel/natural gas operation are discussed in detail for each step of the flowchart (*c.f. Figure 5.1*).

### **5.5.1 STEP 1: PES & SOI SWEEP**

Instead of decoupling the SOI and the PES sweeps into two separate steps as was performed in the low load experiments in Chapter IV, it was deemed more prudent to get data for different PES values at varying different injection timings. The study was able to get a range of PES values from 65 to 95 percent, and the SOI range consisted of 280 to 355 CAD. In total, there

were 30 individual SOI/PES combinations that were studied. The emissions results for each of these combinations are presented in Figure 5.3.

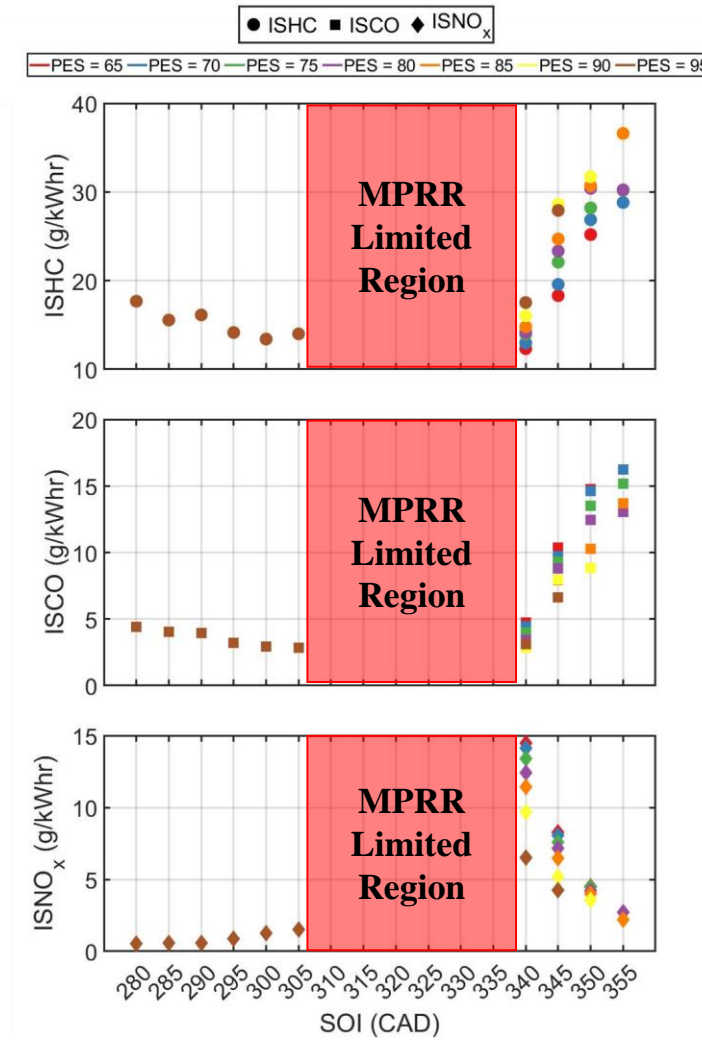


Figure 5.3. ISHC, ISCO, and ISNO<sub>x</sub> values for an SOI sweep using diesel/NG operation at 15 bar IMEPg.

Since there is such a wealth of data available at different PES and SOI combinations, it is important to narrow the scope the analysis. So, before moving to the combustion analysis, a detailed analysis of the emissions is necessary. First, the lowest ISNO<sub>x</sub> values are achieved at early injection timings, namely 280 – 305 CAD. Only one PES value (95%) is feasible at these SOIs for 15 bar IMEPg. Further reduction in PES at the 15 bar IMEPg load resulted in MPRR

values that exceeded the self-imposed limit of 15 bar/CAD for this study. At the late SOIs of 340-355 CAD, multiple PES values were able to be studied. The PES ranged from a minimum of 65% to a maximum of 95% for these SOIs. At these late SOIs, high ISHC and ISCO emissions are observed. ISNO<sub>x</sub> does decrease as the SOI is moved closer to TDC, however the ISHC and ISCO emissions increase to values much higher than seen at the early injection timings (above 15 g/kWhr for both ISCO and ISHC); these were deemed unacceptable at 15 bar IMEP<sub>g</sub>. The ISHC and ISCO did decrease as the injection timing was advanced to 340 CAD, but because of how close this is to the MPRR-limited region, the ISNO<sub>x</sub> values were deemed too high. Therefore, a combustion analysis of the SOI timings at 95% PES is performed to focus on the best PES for ISNO<sub>x</sub>, ISCO, and ISHC.

The cylinder pressure and the apparent heat release rate (AHRR) are shown in Figures 5.4 and 5.4, respectively.

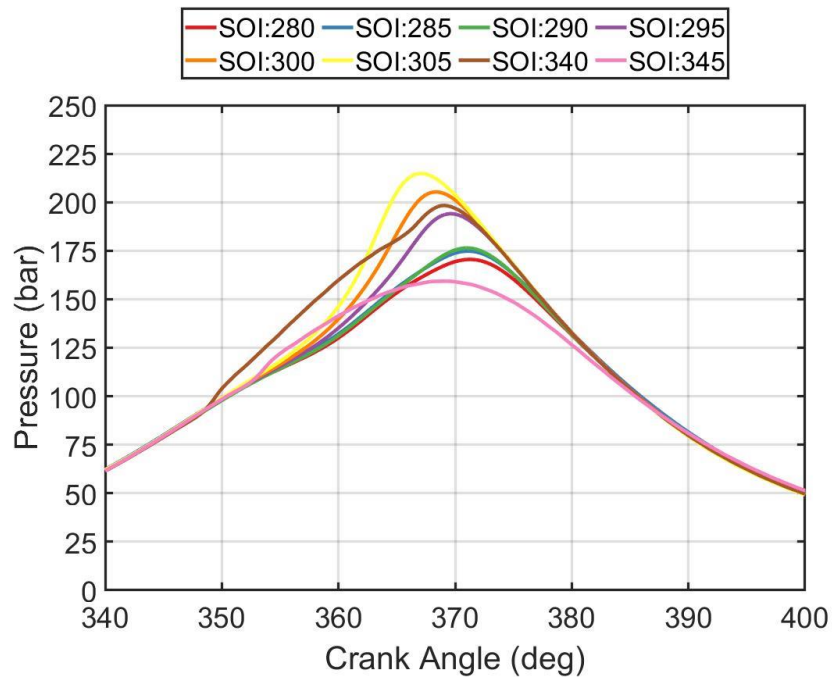


Figure 5.4. Cylinder pressure profiles for SOI sweep at 15 bar IMEPg, 95% PES, with diesel/NG combustion.

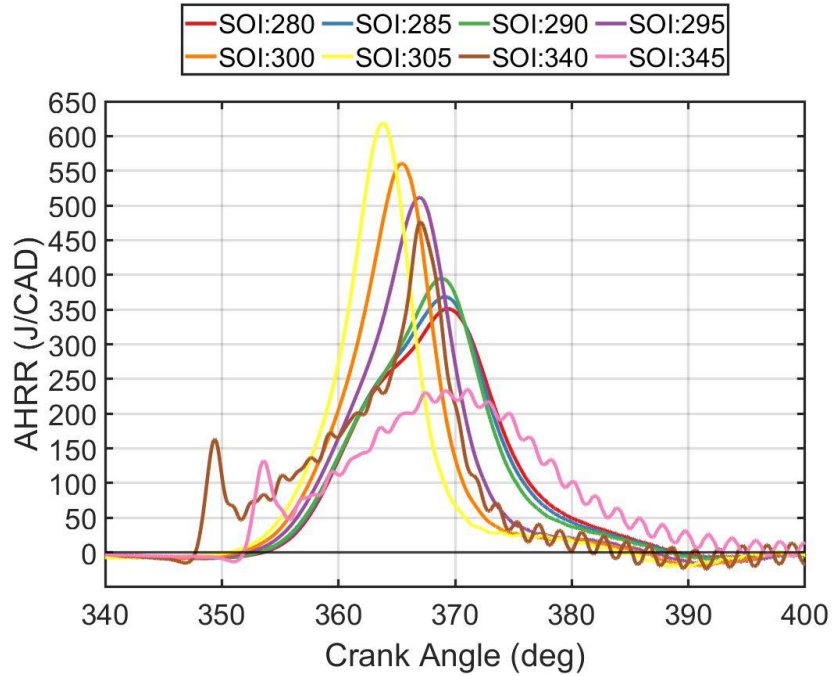


Figure 5.5. AHRR profiles for SOI sweep at 15 bar IMEPg, 95% PES, with diesel/NG combustion.

As shown in Figure 5.4, the maximum peak pressures reach nearly 225 bar, which was achieved for SOI = 305 CAD. The peak cylinder pressure limit for the engine is 245 bar, and that limit was nearly surpassed multiple times during the course of collecting the 15 bar IMEPg data. The AHRR profiles, shown in Figure 5.5, show no signs of LTHR, which is expected since in-cylinder temperatures likely exceed the threshold beyond which low temperature chemical kinetic pathways are not favored at the high load of 15 bar IMEPg. There are differences in the AHRR profiles, with the SOIs that occur closer to TDC, namely 345 and 340 CAD, having a small AHRR peak, followed by a slight decrease in the AHRR, before increasing again. This is likely due to relatively high local equivalence ratios for these injection timings, as the start of HTHR for both 340 and 345 CAD are relatively close to the SOI itself. This would also explain the increased ISNO<sub>x</sub> values for these points, since equivalence ratios that are near-stoichiometric lead to the highest local temperatures, and therefore more NO<sub>x</sub> formation. The start of combustion (CA5), combustion phasing (CA50), and the end of combustion (CA90) are shown in Figure 5.6.

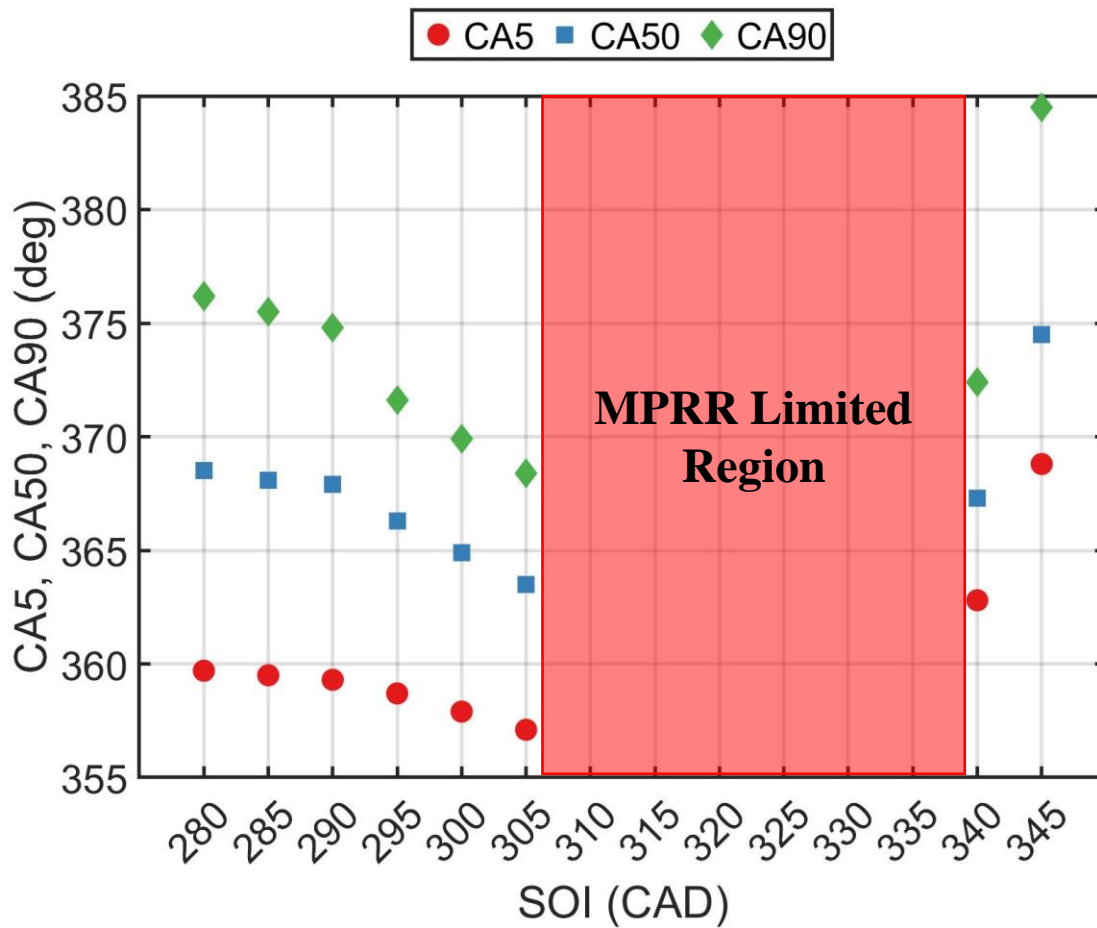


Figure 5.6. CA5, CA50, and CA90 for the SOI sweep of 15 bar IMEPg, 95% PES using diesel/NG.

The combustion phasing for SOI = 340 CAD is roughly equal to the combustion phasing for SOIs of 280, 285, and 290, but the ISNO<sub>x</sub> values are completely different. ISCO and ISHC values are comparable between the SOI = 340 CAD case and the SOIs of 280, 285, and 290 CAD, but the 340 CAD SOI is slightly higher. Because the HC and CO values are more similar than those of the ISNO<sub>x</sub>, this indicates that the NO<sub>x</sub> values might be higher for SOI = 340 CAD because of increased stratification of the combustion chamber in comparison to the other SOIs. Increased stratification ultimately means there will be more local areas at near-stoichiometric

equivalence ratios, which will inevitably increase NO<sub>x</sub> production. The indicated fuel conversion efficiency (IFCE) and combustion efficiency are reported in Figure 5.7.

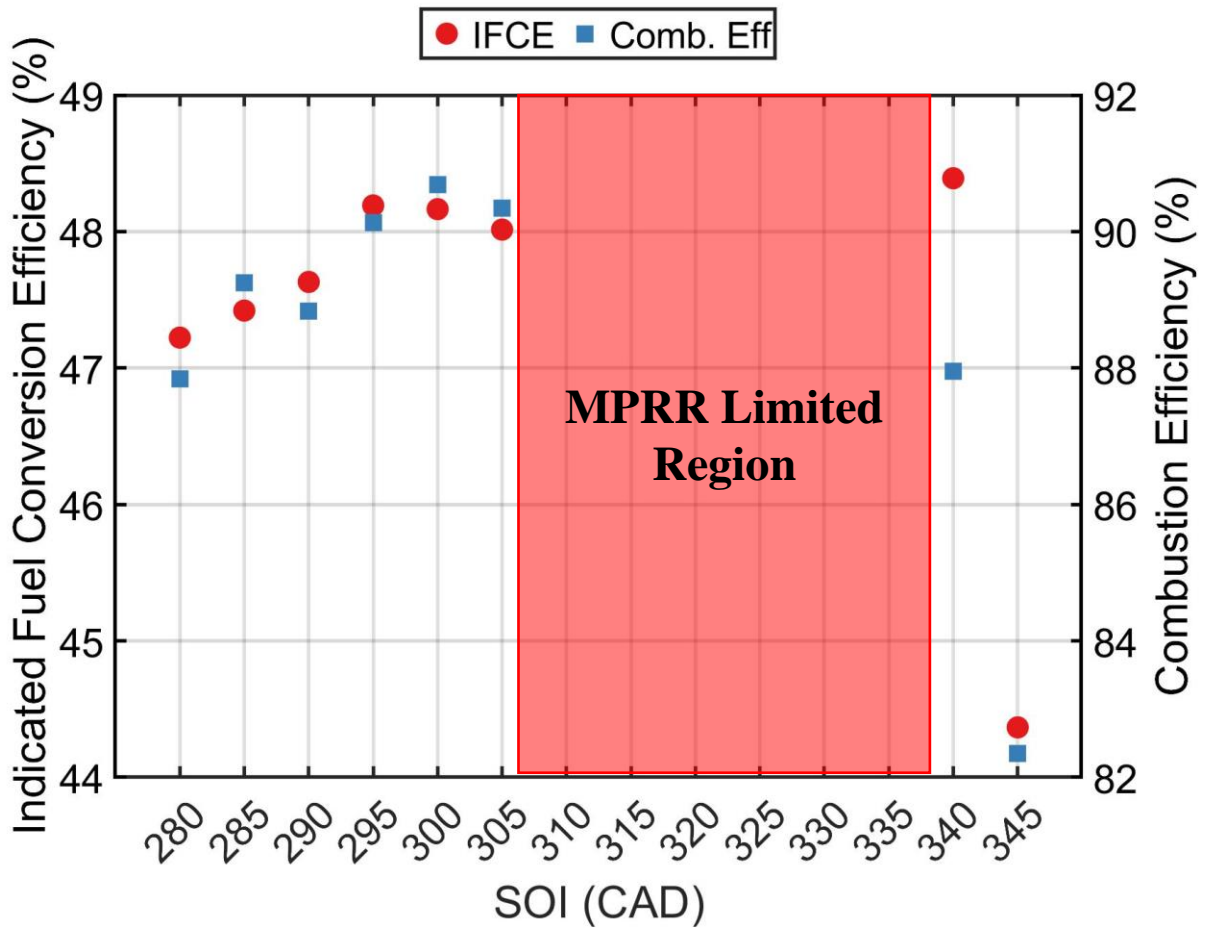


Figure 5.7. IFCE and Combustion Efficiency for an SOI sweep at 15 bar IMEPg and 95% PES using diesel/natural gas

The combustion efficiencies for each SOI are all greater than or equal to 88%, except SOI = 345 CAD. The IFCE is highest for SOI = 340 CAD, but due to the high ISNO<sub>x</sub> values, this operating point could not be considered for the next step. The highest IFCE occurred at SOI = 295 CAD, which had an IFCE of 48%. While the goal of this study was not to prioritize the emissions values, as was done for the 5 bar IMEPg experiments in Chapter IV, it cannot be

ignored that the  $ISNO_x$  value at  $SOI = 295$  CAD was  $0.86$  g/kWhr vs. an  $ISNO_x$  value of  $0.52$  g/kWhr at an  $SOI$  of  $280$  CAD. Therefore, the  $SOI$  of  $280$  CAD was chosen for the next, seeing as keeping  $ISNO_x$  values is of paramount importance.

### **5.5.2 STEP 2: SECOND INJECTION (STARS) SWEEP**

While combustion stability at high load may not be thought of as a problem, the goal of adding the second injection is to utilize more advanced injection timings that would be unstable if used with just a single injection. The STARS sweeps were performed slightly differently for  $15$  bar IMEPg. Instead of reducing the injection duration of the  $SOI1$  that was set in step 1 to the COV limit, it was instead decided to simply divide the injection duration in half. Since PES values are so high, and the IMEPg is at  $15$  bar, natural gas fueling rates are much higher than those previously studied at  $5$  bar IMEPg. This means that high cycle-to-cycle variations (i.e., the COV limit) could cause cycles with tremendously high MPRR values, due to the high natural gas flowrates and residual unburned natural gas. To avoid this, a second injection was slowly introduced while systematically decreasing the  $SOI1$  duration by  $50\%$ . This was determined to be the safest way to introduce a second injection at load.

The cylinder pressure and AHRR curves are shown in Figures 5.8 and 5.9, respectively, for the  $SOI2$  sweep at  $15$  bar IMEPg for  $95\%$  PES and a fixed  $SOI1$  of  $280$  CAD.

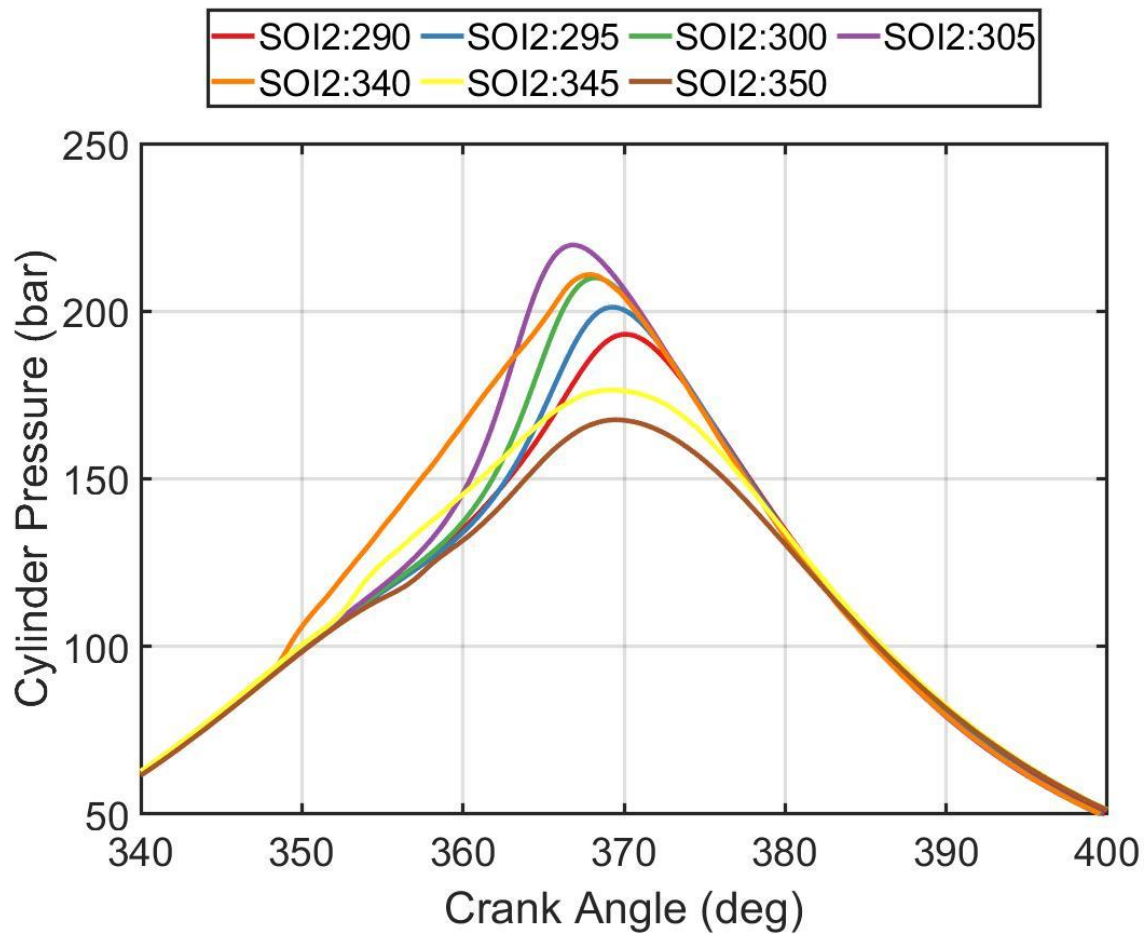


Figure 5.8. Cylinder pressure curves for an SOI2 sweep at 15 bar IMEPg, SOI1 = 280 CAD, PES = 95% with diesel/NG.

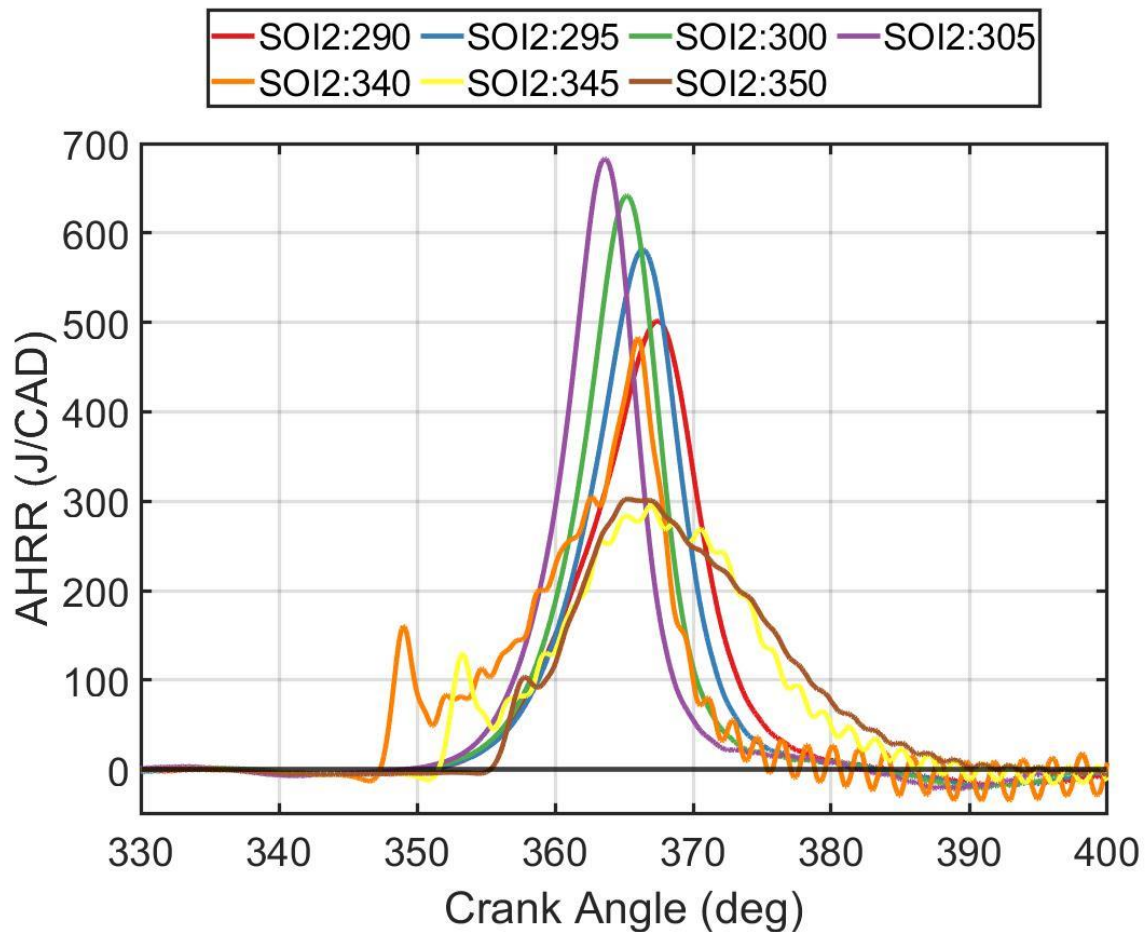


Figure 5.9. AHRR profiles for an SOI2 sweep at 15 bar IMEPg, SOI1 = 280 CAD, PES = 95% with diesel/NG.

The SOI2 sweep showed similar phenomenon to the SOI1 sweep, wherein when the SOI2 was positioned closer to TDC, there was an initial rise in the AHRR profile, possibly due to nonpremixed combustion occurring with the second injection within a combusting environment, followed by a more gradual increase in the AHRR profile to the peak value. For SOI2s that were positioned closer to SOI1 there was simply a single AHRR peak, and the peak AHRRs as well as the peak pressures, were higher than for those SOI2s that were positioned closer to TDC. The

CA5, CA50, CA90, and the combustion efficiency, IFCE, MPRR,  $COV_{IMEP}$ , and the emissions values are shown in Figure 5.10.

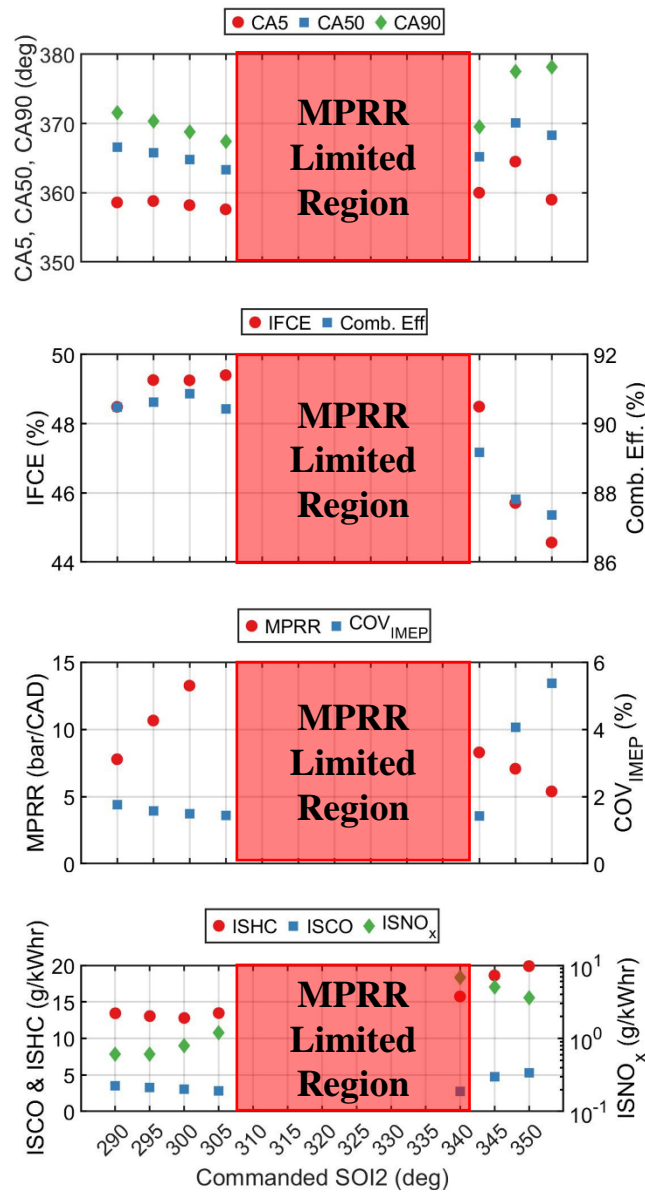


Figure 5.10. CA5, CA50, CA90, IFCE, combustion efficiency, MPRR,  $COV_{IMEP}$ , and emissions for an SOI2 sweep at 15 bar IMEPg, SOI1 = 280 CAD, PES = 95% with diesel/NG.

The IFCE is shown to be the highest at an SOI2 timing of 305 CAD. This also coincides with the combustion phasing occurring near TDC. As the combustion phasing occurs closer to TDC, there

is less fuel needed to achieve the load desired, and therefore the efficiency increases. This has a negative impact on MPRR, with the MPRR value at 305 CAD being right at the limit of 15 bar/CAD. It is also observed that the ISHC values at the advanced SOI2 timings of 290, 295, 300, and 305 CAD are lower than the ‘best’ operating point chosen for step (1), which was a single injection at 280 CAD. For the STARS method at high loads, it is evident that close coupled injections are better not only from an efficiency standpoint, but also from an emissions standpoint. The SOI2 timing of 295 CAD was chosen to move forward with the experimental framework, seeing as it had good emissions values, but also a high IFCE of just over 49%.

### **5.5.3 STEP 3: INJECTION SPLIT RATIO SWEEP**

The injection split ratio sweep is performed in the same fashion as presented in Chapter IV. During the injection ratio sweep for diesel-natural gas at 15 bar IMEPg load, an event occurred that needs to be addressed before discussing the data at length. During saving of a data point for the injection ratio sweep, a load discrepancy occurred wherein the indicated load continually increased while saving, as well as the MPRR values. No changes were being done by the engine operators while the data point was being saved, meaning that the increase in the load was caused by some unknown event occurring inside the combustion chamber. The MPRR for each cycle for the anomalous data point are shown in Figure 5.11.

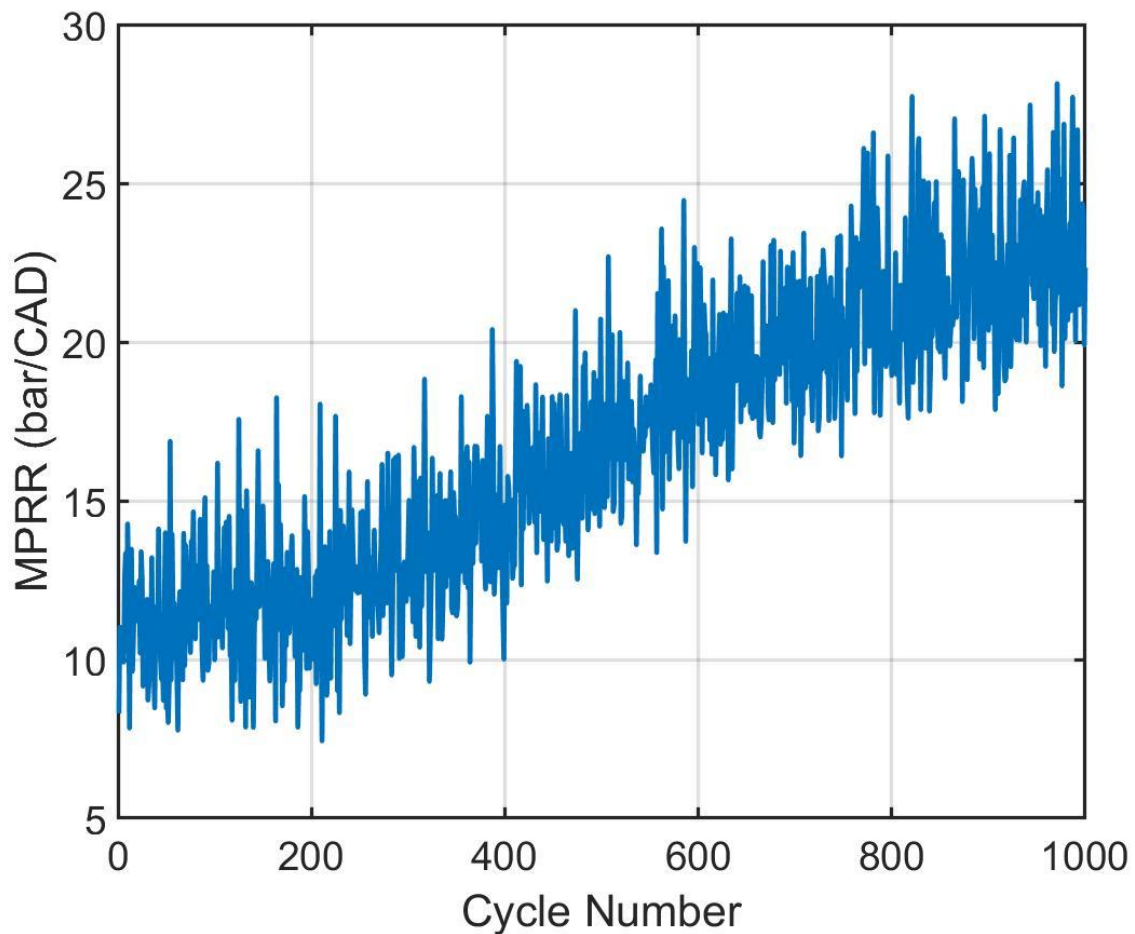


Figure 5.11. MPRR for each cycle for an injection split ratio of 0.48 at 15 bar IMEPg, SOI1 = 280 CAD, SOI2 = 295 CAD, and a PES = 95%.

As shown, the MPRR increased from ~11 bar/CAD at the beginning of saving the data point to over 20 bar/CAD at the end of saving the data point. Since there were no changes being made to the injection timing, injection duration, PES, or any other operating parameter during the course of saving the data point, the reason for the load increase is unknown. It is also important to mention that, after saving this data point, several discrepancies in the emissions data were found (i.e., when repeating the same points from steps (1) and (2), the same emissions values were not able to be achieved). Because of the discrepancies in the emissions values, an

explanation is required for this phenomenon. The first hypothesis was that the HRF injection system had malfunctioned to cause this issue, such as the injector tip becoming overheated and the needle inside the injector malfunctioning. To possibly rule this out, a comparison of specific data points that are taken each day is presented in Figure 5.12. These data points are for pure diesel operation, each of which uses the same injection timing and the same injection durations. These points are recorded for the sole purpose of comparing day-to-day changes in case an event such as that shown in Figure 5.11 ever occurred.

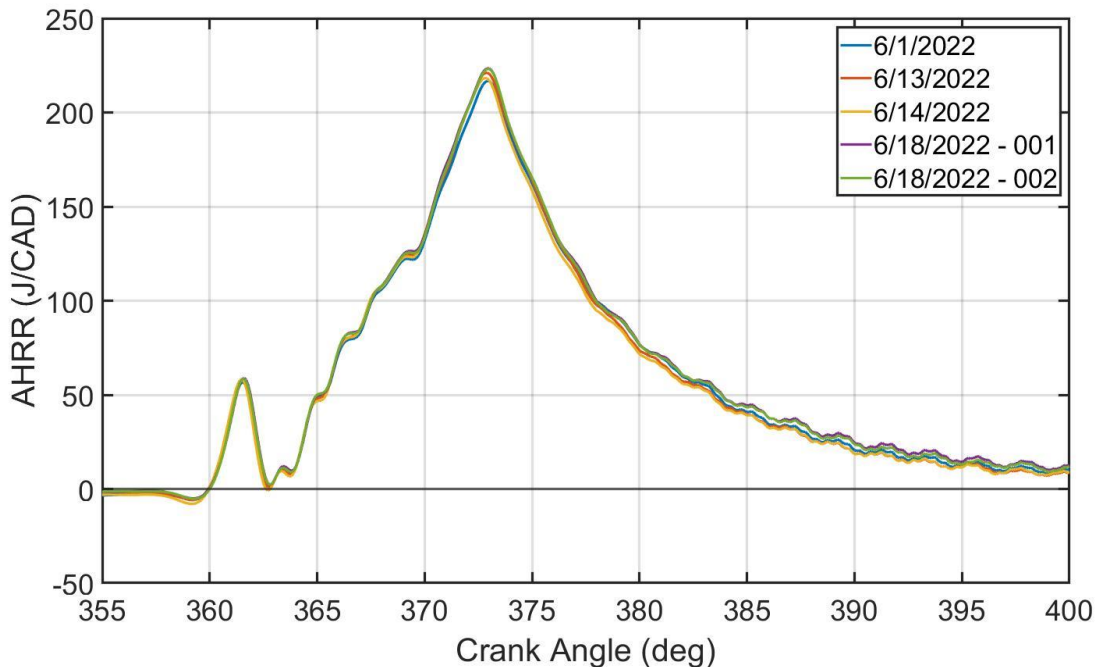


Figure 5.12. AHRR profiles for diesel only operating points.

The data point in question, which is shown in Figure 5.10, was taken on June 14, 2022. As shown in Figure 5.12, above, diesel only operating points for that day, as well as on June 18, 2022 are consistent. This data does not point to the HRF injection system as being the probable cause of the discrepancy. Still, there are significant differences in the emissions that are recorded when comparing data from the SOI2 sweep that was performed on the June 13, 2022 to the

injection ratio split data taken on the June 18, 2022. Figure 5.13 shows a comparison of data taken on the June 13, 2022, during the SOI2 sweep, at an injection split ratio of 0.59 to data taken on June 18, which is after the unexpected load increase event mentioned earlier, that has an injection ratio of 0.55.

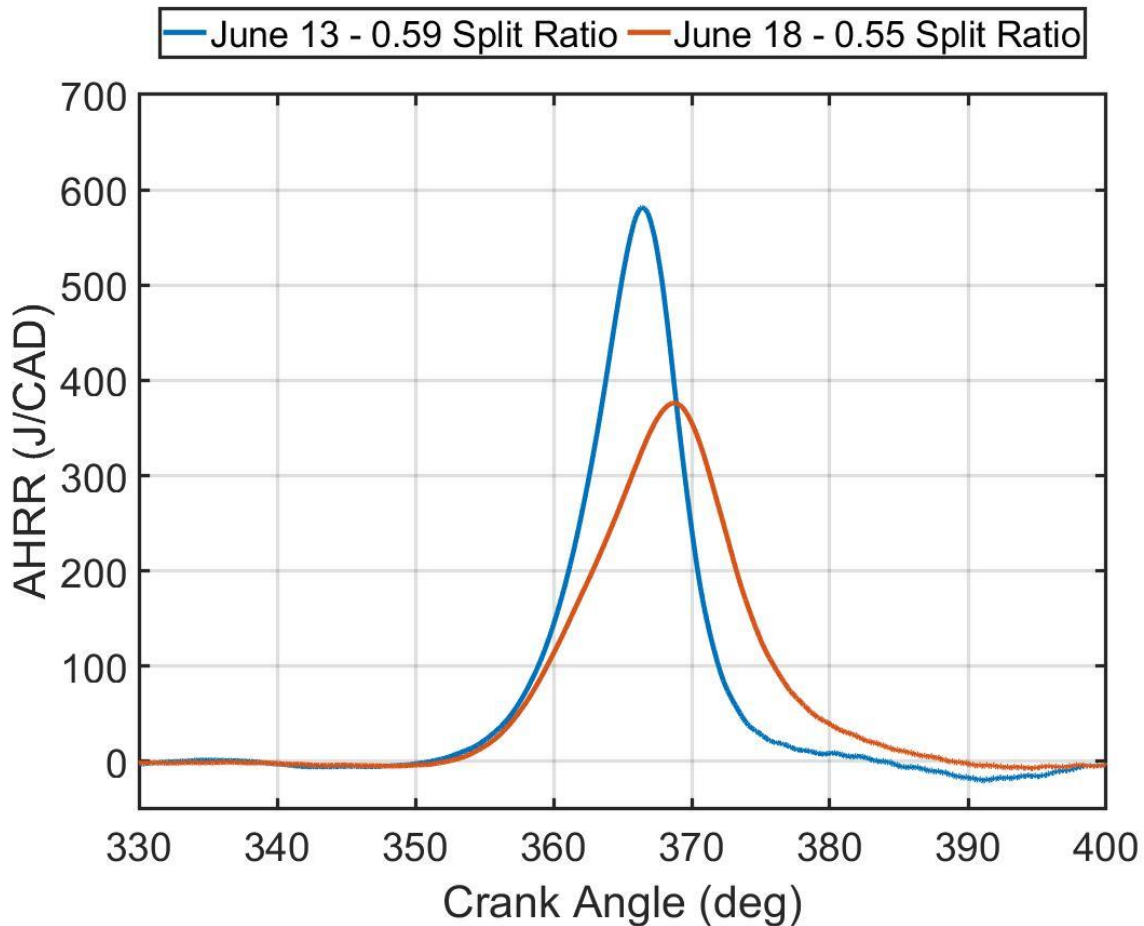


Figure 5.13. AHRR comparison between the data from June 13, 2022 and June 18, 2022 at similar injection split ratios, SOI1 = 280 CAD, SOI2 = 295 CAD, PES = 95%, and at 15 bar IMEPg.

The differences in the AHRR curves are significant from Figure 5.13 with the peak AHRR being significantly lower for the June 18 data compared to the June 13, 2022 data. This impacts the emissions significantly, with the ISHC, ISNO<sub>x</sub>, and ISCO emissions for June 18,

2022 being 17.68, 0.29, and 4.86 g/kWhr, respectively, while for June 13, 2022, the ISHC, ISNO<sub>x</sub>, and ISCO values were 13.05, 0.6, and 3.28 g/kWhr, respectively. To further determine if there is an issue with the HRF or the LRF fueling system, the average flowrates between the two days are presented in Table 5.5.

Table 5.4. Injection Timings, Injection Duration, Flowrates, and IMEP for June 13, 2022 and June 18, 2022 data.

Date / SOI1 dur. / SOI2 dur. / Split Ratio	Avg. Diesel Flowrate	Avg. NG Flowrate	Avg. P <sub>Rail</sub>	Avg. IMEP <sub>g</sub>
June 13 <sup>th</sup> /315u/530u/0.59	0.280 kg/hr	4.27 kg/hr	519 bar	15.1 bar
June 18 <sup>th</sup> /305u/550u/0.55	0.3024 kg/hr	4.29 kg/hr	519 bar	14.86 bar

The flowrates between these dates are comparable, as well as the average rail pressures and the IMEP<sub>g</sub> values. This also rules out any possible fluctuations of fuel composition (HRF or LRF) between these dates because any appreciable change in the LHV of either the HRF or the LRF would necessitate significant changes in the fuel flowrates to achieve the same 95% PES and 15 bar IMEP<sub>g</sub> load combination.

Currently, a working hypothesis for the observed differences is that the combination of low HRF fueling rates (which may have been insufficient to cool the injector tip) at such high PES as well as consistently high in-cylinder temperatures (due to the high load of 15 bar IMEP<sub>g</sub>) may have caused the injector tip to get extremely hot. This may lead to two effects: 1) it can

creates local hot spot(s) on the injector surface, similar to a glow-plug, and 2) it can change the injection characteristics because intense injector tip temperatures can cause erratic behaviors in the needle opening and closing, which could increase the amount of dribble that the injector experiences at these low injection durations. Unfortunately, any such issues with needle lift could not be confirmed because, as stated before, the injector on the 18.5:1 CR SCRE was not amenable for needle lift instrumentation. Nonetheless, this issue persisted throughout the remainder of the diesel-natural gas tests that were performed, as well as the POMDME-natural gas tests that were performed subsequently, meaning that a comparison between different steps of the experimental framework is not possible. Therefore, for the remainder of the work, emphasis will be placed on how the swept parameters impact emissions and combustion trends, rather than focusing on specific emission reductions or efficiency improvements from the start to the end of the experimental procedure.

The cylinder pressure and the AHRR curves for the injection split ratio sweep is shown in Figure 5.14.

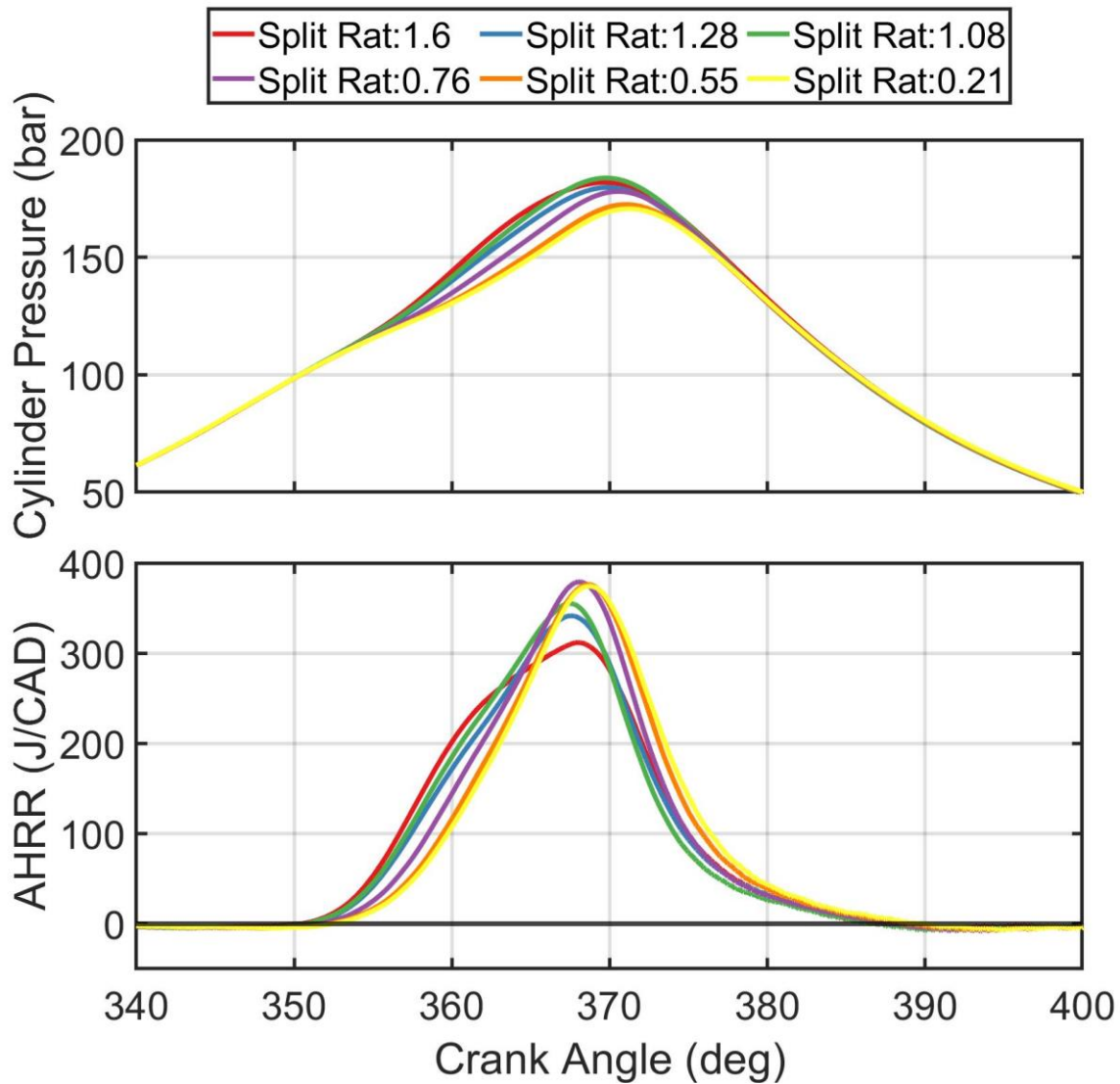


Figure 5.14. Cylinder pressure and AHRR profiles for an injection split ratio sweep at 15 bar IMEPg, SOI1 = 280 CAD, SOI2 = 295 CAD, PES = 95% with diesel/NG.

As the split ratio increases, meaning there is a longer injection duration for SOI1 than for SOI2, the peak cylinder pressure increases, but the peak AHRR decreases. The rate at which the AHRR increases is higher for higher split ratios than for lower split ratios. The CA5, CA50, CA90, as well as the IFCE, combustion efficiency, MPRR,  $COV_{IMEP}$ , and emissions are all shown in Figure 5.15.

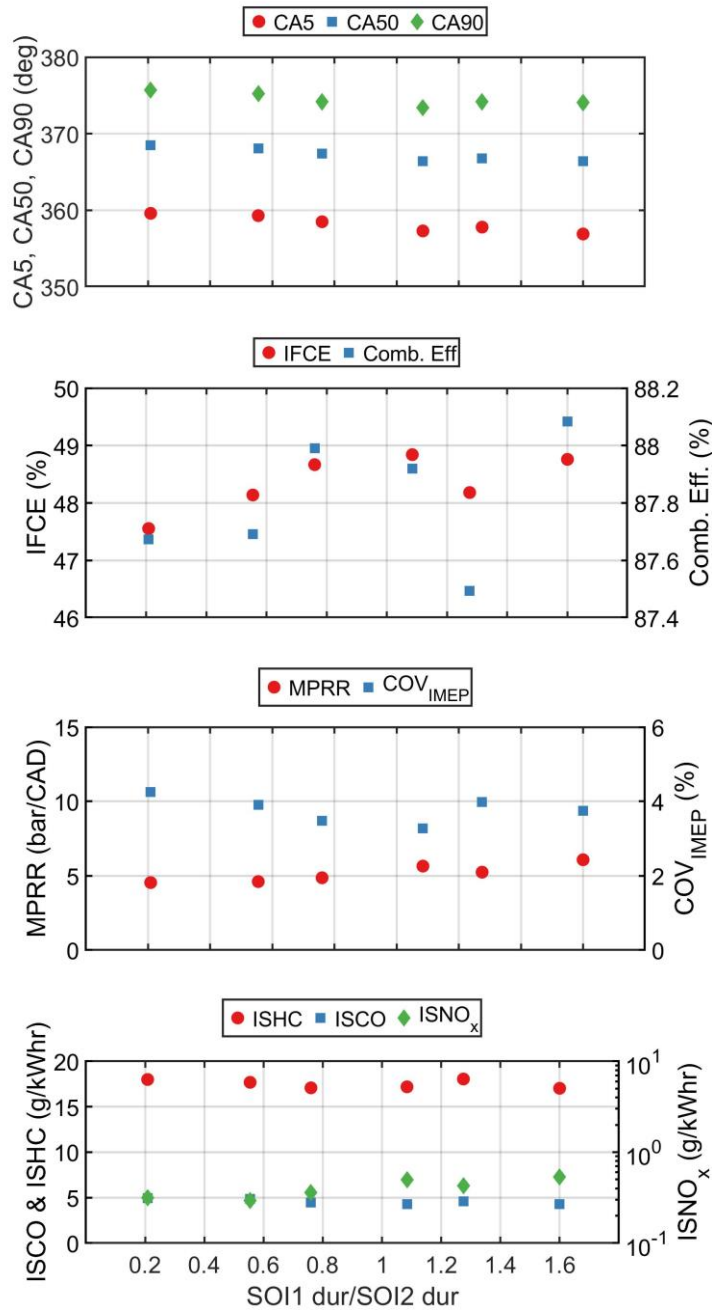


Figure 5.15. CA5, CA50, CA90, IFCE, combustion efficiency, MPRR, COV<sub>IMEP</sub>, and emissions for an injection split ratio sweep at 15 bar IMEPg, SOI1 = 280 CAD, SOI2 = 295 CAD, and a PES = 95% with diesel/NG

The IFCE is shown to increase slightly with increasing split ratio, which is likely due to the combustion phasing being phased slightly closer to TDC compared to lower split ratios. There

does not seem to be any benefit, from an emissions standpoint, in using particularly high or low injection split ratios. A split ratio of 0.59 was chosen to move to the next step, seeing as it had the ‘best’ emissions and efficiency values. This split ratio was chosen before realizing that the discrepancies in the emissions and combustion characteristics discussed at the beginning of this section would persist throughout the remainder of the testing. Therefore, the split ratio of 0.59 may not have been the “best” operating point. This theme will also continue in the following steps.

#### **5.5.4 STEP 4: RAIL PRESSURE SWEEP**

The rail pressure sweep was performed from a rail pressure range of 350 bar to 600 bar. The rail pressure was limited to only a 600 bar maximum pressure because of high  $COV_{IMEP}$  at higher rail pressures. In addition, there was no added benefit from a performance standpoint to increase the rail pressure. The cylinder pressure and the AHRR profiles are shown for the rail pressure sweep in Figure 5.16.

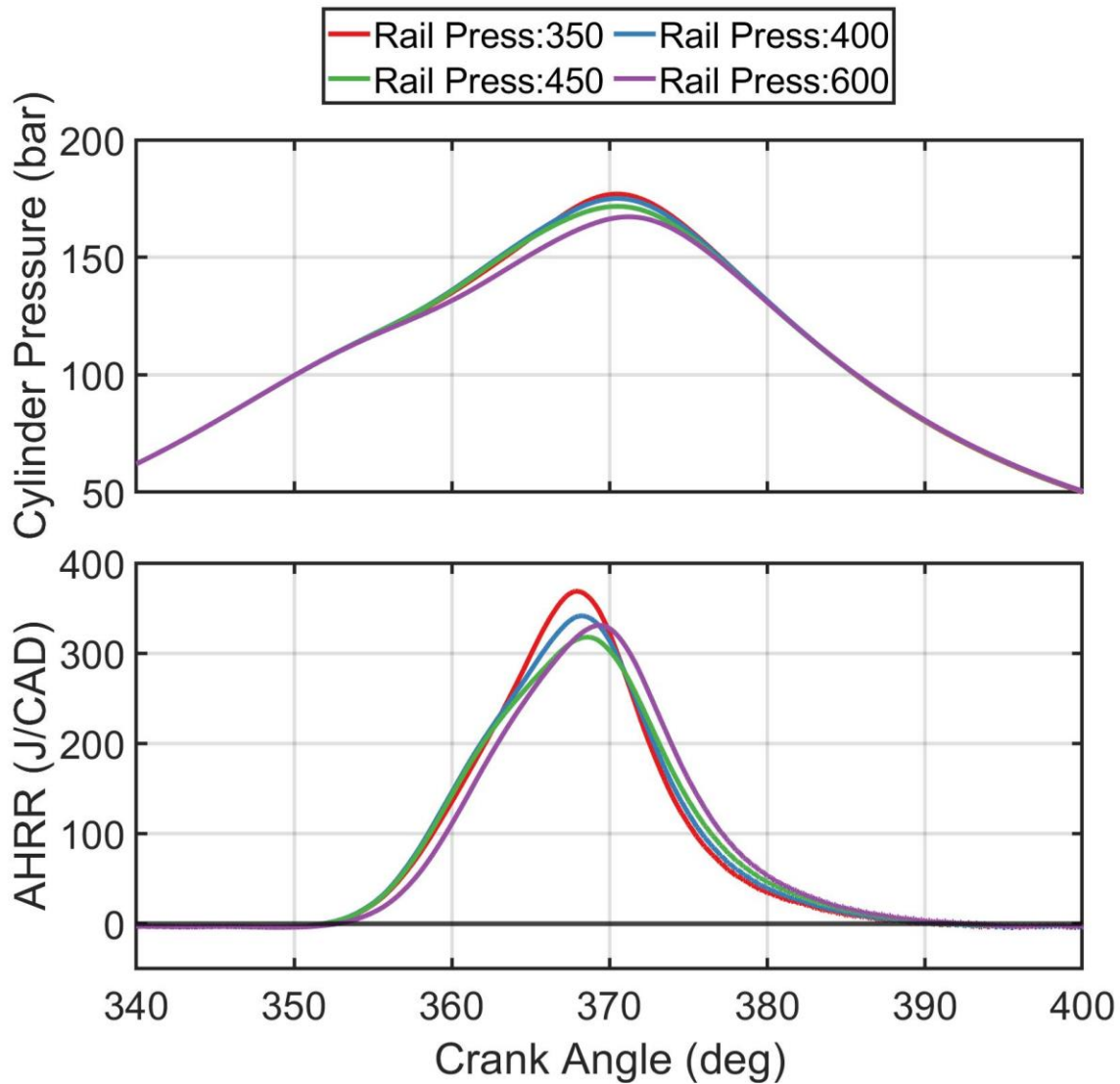


Figure 5.16. Cylinder pressure and AHRR profiles for a rail pressure sweep at 15 bar IMEP<sub>g</sub>, SOI<sub>1</sub> = 280 CAD, SOI<sub>2</sub> = 295 CAD, Split ratio = 0.59, and PES = 95% with diesel/NG.

The rail pressure does not show any significant changes to either the pressure or the AHRR curves over the rail pressure range tested. This is likely because the rail pressure was not varied significantly enough to cause any major changes to the combustion process. To verify this, the CA<sub>5</sub>, CA<sub>50</sub>, CA<sub>90</sub>, as well as the MPRR, COV<sub>IMEP</sub>, IFCE, combustion efficiency, and the emissions for the rail pressure sweep are shown in Figure 5.17.

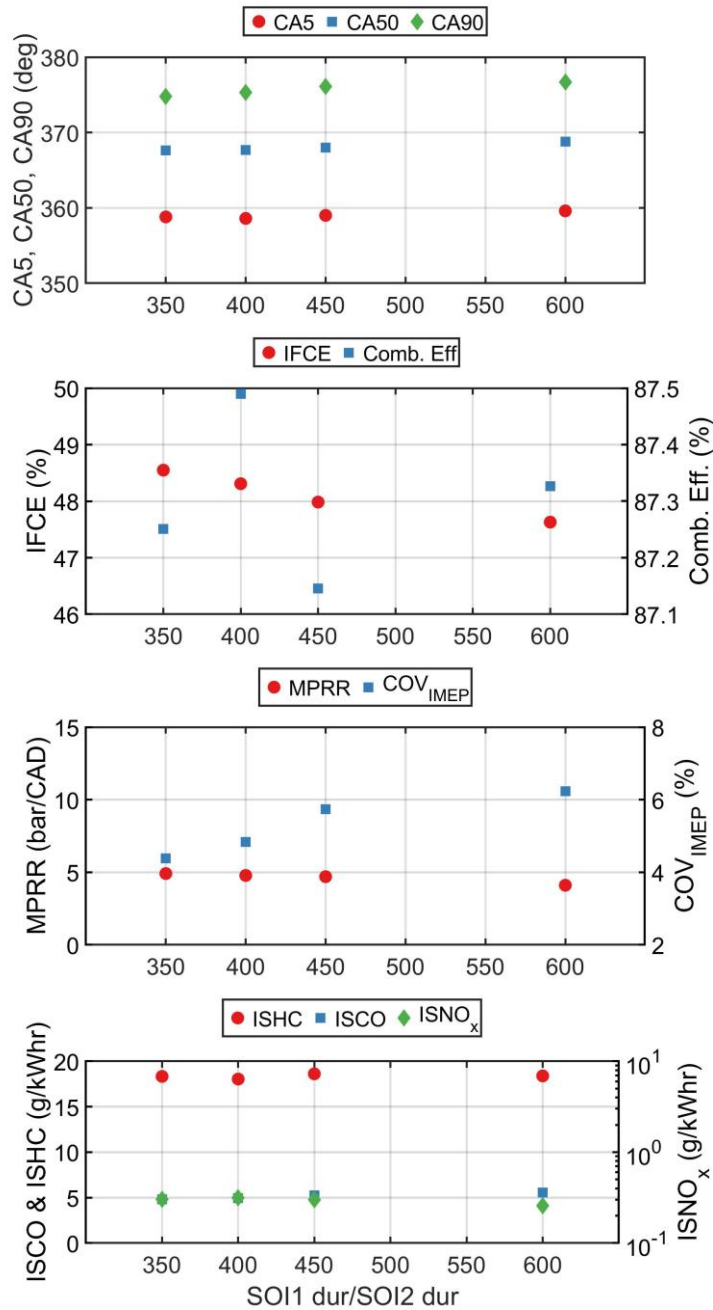


Figure 5.17. CA5, CA50, CA90, IFCE, combustion efficiency, MPRR, COV<sub>IMEP</sub>, and emissions for a rail pressure sweep at 15 bar IMEP<sub>g</sub>, SOI1 = 280 CAD, SOI2 = 295 CAD, Split Ratio = 0.59, and a PES = 95% with diesel/NG.

As shown in Figure 5.17, the rail pressure was not increased beyond 600 bar because there were no signs of any efficiency gains to be made at higher rail pressures, not to mention the increase

in the  $COV_{IMEP}$  that happened as rail pressure increased. The emissions values were also stagnant across the entire rail pressure sweep. For these reasons, a rail pressure of 500 bar was chosen to move forward with, seeing as it had given good results in previous steps.

### 5.5.5 STEP 5: COUPLED SOI SWEEP

The coupled SOI sweep was an addition to the experimental campaign in comparison with the 5 bar IMEPg experiments discussed previously. The idea for the coupled SOI sweep was conceived after performing the 5 bar IMEPg experiments, with the hypothesis being that by using the STARS technique, the operating range of possible injection timings could be expanded, and therefore greater efficiencies could be achieved. The cylinder pressure and AHRR profiles for the coupled SOI sweep are shown in Figures 5.18 and 5.19, respectively.

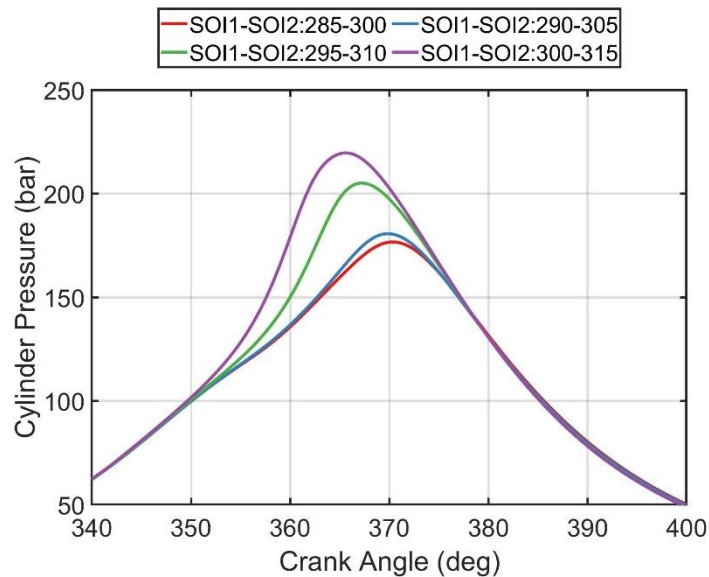


Figure 5.18. Cylinder pressures for a coupled SOI sweep at 15 bar IMEPg, Split ratio = 0.59,  $P_{Rail} = 500$  bar and PES = 95% with diesel/NG.

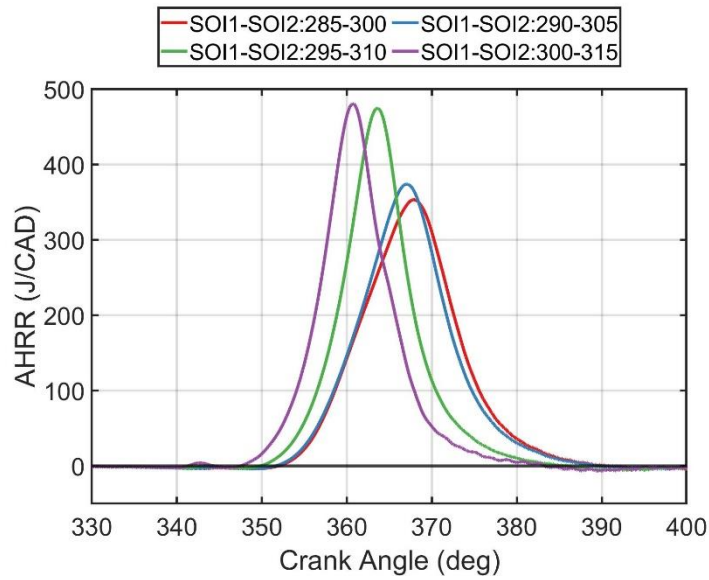


Figure 5.19. AHRR profiles for a coupled SOI sweep at 15 bar IMEP<sub>g</sub>, split ratio = 0.59, P<sub>Rail</sub> = 500 bar and PES = 95% with diesel/NG

With the goal of the 15-bar IMEP<sub>g</sub> study being higher IFCEs, it was decided to move the coupled injection timings toward TDC to attempt to phase the combustion phasing closer to TDC. It was observed that the peak AHRR values increased, and the location of the peak AHRR values advanced, as expected. The peak cylinder pressure also increased and the location advanced as well. To determine the impact of this sweep on efficiency and emissions, further analysis is needed. The CA<sub>5</sub>, CA<sub>50</sub>, CA<sub>90</sub>, as well as the IFCE, combustion efficiency, MPRR, COV<sub>IMEP</sub>, and the emissions values are presented in Figure 5.20.

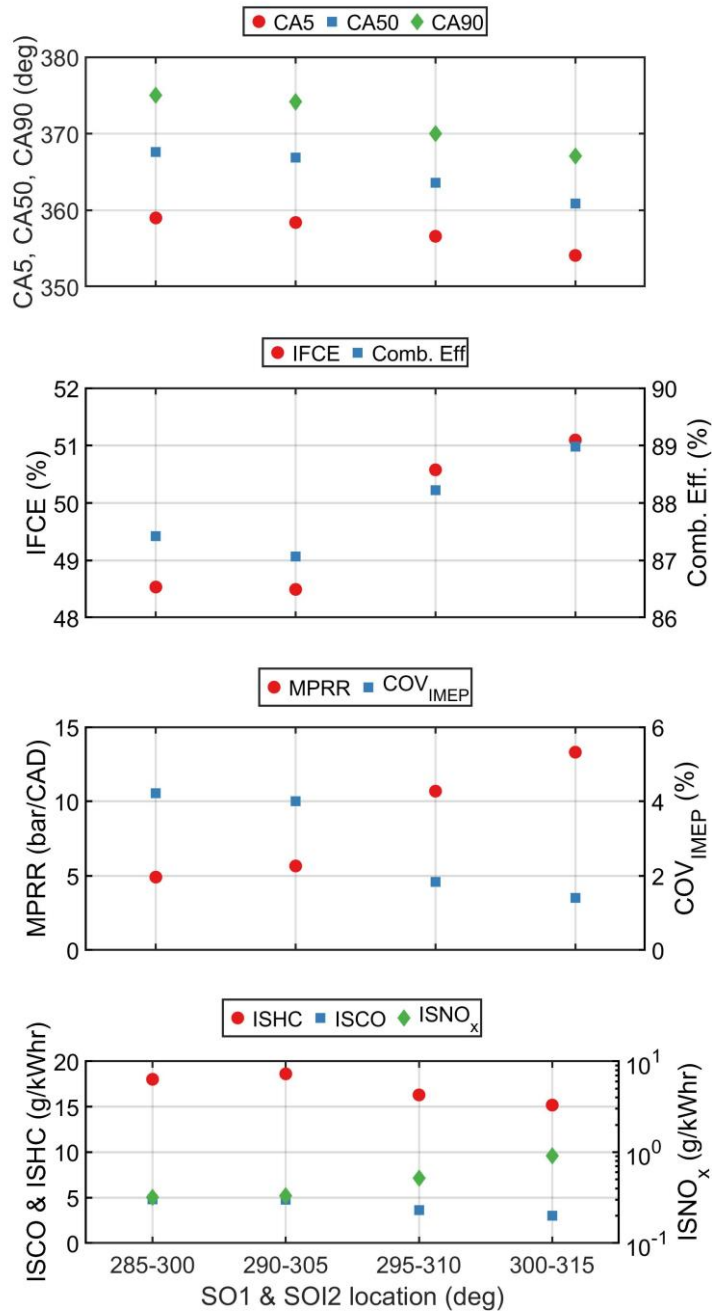


Figure 5.20. CA5, CA50, CA90, IFCE, combustion efficiency, MPRR, COV<sub>IMEP</sub>, and emissions for a coupled SOI sweep at 15 bar IMEP<sub>g</sub>, split ratio = 0.59, P<sub>Rail</sub> = 500 bar, and a PES = 95% with diesel/NG.

As expected, as the coupled SOI pair is moved toward TDC, the combustion phasing advances toward TDC, occurring just after TDC for the 300-315 CAD timing. As the coupled SOI pair is

moved toward TDC, the MPRR also increases, as well as the ISNO<sub>x</sub> values to maximum levels of ~14 bar/CAD and just under 1 g/kWhr, respectively. This is expected because the combustion phasing is closer to TDC, as mentioned earlier. The IFCE also increases to above 51% for the 300-315 CAD SOI pair, and the ISHC and ISCO also decrease to 15 g/kWhr and 4 g/kWhr, respectively.

It should also be noted that the operating range was extended by using the STARS method. In the SOI1 sweep from step (1), the MPRR limited range of injection timings extended between 340 CAD and 305 CAD with 95% PES. With the STARS method, however, the MPRR limited range was reduced seeing as an injection timing of 315 CAD was possible, which was not possible with a single injection.

The coupled SOI pair of 295-310 CAD was chosen to move forward with the intake boost pressure sweep. Even though the 300-315 CAD pair showed a greater IFCE, the MPRR was already near the limit of 15 bar/CAD. Experience with reducing the boost pressure from the 5 bar IMEPg experiments indicated that when the boost pressure is reduced, the MPRR would increase. To give as much room as possible for a boost pressure sweep, but also to choose the 'best' operating point from the coupled SOI sweep, the 295-310 CAD pair was chosen.

### 5.5.6 STEP 6: BOOST PRESSURE SWEEP

The boost pressure sweep is the last parameter to be swept within the experimental framework. The pressure and AHRR curves for the boost sweep are shown in Figure 5.21.

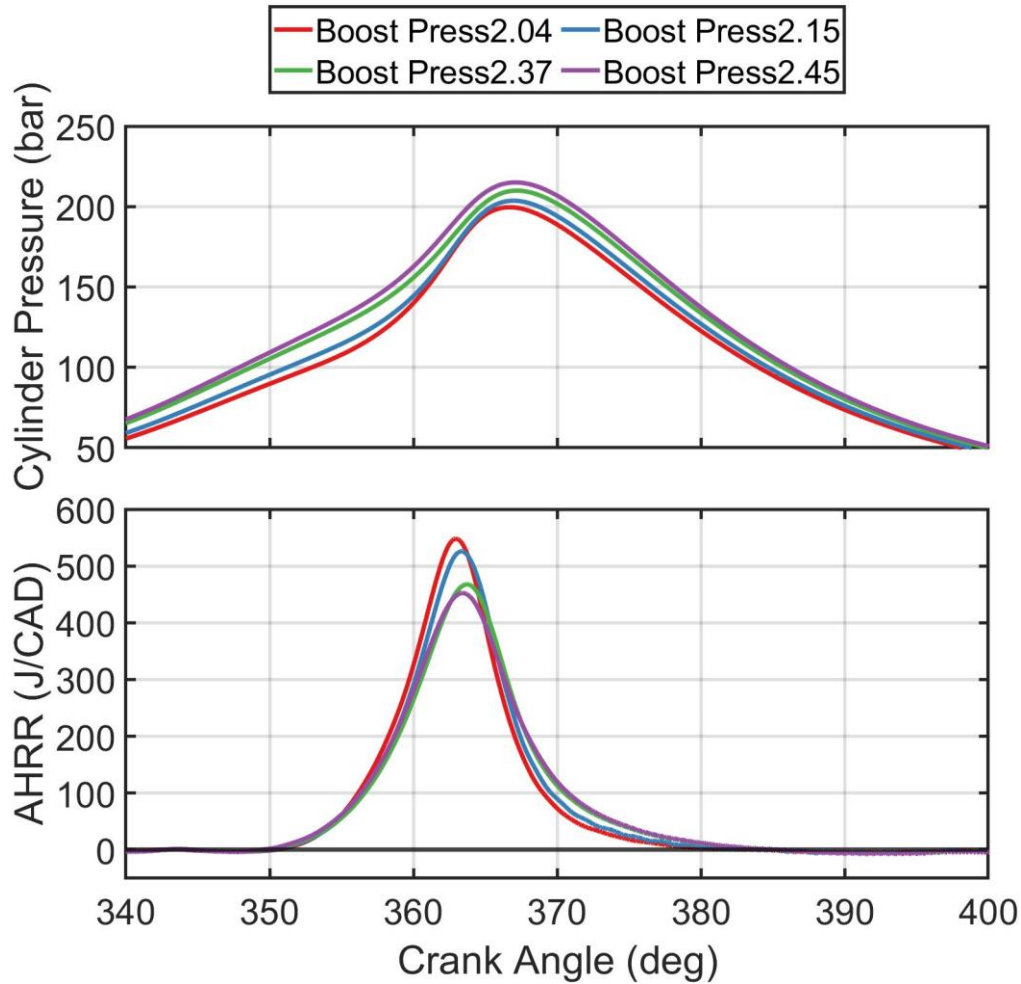


Figure 5.21. Cylinder pressure and AHRR profiles for a boost pressure sweep at 15 bar IMEPg, SOI1 = 295 CAD, SOI2 = 310 CAD, split ratio = 0.59,  $P_{\text{Rail}} = 500$  bar and PES = 95% with diesel/NG.

It is observed that as boost pressure is reduced, the peak AHRR is increased, and the location of peak AHRR is slightly advanced. By decreasing the boost pressure, the air flow rate is reduced, thereby increasing the fuel/air ratio and the global equivalence ratio. A higher global equivalence ratio could lead to higher local equivalence ratios, which in turn, leads to higher

local temperatures, faster reactions, and more rapid heat release. This could explain why the AHRR has a higher peak value at the lower boost pressures. The CA5, CA50, CA90, as well as the IFCE, combustion efficiency, MPRR,  $COV_{IMEP}$ , and the emissions results are presented for the boost pressure sweep in Figure 5.22.

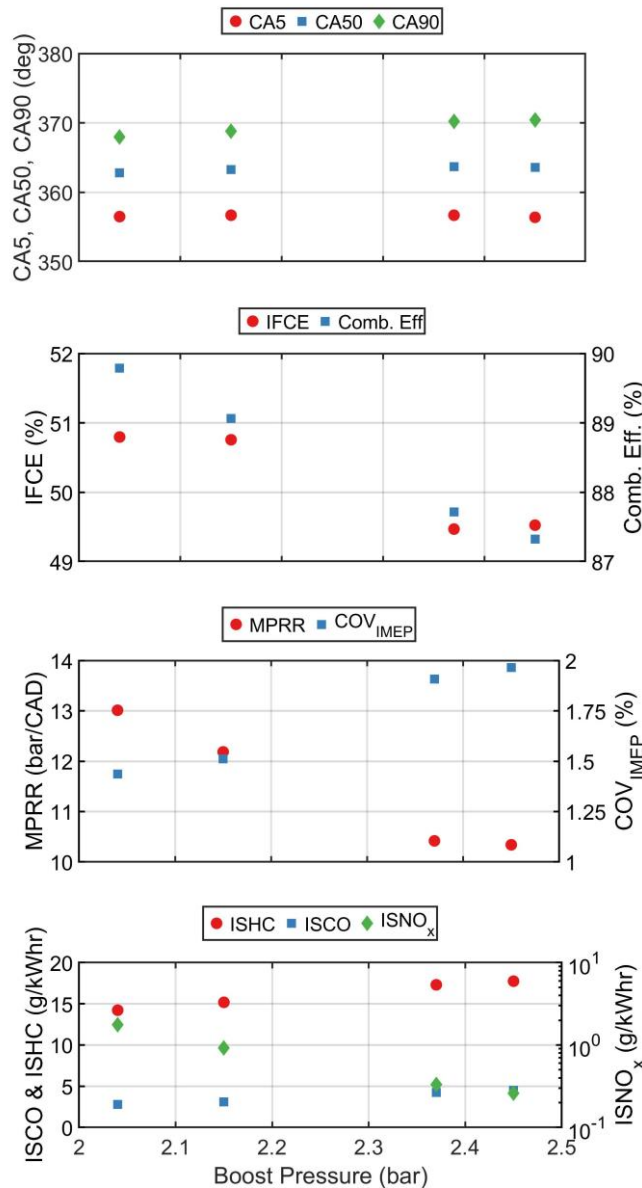


Figure 5.22. CA5, CA50, CA90, IFCE, combustion efficiency, MPRR, COV<sub>IMEP</sub>, and emissions for a coupled SOI sweep at 15 bar IMEP<sub>g</sub>, split ratio = 0.59, P<sub>Rail</sub> = 500 bar, and a PES = 95% with diesel/NG.

As with the 5 bar IMEPg load, the ISCO emissions are slightly reduced as boost pressure is decreased, which is likely due to higher bulk gas temperatures from the increased global equivalence ratios. The IFCE and combustion efficiencies also both increase as the boost pressure is decreased, although it appears that there is a limit to the IFCE increase as decreasing boost pressure from 2.15 bar to 2.04 bar does not result in a huge improvement in IFCE. The ISHC emissions also steadily decrease as boost pressure decreases, which is likely again due to the increased bulk gas temperatures resulting from increased global equivalence ratios. This also impacts ISNO<sub>x</sub>, as the lowest boost pressure of 2.04 bar resulted in ISNO<sub>x</sub> values over 1 g/kWhr.

## **5.6 EXPERIMENTAL RESULTS – POMDME/NATURAL GAS**

As with the 5 bar IMEPg data, the entire experimental campaign was repeated using POMDME as the HRF instead of diesel. One of the main reasons for considering POMDME instead of diesel is because of the potential reduction in particulate matter that accompanies POMDME usage. Unfortunately, the smoke meter that was available to use during testing was not functioning properly at the high load condition, and continuously gave errors in reading, and therefore there are no smoke number results to show for the 15 bar IMEPg experiments. However, if we compare the effect of POMDME at 5 bar IMEPg, we expect the smoke to be even lower for POMDME-NG compared to diesel-NG even for the higher load of 15 bar IMEPg.

### **5.6.1 STEP 1: PES & SOI SWEEP**

As with the diesel-natural gas sweep described in the previous section, the POMDME-natural gas experiments also included a composite PES and SOI sweep. The emissions results for all the data points are shown in Figure 5.23. The goal was to advance the injection timing as much as possible, to achieve the lowest ISNO<sub>x</sub> emissions. Therefore, the PES was swept in a much larger step than for diesel-natural gas, so that the extreme points could be studied.

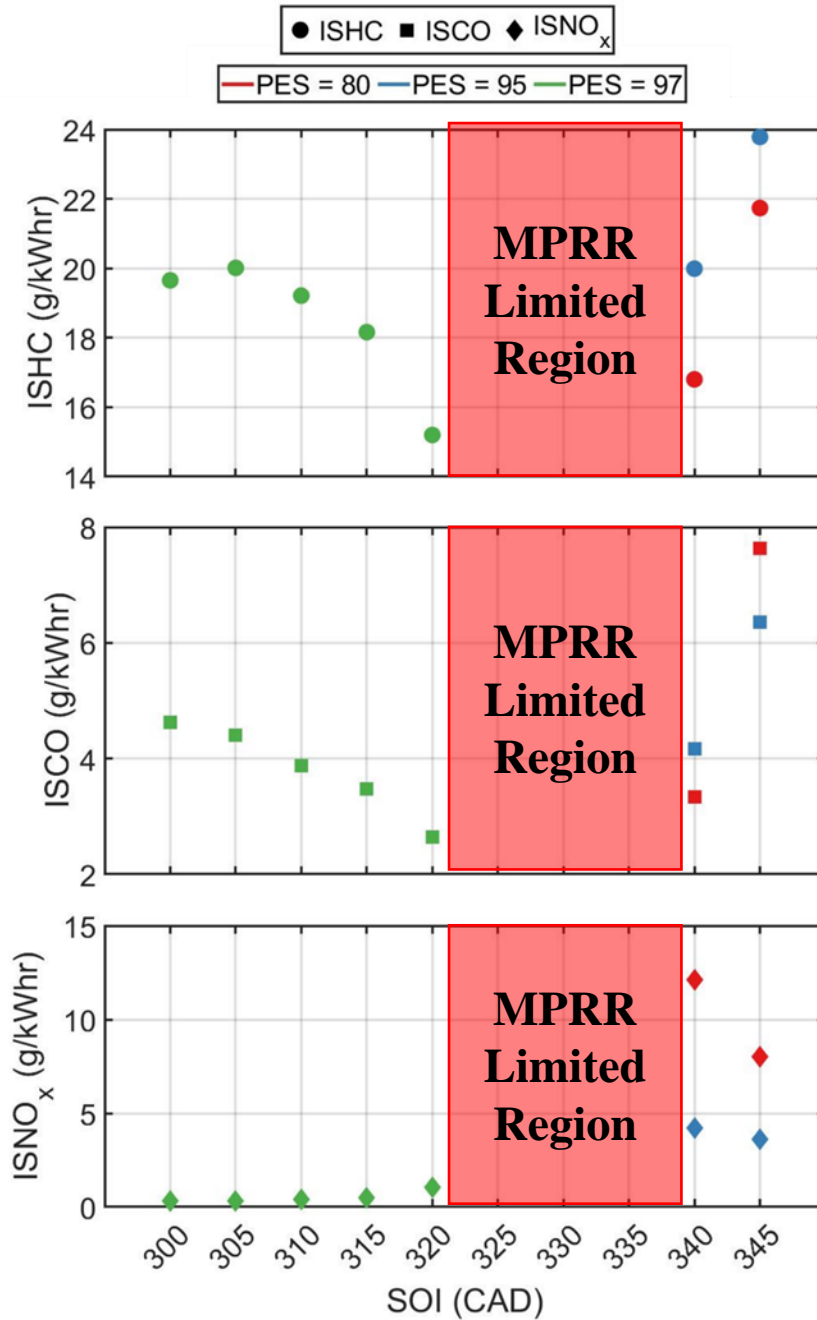


Figure 5.23. ISHC, ISCO, and ISNO<sub>x</sub> values for an SOI and PES sweep using diesel/POMDME operation at 15 bar IMEPg

As shown in Figure 5.23, a PES value of 95%, which was used for diesel-natural gas, could not be used for POMDME-NG for the advanced SOIs. The limitation was the excessive

MPPR for very early SOIs. Therefore, the PES was increased to 97%, and the SOI was able to be advanced all the way to 300 CAD. A detailed analysis of the combustion characteristics, including the AHRR profiles, cylinder pressures, etc. was performed.

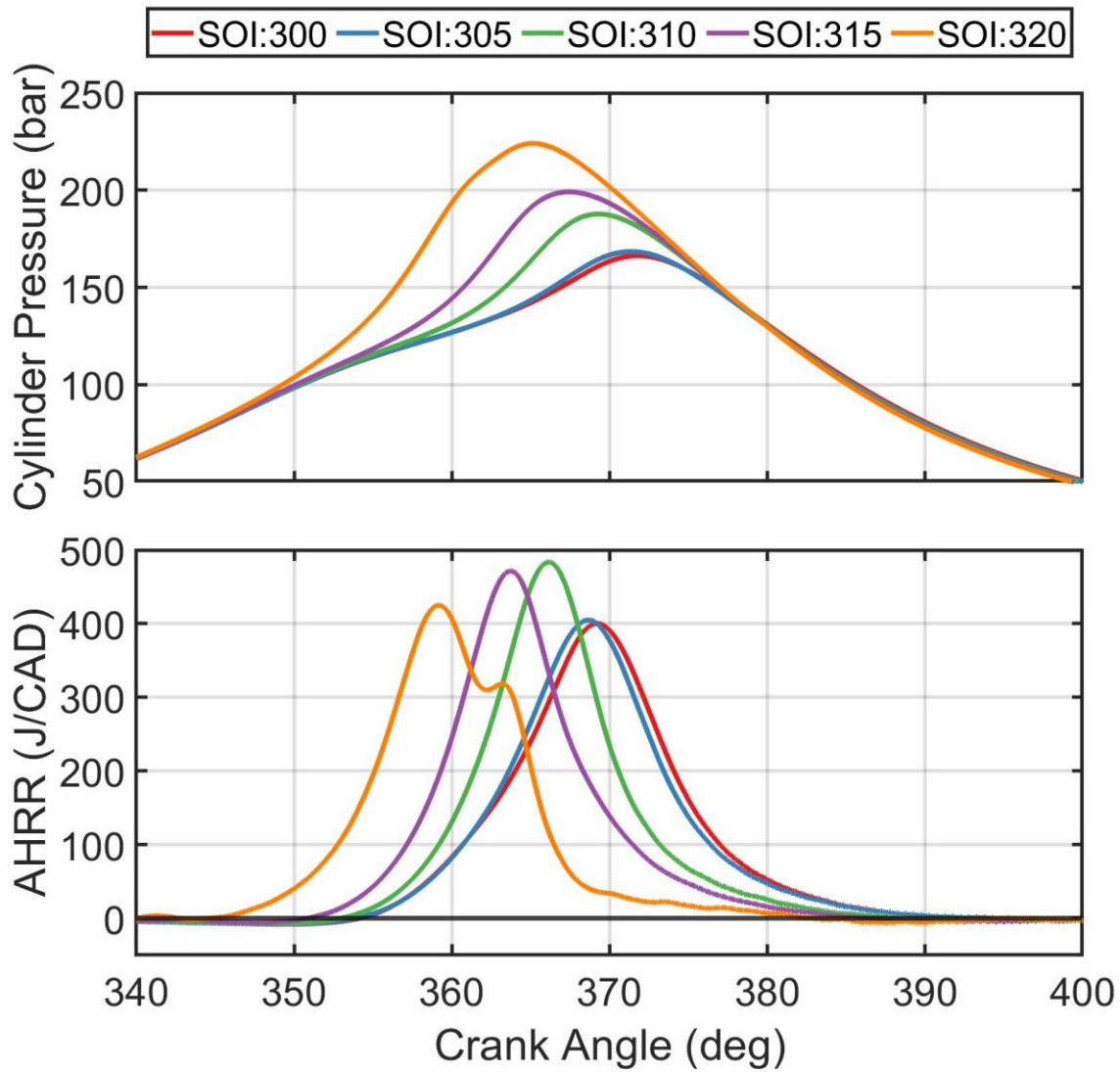


Figure 5.24. Cylinder pressure and AHRR profiles for SOI sweep at 15 bar IMEPg, 97% PES, with POMDME/NG combustion.

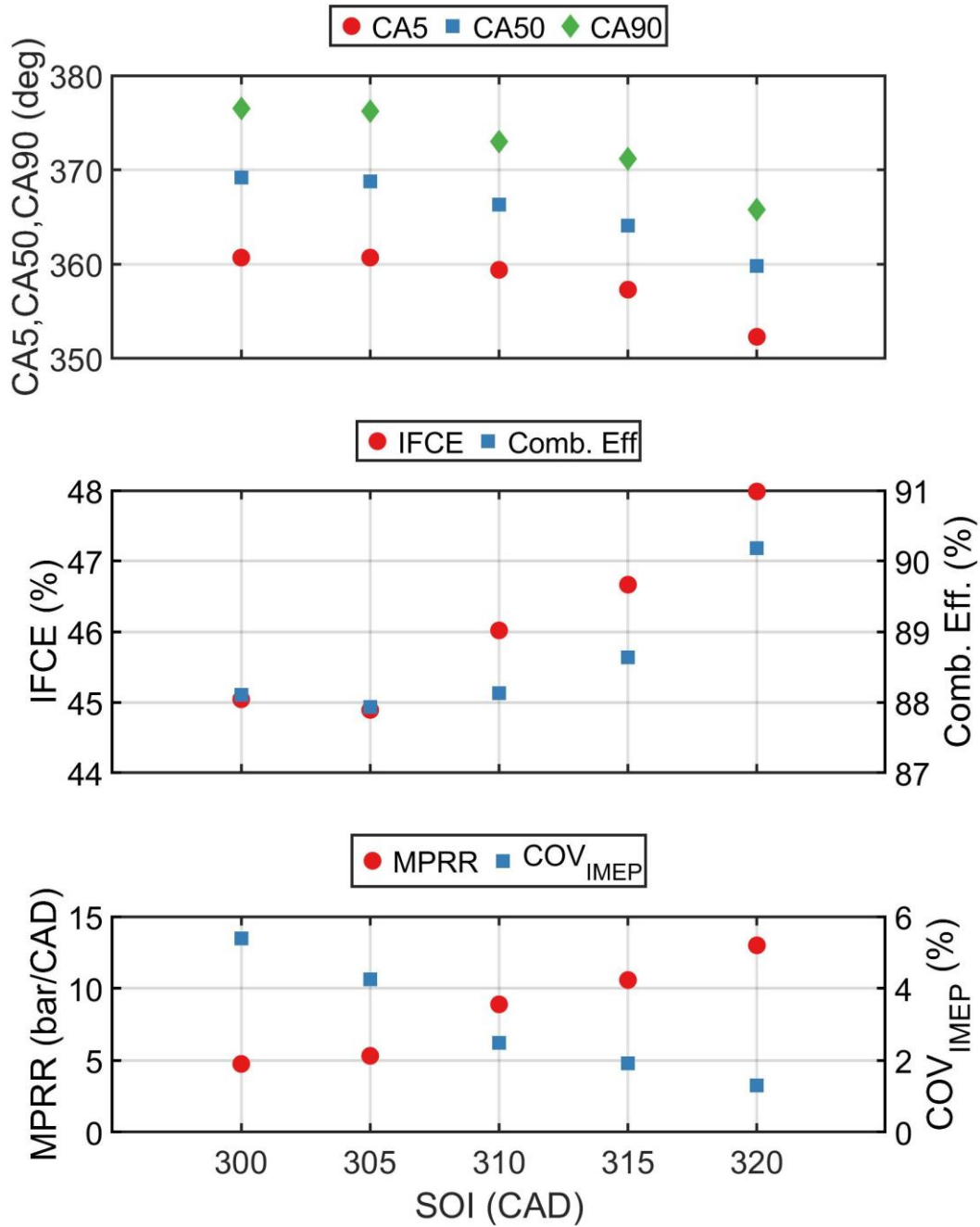


Figure 5.25. CA5, CA50, CA90, IFCE, combustion efficiency, MPRR, and COV<sub>IMEP</sub>, for an SOI sweep at 15 bar IMEPg, PES = 97% with POMDME/NG.

Similar to diesel-NG combustion, as the SOI is advanced, the combustion phasing is phased away from TDC, thereby decreasing the IFCE and the combustion efficiency 45% and 88%, respectively. The MPRR is reduced to 5 bar/CAD as the SOI is advanced, but the COV<sub>IMEP</sub>

increases to 5% with advancing SOI. The  $ISNO_x$  values are all relatively low (at or around 1 g/kWhr) but as the injection timing is advanced, the  $ISNO_x$  decreases further to well under 1 g/kWhr. The ISHC and ISCO emissions do not decrease, and instead increase with advancing SOI, to 20 and 4.6 g/kWhr, respectively. This is likely due to more cycle-to-cycle variations, as well as improper combustion phasing.

To move on to step 2, which is to introduce a second injection (i.e., STARS), a ‘best’ injection timing must first be chosen for 97% PES. The 300 CAD SOI was chosen to move forward for the following reasons: 1) while the  $COV_{IMEP}$  is technically above the not-to-exceed limit of 5%, it was known from both the 5 bar IMEPg data as well as the 15 bar IMEP diesel-NG data that introducing a second injection improves the combustion stability, thereby making  $COV_{IMEP}$  better, 2) the MPRR values (~5 bar/CAD) are very favorable for moving forward with the experimental flowchart, seeing as it gives more room for improvement; if a later SOI with a higher MPRR were to be chosen it could restrict the number of possible operating points in subsequent steps, and 3) the  $ISNO_x$  values are the lowest (0.31 g/kWhr) for the SOI 300 CAD case.

### 5.6.2 STEP 2: SECOND INJECTION (STARS) SWEEP

The cylinder pressure and AHRR curves for the SOI2 sweep are shown in Figure 5.26.

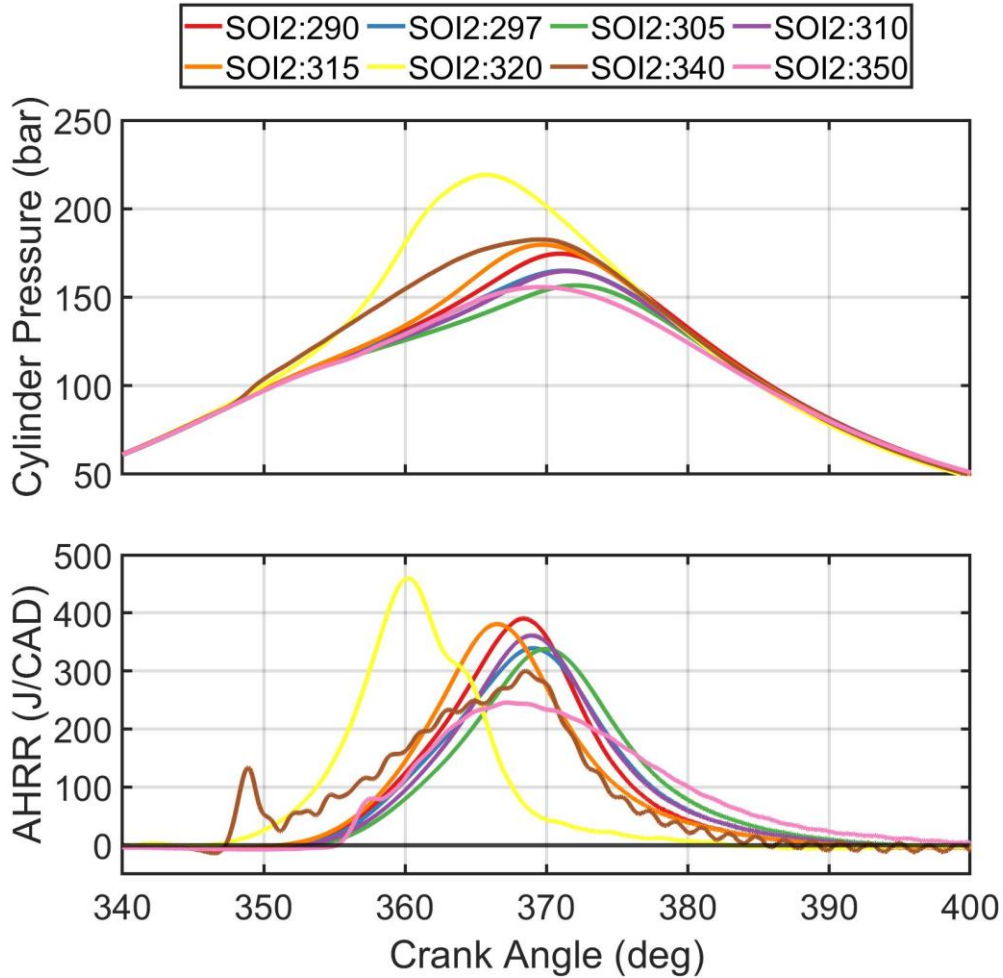


Figure 5.26. Cylinder pressure and AHRR profiles for an SOI2 sweep at 15 bar IMEPg, SOI1 = 300 CAD, PES = 97% with POMDME/NG

As shown in Figure 5.26, as the SOI2 is advanced up to a certain degree, the cylinder pressure curve and the AHRR curve peaks are also advanced, but then start to move closer to TDC with further SOI advancement. There is also an evident transformation of the AHRR curve from two distinct peaks at 340 CAD SOI to a single stage Gaussian heat release at advanced

SOIs. The CA5, CA50, CA90, as well as the MPRR, COV<sub>IMEP</sub>, IFCE, combustion efficiency, and the emissions results are shown in Figure 5.27.

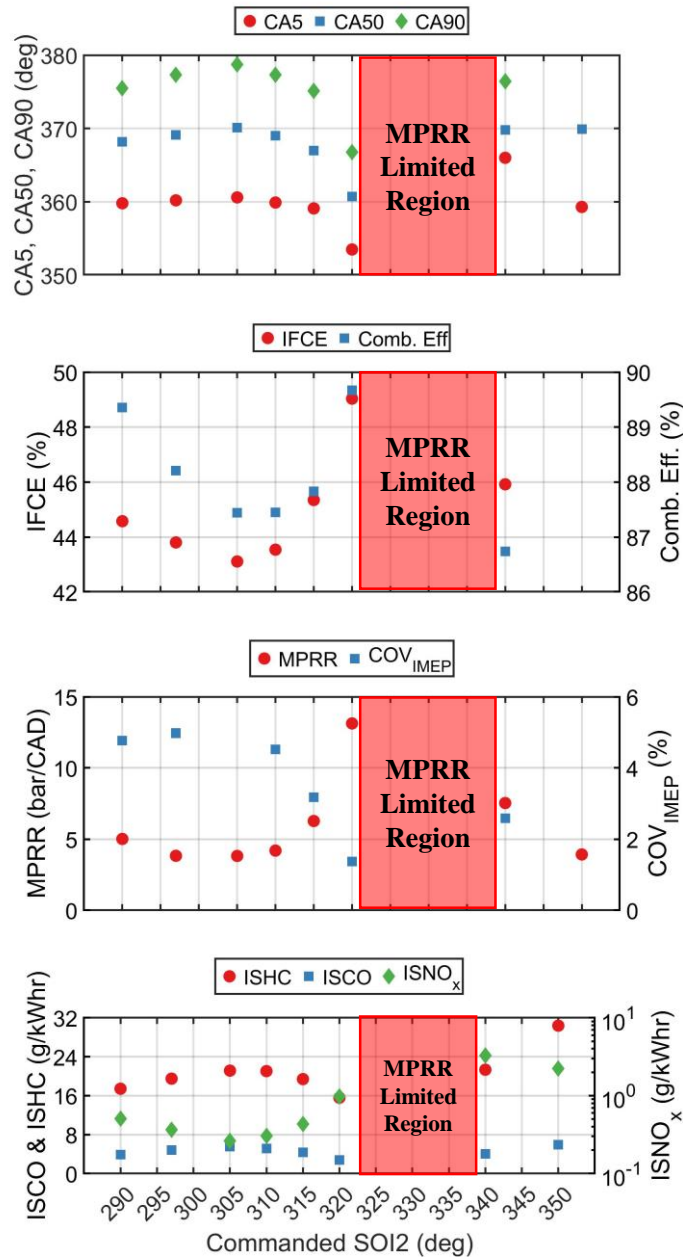


Figure 5.27. CA5, CA50, CA90, IFCE, combustion efficiency, MPRR, COV<sub>IMEP</sub>, and emissions for an SOI2 sweep at 15 bar IMEPg, SOI1 = 300 CAD, and a PES = 97% with POMDME/NG

As SOI2 is advanced, the ISHC emissions are nearly halved from a maximum of 30.39 g/kWhr at an SOI2 of 350 CAD to 17.43 g/kWhr at an SOI2 of 290 CAD. The ISNO<sub>x</sub> emissions also decreased with SOI advancement to a minimum value of 0.26 g/kWhr at an SOI2 of 305 CAD, and all SOI2s from 320 CAD to 290 CAD were below 1 g/kWhr ISNO<sub>x</sub>. The MPRR values were lower for the advanced SOI2 timings, with all MPRR values for SOI2 timings before 315 CAD having less than 6.2 bar/CAD maximum pressure rise. The IFCE reached a peak of ~49% at an SOI2 timing of 320 CAD, but the MPRR value at this SOI2 was too close to the limit of 15 bar/CAD to be considered the ‘best’ operating point for further studies. Ultimately, the 310 CAD SOI2 was chosen to move forward with the experimental framework. While this SOI2 had one of the lowest IFCE values, it was chosen because of the low MPRR values and keeping in mind the potential for significant IFCE and MPRR improvements with the other steps. Using prior knowledge of how the coupled SOI sweep works from the diesel-natural gas experiments (i.e., when sweeping both the SOIs together), it is known that starting from a lower MPRR value is valuable in extending the operability range. This, combined with the low NO<sub>x</sub> values were used as the criteria for selecting this SOI2.

### **5.6.3 STEP 3: INJECTION SPLIT RATIO SWEEP**

The injection split ratio sweep was performed for POMDME-natural gas at 15 bar IMEPg at an SOI1 of 300 CAD, and an SOI2 of 310 CAD, with a PES of 97%. The results from the injection ratio sweep, as with previous injection ratio sweeps, showed little to no variation in the cylinder pressure or AHRR curves, as well as the emissions results. The IFCE, combustion efficiency, and the emissions results are shown in Figure 5.28.

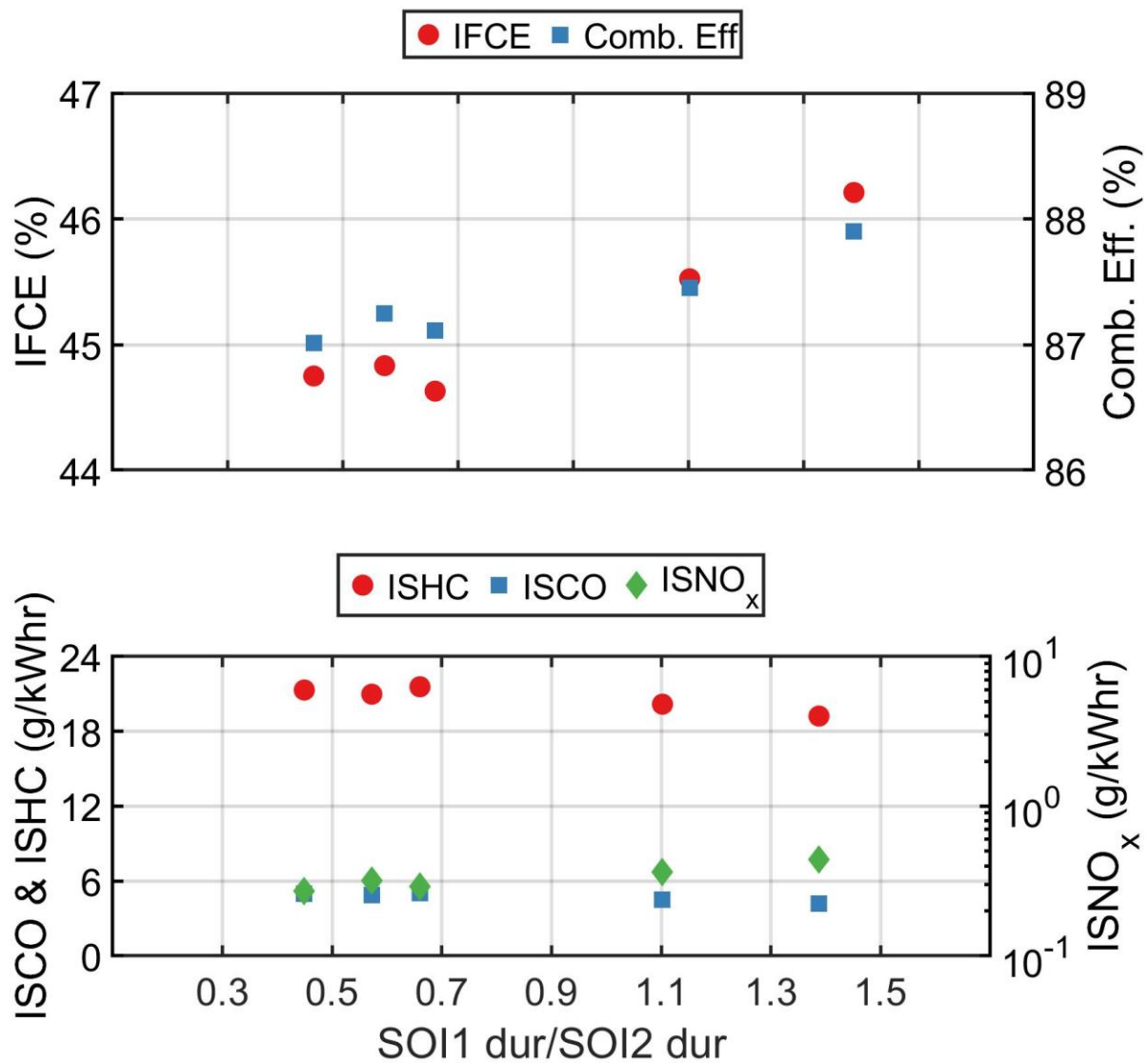


Figure 5.28. IFCE, combustion efficiency, and emissions for an injection ratio sweep at 15 bar IMEPg, SOI1 = 300 CAD, SOI2 = 310 CAD, and a PES = 97% with POMDME/NG

There was a slight increase in the ISHC and a slight decrease in the ISNO<sub>x</sub> values with decreasing split ratio, which coincided with a decrease in the IFCE and combustion efficiency. With the next step in the experimental campaign being the coupled injection sweep, the split ratio of 0.45 was chosen to move on to the next step. Even though this was a low efficiency point, it was thought that the coupled injection sweep could improve the efficiency, and the

added benefit of having a slightly lower  $\text{NO}_x$  value was determined to be beneficial. However, starting from a higher split ratio could result in slightly different ‘best’ operating conditions in subsequent steps, and further studies need to be performed to investigate this.

#### 5.6.4 STEP 4: COUPLED SOI SWEEP

. The cylinder pressure and AHRR profiles are shown in Figures 5.29 and 5.30, respectively.

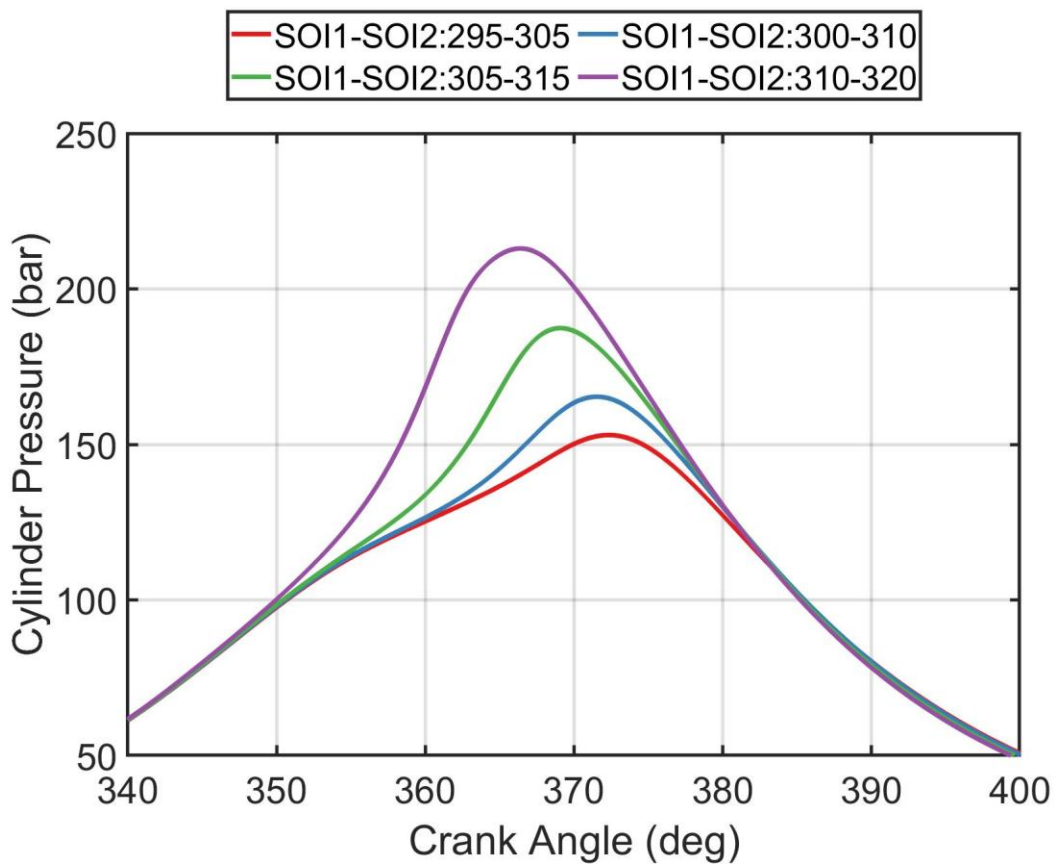


Figure 5.29. Cylinder pressures for a coupled SOI sweep at 15 bar IMEP<sub>g</sub>, split ratio = 0.45, and PES = 97% with POMDME/NG

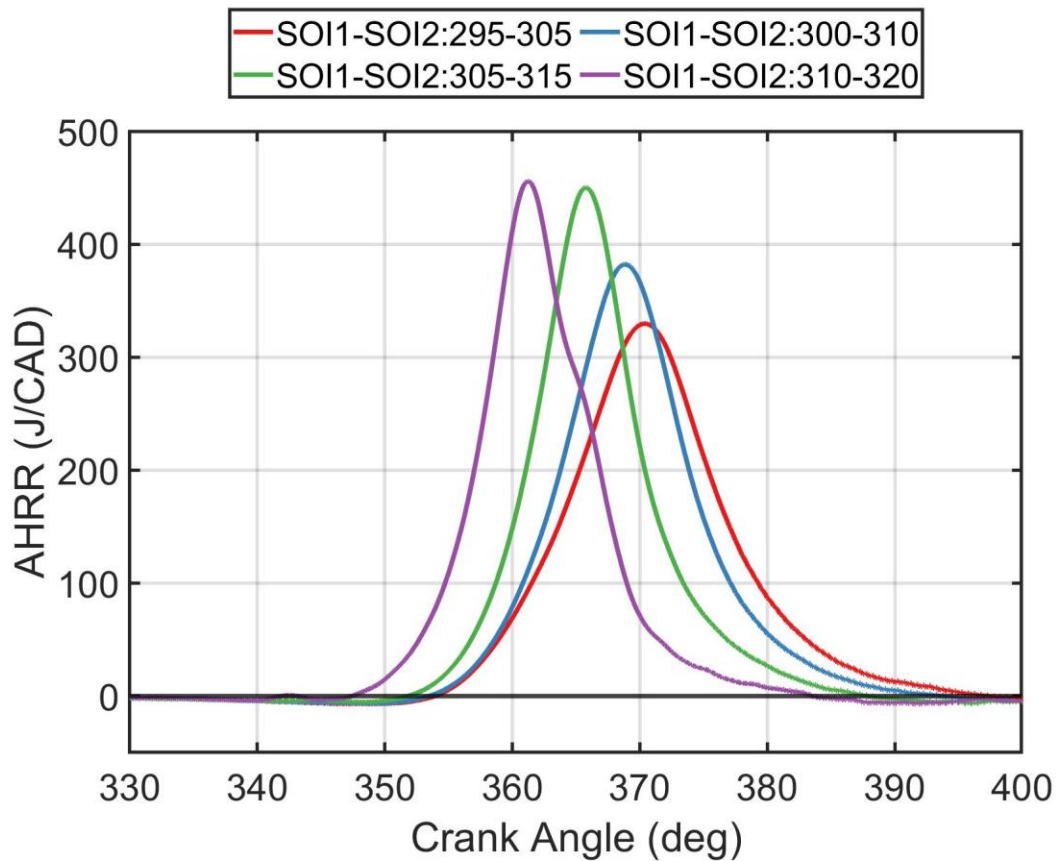


Figure 5.30. AHRR profiles for a coupled SOI sweep at 15 bar IMEP<sub>g</sub>, split ratio = 0.45, and PES = 97% with POMDME/NG

As the SOI pair is moved toward TDC, the peak AHRR and peak cylinder pressures both increase and occur earlier. This aligns with what was observed in the diesel-natural gas data. The CA5, CA50, CA90, as well as the IFCE, combustion efficiency, MPRR, COV<sub>IMEP</sub>, and the emissions results are shown in Figure 5.31.

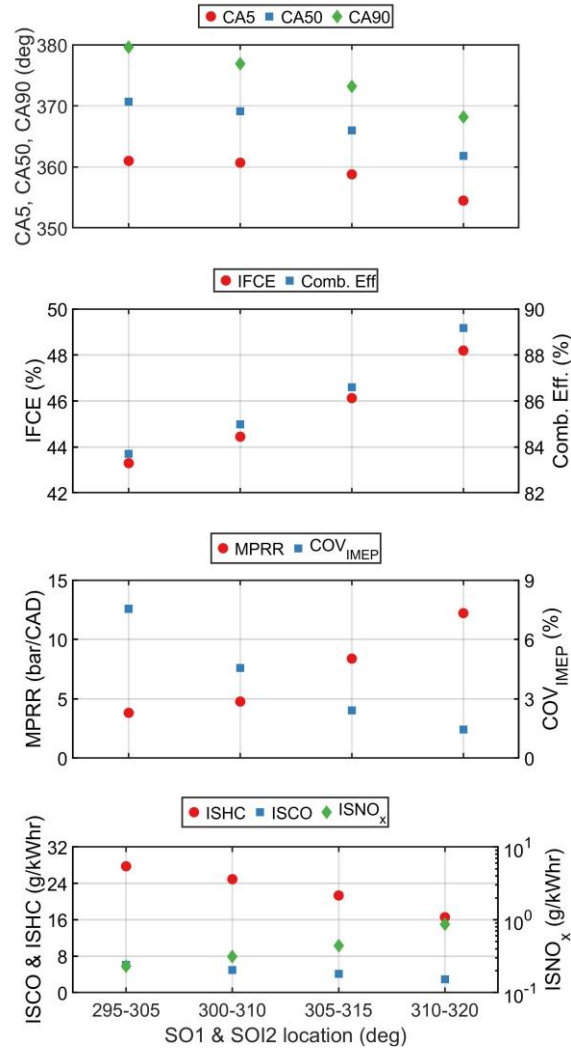


Figure 5.31. CA5, CA50, CA90, IFCE, combustion efficiency, MPRR, COV<sub>IMEP</sub>, and emissions for a coupled SOI sweep at 15 bar IMEPg, split ratio = 0.45, and a PES = 97% with POMDME/NG

As expected, the IFCE increases dramatically from ~41% to ~48% over the coupled SOI timing range studied. This level of IFCE increase may not have been possible if a different split ratio, or a different SOI1 and SOI2 timing were chosen, especially if the starting MPRR values or ISNO<sub>x</sub> emissions had been higher. Therefore, it was advantageous to select points that had low MPRR up to this stage, so that the maximum IFCE benefit could be achieved, while also maintaining

ISNO<sub>x</sub> values below 1 g/kWhr. The ISHC and ISCO emissions also decreased over the coupled SOI range studied. This is likely due to a more optimized combustion phasing, as combustion phasing was phased closer to TDC as the coupled SOI pair was moved toward TDC.

Based on the efficiency and emissions results discussed here, it was decided to move forward with the 305-315 CAD coupled SOI pair. While the IFCE of the 310-320 CAD coupled SOI pair was better than the 305-315 CAD coupled SOI pair, the MPRR was also too close to the limit of 15 bar/CAD for any further significant sweeps to be performed, especially considering that boost pressure reduction raises MPRR significantly, as observed from the diesel-natural gas data. Therefore, to make sure the rest of the experimental framework could be performed, the 305-315 CAD coupled SOI pair was chosen.

#### **5.6.5 STEP 5: RAIL PRESSURE SWEEP**

The rail pressure was swept both higher than the baseline of 500 bar and lower to determine if there were any improvements in the emissions or the efficiency values. The cylinder pressure and the AHRR profiles for the rail pressure sweep are shown in Figure 5.32.

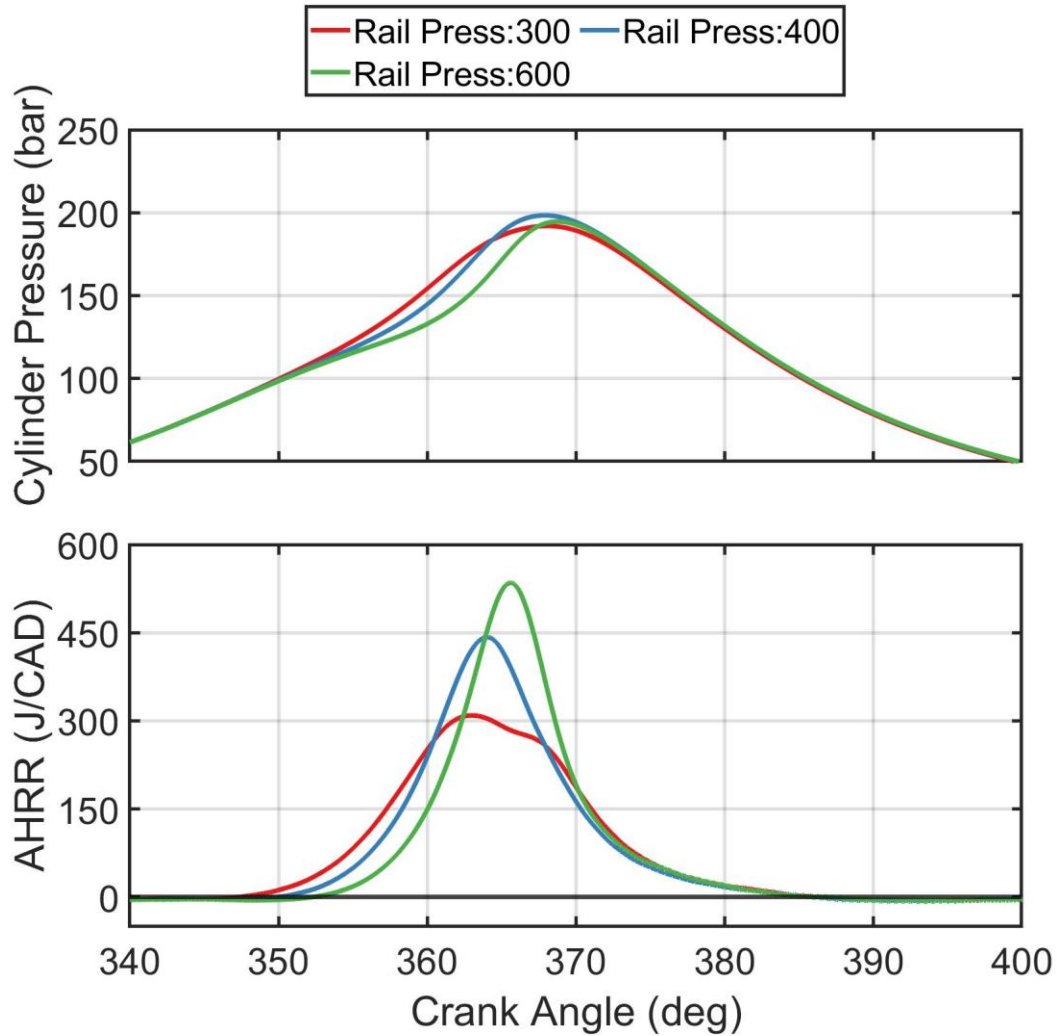


Figure 5.32. Cylinder pressure and AHRR profiles for a rail pressure sweep at 15 bar IMEP<sub>g</sub>, SOI<sub>1</sub> = 305 CAD, SOI<sub>2</sub> = 315 CAD, split ratio = 0.45, and PES = 97% with POMDME/NG

The peak AHRR value increases with increasing rail pressure while the value of peak cylinder pressure appears less affected by the increase in rail pressure. The changes are manifested in the pressure rise rates. As the rail pressure is increased, the pressure rise rates increase, most likely due to greater distributed ignition occurring throughout the cylinder because of better mixing due to greater spray penetration. This phenomenon was not noticed in the diesel-natural gas data for the rail pressure sweep, most likely because diesel has a higher

LHV than that of POMDME, which means there is less fuel requirement for diesel than for POMDME to achieve the same PES and load. With the higher fuel flow rate of POMDME, the injector remain open for longer, meaning there was more time for greater spray penetration and atomization that eventually affect combustion. The CA5, CA50, CA90, as well as the IFCE, combustion efficiency, MPRR,  $COV_{IMEP}$ , and the emissions results are all shown in Figure 5.33.

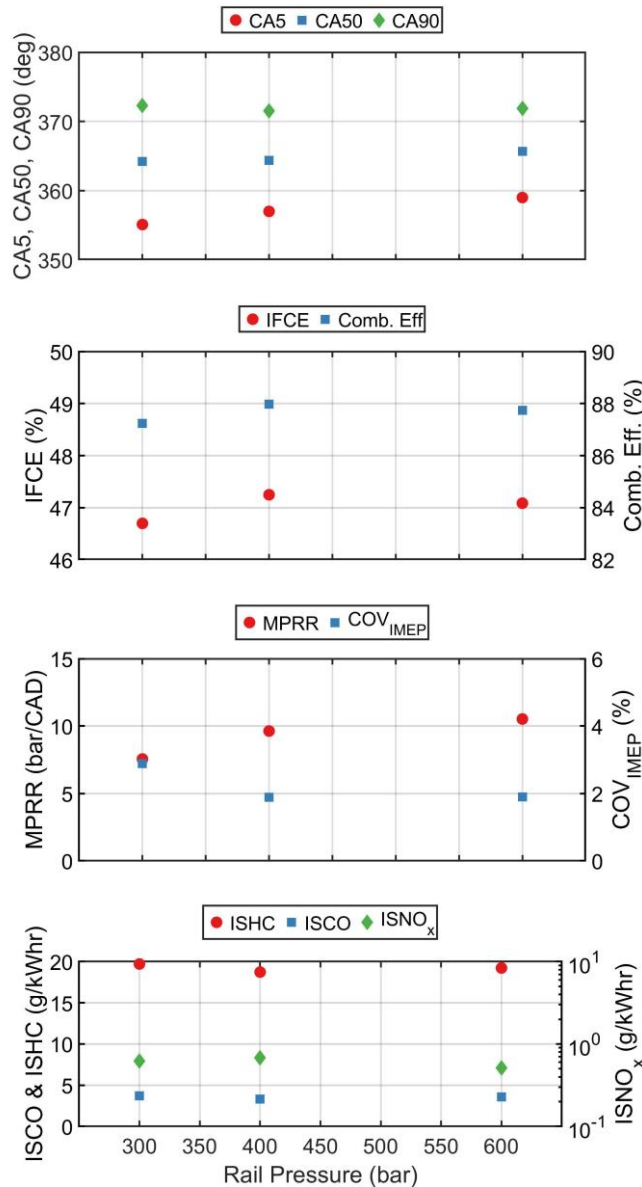


Figure 5.33. CA5, CA50, CA90, IFCE, combustion efficiency, MPRR, COV<sub>IMEP</sub>, and emissions for a rail pressure sweep at 15 bar IMEPg, SOI1 = 305 CAD, SOI2 = 315 CAD, split ratio = 0.45, and a PES = 97% with POMDME/NG.

As the rail pressure increases, the ISHC, ISCO and ISNO<sub>x</sub> emissions remain invariant. The IFCE and combustion efficiency are also invariant across the range of rail pressures. The only parameter that is affected is the start of combustion, CA5. As the rail pressure is increased, the CA5 decreases. Since the engine is operating at a high PES value (97%), increasing the rail

pressure could be leaning out the HRF mixture so much so that it delays the start of combustion. The CA5 variations did not have a significant impact on the emissions or the efficiency values, and therefore the rail pressure was maintained at 500 bar for the final step of the boost pressure sweep.

#### **5.6.6 STEP 6: ABSOLUTE BOOST PRESSURE SWEEP**

The boost pressure sweep was performed for POMDME-natural gas combustion at an SOI1 of 305 CAD, and SOI2 of 315 CAD, a rail pressure of 500 bar, an injection split ratio of 0.45, and a PES of 97% at a load of 15 bar IMEPg. The cylinder pressure and AHRR profiles for the sweep are shown in Figure 5.34.

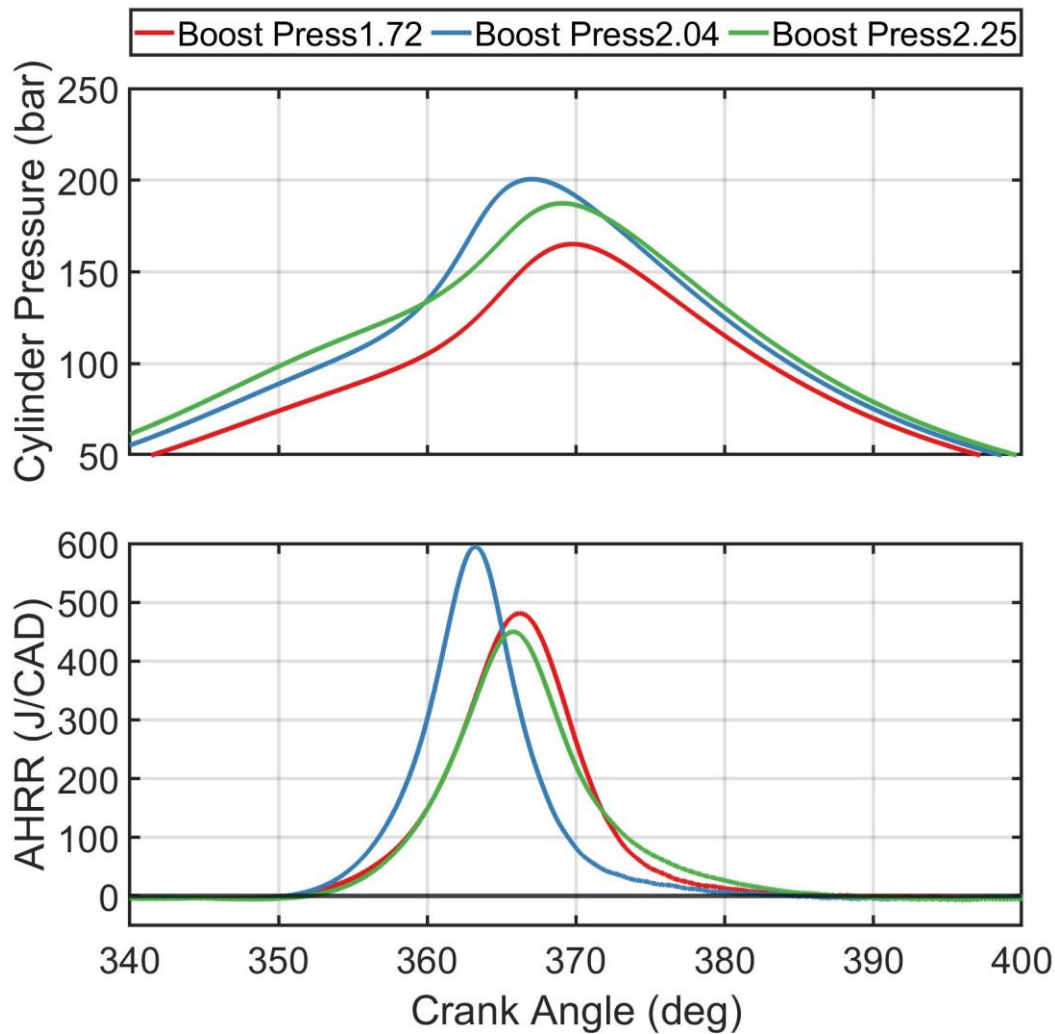


Figure 5.34. Cylinder pressure and AHRR profiles for a boost pressure sweep at 15 bar IMEP<sub>g</sub>, SOI<sub>1</sub> = 305 CAD, SOI<sub>2</sub> = 315 CAD, split ratio = 0.45, rail pressure of 500 bar, and PES = 97% with POMDME/NG.

The peak cylinder pressure for 2.04 bar boost pressure is higher than that for a peak pressure of 2.25 bar boost. This is counterintuitive and different from what was observed in the diesel-natural gas 15 bar IMEP<sub>g</sub> experiments, wherein reducing the boost pressure led to lower peak cylinder pressures. Similarly, the AHRR profile for the 2.04 bar boost pressure is significantly different from either 2.25 bar or 1.72 bar boost pressures. To attempt to explain this

phenomenon, a detailed analysis of the CA5, CA50, CA90, as well as the IFCE, combustion efficiency, MPRR,  $COV_{IMEP}$ , and the emissions results are shown in Figure 5.35.

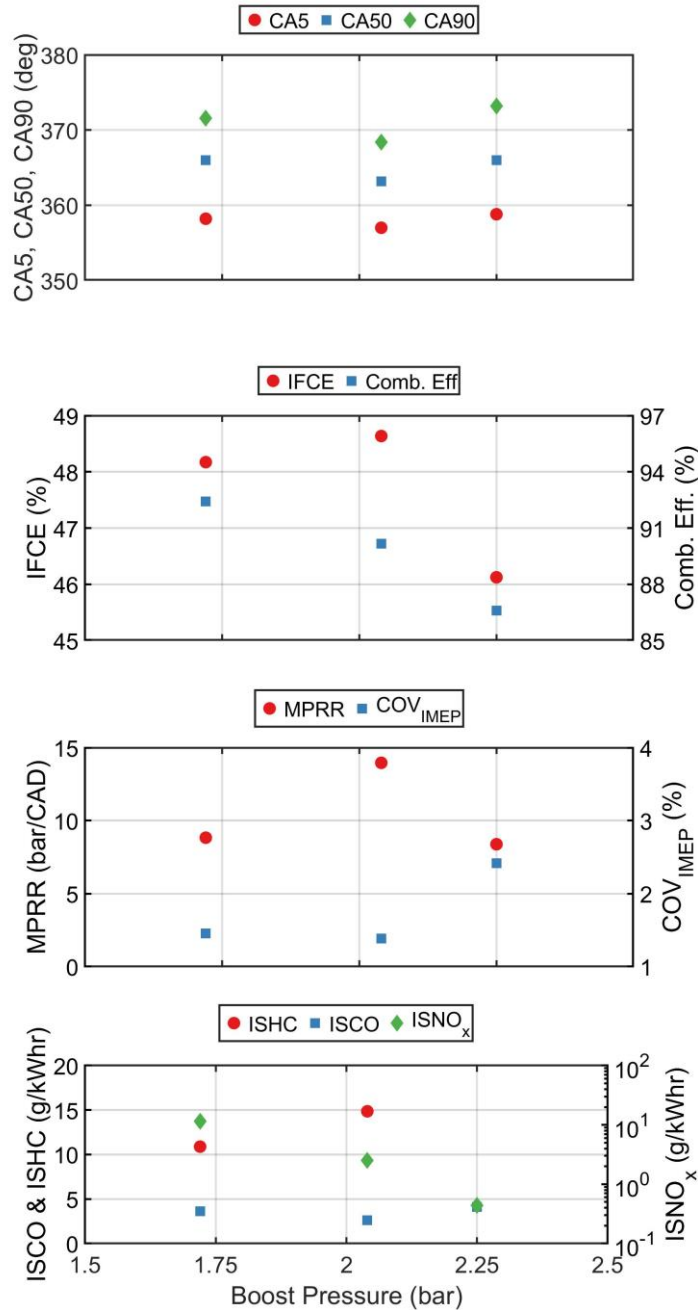


Figure 5.35. CA5, CA50, CA90, IFCE, combustion efficiency, MPRR,  $COV_{IMEP}$ , and emissions for a boost pressure sweep at 15 bar IMEPg, SOI1 = 305 CAD, SOI2 = 315 CAD, split ratio = 0.45, rail pressure of 500 bar, and a PES = 97% with POMDME/NG.

The combustion phasing advances slightly when reducing the boost pressure from 2.25 to 2.04 bar, but then moves back toward TDC again when reducing the boost pressure further. This differs from diesel-NG operation, where the CA50 remained relatively consistent throughout the boost pressure sweep. This could perhaps be a phenomenon of changing the HRF from diesel. Since POMDME has a lower LHV, more mass is required to achieve the same load. This, combined with the lower boost pressures, could allow for slightly more penetration of the HRF, which could enhance the distributed ignition effect. This could explain the lowered MPRR values at the lower boost pressure condition, as well; further numerical studies would need to be performed to definitively conclude if this is the case.

The  $COV_{IMEP}$  also continually decreases as the boost pressure is decreased.  $ISNO_x$  emissions increase dramatically as the boost pressure is decreased, since the global equivalence ratio increases as the air flowrate is decreased, resulting in less inert species and higher local temperatures. Due to high  $ISNO_x$  emissions, the boost pressure was not lowered any further, as the  $NO_x$  value reached 11 g/kWhr at the lowest boost pressure studied, which was deemed too high for the study.

As with Chapter IV, above, the emissions values for the boost pressure sweeps for both diesel/NG and POMDME/NG were presented without the use of aftertreatment devices. Seeing as aftertreatment devices can be utilized to reduce the emissions values further, and aftertreatment devices require a minimum operating temperature to work, the exhaust temperatures of both diesel/NG and POMDME/NG for the boost pressure sweep is presented in Figure 5.37, below, for future researcher to determine the applicability of certain after treatment devices with this combustion method.

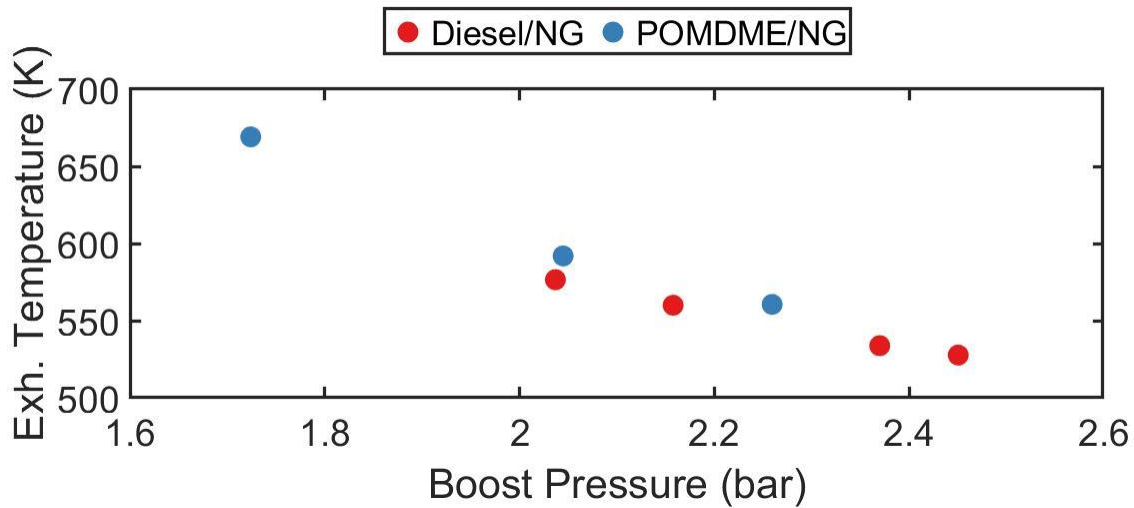


Figure 5.36. Exhaust temperatures for both diesel/NG and POMDME/NG as a function of boost pressure

## 5.7 CONCLUSIONS

An experimental campaign, consisting of multiple steps, was completed for both diesel-natural gas combustion as well as POMDME-natural gas combustion on a single cylinder research engine at a load of 15 bar IMEP<sub>g</sub>. These steps included implementing the STARS combustion strategy, with the goal of reducing emissions and improving IFCE at the high engine load. The salient conclusions are provided below:

- Operating at high loads requires much higher boost pressures and PES values compared to low load operation at 5 bar IMEP<sub>g</sub>. A boost pressure of 2.25 bar was required to start the experimental campaign for both diesel and POMDME, and PES values over 95% were needed for both fuels as well.
- The STARS strategy can be implemented at high engine loads. By implementing STARS, the MPRR limited region that typically exists with single injections is reduced, and further efficiency improvements can be made.

- Moving the coupled SOI pairs together toward TDC served as a major lever for increasing indicated fuel conversion efficiencies, with diesel natural gas combustion able to achieve upwards of 51% IFCE within the coupled SOI sweep, and POMDME-natural gas combustion able to achieve upward of 48% IFCE.
- Injection split ratio and the rail pressure do not greatly impact the efficiency values, nor the emissions values.
- Boost pressure was not as strong of a lever for reducing ISCO as it was for the 5 bar IMEPg case. This is likely due to 15 bar IMEPg already having high starting combustion efficiencies compared to the starting combustion efficiencies of 15 bar IMEPg, meaning there is not as much room for improvement.
- The order in which the coupled injection sweep and the rail pressure sweep are performed did not have any significant impact on the combustion process. This is likely due to the narrow range of pressures that can be achieved in the rail pressure sweep, which in turn limits the effectiveness of rail pressure to improve efficiency and reduce emissions.

## VI. SUMMARY OF CONCLUSIONS AND RECOMMENDATIONS FOR FUTURE WORK

Experiments were performed on two different engine platforms, one with a lower compression ratio (17:1) and one with a relatively higher compression ratio (18.5:1). The transformation region that is associated with dual fuel combustion was observed for both engines. In addition, a framework for reduced emissions implementing Spray Targeted Reactivity Stratification (STARS) was introduced. The salient conclusions from the dissertation are as follows:

- For the 17:1 compression ratio engine, in-cylinder pressure and in-cylinder bulk gas temperature do not vary significantly at the start of LTHR and the start of HTHR over the range of SOIs from 330 CAD to 320 CAD. The minimal variations in in-cylinder pressure and temperature indicated that they may not be important causes for the AHRR shape transformation and NO<sub>x</sub> reductions.
- From 0-D kinetic simulations, it is evident that large changes in the initial pressure (~ 20 bar) and initial temperature (~100 K) are needed to significantly impact heat release rates. Combining experimental and 0D chemical kinetic simulation results, it can be concluded that the minor variations in-cylinder pressure and bulk gas temperature across the SOI range are insufficient to cause the significant AHRR shape transformation observed experimentally.

- By comparison, smaller changes in the equivalence ratio can lead to larger changes in heat release rates. Combining 0D chemical kinetic and 3D CFD simulation results (including in-cylinder T, reaction ratio, CO, OH, and CO<sub>2</sub> distributions), it is concluded that local equivalence ratio stratification differences are the most likely cause for not only the AHRR shape transformation but also for the sharp decrease in NO<sub>x</sub> emissions when SOI is advanced over a narrow range (~ 10 CAD).
- Finally, since local equivalence ratio stratifications are dependent only on the fuel-air mixing process (governed by in-cylinder turbulence) at different SOIs and not necessarily on other operating conditions, it is likely that differences in local equivalence ratio stratification drive the AHRR shape transformation and the associated sharp decrease in NO<sub>x</sub> emissions observed in the literature across a narrow SOI range for other engines and under other operating conditions (e.g., specific combination of high reactivity and low reactivity fuels).
- The transformation region is also observed on a higher compression ratio engine of 18.5:1, operating at a different speed and with a different low reactivity fuel. The transformation region was also observed for both diesel-NG and POMDME -NG fueling conditions
- By using POMDME as the HRF, the effective SOI range over which the transformation region occurred diminished in size. Diesel operation showed the transformation occurring over the entire SOI= 320 to 330 range, whereas POMDME only showed significant transformation to occur from SOI = 320 to 326 CAD.
- Indicated specific carbon monoxide trends were strongly correlated with the amount of time (in crank angle degrees) that the bulk gas temperature stayed at temperatures above 20% of the maximum calculated temperature within the cylinder.

- Utilizing STARS increased the combustion stability at advanced injection timings, which is shown in the reduction in  $COV_{IMEP}$  for second injections that occurred after the first injection.
- ISHC emissions decreased the most during the PES sweep for both diesel and POMDME. This can be attributed to more diesel or POMDME being utilized to achieve a better distributed ignition, leading to faster burn rates and less unburned hydrocarbons.
- Indicated fuel conversion efficiencies as high as 45% were achieved for both fueling combination after the experimental framework was implemented. This value increased from baseline values of around 37% for both fueling combinations. Most of this IFCE improvement came from an increase in combustion efficiency, which ended with values over 95% for both fueling combinations.
- Injection split ratio experiments did not provide any significant improvement in the emissions or efficiency values across any split ratio studied.
- A decrease in the boost pressure had the most profound impact on ISCO emissions, due to the increased residence times at higher temperatures, allowing for more time for CO oxidation to occur.
- The STARS strategy can successfully be implemented at high engine loads. By implementing STARS, the MPRR limited region that typically exists with single injections is reduced, and further efficiency improvements can be made.
- Moving the coupled SOI pairs together toward TDC served as a major lever for increasing indicated fuel conversion efficiencies, with diesel natural gas combustion able to achieve upwards of 51% IFCE within the coupled SOI sweep, and POMDME-natural gas combustion able to achieve upward of 48% IFCE.

Based on the new knowledge gained in the present work, some recommendations for future work are:

- Perform an optimization study on the experimental framework presented in this dissertation, wherein the final ‘best’ point is cycled back through the experimental framework to see if any changes to the previously set experimental parameters are observed.
- Utilize the endoscope access that is currently on the cylinder head to collect further visual data within the AHRR transformation region with different fueling combinations.
- Perform the transformation region sweeps at differing intake temperatures, boost pressures, and PES values to determine the impacts that these parameters have on the transformation.
- Perform cooled and uncooled exhaust gas recirculation (EGR) experiments on the engine, and pair the EGR with the STARS strategy with diesel, and POMDME to further reduce UHC and CO emissions and to improve combustion efficiencies and engine stability.
- Perform the AHRR transformation region experiments with different low reactivity fuels, such as propane or gasoline, to determine how vastly different LRFs affect the transformation region.
- Measure engine-out emissions on a cycle-by-cycle, or if possible, on a crank angle-resolved basis using the fast FID and fast NO<sub>x</sub> analyzers to determine how cycle to cycle variations impact the emissions values.
- Implement a next-cycle control strategy using crank resolved engine out emissions measurements, and combustion phasing as feedback parameters to try to limit cycle to cycle variations and improve engine out emissions.

- Perform detailed exergy analysis on the entirety of the SCRE to determine how overall engine efficiency (IFCE) can be increased by utilizing as much of the exergy available within every aspect of the engine.
- Attach an appropriately sized motor and battery pack to the opposite side of the dual-ended dynamometer and perform hybrid heavy-duty engine studies over different emissions test cycles while varying different deployments of the hybrid system. Then use the data collected to model different series hybrid, series-parallel hybrid, or parallel hybrid configurations within a 1D simulation software.

## REFERENCES

1. Heywood, John B. Internal combustion engine fundamentals. McGraw-Hill Education, 2018.
2. "International Energy Outlook - U.S. Energy Information Administration (EIA)." International Energy Outlook 2021 - U.S. Energy Information Administration (EIA). Accessed October 5, 2022. <https://www.eia.gov/outlooks/ieo/>.
3. "Annual Energy Outlook - U.S. Energy Information Administration (EIA)." Annual Energy Outlook 2022 - U.S. Energy Information Administration (EIA). Accessed October 5, 2022. <https://www.eia.gov/outlooks/aeo/>.
4. Akihama, Kazuhiro, Yoshiki Takatori, Kazuhisa Inagaki, Shizuo Sasaki, and Anthony M. Dean. "Mechanism of the smokeless rich diesel combustion by reducing temperature." *Sae Transactions* (2001): 648-662.
5. Neely, Gary D., Shizuo Sasaki, Yiqun Huang, Jeffrey A. Leet, and Daniel W. Stewart. "New diesel emission control strategy to meet US Tier 2 emissions regulations." *SAE transactions* (2005): 512-524.
6. Srivastava, Dhananjay Kumar, Avinash Kumar Agarwal, Amitava Datta, and Rakesh Kumar Maurya, eds. *Advances in internal combustion engine research*. Springer Singapore, 2018.
7. Polk, Andrew C., Chad D. Carpenter, E. Scott Guerry, U. Dwivedi, Kalyan Kumar Srinivasan, Sundar Rajan Krishnan, and Zach L. Rowland. "Diesel-ignited propane dual fuel low temperature combustion in a heavy-duty diesel engine." *Journal of Engineering for Gas Turbines and Power* 136, no. 9 (2014). Miyamoto, Noboru, Hideyuki Ogawa, Nabi Md Nurun, Kouichi Obata, and Teruyoshi Arima. "Smokeless, low NOx, high thermal efficiency, and low noise diesel combustion with oxygenated agents as main fuel." *SAE transactions* (1998): 171-177.
8. Nabi, Md Nurun, Masahiro Minami, Hideyuki Ogawa, and Noboru Miyamoto. Ultra low emission and high performance diesel combustion with highly oxygenated fuel. No. 2000-01-0231. SAE Technical Paper, 2000.
9. Siebers, Dennis, Brian Higgins, and Lyle Pickett. "Flame lift-off on direct-injection diesel fuel jets: oxygen concentration effects." *Sae Transactions* (2002): 1490-1509.
10. Buchholz, Bruce A., A. S. E. Cheng, and R. W. Dibble. "The effect of oxygenates on diesel engine particulate matter." SP-1716, SAE (2002): 01-1705.

11. Wagner, H. Gg. "Soot formation—an overview." *Particulate Carbon* (1981): 1-29.
12. Dec, John E. "A conceptual model of DL diesel combustion based on laser-sheet imaging." *SAE transactions* (1997): 1319-1348.
13. Iannuzzi, Stefano Emanuele, Christophe Barro, Konstantinos Boulouchos, and Jakob Burger. "Combustion behavior and soot formation/oxidation of oxygenated fuels in a cylindrical constant volume chamber." *Fuel* 167 (2016): 49-59.
14. Parravicini, Matteo, Christophe Barro, and Konstantinos Boulouchos. "Compensation for the differences in LHV of diesel-OME blends by using injector nozzles with different number of holes: Emissions and combustion." *Fuel* 259 (2020): 116166.
15. Pellegrini, Leonardo, Mario Marchionna, Renata Patrini, and Salvatore Florio. "Emission performance of neat and blended polyoxymethylene dimethyl ethers in an old light-duty diesel car. No. 2013-01-1035. SAE Technical Paper, 2013.
16. Pellegrini, Leonardo, Renata Patrini, and Mario Marchionna. "Effect of POMDME blend on PAH emissions and particulate size distribution from an in-use light-duty diesel engine." In *SAE 2014 World Congress & Exhibition* SAE International, no. 2014-01-1951. 2014.
17. Pellegrini, Leonardo, Mario Marchionna, Renata Patrini, Carlo Beatrice, Nicola Del Giacomo, and Chiara Guido. "Combustion behaviour and emission performance of neat and blended polyoxymethylene dimethyl ethers in a light-duty diesel engine." In *SAE 2012 World Congress & Exhibition*, no. 2012-01-1053. 2012.
18. Omari, Ahmad, Benedikt Heuser, and Stefan Pischinger. "Potential of oxymethylenether-diesel blends for ultra-low emission engines." *Fuel* 209 (2017): 232-237.
19. García, Antonio, Javier Monsalve-Serrano, Rafael Lago Sari, and Santiago Martinez-Boggio. "Energy sustainability in the transport sector using synthetic fuels in series hybrid trucks with RCCI dual-fuel engine." *Fuel* 308 (2022): 122024.
20. García, Antonio, Javier Monsalve-Serrano, David Villalta, and María Guzmán-Mendoza. "Parametric assessment of the effect of oxygenated low carbon fuels in a light-duty compression ignition engine." *Fuel Processing Technology* 229 (2022): 107199.
21. Burger, Jakob, Markus Siegert, Eckhard Ströfer, and Hans Hasse. "Poly (oxymethylene) dimethyl ethers as components of tailored diesel fuel: Properties, synthesis and purification concepts." *Fuel* 89, no. 11 (2010): 3315-3319.
22. Voelker, Simon, Sarah Deutz, Jannik Burre, Dominik Bongartz, Ahmad Omari, Bastian Lehrheuer, Alexander Mitsos, Stefan Pischinger, André Bardow, and Niklas von der Assen. "Blend for all or pure for few? Well-to-wheel life cycle assessment of blending electricity-based OME 3–5 with fossil diesel." *Sustainable Energy & Fuels* 6, no. 8 (2022): 1959-1973.

23. Garcia, Antonio, Javier Monsalve-Serrano, David Villalta, and Maria Guzman-Mendoza. "Methanol and OME<sub>x</sub> as fuel candidates to fulfill the potential EURO VII emissions regulation under dual-mode dual-fuel combustion." *Fuel* 287 (2021): 119548.
24. Hank, Christoph, Lukas Lazar, Franz Mantei, Mohamed Ouda, Robin J. White, Tom Smolinka, Achim Schaadt, Christopher Hebling, and Hans-Martin Henning. "Comparative well-to-wheel life cycle assessment of OME<sub>3-5</sub> synfuel production via the power-to-liquid pathway." *Sustainable Energy & Fuels* 3, no. 11 (2019): 3219-3233.
25. Benajes, Jesús, Antonio García, Javier Monsalve-Serrano, and Santiago Martínez-Boggio. "Potential of using OME<sub>x</sub> as substitute of diesel in the dual-fuel combustion mode to reduce the global CO<sub>2</sub> emissions." *Transportation Engineering* 1 (2020): 100001.
26. Partridge, Kendyl, Prabhat Ranjan Jha, Kalyan Kumar Srinivasan, and Sundar Rajan Krishnan. "An experimental and computational analysis of combustion heat release transformation in dual fuel combustion." *Fuel* (Under Review)
27. Bipartisan Policy Center, *Annual Energy Outlook 2020*, Energy Information Administration, Washington, DC (2020).
28. Papagiannakis, R. G., S. R. Krishnan, D. C. Rakopoulos, K. K. Srinivasan, and C. D. Rakopoulos. "A combined experimental and theoretical study of diesel fuel injection timing and gaseous fuel/diesel mass ratio effects on the performance and emissions of natural gas-diesel HDDI engine operating at various loads." *Fuel* 202 (2017): 675-687.
29. Singh, Satbir, Sundar Rajan Krishnan, Kalyan Kumar Srinivasan, K. C. Midkiff, and S. R. Bell. "Effect of pilot injection timing, pilot quantity and intake charge conditions on performance and emissions for an advanced low-pilot-ignited natural gas engine." *International journal of Engine research* 5, no. 4 (2004): 329-348.
30. H, Guo, W. Neill, B. Liko. ASME Internal Combustion Engine Division Fall Technical Conference. ICEF2015-1051, Paper No: ICEF2015-1041, American Society of Mechanical Engineers, 2015.
31. Karim, Ghazi A. "Combustion in gas fueled compression: ignition engines of the dual fuel type." *J. Eng. Gas Turbines Power* 125, no. 3 (2003): 827-836.
32. Krishnan, Sundar R., Kalyan K. Srinivasan, S. Singh, S. R. Bell, K. C. Midkiff, W. Gong, S. B. Fiveland, and Martin Willi. "Strategies for reduced NO<sub>x</sub> emissions in pilot-ignited natural gas engines." *J. Eng. Gas Turbines Power* 126, no. 3 (2004): 665-671.
33. Yousefi, Amin, Hongsheng Guo, Shouvik Dev, Brian Liko, and Simon Lafrance. "Effect of pre-main-post diesel injection strategy on greenhouse gas and nitrogen oxide emissions of natural gas/diesel dual-fuel engine at high load conditions." *Fuel* 302 (2021): 121110.

34. Ryan Walker, N., Martin L. Wissink, Dan A. DeVescovo, and Rolf D. Reitz. "Natural gas for high load dual-fuel reactivity controlled compression ignition in heavy-duty engines." *Journal of Energy Resources Technology* 137, no. 4 (2015).
35. Karim, Ghazi A. "A review of combustion processes in the dual fuel engine—the gas diesel engine." *Progress in Energy and Combustion Science* 6, no. 3 (1980): 277-285.
36. Guerry, E. Scott, Mostafa S. Raihan, Kalyan K. Srinivasan, Sundar R. Krishnan, and Aamir Sohail. "Injection timing effects on partially premixed diesel–methane dual fuel low temperature combustion." *Applied energy* 162 (2016): 99-113.
37. Roberts, Gregory, Christine Mounaim Rousselle, Mark Musculus, Martin Wissink, Scott Curran, and Ethan Eagle. "RCCI combustion regime transitions in a single-cylinder optical engine and a multi-cylinder metal engine." *SAE International Journal of Engines* 10, no. 5 (2017): 2392-2413.
38. Wang, Zhongshu, Zhongxiang Zhao, Dan Wang, Manzhi Tan, Yongqiang Han, Zhongchang Liu, and Huili Dou. "Impact of pilot diesel ignition mode on combustion and emissions characteristics of a diesel/natural gas dual fuel heavy-duty engine." *Fuel* 167 (2016): 248-256.
39. Willems, Robbert, Frank Willems, Niels Deen, and Bart Somers. "Heat release rate shaping for optimal gross indicated efficiency in a heavy-duty RCCI engine fueled with E85 and diesel." *Fuel* 288 (2021): 119656.
40. Yousefi, Amin, Hongsheng Guo, and Madjid Birouk. "Effect of diesel injection timing on the combustion of natural gas/diesel dual-fuel engine at low-high load and low-high speed conditions." *Fuel* 235 (2019): 838-846.
41. Yousefi, Amin, Madjid Birouk, and Hongsheng Guo. "An experimental and numerical study of the effect of diesel injection timing on natural gas/diesel dual-fuel combustion at low load." *Fuel* 203 (2017): 642-657.
42. Gatowski, J. A., Balles, E.N., Chun, K. M., Nelson, F. E., Ekchian, J. A., and Heywood, J.B., "Heat release analysis of engine pressure data." SAE Technical Paper 841359. 1984.
43. Redlich, Otto, and Joseph NS Kwong. "On the thermodynamics of solutions. V. An equation of state. Fugacities of gaseous solutions." *Chemical reviews* 44.1 (1949): 233-244.
44. E. Ranzi, A. Frassoldati, R. Grana, A. Cuoci, T. Faravelli, A.P. Kelley, C.K. Law, Hierarchical and comparative kinetic modeling of laminar flame speeds of hydrocarbon and oxygenated fuels, *Progress in Energy and Combustion Science*, 38 (4), pp. 468-501 (2012), DOI: 10.1016/j.pecs.2012.03.004
45. Ansys® CHEMKIN, Release 2019 R2, Help System, Workbench 2019 R2, ANSYS, Inc.

46. Curran, Henry J., et al. "A comprehensive modeling study of n-heptane oxidation." *Combustion and flame* 114.1-2 (1998): 149-177.
47. Richards, K.J., Senecal, P.K., and Pomraning, E., CONVERGE 3.0\*, Convergent Science, Madison, WI (2021).
48. Jha, P. R., S. Wijeyakulasuriya, S. R. Krishnan, and K. K. Srinivasan. "Numerical investigations of low load diesel-methane dual fuel combustion at early diesel injection timings." *Fuel* 315 (2022): 123077.
49. Frassoldati, Alessio, Gianluca D'Errico, Tommaso Lucchini, Alessandro Stagni, Alberto Cuoci, Tiziano Faravelli, Angelo Onorati, and Eliseo Ranzi. "Reduced kinetic mechanisms of diesel fuel surrogate for engine CFD simulations." *Combustion and Flame* 162, no. 10 (2015): 3991-4007.
50. Jha, P. R., K. K. Srinivasan, and S. R. Krishnan. "Influence of Swirl Ratio on Diesel-Methane Dual Fuel Combustion: A CFD Investigation." *Internal Combustion Engine Division Fall Technical Conference*. Vol. 58318. American Society of Mechanical Engineers, 2017.
51. Kamimoto, Takeyuki, and Myurng-hoan Bae. "High combustion temperature for the reduction of particulate in diesel engines." *SAE transactions* (1988): 692-701.
52. Dec, John E. "Advanced compression-ignition engines—understanding the in-cylinder processes." *Proceedings of the combustion institute* 32, no. 2 (2009): 2727-2742.
53. Law, Chung K. *Combustion physics*. Cambridge university press, 2010.
54. Dec, John E., and Edward B. Coy. "OH radical imaging in a DI diesel engine and the structure of the early diffusion flame." *SAE transactions* (1996): 1127-1148.
55. Musculus, Mark PB, Paul C. Miles, and Lyle M. Pickett. "Conceptual models for partially premixed low-temperature diesel combustion." *Progress in energy and combustion science* 39, no. 2-3 (2013): 246-283.
56. Hannah Ritchie, Max Roser and Pablo Rosado (2020) - "CO<sub>2</sub> and Greenhouse Gas Emissions". Published online at OurWorldInData.org. Retrieved from: '<https://ourworldindata.org/co2-and-other-greenhouse-gas-emissions>' [Online Resource]
57. Kalghatgi, Gautam T., Per Risberg, and H. Ångström. "Partially pre-mixed auto-ignition of gasoline to attain low smoke and low NO<sub>x</sub> at high load in a compression ignition engine and comparison with a diesel fuel." *SAE technical paper 10006* (2007): 2007.

58. Kalghatgi, Gautam, and Bengt Johansson. "Gasoline compression ignition approach to efficient, clean and affordable future engines." *Proceedings of the institution of mechanical engineers, part D: journal of automobile engineering* 232, no. 1 (2018): 118-138.
59. Cung, Khanh Duc, Stephen Anthony Ciatti, Slavey Tanov, and Öivind Andersson. "Low-temperature combustion of high octane fuels in a gasoline compression ignition engine." *Frontiers in Mechanical Engineering* 3 (2017): 22.
60. Ciatti, Stephen, and Swami Nathan Subramanian. "An experimental investigation of low-octane gasoline in diesel engines." *Journal of engineering for gas turbines and power* 133, no. 9 (2011).
61. Christensen, Magnus, and Bengt Johansson. Supercharged homogeneous charge compression ignition (HCCI) with exhaust gas recirculation and pilot fuel. No. 2000-01-1835. SAE Technical Paper, 2000.
62. Thring, Robert H. Homogeneous-charge compression-ignition (HCCI) engines. No. 892068. SAE Technical paper, 1989.
63. Christensen, Magnus, Anders Hultqvist, and Bengt Johansson. "Demonstrating the multi fuel capability of a homogeneous charge compression ignition engine with variable compression ratio." *SAE transactions* (1999): 2099-2113.
64. Singh, Akhilendra Pratap, and Avinash Kumar Agarwal. "Combustion characteristics of diesel HCCI engine: an experimental investigation using external mixture formation technique." *Applied Energy* 99 (2012): 116-125.
65. Attard, William P., and Hugh Blaxill. A lean burn gasoline fueled pre-chamber jet ignition combustion system achieving high efficiency and low NO<sub>x</sub> at part load. No. 2012-01-1146. SAE Technical Paper, 2012.
66. Attard, William P., Hugh Blaxill, Eric K. Anderson, and Paul Litke. "Knock limit extension with a gasoline fueled pre-chamber jet igniter in a modern vehicle powertrain." *SAE International Journal of Engines* 5, no. 3 (2012): 1201-1215.
67. Gentz, Gerald, Masumeh Gholamisheeri, and Elisa Toulson. "A study of a turbulent jet ignition system fueled with iso-octane: Pressure trace analysis and combustion visualization." *Applied Energy* 189 (2017): 385-394.
68. Lawler, Benjamin, Derek Splitter, James Szybist, and Brian Kaul. "Thermally Stratified Compression Ignition: A new advanced low temperature combustion mode with load flexibility." *Applied energy* 189 (2017): 122-132.

69. Reitz, Rolf D., and Ganesh Duraisamy. "Review of high efficiency and clean reactivity controlled compression ignition (RCCI) combustion in internal combustion engines." *Progress in Energy and Combustion Science* 46 (2015): 12-71.
70. Hanson, Reed M., Sage L. Kokjohn, Derek A. Splitter, and Rolf D. Reitz. "An experimental investigation of fuel reactivity controlled PCCI combustion in a heavy-duty engine." *SAE international journal of engines* 3, no. 1 (2010): 700-716.
71. Ma, Shuaiying, Zunqing Zheng, Haifeng Liu, Quanchang Zhang, and Mingfa Yao. "Experimental investigation of the effects of diesel injection strategy on gasoline/diesel dual-fuel combustion." *Applied energy* 109 (2013): 202-212.
72. Splitter, Derek, Rolf Reitz, and Reed Hanson. "High efficiency, low emissions RCCI combustion by use of a fuel additive." *SAE International Journal of Fuels and Lubricants* 3, no. 2 (2010): 742-756.
73. Srinivasan, Kalyan K., Sundar R. Krishnan, Sabir Singh, K. Clark Midkiff, Stuart R. Bell, Weidong Gong, Scott B. Fiveland, and Martin Willi. "The advanced injection low pilot ignited natural gas engine: A combustion analysis." (2006): 213-218.
74. Srinivasan, Kalyan K., Sundar R. Krishnan, Satbir Singh, K. Clark Midkiff, Stuart R. Bell, Weidong Gong, Scott B. Fiveland, and Martin Willi. "The Advanced Low Pilot Ignited Natural Gas Engine: A Low NO<sub>x</sub> Alternative to the Diesel Engine." In *International Joint Power Generation Conference*, vol. 36924, pp. 905-912. 2003.
75. Srinivasan, K. K., P. J. Mago, G. J. Zdaniuk, L. M. Chamra, and K. C. Midkiff. "Improving the efficiency of the advanced injection low pilot ignited natural gas engine using organic Rankine cycles." *Journal of Energy Resources Technology* 130, no. 2 (2008).
76. Reitz, Rolf D. "Directions in internal combustion engine research." *Combustion and Flame* 160, no. 1 (2013): 1-8.
77. Agarwal, Avinash K., Akhilendra P. Singh, Antonio García, and Javier Monsalve-Serrano. "Challenges and Opportunities for Application of Reactivity-Controlled Compression Ignition Combustion in Commercially Viable Transport Engines." *Progress in Energy and Combustion Science* 93 (2022): 101028.
78. Leach, Felix, Gautam Kalghatgi, Richard Stone, and Paul Miles. "The scope for improving the efficiency and environmental impact of internal combustion engines." *Transportation Engineering* 1 (2020): 100005.
79. National Research Council. *Assessment of fuel economy technologies for light-duty vehicles*. National Academies Press, 2011.

80. EIA, U. "US Energy Information Administration Annual Energy Outlook 2022." US Department of Energy: Washington, DC, USA (2022).
81. "Final Regulation Order Title 13 - California Air Resources Board." Accessed August 31, 2022. <https://ww2.arb.ca.gov/sites/default/files/barcu/regact/2020/hdomnibuslownox/froa-1.pdf>.
82. Boyer, Ralph L. Status of dual fuel engine development. No. 490018. SAE Technical Paper, 1949.
83. Elliott, Martin A., and Rogers F. Davis. "Dual-Fuel Combustion in Diesel Engines." *Industrial & Engineering Chemistry* 43, no. 12 (1951): 2854-2864.
84. Singh, Akhilendra Pratap, and Avinash Kumar Agarwal. "Combustion characteristics of diesel HCCI engine: an experimental investigation using external mixture formation technique." *Applied Energy* 99 (2012): 116-125.
85. Singh, Gajendra, Akhilendra Pratap Singh, and Avinash Kumar Agarwal. "Experimental investigations of combustion, performance and emission characterization of biodiesel fuelled HCCI engine using external mixture formation technique." *Sustainable Energy Technologies and Assessments* 6 (2014): 116-128.
86. Yousefi, Amin, Hongsheng Guo, Shouvik Dev, Simon Lafrance, and Brian Liko. "A study on split diesel injection on thermal efficiency and emissions of an ammonia/diesel dual-fuel engine." *Fuel* 316 (2022): 123412.
87. Wüthrich, Silas, Patrick Cartier, Pascal Süess, Bruno Schneider, Peter Obrecht, and Kai Herrmann. "Optical investigation and thermodynamic analysis of premixed ammonia dual-fuel combustion initiated by dodecane pilot fuel." *Fuel Communications* 12 (2022): 100074.
88. Yousefi, Amin, Hongsheng Guo, and Madjid Birouk. "Split diesel injection effect on knocking of natural gas/diesel dual-fuel engine at high load conditions." *Applied Energy* 279 (2020): 115828.
89. Ulishney, Christopher J., and Cosmin E. Dumitrescu. "Effect of gas composition on the performance and emissions of a dual-fuel diesel-natural gas engine at low load conditions." *Fuel* 324 (2022): 124531.
90. Kang, Jaegu, Sanghyun Chu, Jeongwoo Lee, Gyujin Kim, and Kyoungdoug Min. "Effect of operating parameters on diesel/propane dual fuel premixed compression ignition in a diesel engine." *International Journal of Automotive Technology* 19, no. 1 (2018): 27-35.
91. Hodges, Kyle A., Andrea Aniello, Sundar Rajan Krishnan, and Kalyan Kumar Srinivasan. "Impact of propane energy fraction on diesel-ignited propane dual fuel low temperature combustion." *Fuel* 209 (2017): 769-775.

92. Li, Yaopeng, Ming Jia, Yachao Chang, Maozhao Xie, and Rolf D. Reitz. "Towards a comprehensive understanding of the influence of fuel properties on the combustion characteristics of a RCCI (reactivity controlled compression ignition) engine." *Energy* 99 (2016): 69-82.
93. Walker, N. Ryan, Adam B. Dempsey, Michael J. Andrie, and Rolf D. Reitz. "Use of low-pressure direct-injection for reactivity controlled compression ignition (RCCI) light-duty engine operation." *SAE International Journal of Engines* 6, no. 2 (2013): 1222-1237.
94. DelVescovo, Dan, Sage Kokjohn, and Rolf Reitz. "The effects of charge preparation, fuel stratification, and premixed fuel chemistry on reactivity controlled compression ignition (RCCI) combustion." *SAE International Journal of Engines* 10, no. 4 (2017): 1491-1505.
95. Srinivasan, Kalyan Kumar, Sundar Rajan Krishnan, Prabhat Ranjan Jha, and Hamidreza Mahabadipour. "Cyclic combustion variations in diesel–natural gas dual fuel engines." *Natural Gas Engines* (2019): 329-358.
96. Carlucci, A. P., A. Ficarella, D. Laforgia, and L. Strafella. "Improvement of dual-fuel biodiesel-producer gas engine performance acting on biodiesel injection parameters and strategy." *Fuel* 209 (2017): 754-768.
97. Yadav, Jaykumar, and A. Ramesh. "Injection strategies for reducing smoke and improving the performance of a butanol-diesel common rail dual fuel engine." *Applied energy* 212 (2018): 1-12.
98. Bartolucci, Lorenzo, Stefano Cordiner, Vincenzo Mulone, Sundar R. Krishnan, and Kalyan K. Srinivasan. "A Computational Investigation of the Impact of Multiple Injection Strategies on Combustion Efficiency in Diesel–Natural Gas Dual-Fuel Low-Temperature Combustion Engines." *Journal of Energy Resources Technology* 143, no. 2 (2021).
99. Hariharan, D., Krishnan, S.R., Srinivasan, K.K., and Sohail, A., "Multiple Injection Strategies for Reducing HC and CO Emissions in Diesel-Methane Dual-Fuel low Temperature Combustion, 121372," *Fuel* 305 (2021).
100. Tong, Laihui, Hu Wang, Zunqing Zheng, Rolf Reitz, and Mingfa Yao. "Experimental study of RCCI combustion and load extension in a compression ignition engine fueled with gasoline and PODE." *Fuel* 181 (2016): 878-886.
101. Narayanan, A., Partridge, K., Anandaraman, N., Hariharan, D., Krishnan, S., and Srinivasan, K. "Effect of Injection Timing on Cyclic Variability of Diesel Pilot Ignited Methane Combustion in a Compression Ignition Engine", in 12th U. S. National Combustion Meeting, May 2021

102. Hariharan, Deivanayagam, Kendyl Partridge, Abhinandhan Narayanan, Kalyan Srinivasan, Sundar Rajan Krishnan, and Nandagopalan Anandaraman. Strategies for Reduced Engine-Out HC, CO, and NO<sub>x</sub> Emissions in Diesel-Natural Gas and POMDME-Natural Gas Dual-Fuel Engine. No. 2022-01-0460. SAE Technical Paper, 2022.
103. McBride, Bonnie J. Coefficients for calculating thermodynamic and transport properties of individual species. Vol. 4513. National Aeronautics and Space Administration, Office of Management, Scientific and Technical Information Program, 1993.
104. Krishnan, Sundar Rajan, Kalyan Kumar Srinivasan, and Mostafa Shameem Raihan. "The effect of injection parameters and boost pressure on diesel-propane dual fuel low temperature combustion in a single-cylinder research engine." *Fuel* 184 (2016): 490-502.
105. Raihan, Mostafa S., Edward S. Guerry, Umang Dwivedi, Kalyan Kumar Srinivasan, and Sundar Rajan Krishnan. "Experimental analysis of diesel-ignited methane dual-fuel low-temperature combustion in a single-cylinder diesel engine." *Journal of Energy Engineering* 141, no. 2 (2015): C4014007.
106. Zeldvich, Ya B. "The oxidation of nitrogen in combustion and explosions." *J. Acta Physicochimica* 21 (1946): 577.
107. Sjöberg, Magnus, and John E. Dec. "An investigation into lowest acceptable combustion temperatures for hydrocarbon fuels in HCCI engines." *Proceedings of the Combustion Institute* 30, no. 2 (2005): 2719-2726.
108. Meinshausen, Malte, Nicolai Meinshausen, William Hare, Sarah CB Raper, Katja Frieler, Reto Knutti, David J. Frame, and Myles R. Allen. "Greenhouse-gas emission targets for limiting global warming to 2 C." *Nature* 458, no. 7242 (2009): 1158-1162.
109. O'Donnell, Ryan N., Thomas R. Powell, Zoran S. Filipi, and Mark A. Hoffman. "Estimation of thermal barrier coating surface temperature and heat flux profiles in a low temperature combustion engine using a modified sequential function specification approach." *Journal of Heat Transfer* 139, no. 4 (2017).
110. Powell, Tommy, Nick Killingsworth, Mark Hoffman, Ryan O'Donnell, Robert Prucka, and Zoran Filipi. "Predicting the gas-wall boundary conditions in a thermal barrier coated low temperature combustion engine using sub-coating temperature measurements." *International Journal of Powertrains* 6, no. 2 (2017): 125-150.
111. Li, Yangtao, Amir Khajepour, and Cécile Devaud. "Realization of variable Otto-Atkinson cycle using variable timing hydraulic actuated valve train for performance and efficiency improvements in unthrottled gasoline engines." *Applied energy* 222 (2018): 199-215.

112. Osorio, Julian D., and Alejandro Rivera-Alvarez. "Efficiency enhancement of spark-ignition engines using a Continuous Variable Valve Timing system for load control." *Energy* 161 (2018): 649-662.
113. Wang, Tianyou, Yajun Zhang, Zhijun Peng, and Gequn Shu. "A review of researches on thermal exhaust heat recovery with Rankine cycle." *Renewable and sustainable energy reviews* 15, no. 6 (2011): 2862-2871.
114. Xie, Hui, Le Li, Tao Chen, Weifei Yu, Xinyan Wang, and Hua Zhao. "Study on spark assisted compression ignition (SACI) combustion with positive valve overlap at medium-high load." *Applied energy* 101 (2013): 622-633.
115. Manofsky, Laura, Jiri Vavra, Dennis Assanis, and Aristotelis Babajimopoulos. "Bridging the gap between HCCI and SI: spark-assisted compression ignition." *SAE technical paper 2* (2011): 011-01.
116. Olesky, Laura Manofsky, Jason B. Martz, George A. Lavoie, Jiri Vavra, Dennis N. Assanis, and Aristotelis Babajimopoulos. "The effects of spark timing, unburned gas temperature, and negative valve overlap on the rates of stoichiometric spark assisted compression ignition combustion." *Applied Energy* 105 (2013): 407-417.
117. National Research Council. *Review of the 21st Century Truck Partnership, second report.* National Academies Press, 2012.
118. Genzale, C. L., S-C. Kong, and Rolf D. Reitz. "Modeling the effects of variable intake valve timing on diesel HCCI combustion at varying load, speed, and boost pressures." *Journal of engineering for gas turbines and power* 130, no. 5 (2008).
119. Canakci, M., and R. D. Reitz. "Effect of optimization criteria on direct-injection homogeneous charge compression ignition gasoline engine performance and emissions using fully automated experiments and microgenetic algorithms." *J. Eng. Gas Turbines Power* 126, no. 1 (2004): 167-177.
120. Nieman, Derek E., Adam B. Dempsey, and Rolf D. Reitz. "Heavy-duty RCCI operation using natural gas and diesel." *SAE International Journal of Engines* 5, no. 2 (2012): 270-285.
121. Lim, Jae Hyung, and Rolf D. Reitz. "High load (21 bar IMEP) dual fuel RCCI combustion using dual direct injection." *Journal of Engineering for Gas Turbines and Power* 136, no. 10 (2014).
122. Agarwal, Avinash Kumar, Akhilendra Pratap Singh, and Rakesh Kumar Maurya. "Evolution, challenges and path forward for low temperature combustion engines." *Progress in energy and combustion science* 61 (2017): 1-56.

123. Ra, Youngchul, Paul Loeper, Rolf Reitz, Michael Andrie, Roger Krieger, David Foster, Russ Durrett et al. "Study of high speed gasoline direct injection compression ignition (GDICI) engine operation in the LTC regime." *SAE International Journal of Engines* 4, no. 1 (2011): 1412-1430.
124. Yousefi, Amin, Hongsheng Guo, Madjid Birouk, Brian Liko, and Simon Lafrance. "Effect of post-injection strategy on greenhouse gas emissions of natural gas/diesel dual-fuel engine at high load conditions." *Fuel* 290 (2021): 120071.
125. Ryan Walker, N., Martin L. Wissink, Dan A. DeVescovo, and Rolf D. Reitz. "Natural gas for high load dual-fuel reactivity controlled compression ignition in heavy-duty engines." *Journal of Energy Resources Technology* 137, no. 4 (2015).
126. Guo, Hongsheng, and Brian Liko. "Injector tip temperature and combustion performance of a natural gas-diesel dual fuel engine at medium and high load conditions." In *Internal Combustion Engine Division Fall Technical Conference*, vol. 51982, p. V001T03A021. American Society of Mechanical Engineers, 2018.
127. Guo, Hongsheng, Brian Liko, and Jennifer Littlejohns. "Combustion and greenhouse gas emissions of a natural gas-Diesel dual fuel engine at low and high load conditions." In *Internal Combustion Engine Division Fall Technical Conference*, vol. 59346, p. V001T02A004. American Society of Mechanical Engineers, 2019.

## APPENDIX

As mentioned in Chapter II, a 0D chemical kinetic simulation was performed in ANSYS Chemkin [46] using an HCCI IC engine model. The model was setup using the 18.5 compression ratio engine which has been described in the chapters above. Table A.1 below details the specific operating parameters that were chosen.

Table A.1. HCCI IC engine model parameters.

Parameter	Value
Starting Crank Angle (degrees after TDC)	-150
Ending Crank Angle (degrees after TDC)	180
Engine Speed (RPM)	1339
Compression Ratio	18.5
Bore (mm)	123
Stroke (mm)	152
Connecting Rod Length (mm)	244.5
Initial Temperature (K)	324
Initial Pressure (bar)	1.69

The initial temperature and pressure were determined based off of measured in-cylinder pressure and calculated in-cylinder temperature values at IVC for experiments performed in Chapter III, which looked at the transformation region on the 18.5 compression ratio engine platform.

The catalyst for performing these experiments was to rule out the possibility that changes in the instantaneous volume (seeing as an IC engine is a crank slider mechanism, and volume will change as a function of crank angle) would impact the transformation region. The same underlying hypothesis that the local reactivity within the combustion chamber is the underlying governing cause for the transformation region still exists. To test this using the HCCI engine model, the amount of fuel split between the n-dodecane and the methane used inside the cylinder was varied, while keeping the global equivalence ratio a constant. Table A.2 shows the operating parameters for five different cases that were considered for these simulations.

Table A.2. Operating parameters for each case

	Case 1	Case 2	Case 3	Case 4	Case 5
Equivalence Ratio	0.315	0.315	0.315	0.315	0.315
CH4 Fuel Fraction of Total Species	0.974	0.904	0.840	0.783	0.734
Dodecane Fuel Fraction of Total Species	0.026	0.096	0.160	0.217	0.266

The fuel fraction splits were selected from the equivalence ratio sweep section of the 0D chemical kinetic simulations studied in Chapter II. By choosing these values, and performing them in a model that is based off of the 18.5:1 compression ratio engine, two things can be accomplished: 1) the effects that varying volume have or do not have on the transformation region can be compared directly with the constant volume cases, and 2) since pressure and temperature are allowed to vary with volume in the HCCI reactor, the direct effects that differing fuel splits have on the combustion process can be evaluated. The net heat release rate for each one of the cases described above can be seen in Figure A.1.

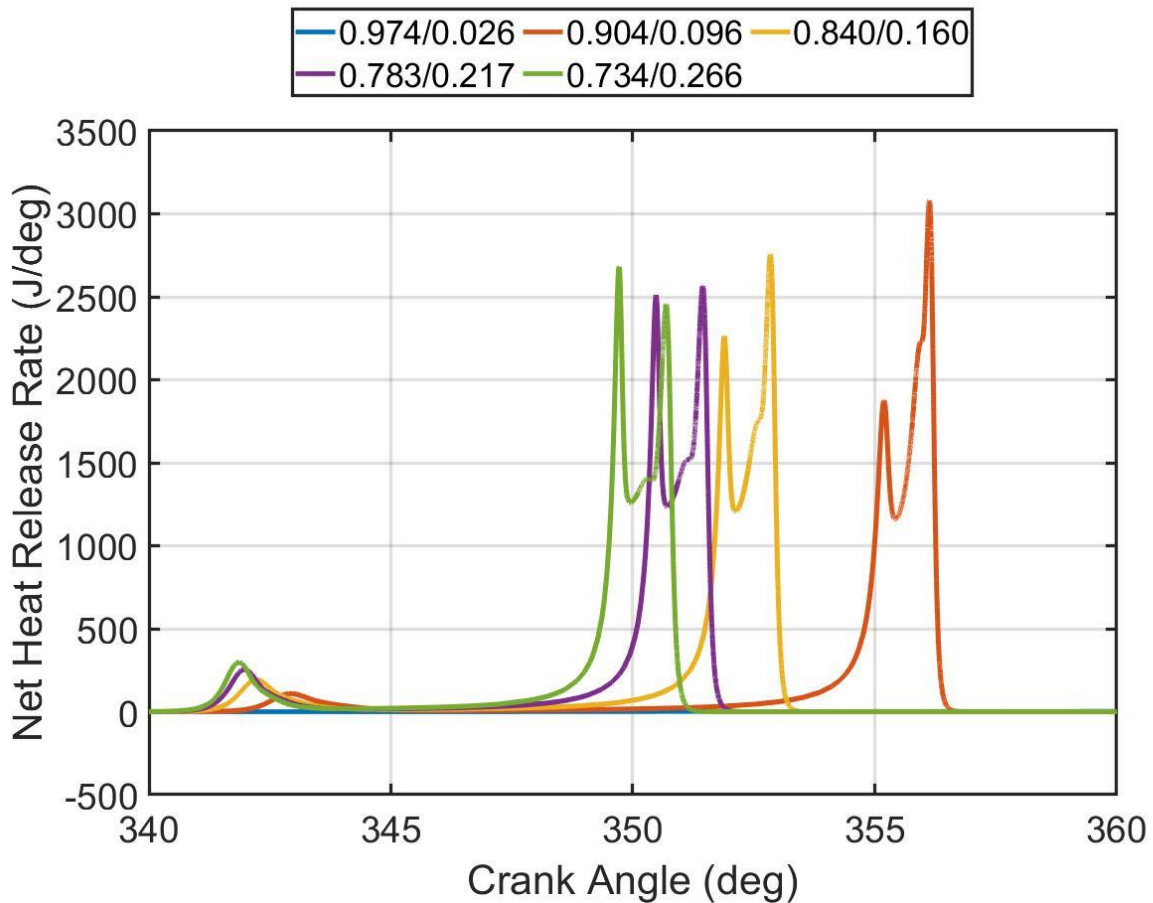


Figure A.1. Net heat release rate for each HCCI IC engine case.

When comparing the results to the constant volume analysis to the results from the HCCI engine analysis, it is clear that there are similarities when increasing the amount of n-dodecane that is present within the combustion chamber. Firstly, the amount of time between the low temperature heat release spike, and the high temperature heat release spike reduces as the amount of n-dodecane is increased. Secondly, the low temperature heat release profile increases in magnitude, and also increases earlier as the amount of n-dodecane is increased. This mirrors what was shown in the constant volume analysis; therefore, the conclusions based on the 0D analysis put forth in Chapter II are deemed valid. Furthermore, since these results appear to be

consistent with the results from the constant volume simulations, it can be concluded that the changes in volume from crank angle to crank angle do not significantly impact the transformation region process, and rather the process is governed by the changes in the fuel reactivity that occur locally within the cylinder.